

# **RESERVOIR ENGINEERING RESEARCH INSTITUTE**

**Research Program on Fractured Petroleum Reservoirs**

**DE-FG26-99BC15177**

**Final Report**

**Contract Date: 3/14/99 – 3/13/02**

**DOE Program Manager: Mr. Purna Halder**

**Principal Investigator: Dr. Abbas Firoozabadi**

**April 12, 2002**

**385 Sherman Ave., Suite 2B  
Palo Alto, CA 94306  
(650) 326-9172**

# Table of Contents

Disclaimer .....	iii
Acknowledgements .....	iv
List of Tables .....	v
List of Figures .....	vii
Summary .....	xiii
Chapter I – Water Injection in Fractured Porous Media .....	1
Part I – Numerical Simulation of Water Injection in 2D Fractured Media Using Discrete-Fracture Model .....	1
Part II – Analytical Solutions for 1-D Countercurrent Imbibition in Water-Wet Media .....	35
Part III – Effect of Viscous Forces and Initial Water Saturation on Water Injection in Water-Wet and Mixed-Wet Fractured Porous Media .....	53
Part IV – Recovery Mechanisms in Fractured Reservoirs and Field Performance .....	72
Chapter II – Gravitational Potential Variations of the Sun and Moon for the Estimation of Reservoir Properties .....	83
Part I – Gravitational Potential Variations of the Sun and Moon for the Estimation of Reservoir Compressibility .....	83
Part II – Gravitational Potential Variations of the Sun and Moon for the Estimation of Reservoir Permeability .....	106
Chapter III – Diffusion in Porous Media from Irreversible Thermodynamics .....	126
Part I – Two-Phase Multicomponent Diffusion and Convection for Reservoir Initialization .....	126
Part II – Interpretation of the Unusual Fluid Distribution in the Yufutsu Gas-Condensate Field .....	146
Part III – Modeling of the Unusual GOR Performance in the Yufutsu Gas-Condensate Field .....	177
Chapter IV – Bubble Nucleation in Porous Media and Solution Gas Drive in Heavy Oil Reservoirs .....	203
Part I – Gas and Liquid-Phase Relative Permeabilities for Cold Production from Heavy Oil Reservoirs. ....	203
Part II – Effect of GOR, Temperature, and Initial Water Saturation on Solution-Gas Drive in Heavy-Oil Reservoirs. ....	243
Part III – Mechanisms of Solution Gas Drive in Heavy Oil Reservoirs. ....	260

## **Disclaimer**

This report was prepared as an account of work sponsored by an agency of the United States Government. Neither the United States Government nor any agency thereof, nor any of their employees, makes any warranty, express or implied, or assumes any legal liability or responsibility for the accuracy, completeness, or usefulness of any information, apparatus, product, or process disclosed, or represents that its use would not infringe privately owned rights. Reference herein to any specific commercial product, process, or service by trade name, trademark, manufacturer or otherwise does not necessarily constitute or imply its endorsement, recommendation, or favoring by the United States government or any agency thereof. The views and opinions of authors expressed herein do not necessarily state or reflect those of the United States Government or any agency thereof.

## Acknowledgements

The work presented in the final report prepared for the US DOE National Petroleum Technology Office was sponsored by the US DOE grant DE-FG26-99BC15177 and major oil companies in the period of March 1999-March 2002. The major oil companies included: Abu Dhabi National Oil Company (ADNOC) (UAE), BHP Petroleum Pty. Ltd. (Australia), BP Amoco (UK), Chevron Petroleum Technology Company (USA), Conoco Inc. (USA), Elf Aquitaine Production (France), Exxon Production Research Company (USA), ExxonMobil Upstream Research Company (USA), JAPEx (Japan), Maersk Oil and Gas (Denmark), Marathon Oil Company (USA), Mobil Technology Corporation (USA), Norsk Hydro Production, A. S. (Norway), Petrobras, S. A. (Brazil), Petronas Research and Scientific Services SDN BHD (Malaysia), Phillips Petroleum Company (USA), SAGA Petroleum A/S (Norway), Saudi Aramco (Saudi Arabia), Shell Exploration and Production Company (USA), Statoil, A/S (Norway), Texaco, Inc. (USA), Total (France), TotalFinaElf (France).

DOE's support was crucial to undertake a comprehensive research effort on theoretical, computational, and experimental research on fractured petroleum reservoirs and fundamental understanding of multiphase flow in permeable media. The combination of DOE support and the major oil companies from the US, Europe, Middle East, South America, Japan, and Asia has helped RERI to perform research on some of the most challenging aspects of fractured reservoirs. In a field example from a gas condensate fractured reservoir, there is data indicating that a heavy fluid can float on top of a light fluid. Interestingly, our work on thermodynamics of irreversible processes can model this behavior. This is an example of the type of fun we have had in our research work. During the 1999-2002 period, our project managers with DOE were Dr. Bob Lemmon, Mr. Purna Halder, and Mr. Chandra Nautiyal. Their support allowed us to focus on topics of a diverse nature in our research program.

# List of Tables

## Chapter I

### Part I

1	Fluid properties . . . . .	22
2	Relative permeability and capillary pressure for water-wet fractured media . . . . .	22
3	Relative permeability and capillary pressure for water-wet fractured media. Matrix data (top), fracture data (bottom) . . . . .	22
4	Relative permeability and capillary pressure for mixed-wet fractured media. Matrix data (top), fracture data (bottom) . . . . .	23
5	Relative error in oil recovery due to mesh quality. Single fracture configuration with $q = +45^\circ$ . . . . .	23
6	Number of mesh points for the discrete-fracture and single-porosity models. Single fracture configuration. . . . .	23

### Part II

1	Values of Various Parameters Used for Numerical and Graphical Illustrations . . . . .	49
---	--	----

### Part III

1	Relevant Data for Configuration A . . . . .	63
2	Relevant Data for Configuration B. . . . .	64

## Chapter II

### Part I

1	Estimated compressibility . . . . .	89
B-1	Variants of $r$ , $I_1$ , and $I_2$ in the outer core of the earth. . . . .	97

## Chapter III

### Part II

1	Data at the reference-interval in well AK1 . . . . .	167
2	Relevant data at the reference-interval in wells MY1 and NM1 . . . . .	168

### Part III

1	Well depth in the formation . . . . .	190
2	Composition ( $x_i$ ) and molecular weight ( $M$ ) for the PVT sample AK1 No. 4 . . . . .	190

## **Chapter IV**

### **Part I**

1	Properties of the Live Oils. ....	214
2	Data of Sandpack and Coreholder. ....	214
3	Experimental Data. ....	214
4	Gas Bubble Flow Pattern for Test 2. ....	215
5	Data of Differential Pressure Fluctuation for Tests 4, 5, and 6. ....	215

### **Part II**

1	Oil Relevant Properties. ....	254
2	Properties of Sandpacks. ....	254
3	Table-3 Test Conditions and Results. ....	255

# List of Figures

## Chapter I

### Part I

1	Schematic representation of the discrete fracture approximation. ....	24
2	Discretization of the discrete-fractured media: matrix is discretized using linear triangular elements, fractures are discretized by linear line elements. ....	24
3	Influence of gridding on the sharpness of the interface along the diagonal at 0.4 PV water injection. Homogeneous porous media. Domain size = 1m x 1m. ....	25
4	Geometrical configuration of the fracture in the fractured media with a single fracture. ....	25
5	Gridding of the fractured media with a single fracture. From left to right: 153, 289, 581, 817, and 1266 mesh points. ....	25
6	Oil recovery vs PV injection for different griddings: fractured media with a single fracture (water-wet), $q = +45^\circ$ . Domain size = 1m x 1m. ....	26
7	Water saturation profiles at 0.5 PV water injection: fractured media with a single fracture. Domain size = 1m x 1m. ....	27
8	Oil production history: fractured media with a single fracture. Domain size = 1m x 1m. ....	28
9	Water saturation profile along the fracture (left) and saturation evolution with time in the fracture at the center of the porous media (right). Single fracture configuration with $q = +45^\circ$ . Domain size = 1m x 1m. ....	29
10	Gridding for the complex fractured media: number of mesh points = 898, domain size = 1m x 1m. ....	30
11	Water saturation profiles at 0.15, 0.30, 0.45, and 0.60 PV (from top to bottom) water injection: complex fractured media. Domain size = 1m x 1m. $P_c^f$ . ....	31
12	Effect of capillary pressure on oil recover: fractured media with complex fractures, domain size = 1m x 1m. ....	32
13	Gridding of the fractured porous media with complex fractures: Domain size = 25m x 25m, number of mesh points = 2277. ....	32
14	Influence of matrix and fractures capillary pressure on oil recovery. ....	33
15	Water saturation profiles at 1 and 1.5 PV (from left to right) water injection: Domain size = 25m x 25m. ....	34

### Part II

1	Dependence of the “diffusion” coefficient on the reduced water saturation: solid curve – equation (6); dashed curve – equation (9). ....	49
2	Schematic of oil-saturated (a) rod-like, (b) cylindrical, and (c) spherical water-wet core immersed in water (the arrows indicate water (W) inflow and oil (O) outflow). ....	50
3	Time dependence of the distance $t$ raveled by the water front in linear countercurrent imbibition: circles – numerical data of <i>Pooladi-Darvish and Firoozabadi</i> [2000]; line – best fit according to (19). ....	50
4	Water saturation profile in linear countercurrent imbibition. ....	51
5	Water saturation profile in (a) cylindrical, and (b) spherical countercurrent imbibition: equation (44) in (a) and equation (50) in (b). ....	51
6	Time dependence of the fraction of oil recovered in countercurrent imbibition:	

	curves L, C and S – equations (58), (66) and (72) for linear, cylindrical and spherical imbibition, respectively; circles – numerical data of <i>Pooladi-Darvish and Firoozabadi</i> [2000] for linear imbibition. The arrows indicate the end of the initial stage of the process	52
7	Time dependence of the fraction of oil recovered in spherical countercurrent imbibition: circles – experimental data of <i>Tang and Firoozabadi</i> [2001]; line – equation (72). The arrow indicates the end of the initial stage of the process	52

### Part III

1	Configurations of Kansas Outcrop Chalks Used in the Experiments.	65
2	Schematic of Apparatuses for Water Injection and Spontaneous Imbibition Tests	65
3	Spontaneous Imbibition of the Chalk Prior to Wettability Alteration: Configuration A	66
4	Wettability Transition Towards More Water-Wetness with Repeated Spontaneous Imbibition Tests: Configuration A (CSA=100 ppm)	66
5	Spontaneous Imbibition of the Chalk after Wettability Alteration: Configuration A (CSA=200 ppm)	66
6	Spontaneous Imbibition of the Chalk after Wettability Alteration: Configuration A (CSA=500 ppm)	67
7	Spontaneous Imbibition of the Chalk after Wettability Alteration: Configuration A (CSA=1,000 ppm)	67
8	Effect of Pressure Gradient on Oil Recovery by Water Injection: Strongly Water-Wet, Configuration A	67
9	Effect of Pressure Gradient on Oil Recovery by Water Injection: Weakly Water-Wet, Configuration A (CSA=500 ppm)	68
10	Effect of Pressure Gradient on Oil Recovery by Water Injection: Intermediate-Wet, Configuration A (CSA=1,000 ppm)	68
11	Effect of Pressure Gradient on Oil Recovery by Water Injection for Three Wettability States: Configuration A.	68
12	Effect of Initial Water Saturation on Oil Recovery by Water Injection: Strongly Water-Wet, Configuration A	69
13	Effect of Initial Water Saturation on Oil Recovery by Water Injection: Weakly Water-Wet, Configuration A (CSA=500 ppm)	69
14	Effect of Initial Water Saturation on Oil Recovery by Water Injection: Intermediate-Wet, Configuration A (CSA=1,000 ppm)	69
15	Effect of Pressure Gradient on Oil Recovery by Water Injection: Strongly Water-Wet, Configuration B.	70
16	Effect of Pressure Gradient on Oil Recovery by Water Injection: Weakly Water-Wet, Configuration B (CSA=500 ppm)	70
17	Effect of Initial Water Saturation on Oil Recovery by Water Injection: Strongly Water-Wet, Configuration B.	70
18	Effect of Initial Water Saturation on Oil Recovery by Water Injection: Weakly Water-Wet, Configuration B (CSA=500 ppm)	71
19	Estimated Capillary Pressure Curves from Water Injection: Configuration A	71

### Part IV

1	Gas-oil gravity drainage in a homogenous and in a layered column (adapted from Ref. 6)	80
2	Gas-oil gravity from a tall block, and a stacked-block system (adapted from Ref. 7)	80
3	Matrix and fracture capillary pressures (Ref. 8).	80



4	Ekofisk Field oil production rates and the response to water injection (adapted from Ref. 1) . . . . .	81
5	Fracture water saturation, and water and oil fluxes from fine-grid simulation (Ref. 14). . . . .	81
6	Recovery Performance of a Water-Wet Chalk Matrix Block ( $k=1.5\text{md}$ , $d=30\%$ ) to water injection and to immersion (adapted from Ref. 12) . . . . .	81
7	Effect of Pressure Gradient on Oil Recovery from the Chalk Sample ( $k=1.3\text{md}$ , $f=30\%$ ): Water-Wet ( $I_{aw}=1.0$ ) (adapted from Ref. 15) . . . . .	81
8	Effect of Pressure Gradient on Oil Recovery from the Chalk Sample ( $k=1.3\text{md}$ , $f=30\%$ ): Water-Wet ( $I_{aw}=1.0$ ) and Weakly Water-Wet ( $I_{aw}=0.09$ ) (adapted from Ref. 15). . . . .	82
9	Estimated Negative Capillary Pressure Curves for Water-Wet ( $I_{aw}=1.0$ ) and Weakly Water-Wet ( $k=1.3\text{md}$ ) Chalk Sample (adapted from Ref. 15) . . . . .	82

## Chapter II

### Part I

1	Amplitude squared of pressure variation as a function of frequency from a 128K FFT - Well T . . . . .	98
2	Short interval of pressure data plotted in the time domain, which was used for the spectral plot of Fig. 1 - Well T: Starting at 1215 10/17/96. . . . .	98
3a	Pressure Data from Well T: Starting at 1215, 10/17/96 . . . . .	98
3b	Pressure Data from Well T: Starting at 1231 4/22/97 . . . . .	98
4a	Potential and Pressure from Well T: Starting at 1215 10/17/96 (time lag adjusted) . . . . .	99
4b	Potential and Pressure from Well T: Starting at 1215 10/17/96 (time lag adjusted). . . . .	99
4c	Potential and Pressure from Well T: Starting at 1215 10/17/96 (time lag adjusted). . . . .	99
4d	Potential and Pressure from Well T: Starting at 1231 4/22/97 (time lag adjusted). . . . .	99
4e	Potential and Pressure from Well T: Starting at 1231 4/22/97 (time lag adjusted). . . . .	100
A-1	Bispherical axisymmetric coordinate system about the earth and the moon. . . . .	101
A.2	Geocentric coordinates for the potential expression. $P$ is the observation point, $Z$ is the lunar zenith point, and $t_1$ is the moon sidereal time. . . . .	102
A.3	The right spherical triangle with the lunar orbit as its hypotenuse. $s_l$ is the lunar longitude, $a$ is the right ascension, and $d$ is the declination. . . . .	103
A.4	The two spherical triangles formed by the equator, the ecliptic, and the lunar orbit. $b$ is the declination of the lunar orbit with respect to the ecliptic, $N$ is the angle between the spring equinox and the ascending intersection between the lunar orbit and the ecliptic, and $g$ is the spring equinox. . . . .	104
B.1	First order deformation, shown by the dotted contour, in response to the gravitational field generated by a mass in proximity to the earth. The scale of the deformation is exaggerated for clarity. Points at the top and bottom of the earth undergo differential expansion, and points along the axis of the line joining the earth and the mass undergo differential compaction. . . . .	105

## Part II

1	Observations of the wellbore pressure in the Italian field. The phase lag appears to be nearly 12 hours..	123
2	Observations of the wellbore pressure in the Colombian field. Note the evidence of high mobility in the near absence of phase lag between the potential excitation and the wellbore pressure response..	123
3	Problem domain: radial axisymmetric system centered about the wellbore with radius $R_1$ . The region outside the wellbore is filled with a dilatating porous medium with porosity $f$ and permeability $k$ ..	124
4	Phase lag and amplitude factor $b$ vs. the Fourier number $x$ for $a = 200$	124
5	Phase lag and amplitude factor $b$ vs. the Fourier number $x$ for $a = 5000$	125
6	The ratio of the maximum flow rate to the maximum of the flow rate at $r = 1$ vs. $r$ for different values of $x$ $a = 200$ ..	125

## Chapter III

### Part I

1	Geometry .....	142
2	Pressure-composition diagram for $C_1/C_3$ mixture at $T = 346$ K. ....	142
3	Methane Composition vs. time at $x = 100$ m, $z = 50$ m for different permeabilities .....	142
4	Liquid saturation for different permeabilities: steady state (the dark color represents the liquid phase) .....	143
5	GOC location vs. $x$ for $k = 0$ md (convection-free) and $k = 0.01$ md: steady state .....	143
6	Methane composition vs. depth at $x = 500$ m in both the gas and liquid columns for various permeabilities: steady state .....	143
7	Methane composition vs. depth at $x = 100$ m in both the gas and liquid columns for various permeabilities: steady state .....	144
8	Velocity contours of the gas and liquid regions for different permeabilities: steady state .....	144
9	Horizontal velocity vs. depth at $x = 500$ m in both the gas and liquid regions for three different permeabilities: steady state. ....	145

### Part II

1	Schematic of a well tube and the hydrocarbon formation .....	169
2	Measured pressure (a) and density (b) data of four different wells .....	170
3	Location of wells in the horizontal plane .....	171
4	Measured pressure (a) and density (b) data of Well MY2 .....	172
5	Measured data at four different depths from well AK1 .....	173
6	Measured data and model predictions for well AK1 .....	174
7	Measured data and model predictions from two different shut-in wells .....	175
8	Predicted phase envelopes (pressure-temperature diagrams) at five depths for well MY1 .....	176

### Part III

1	Measured GOR data: Well MY1 .....	191
2	Constant volume depletion data for well AK1 measured from different depths .....	192
3	2D-reservoir geometry .....	193

4	Constant-volume depletion from data and theory for the PVT sample AK1 No. 4	194
5	Composition, pressure, vapor saturation, density, and in-place-fluid GOR contour plots at the initial conditions (Geometrics I and II).	195
6	Initial methane composition, density, GOR, and pressure and saturation pressure for the 1D simulation of the GOR performance. Part of the column (around 50m at the top) exhibits a bubblepoint-pressure behavior	196
7	1D results at fixed production rate – 83m <sup>3</sup> /day (reservoir conditions).	197
8	Pressure (bar) and liquid saturation, 2D model	198
9	Pressure (bar) and liquid saturation, 2D model	199
10	GOR vs. time from well MY1, 2D model. Perforation interval: 4500-4580 mSSL	200
11	Relative permeability functions used in the sensitivity study	201
12	GOR performance for different relative permeability functions	202

## Chapter IV

### Part I

1	Schematic of the Experimental Apparatus	218
2	Pressure vs. Expansion Volume for Test 2: Silicone Oil	219
3	Growth and Coalescence of Gas Bubbles for Test 2 (Silicone Oil):T=24°C	220
4	Response of Differential Pressure to Nucleation of Gas Bubbles for Test 2: Silicone Oil	221
5	Response of Differential Pressure to Growth of Gas Bubbles for Test 2: Silicone Oil	222
6	Differential Pressure vs. Expansion Volume for Test 2: Silicone Oil.	223
7	Oil Recovery vs. Expansion Volume for Test 2: Silicone Oil	224
8	Oil and Gas Production Rates at Outlet End vs. Expansion Volume for Test 2: Silicone Oil	225
9	Pressure and Differential Pressure vs. Expansion Volume for Test 4: Oil-E	226
10	Gas Bubbles at Four Expansion Volumes for Test 4 (Oil-E):T=35°C	227
11	Oil Recovery vs. Expansion Volume for Test 4: Oil-E	228
12	Oil and Gas Production Rates at Outlet End vs Expansion Volume for Test 4: Oil-E	229
13	Pressure vs. Expansion Volume for Test 4 (T=35°C) and Test 5 (T=24°C): Oil-E	230
14	Differential Pressure vs. Expansion Volume for Test 4 (T=35°C) and Test 5 (T=24°C): Oil-E	231
15	Gas Bubble Distribution on the Surface of Coreholder for Test 4 (T=35°C) and Test 5 (T=24°C)	232
15b	Gas Bubble Distribution on the Surface of Coreholder at DV=37 cm <sup>3</sup> for Tests 4 and 5	233
16	Oil Recovery for Test 4 (T=35°C) and Test 5 (T=24°C): Oil-E	234
17	Effect of Temperature on Gas Release in Open Space: Oil-E	235
18	Pressure vs. Expansion Volume for Test 5 (Vertical) and Test 6 (Horizontal): Oil-5.	236
19	Differential Pressure vs. Expansion Volume for Test 5 (Vertical) and Test 6 (Horizontal): Oil-E	237
20	Oil Recovery from Oil-E for Test 5 (Vertical) and Test 6 (Horizontal): Oil-E	238
21	Gas and Oil Relative Permeabilities for Test 2: Silicone Oil	239
22	Gas and Oil Relative Permeabilities for Test 4: Oil-E	240
23	Gas and Oil Relative Permeabilities for Test 4 (T=35°C) and Test 5 (T=24°C): Oil-E	241
24	Gas and Oil Relative Permeabilities for Test 5 (Vertical ) and Test 6 (Horizontal): Oil-E	242

## Part II

1	Schematic of the Experimental Setup .....	256
2	Pressure Evolution vs. Expansion Volume for Tests 8 ( $S_{wi}=5.2\%$ ) and 7 ( $S_{wi}=0$ ) .....	256
3	Effect of Initial Water Saturation on Gas Bubble Nucleation .....	256
4	Differential Pressure vs. Expansion Volume for Test 8 ( $S_{wi}=5.2\%$ ) and Test 7 ( $S_{wi}=0$ ) .....	257
5	Oil Recovery vs. Expansion Volume for Tests 8 ( $S_{wi}=5.2\%$ ) and 7 ( $S_{wi}=0$ ) .....	257
6a	Gas and Oil Production Rates vs. Expansion Volume for Tests 8 ( $S_{wi}=5.2\%$ ) and 7 ( $S_{wi}=0$ ) .....	257
6b	Gas and Oil Relative Permeabilities for Tests 8 ( $S_{wi}=5.2\%$ ) and 7 ( $S_{wi}=0$ ) .....	257
7	Pressure Evolution vs. Expansion Volume for Tests 10 ( $T=46^{\circ}\text{C}$ ) and 7 ( $T=35^{\circ}\text{C}$ ) .....	257
8	Effect of Temperature on Gas Bubble Nucleation ( $\Delta V=0.26$ PV) .....	257
9	Differential Pressure vs. Expansion Volume for Tests 10 ( $T=46^{\circ}\text{C}$ ) and 7 ( $T=35^{\circ}\text{C}$ ) .....	258
10	Oil Recovery vs. Expansion Volume for Tests 10 ( $T=46^{\circ}\text{C}$ ) and 7 ( $T=35^{\circ}\text{C}$ ) .....	258
11	Gas and Oil Production Rates for Tests 10 ( $T=46^{\circ}\text{C}$ ) and 7 ( $T=35^{\circ}\text{C}$ ) .....	258
12	Gas and Oil Relative Permeabilities for Tests 10 ( $T=46^{\circ}\text{C}$ ) and 7 ( $T=35^{\circ}\text{C}$ ) .....	258
13	Pressure Evolution vs. Expansion Volume for Tests 12 (GOR=12.2), 11 (GOR=9.0), and 7 (GOR=6.5) .....	258
14	Effect of Solution GOR on Gas Bubble Nucleation .....	259
15	Differential Pressure vs. Expansion Volume for Tests 12 (GOR=12.2), 11 (GOR=9.0), and 7 (GOR=6.5) .....	259
16	Oil Recovery vs. Expansion Volume for Tests 12 (GOR=12.2), 11 (GOR=9.0), and 7 (GOR=6.5) .....	259
17	Oil and Gas Relative Permeabilities for Tests 12 (GOR=12.2), 11 (GOR=9.0), and 7 (GOR=6.5) .....	259

## Part III

1	Critical gas saturation vs. pressure decline rates for different interfacial tensions (from Ref. 17)...	269
2	Gas and Oil Relative Permeabilities for a Heavy Oil at $35^{\circ}\text{C}$ (from Ref. 13) .....	270
3	Gas and Oil Relative Permeabilities for a Viscous Silicone Oil at $24^{\circ}\text{C}$ (from Ref. 13) .....	270
4	Gas Bubbles at Four Expansion Volumes for a Heavy Crude at $35^{\circ}\text{C}$ (from Ref. 13) .....	270
5	Gas Bubbles at Three Expansion Volumes for a Viscous Silicone at $24^{\circ}\text{C}$ (from Ref. 13) .....	271
6	Differential Pressure vs. Expansion Volume Across a Core for a Heavy Crude at $35^{\circ}\text{C}$ and $24^{\circ}\text{C}$ (from Ref. 13) .....	272
7	Differential Pressure vs. Expansion Volume Across a Core for a Viscous Silicone at $24^{\circ}\text{C}$ (from Ref. 13) .....	272

## Summary

The research work carried out at RERI in the three year period from March 1999 to April 2002 can be divided into four areas: 1 – fractured reservoirs simulation and physics, 2 – gravitational potential variation of the sun and moon for the prediction of reservoir properties, 3 – use of concepts from irreversible thermodynamics in undertaking of diffusion process in hydrocarbon reservoirs, and 4 – new phase formation in relation to solution gas drive in heavy oil reservoirs.

Chapter I covers water injection in water-wet and mixed-wet fractured reservoirs. Part I presents the use of the Galerkin finite element method for numerical simulation of water injection in water-wet and mixed-wet oil reservoirs. It is demonstrated that capillary pressure has a significant effect both in water-wet and mixed porous media. The numerical model is currently being extended to 3-D. Part II presents an analytical solution to the problem of 1-D countercurrent imbibition in water-wet media. The analytical solution is presented for the first time without a restriction to capillary pressure and relative permeability. Part III covers experimental data on water injection in water-wet and mixed-wet media. Viscous forces are used to represent gravity effect which can be very important in mixed-wet media. Part IV covers a review of water injection in fractured reservoirs prepared as a distinguished article.

Chapter II covers the estimation of reservoir compressibility and permeability from the gravitational potential variations of the sun and moon. In Part I, the total compressibility in a fractured reservoir is estimated from pressure variations in a non-flowing well. There is agreement between the estimated compressibility and the compressibility from reservoir depletion. In Part II, we develop the mathematical model for the estimation of effective permeability from gravitational potential measurements. Results indicate that we can mainly estimate the range of effective permeability.

Chapter III is divided into three parts. Part II covers the numerical simulation of convection and diffusion in two-phase flow. The results show that GOC contact can be tilted in two-phase systems. In Parts II and III, the unusual fluid distribution and GOR performance in a fractured gas-condensate reservoir is modeled. In this reservoir, heavier fluids float on top of a light fluid. The GOR also decreases with production. Both the fluid distribution and the GOR are reported for the first time in the petroleum literature. In recent past work we have formulated the thermal, molecular, and pressure diffusion in nonideal multicomponent mixtures from irreversible thermodynamics. The total species flux is a result of both convection and diffusions (molecular, pressure, and thermal). When these effects are accounted for, the unusual fluid distribution and GOR performance can be predicted.

Chapter IV presents the work on solution gas drive in heavy oil reservoirs. In three parts, the essence of our findings related to low gas mobility in such systems are discussed. In Part I we present gas and liquid relative permeabilities for solution gas drive in heavy oil reservoirs for the first time in the literature. In Part II, the effect of GOR, temperature, and initial water saturation on recovery performance are covered. Our interests in this topic include both practical applications and interfacial thermodynamics in relation to new phase formation in porous media. The latter has wide application in other areas of petroleum engineering from wettability to production and transport of petroleum fluids. The last part of chapter IV covers an invited paper for the Journal of Canadian Petroleum Technology to review significant aspects of solution gas drive in heavy oil reservoirs.

# **Chapter I- Water Injection in Fractured Porous Media**

## **Part I- Numerical Simulation of Water Injection in Fractured Media**

**MOHAMMAD KARIMI-FARD AND ABBAS FIROOZABADI**

### **Abstract**

Numerical simulation of water injection in discrete fractured media with capillary pressure is a challenge. Dual-porosity models in view of their strength and simplicity can be mainly used for sugar-cube representation of fractured media. In such a representation, the transfer function between the fracture and the matrix block can be readily calculated for water-wet media. For a mixed-wet system, the evaluation of the transfer function becomes complicated due to the effect of gravity.

In this work, we use a discrete-fracture model in which the fractures are discretized as one dimensional entities to account for fracture thickness by an integral form of the flow equations. This simple step greatly improves the numerical solution. Then the discrete-fracture model is implemented using a Galerkin finite element method. The robustness and the accuracy of the approach are shown through several examples. First we consider a single fracture in a rock matrix and compare the results of the discrete-fracture model with a single-porosity model. Then, we use the discrete-fracture model in more complex configurations. Numerical simulations are carried out in water-wet media as well as in mixed-wet media to study the effect of matrix and fracture capillary pressures.

## Introduction

Numerical simulation of oil recovery from fractured petroleum reservoirs remains a challenge. The heterogeneity of the porous media and the connectivity of the fractures have a significant effect on two-phase flow with capillary pressure and gravity effects. Dual-porosity models<sup>1,2,3</sup> have been used to simulate two-phase flow with connected fractures; the sugar-cube model configuration has been studied in such a model. This approach, although very efficient, suffers from some important limitations. One limitation is that the method cannot be applied to disconnected fractured media and cannot represent the heterogeneity of such a system. Another shortcoming is the complexity in the evaluation of the transfer function between the matrix and the fractures. In fact, in mixed-wet fractured media, a dual-porosity model may lose accuracy due to the effect of gravity.

The single-porosity model provides the accuracy, but it is not practical due to very large number of grids. A large number of grids is required because of two different length scales (matrix size and fracture thickness). A geometrical simplification of the single-porosity model can make it applicable to larger configurations. The simplified model is called the discrete-fracture model. In this model, the fractures are discretized as one dimensional entities. The heterogeneity is accounted accurately and there is no need for the transfer function; it can also be applied to both water-wet and mixed-wet media.

The discrete-fracture model was first introduced for single-phase flow. Noorishad and Mehran<sup>4</sup> and Baca, Arnett and Langford<sup>5</sup> were among the early authors to use one dimensional entities to represent fractures. These authors used finite element formulation to simulate 2D single-phase flow through fractured porous media. Noorishad and Mehran<sup>4</sup> solved the transient transport equation in fractured porous media using an upstream

finite element method to avoid oscillation for convective-dominated flow. Baca *et al.*<sup>5</sup> considered a 2D single-phase flow with heat and solute transport. The two media (matrix and fractures) are coupled using the superposition principle.

For two-phase flow with capillary pressure, very limited work can be found in the literature using the discrete-fracture model. The work of Bourbiaux *et al.*<sup>6</sup> is based on finite volume discretization; they use the so-called joint-element technique to represent the fractures. The same approach is used by Granet *et al.*<sup>7</sup> for single-phase flow. The work of Kim and Deo<sup>8,9</sup> is based on the finite element method and the use of the superposition principle to couple the two media. Their approach is similar, in principle, to the work of Noorishad and Mehran<sup>4</sup> and Baca *et al.*<sup>5</sup>. Kim and Deo employ a fully-implicit formulation and solve the set of nonlinear differential equations using the inexact Newton method. The numerical results presented by Kim and Deo show that the agreement between the discrete-fracture model from the finite element method and the single-porosity results from the conventional approach are sometimes not close.

The main advantage of the finite element method in reservoir simulation is the possibility to discretize a geometrically-complex reservoir with an optimal use of mesh points. Mesh refinement around a well can be limited to the well zone which may not be practical in the standard finite difference method. In a recent work<sup>10</sup>, multi-block gridding is used in the finite difference discretization to represent a complex geometry. This approach although effective, may cause the loss of the simplicity and the efficiency of the standard finite difference method.

The standard finite element approach is more complicated than the finite difference method and numerically less efficient. These disadvantages can be overcome by using



a simplified finite element approach. Dalen<sup>11</sup> presents a simplified approach for two-dimensional flow in homogeneous media.

In this work, we use a Galerkin variational method with the finite element discretization. The variational method has been used successfully in single-phase flow<sup>12,13,14</sup> and two-phase flow<sup>15,16,17,18,19</sup>. Our approach is similar to the work of Kim and Deo<sup>9</sup>. In our work we use the implicit pressure - explicit saturation method (IMPES), whereas Kim and Deo used a fully-implicit approach. We demonstrate excellent agreement between the discrete-fracture model and fine grid simulation. An extensive set of examples including a  $25 \times 25$  m cross-section with a set of discrete fractures are studied for water injection in water-wet and mixed-wet systems and the effect of fracture capillary pressure. The cross-section example cannot be presently modeled in a finite difference simulator.

In the following, we first present the mathematical formulation of the problem followed by the numerical approach to solve the system of equations that defines the problem. In the Results section, we first present the effect of gridding on numerical dispersion, and then validate the discrete-fracture model. We also include the numerical results from water injection in a complex fractured media of different dimensions and wettability.

## **Mathematical Formulation**

The basic equations of an incompressible two-phase flow accounting for capillary pressure and gravity effect are obtained by combining Darcy's law and mass conservation for each phase.

$$\frac{\partial (\phi S_n)}{\partial t} = \nabla \cdot (\lambda_n (\nabla p_n - \rho_n \vec{g})) + q_n, \quad (1)$$

$$\frac{\partial (\phi S_w)}{\partial t} = \nabla \cdot (\lambda_w (\nabla p_w - \rho_w \vec{g})) + q_w, \quad (2)$$

$$S_n + S_w = 1, \quad (3)$$

$$p_n - p_w = P_c (S_w). \quad (4)$$

In the above equations subscripts  $n$  and  $w$  represent the non-wetting and wetting phase, respectively. The symbols are defined in the Nomenclature. The mobility of each phase is defined by

$$\lambda_n = \frac{k k_{rn}}{\mu_n}, \quad \lambda_w = \frac{k k_{rw}}{\mu_w}, \quad (5)$$

where  $k$  is the absolute permeability,  $k_r$  the relative permeability and  $\mu$  the viscosity.

Assuming  $\vec{g} = -g\vec{z}$ , we define a flow potential for each phase

$$\Phi_n = p_n + \rho_n g z, \quad (6)$$

$$\Phi_w = p_w + \rho_w g z, \quad (7)$$

where  $z$  is the vertical direction; it is positive upward. For practical reasons we define  $\Phi_c$  to include the gravity and the capillary effects.

$$\Phi_c = \Phi_n - \Phi_w = P_c + (\rho_n - \rho_w)gz. \quad (8)$$

Based on these definitions, the flow equations for two-phase flow are written as

$$\frac{\partial (\phi S_n)}{\partial t} = \nabla \cdot (\lambda_n \nabla \Phi_n) + q_n, \quad (9)$$

$$\frac{\partial (\phi S_w)}{\partial t} = \nabla \cdot (\lambda_w \nabla \Phi_w) + q_w, \quad (10)$$

$$S_n + S_w = 1, \quad (11)$$

$$\Phi_n - \Phi_w = \Phi_c. \quad (12)$$

In this work, we assume that the boundary of the domain is impervious. Therefore, the normal velocity of each phase is equal to zero at the boundary.

$$\vec{v}_n \cdot \vec{n} = -(\lambda_n \nabla \Phi_n) \cdot \vec{n} = 0, \quad (13)$$

$$\vec{v}_w \cdot \vec{n} = -(\lambda_w \nabla \Phi_w) \cdot \vec{n} = 0. \quad (14)$$

The above two equations provide our basic boundary condition.

Equations ??-?? can be combined and formulated in terms of only two dependent variables<sup>20</sup>.

In our formulation, the two dependent variables are saturation and flow potential for the wetting phase.

$$\nabla \cdot ((\lambda_n + \lambda_w) \nabla \Phi_w) = -\nabla \cdot (\lambda_n \nabla \Phi_c) - (q_n + q_w), \quad (15)$$

$$\frac{\partial (\phi S_w)}{\partial t} = \nabla \cdot (\lambda_w \nabla \Phi_w) + q_w. \quad (16)$$

Equations ?? and ?? are written separately for the matrix and the fracture media. Our work centers on the idea of the use of the discrete-fracture approach which is a one-dimensional representation of the fractures. As a result, Eqs ?? and ?? will be discretized in two-dimensional form for the matrix and in one-dimensional form for the fractures. To examine this idea, we consider a portion of a porous medium that includes one fracture (see Fig. ??). The whole domain is represented by  $\Omega$ , the matrix by  $\Omega_m$  and the fracture by  $\Omega_f$ .

Let  $FEQ$  represent the flow equations ?? and ?. According to Fig. ??, the integral form of these equations for the single-porosity model can be written as

$$\begin{aligned} \iint_{\Omega} FEQ \, d\Omega &= \iint_{\Omega_m} FEQ \, d\Omega_m \\ &+ \iint_{\Omega_f} FEQ \, d\Omega_f \end{aligned} \quad (17)$$

The same integral for the discrete-fracture model is written as

$$\begin{aligned}
\iint_{\Omega} FEQ \, d\Omega &= \iint_{\Omega_m} FEQ \, d\Omega_m \\
&+ e \times \int_{\bar{\Omega}_f} FEQ \, d\bar{\Omega}_f
\end{aligned} \tag{18}$$

where  $\bar{\Omega}_f$  represents the fracture part of the domain as a 1D entity.

In the discrete-fracture model, it is assumed that inside the fractures, all variables remain constant in the lateral direction; the thickness  $e$  of the fracture appears as a factor in front of the one dimensional integral for the consistency of the integral form. Comparison of the discrete-fracture model to the single-porosity model reveals that the only difference is the evaluation of the integral inside the fracture which considerably simplifies the problem. This is the main idea of the discrete-fracture model which can be applied in any complex configuration for fractured porous media. In the next section, we will present the numerical solution of the flow equations using finite element discretization and the IMPES technique.

## Numerical Method

We use the Galerkin variational method and the finite element discretization to solve the flow equations ?? and ??. The variational form of these equations including, the impervious boundary condition can be written as

$$\begin{aligned}
\iint_{\Omega} (\lambda_n + \lambda_w) \nabla \Phi_w \nabla \Psi \, d\Omega &= - \iint_{\Omega} \lambda_n \nabla \Phi_c \nabla \Psi \, d\Omega \\
&+ \iint_{\Omega} (q_n + q_w) \Psi \, d\Omega
\end{aligned} \tag{19}$$

$$\begin{aligned} \iint_{\Omega} \frac{\partial (\phi S_w)}{\partial t} \Psi \, d\Omega &= - \iint_{\Omega} \lambda_w \nabla \Phi_w \nabla \Psi \, d\Omega \\ &+ \iint_{\Omega} q_w \Psi \, d\Omega \end{aligned} \quad (20)$$

where  $\Psi$  is the weight function. The geometry is discretized using triangular elements for the matrix and line elements for the fractures. Figure ?? presents the discretization. In the discretized geometry we define a basis of weight and shape functions which are the same in the Galerkin method. We consider piecewise linear weight and shape functions verifying

$$\Psi_i(x_j, y_j) = \delta_{ij} \quad (21)$$

All dependent variables are approximated as

$$\chi(x, y) = \sum_i (\chi)_i \Psi_i(x, y) \quad (22)$$

where  $(\chi)_i$  is the value of  $\chi$  at node  $i$  and  $\chi$  is any of  $\Phi_w$ ,  $\Phi_c$ ,  $S_w$ ,  $q_n$  or  $q_w$  variables.

Eqs ?? and ?? can be written in a matrix form when using the discrete weight and shape functions.

$$\mathbb{T} \Phi_w = \mathbb{B}_\Phi \quad (23)$$

$$\mathbb{M} \dot{S} = \mathbb{B}_S \quad (24)$$

The elements of the flow matrix  $\mathbb{T}$  and the mass matrix  $\mathbb{M}$  are defined by

$$[\mathbb{T}]_{ij} = \iint_{\Omega} (\lambda_n + \lambda_w) \nabla \Psi_i \nabla \Psi_j \, d\Omega \quad (25)$$

$$[\mathbb{M}]_{ij} = \iint_{\Omega} \phi \Psi_i \Psi_j \, d\Omega \quad (26)$$

and the right hand sides of ?? and ?? are defined by

$$\begin{aligned} [B_{\Phi}]_j &= - \sum_i \iint_{\Omega} \lambda_n(\Phi_c)_i \nabla \Psi_i \nabla \Psi_j \, d\Omega \\ &\quad + \sum_i \iint_{\Omega} ((q_n)_i + (q_w)_i) \Psi_i \Psi_j \, d\Omega \end{aligned} \quad (27)$$

$$\begin{aligned} [B_S]_j &= - \sum_i \iint_{\Omega} \lambda_w(\Phi_w)_i \nabla \Psi_i \nabla \Psi_j \, d\Omega \\ &\quad + \sum_i \iint_{\Omega} (q_w)_i \Psi_i \Psi_j \, d\Omega \end{aligned} \quad (28)$$

The mobilities of the phases are written as

$$\lambda_n = k \frac{k_{rn}}{\mu_n} = k \bar{\lambda}_n, \quad \lambda_w = k \frac{k_{rw}}{\mu_w} = k \bar{\lambda}_w, \quad (29)$$

the absolute permeability  $k$  is defined inside each element and the relative mobility  $\bar{\lambda}$  is defined at each node. These relative mobilities are subject to upstream weighting based on flow direction<sup>11</sup>. Thus, the upstream mobility between two nodes is defined by

$$\bar{\lambda}^{up} = \begin{cases} \bar{\lambda}_i & \text{if } \Phi_i > \Phi_j \\ \bar{\lambda}_j & \text{if } \Phi_i < \Phi_j \end{cases} \quad (30)$$

In the standard finite element approach, the mass matrix is not diagonal. To be able to update the saturation explicitly and improve the efficiency of the method we use a lumped mass matrix. This diagonal form may be obtained by adding off-diagonal elements onto the diagonal, either by rows or by columns. The lumped mass matrix is defined as

$$[\mathbb{D}]_{jj} = \iint_{\Omega} \phi \Psi_j \, d\Omega \quad (31)$$

All integrals over  $\Omega$  are separated to a matrix part,  $\Omega_m$  and a fracture part,  $\bar{\Omega}_f$ . The thickness of the fractures,  $e$  appears as a factor in the fracture integral (see Eq. ??). Details of the numerical integration and the finite element discretization are provided by Reddy<sup>21</sup>.

The time derivation is discretized using the backward Euler method. We use an adaptative time step based on saturation change. This empirical method is very simple to implement and provides good results.

The gridding is performed using the public domain software, `emc2`<sup>22</sup>. This software is able to generate a Delaunay triangulation of a 2D geometry.

The flow matrix is inversed using a direct solver optimized for band matrix (DGBSV from LAPACK). Even for the unstructured gridding by proper numbering of mesh points one can concentrate the matrix coefficients around the main diagonal and improve considerably the efficiency of the direct solver.

## Results

The robustness and the accuracy of the algorithm are shown through several examples for water injection. First, we consider a rock matrix with a single fracture at different orientations and compare the results from the discrete-fracture model with a single-porosity model for validation. Then water flooding is performed in a more complex fractured media. The complex fractured media include both water-wet and mixed-wet systems.



Table ?? presents the density and viscosity of water and oil phases. We choose water for the wetting phase and oil for the non-wetting phase for a water-wet system. For a mixed-wet system there is no need for such a phase identification. The porosity and the permeability of the matrix are  $\phi = 20\%$  and  $k_m = 1$  md, respectively. We use the following relationship to estimate the fracture permeability,

$$k_f = 837 \times 10^5 e^2 \text{ md} \quad (e = \text{mm}) \quad (32)$$

Different sets of relative permeability and capillary pressure are considered in this work. These data are listed in Tables ??, ?? and ??.

Our numerical model can account for different types of relative permeabilities and capillary pressure variation in different zone of the computational domain.

**Numerical dispersion** - Before proceeding to the examples for fractured media, we first examine the numerical dispersion from the model in a homogeneous media. We consider a homogeneous matrix block of  $1\text{m} \times 1\text{m}$  dimension  $(x, z)$ . Water flooding is studied at an injection rate of 0.01 PV/day with  $P_c = 0$  and linear relative permeability. The aim of the simulation is to examine the sharpness of the interface. Three different gridings are considered (153, 581 and 1266 mesh points); the results are presented in Fig. ?? which shows the water saturation profile along the diagonal (between injection and production well, see Fig. ??) at 0.4 PV water injection. Some numerical dispersion exists due to the use of upstream weighting for mobilities. The sharpness of the interface is directly related to the fineness of the grid. In the simulation we obtain the sharpest interface with the grid refining. We should point out that in our model there is no oscillation around the

interface. Various authors in the past have observed oscillations in saturation in the finite element method. Indeed the non-physical oscillation around the interface can breakdown completely the numerical model.

**Fractured porous media with a single discrete fracture ( $1\text{m} \times 1\text{m}$ )** - We consider a single fracture in the matrix block. Water flooding simulations are carried out for three different orientations of the fracture. Figure ?? represents the geometrical configuration  $(x, z)$ . We consider a fracture thickness  $e = 0.1\text{ mm}$  ( $k_f = 8.37 \times 10^5\text{ md}$ ). The medium is initially filled with oil. We inject water at the bottom left corner at the rate of  $q_w = 0.01\text{ PV/day}$ . Liquid is produced from the top right corner.

We first present the grid sensitivity for the discrete-fracture model. Note that because of the complexity of an unstructured grid it is difficult to define an optimal grid. Our aim is only to obtain a grid 'good' enough to allow the evaluation of the accuracy of the model. For that prupose, we will consider the tilted fracture ( $\theta = +45^\circ$ ). The geometry is discretized using five different griddings and the finest gridding is considered as the reference solution. These griddings and the number of mesh points are depicted in Fig. ?. Simulation of water flooding is performed for each grid system. In the first set of simulations, the capillary pressure is not considered. Without capillary pressure there is more restriction on mesh quality. The history of oil production versus water injection during 5 PV water injection is plotted in Fig. ?. The maximum relative error in recovery is evaluated by comparing the maximum relative difference between the recovery curve of the coarse grid with the finest gridding. The relative errors are presented in Table ?.

We note that the grid system with 581 mesh points may be suitable for this example.

Even the gridding with 289 and 153 mesh points provides good results and can be acceptable. We will, therefore, use the gridding system with 581 mesh points for our simulations. The number of mesh points for various configurations of the fracture is presented in Table ???. There are more mesh points for the single-porosity model because of two dimensional representation of the fracture.

Let us evaluate the accuracy of discrete-fracture model by comparing the results with those obtained by the single porosity model. Two different sets of simulations are considered. In one set we neglect the capillary pressure and in the other, only matrix capillary pressure is included. The data used for these simulations are summarized in Table ??. Each set is represented by a matrix block with one fracture at three different tilts. Figure ?? presents the water saturation profile at 0.5 PV water injection. As can be seen, the results from the discrete-fracture model are in excellent agreement with the single-porosity model. Also note that capillary pressure has a significant effect on saturation and flow.

The histories of oil recovery at 3 PV water injection are plotted in Fig. ??. There is very good agreement between the results from the discrete-fracture model and the single-porosity model. For the geometrically-simple case of a horizontal fracture we also used the ECLIPSE simulator<sup>23</sup> (based on the finite difference technique) to validate our results. We show only the production history from ECLIPSE. Figure ?? shows that our results match very well with those by ECLIPSE;  $44 \times 62$  grid points were used for the simulation with ECLIPSE with very fine grids around the fracture. The grid-block sizes in horizontal and vertical directions are:  $2 \times 1$ ,  $2 \times 1.5$ ,  $36 \times 2.5$ ,  $2 \times 1.5$ ,  $2 \times 1$  cm, and  $24 \times 2$ , 1, 0.7, 0.2, 0.8, 0.01,  $4 \times 0.005$ , 0.01, 0.08, 0.2, 0.7, 1,  $24 \times 2$  cm, respectively. The position of the fracture is from block 5 to block 39 in the horizontal direction and from

block 31 to block 32 in the vertical direction.

Let us study the inclined fracture at  $+45^\circ$ . We examine the saturation profile along the fracture and the saturation evolution with time in the middle of the fracture at the center of the porous media. We consider the water-wet system with and without matrix  $P_c$  and neglect the fracture capillary pressure. The injection rate is 0.01 PV/day. The results are summarized in Fig. ?? where we present the saturation profiles along the fracture at different pore volumes of water injection, and the evolution of the saturation with time. As seen, the profiles are sharper when we account for matrix  $P_c$ . Due to the capillary pressure, water imbibes into the matrix from the fracture. As a result, the water front becomes sharper and delays the breakthrough.

**Fractured porous media with complex fracture network ( $1\text{m} \times 1\text{m}$ )** - In this configuration, the fractured media consists of a set of six unstructurally-interconnected fractures. The gridding is presented in Figure ?. The fracture thickness is  $e = 0.1$  mm and the fracture permeability is  $k_f = 837000$  md. The matrix block size is  $1\text{m} \times 1\text{m}$  ( $x, z$ ). The fractures are defined by six pairs of points, as follows:  $[(-.32, -.1), (.35, .2)]_1$ ,  $[(-.2, .33), (.35, -.17)]_2$ ,  $[(.05, .24), (.37, .03)]_3$ ,  $[(0, .25), (-.10, -.34)]_4$ ,  $[(-.5, -.5), (.5, -.5)]_5$ ,  $[(-.15, -.2), (.3, -.35)]_6$ . The reference point (0,0) is the center of the porous media. The relative permeability and capillary pressure are presented in Table ?? which correspond to a water-wet media. The fracture capillary pressure is assumed to be zero. The injection rate is 0.01 PV/day.

In this example, we study the influence of capillary pressure on oil recovery performance. Figure ?? depicts different stages of water flooding with and without matrix

capillary pressure. When the capillary pressure is neglected, the water front progresses quickly through the high permeable fractures and reaches the production well. The effect is a low oil recovery efficiency. On the other hand, with capillary pressure the water front progresses faster inside the matrix and reaches the production well later. As a result, the oil recovery is more efficient.

We present in Fig. ?? the oil recovery. Without capillary pressure water front reaches the production well after about 0.4 PV water injection. As soon as there is a connection between the injector and the producer the oil recovery increases slowly with time. Without capillary pressure at 3 PV water injection there is about 23% less oil recovery than the case with  $P_c$ .

**Fractured porous media with complex fracture network (25m  $\times$  25m)** - The complex fractured media is enlarged to 25m  $\times$  25m ( $x, z$ ) to study the effect of gravity. The injection rate is set to 0.1 PV/year.

Water injection simulations are carried out with and without the matrix and fracture capillary pressures. First we neglect the capillary pressure. Then we study water injection in water-wet media with and without fracture capillary pressure. We also study water injection in mixed-wet media with and without fracture capillary pressure. The matrix and fracture data for water-wet and mixed-wet media are tabulated in Tables ?? and ??, respectively. The gridding used for 25m $\times$ 25m cross section is presented in Figure ??. Various coarser grids were used for all the simulations on the 25m $\times$ 25m cross section; the results revealed that the gridding in Fig. ?? is adequately fine. Figure ?? shows oil recovery, and water saturation profiles are shown in Figure ??. Figure ?? shows that for

the water-wet media, the fracture capillary pressure has very little effect on oil recovery. In contrast, for the mixed-wet media the fracture capillary pressure has a noticeable effect on recovery as it can be seen in Fig. ???. The effect of fracture capillary pressure on recovery performance is in line with the same effect on gas-oil gravity drainage<sup>24,25</sup>. The evolution of water saturation is presented in Fig. ???. Water saturation is plotted at 1 and 1.5 PV water injection. As can be seen, when  $P_c^f \neq 0$  the fractures are more saturated with water which results in a higher oil recovery. For mixed-wet media at 1 PV water injection when  $P_c^f \neq 0$  all fractures are nearly saturated with water. For  $P_c^f = 0$  even at 1.5 PV water injection, there is still some appreciable oil in the fractures.

## Concluding Remarks

The combination of the finite element and the discrete fracture model provides a powerful tool to study multi-phase flow in discrete-fractured media. The finite element method allows for an explicit and accurate representation of the fractures; such a representation may not be possible using a finite difference approach. We have carried out several water injection tests to show the robustness and the accuracy of the proposed methodology for both water-wet and mixed-wet systems. In our simulations, we found a complete agreement between the discrete-fracture model and the single-porosity model; the two models give nearly identical results. Numerically, the discrete fracture approach has several advantages which are summarized in the following

- The pre-processing is simple and does not require gridding inside the fractures.
- Avoiding small two-dimensional elements inside the fractures improves the condi-

tioning of the discrete operator and also permits large time steps.

One should note that when the ratio of the two length scales in a fractured system as well as the permeability ratio of matrix and fracture are very high, the single-porosity approach becomes very inefficient numerically. The discrete fracture approach does not suffer from this limitation.

Finally, the discrete-fracture model can keep its advantages for 3D modeling. We have embarked upon the work on 3D extension. Results will be published as they become available.

## Nomenclature

$e$  = fracture thickness

$\vec{g}$  = gravity vector

$k$  = single-phase permeability

$k_r$  = relative permeability

$\vec{n}$  = normal unit vector

$p$  = pressure

$P_c$  = capillary pressure

$q$  = volumetric flow rate (source or sink)

$S$  = saturation

$t$  = time

$\vec{v}$  = velocity

$x$  = x-axis

$z$  = z-axis (vertical)

## Greek Symbols

$\lambda$  = mobility

$\bar{\lambda}$  = relative mobility

$\mu$  = viscosity

$\rho$  = density

$\phi$  = porosity

$\Phi$  = flow potential

$\Psi$  = shape and weight function

$\Omega$  = flow domain

### **Subscripts and Superscripts**

$f$  = fracture

$i$  = nodal point

$m$  = matrix

$n$  = no wetting phase

$w$  = wetting phase

### **Acknowledgments**

This work was supported by National Petroleum Technology Office of the U.S. DOE Grant No. DE-FG26-99BC15177 and the oil company members of the Reservoir Engineering Research Institute (RERI).

### **References**

1. Warren, J.E. and Root, P.J.: "The Behavior of Naturally Fractured Reservoirs," *SPE Journal* (Sep. 1968) 245.
2. Kazemi, H.: "Pressure transient analysis of naturally fractured reservoirs with uniform fracture distribution," *SPE Journal* (Dec. 1969) 451.



3. Thomas, L. K., Dixon, T. N. and Pierson, R. G.: "Fractured Reservoir Simulation," *SPE Journal* (Feb. 1983) 42.
4. Noorishad, J. and Mehran, M.: "An Upstream Finite Element Method for Solution of Transient Transport Equation in Fractured Porous Media," *Water Resour. Res.*, 18(3), 588, June 1982.
5. Baca, R. G., Arnett R. C., Langford D. W.: "Modelling fluid flow in fractured-porous rock masses by finite-element techniques," *Int. J. Num. Meth. Fluids*, 4, 337-348, 1984.
6. Bourbiaux, B., Granet, S., Landereau, P., Noettinger, B., Sarda, S. and Sabathier J-C.: "Scaling Up Matrix-Fracture Transfers in Dual-Porosity Models: Theory and Application," paper SPE 56557 presented at the 1999 SPE Annual Technical Conference and Exhibition held in Houston, Texas, 3-6 October 1999.
7. Granet, S., Fabrie, P., Lemonnier, P. and Quintard M.: "A Single-Phase Flow Simulation of Fractured Reservoir Using a Discrete Representation of Fractures," 6th European Conference on the Mathematics of Oil Recovery, Peebles-Scotland, 8-11 September 1998.
8. Kim, J.G. and Deo, M.D.: "Comparison of the Performance of the Discrete-Fracture Multiphase Model With Those Using Conventional Methods," paper SPE 51928 presented at SPE Reservoir Simulation Symposium held in Houston, Texas, 14-17 February 1999.
9. Kim, J-G. and Deo M. D.: "Finite Element, Discrete-Fracture Model for Multiphase Flow in Porous Media," *AIChE Journal* (June 2000) 1120.
10. Jenny, P., Wolfsteiner, Ch., Lee, S.H., Durlofsky, L.J.: "Modeling Flow in Geometrically Complex Reservoirs Using Hexahedral Multi-Block Grids," paper SPE 66357 presented at SPE Reservoir Simulation Symposium held in Houston, Texas, 11-14 February 2001.
11. Dalen, V.: "Simplified Finite-Element Models for Reservoir Flow Problems," *SPE Journal* (Oct. 1979) 333.
12. Price, H.S., Cavendish, J.C. and Varga, R.S.: "Numerical Methods of Higher-Order Accuracy for Diffusion-Convection Equations," *SPE Journal* (Sep. 1968) 293.
13. Settari, A., Price, H.S. and Dupont, T.: "Development and Application of Variational Methods for Simulation of Miscible Displacement in Porous Media," *SPE Journal* (Dec. 1975) 228.
14. Young, L.C.: "A Finite-Element Method for Reservoir Simulation," *SPE Journal* (Feb. 1981) 115.
15. McMichael, A.L. and Thomas, G.W.: "Reservoir Simulation by Galerkin's Method," paper SPE 3558 presented at SPE-AIME 46<sup>th</sup> Annual Fall Meeting, held in New Orleans, Oct. 3-6, 1971.
16. Spivak, A., Price, H.S. and Settari, A.: "Solution of the Equations for Multidimensional, Two-Phase, Immiscible Flow by Variational Methods," *SPE Journal* (Feb. 1977) 27.
17. Chavent, G., Cohen, G., Jaffré, J., Dupuy, M. and Ribera, I.: "Simulation of Two-Dimensional Waterflooding By Using Mixed Finite Elements," *SPE Journal* (Aug. 1984) 382.

18. Kaluarachchi, J.J. and Parker J.C.: "An Efficient Finite Element Method for Modeling Multiphase Flow," *Water Resour. Res.*, 25(1), 43, January 1989.
19. Chavent, G., Cohen, G., Jaffré, J., Eymard, R., Guérillot, D.R. and Weill, L.: "Discontinuous and Mixed Finite Elements for Two-Phase Incompressible Flow," *SPE Reservoir Engineering* (Nov. 1990) 567.
20. Aziz, K. and Settari, A.: "Petroleum Reservoir Simulation," Applied science publishers Ltd, London, 1979.
21. Reddy, J.N.: "An introduction to the Finite Element Method," McGraw-Hill Inc., 1993.
22. Saltel, E. and Hecht, F.: "EMC2 Wysiwg 2D finite elements mesh generator"  
<http://www-rocq.inria.fr/gamma/cdrom/www/emc2/eng.htm>
23. ECLIPSE 100, Schlumberger GeoQuest, 1998.
24. Firoozabadi, A. and Hauge, J.: "Capillary Pressure in Fractured Porous Media," *JPT* (June 1990) 784-791, also AIME Transactions, Vol. 289 (1990).
25. Firoozabadi, A. and Markeset, T.: "Fracture-Liquid Transmissibility in Fractured Porous Media," *SPE Reservoir Engineering* (Aug. 1994) 201-207.

	Viscosity (cp)	Density (kg/m <sup>3</sup> )
Water	1	1000
Oil	0.45	660

Table 1: Fluid properties.

$S_w$	$k_{rw}$	$k_{rn}$	$P_c^m$ (atm)
0.0	0.0	1.0	1.00
0.1	0.1	0.9	0.60
0.2	0.2	0.8	0.40
0.3	0.3	0.7	0.24
0.4	0.4	0.6	0.18
0.5	0.5	0.5	0.14
0.6	0.6	0.4	0.10
0.7	0.7	0.3	0.07
0.8	0.8	0.2	0.04
0.9	0.9	0.1	0.02
1.0	1.0	0.0	0.00

Table 2: Relative permeability and capillary pressure for water-wet fractured media.

$S_w$	$k_{rw}$	$k_{rn}$	$P_c^m$ (atm)
0.0	0.0	0.6	1.0000
0.1	$4.51 \times 10^{-6}$	$4.12 \times 10^{-1}$	0.6420
0.2	$1.44 \times 10^{-4}$	$2.68 \times 10^{-1}$	0.4341
0.3	$1.10 \times 10^{-3}$	$1.63 \times 10^{-1}$	0.3124
0.4	$4.62 \times 10^{-3}$	$8.90 \times 10^{-2}$	0.2261
0.5	$1.41 \times 10^{-2}$	$4.19 \times 10^{-2}$	0.1592
0.6	$3.51 \times 10^{-2}$	$1.53 \times 10^{-2}$	0.1045
0.7	$7.58 \times 10^{-2}$	$3.30 \times 10^{-3}$	0.0582
0.8	$1.48 \times 10^{-1}$	$1.22 \times 10^{-4}$	0.0182
0.85	0.2	0.0	0.0000

$S_w$	$k_{rw}$	$k_{rn}$	$P_c^f$ (atm)
0.0	0.0	1.0	1.000
0.02	$2.35 \times 10^{-2}$	$9.78 \times 10^{-1}$	0.350
0.05	$5.88 \times 10^{-2}$	$9.41 \times 10^{-1}$	0.150
0.1	$1.18 \times 10^{-1}$	$8.82 \times 10^{-1}$	0.080
0.2	$2.35 \times 10^{-1}$	$7.65 \times 10^{-1}$	0.040
0.3	$3.53 \times 10^{-1}$	$6.47 \times 10^{-1}$	0.025
0.5	$5.88 \times 10^{-1}$	$4.12 \times 10^{-1}$	0.010
0.6	$7.06 \times 10^{-1}$	$2.94 \times 10^{-1}$	0.005
0.7	$8.24 \times 10^{-1}$	$1.76 \times 10^{-1}$	0.001
0.85	1.0	0.0	0.000

Table 3: Relative permeability and capillary pressure for water-wet fractured media. Matrix data (top), fracture data (bottom).

$S_w$	$k_{rw}$	$k_{rn}$	$P_c^m$ (atm)
0.0	0.0	0.2	1.00
0.1	$1.35 \times 10^{-5}$	0.11	0.50
0.2	$4.32 \times 10^{-4}$	$5.23 \times 10^{-2}$	0.22
0.3	$3.29 \times 10^{-3}$	$2.27 \times 10^{-2}$	0.10
0.4	$1.38 \times 10^{-2}$	$8.32 \times 10^{-3}$	0.02
0.5	$4.23 \times 10^{-2}$	$2.37 \times 10^{-3}$	-0.04
0.6	0.11	$4.40 \times 10^{-4}$	-0.20
0.7	0.23	$3.42 \times 10^{-5}$	-0.60
0.8	0.44	$1.41 \times 10^{-7}$	-2.00
0.85	0.6	0.0	-5.00

$S_w$	$k_{rw}$	$k_{rn}$	$P_c^f$ (atm)
0.0	0.0	1.0	1.0
0.01	$1.18 \times 10^{-2}$	$9.88 \times 10^{-1}$	0.3
0.04	$4.71 \times 10^{-2}$	$9.53 \times 10^{-1}$	0.1
0.1	$1.18 \times 10^{-1}$	$8.82 \times 10^{-1}$	0.05
0.4	$4.71 \times 10^{-1}$	$5.29 \times 10^{-1}$	0.001
0.5	$5.88 \times 10^{-1}$	$4.12 \times 10^{-1}$	-0.004
0.7	$8.23 \times 10^{-1}$	$1.76 \times 10^{-1}$	-0.02
0.8	$9.41 \times 10^{-1}$	$5.88 \times 10^{-2}$	-0.5
0.83	$9.76 \times 10^{-1}$	$2.35 \times 10^{-2}$	-1.5
0.85	1.0	0.0	-5.0

$\theta$	discrete-fracture	single-porosity
+45°	581	638
0°	580	605
-45°	573	637

Table 4: Relative permeability and capillary pressure for mixed-wet fractured media. Matrix data (top), fracture data (bottom).

Table 6: Number of mesh points for the discrete-fracture and single-porosity models. Single fracture configuration.

mesh points	maximum relative error
153	5.3 %
289	3.7 %
581	1.5 %
817	0.65 %
1266	- -

Table 5: Relative error in oil recovery due to mesh quality. Single fracture configuration with  $\theta = +45^\circ$ .

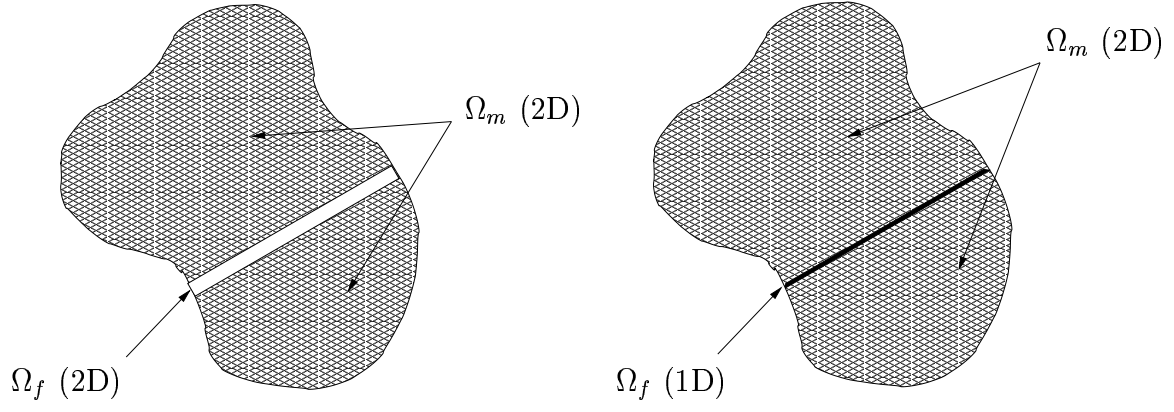


Figure 1: Schematic representation of the discrete fracture approximation

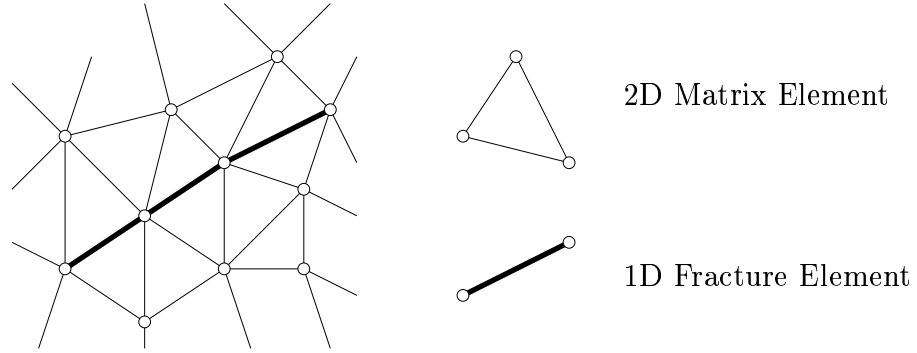


Figure 2: Discretization of the discrete-fractured media: matrix is discretized using linear triangular elements, fractures are discretized by linear line elements

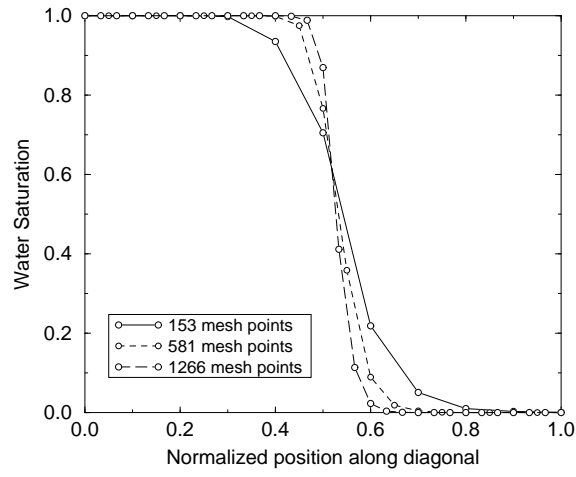


Figure 3: Influence of gridding on the sharpness of the interface along the diagonal at 0.4 PV water injection. Homogeneous porous media. Domain size =  $1\text{m} \times 1\text{m}$ .

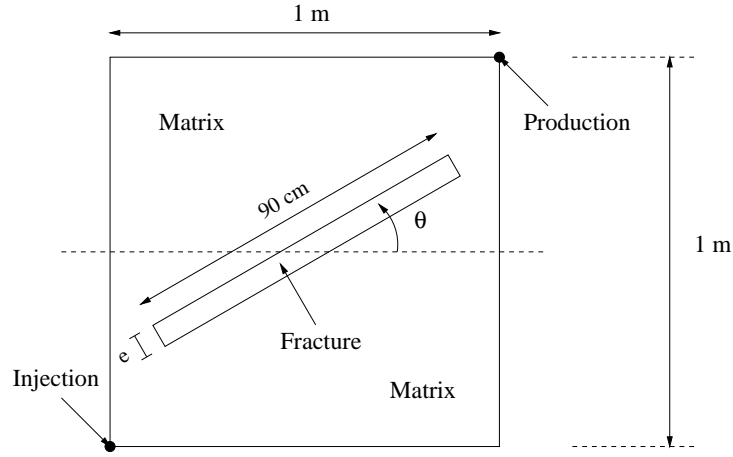


Figure 4: Geometrical configuration of the fracture in the fractured media with a single fracture.

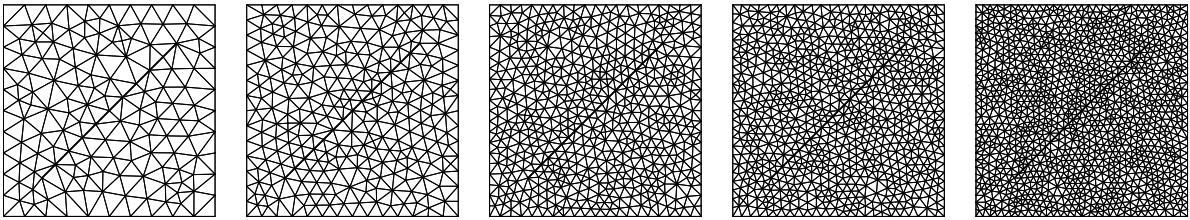


Figure 5: Gridding of the fractured media with a single fracture. From left to right: 153, 289, 581, 817 and 1266 mesh points.

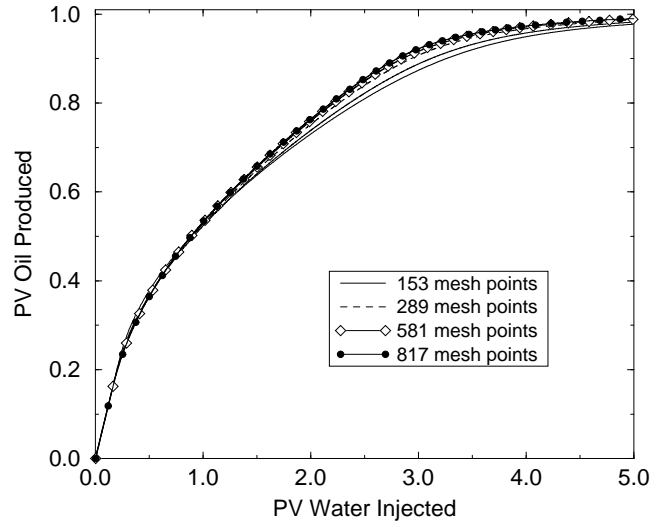
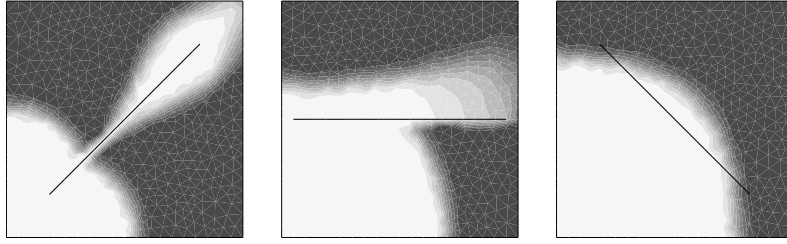


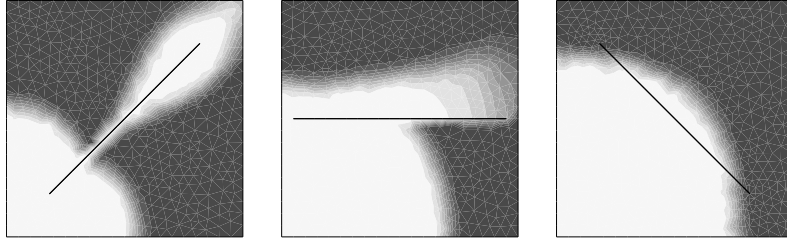
Figure 6: Oil recovery vs PV injection for different griddings: fractured media with a single fracture (water-wet),  $\theta = +45^\circ$ . Domain size =  $1\text{m} \times 1\text{m}$ .

$$(P_c^m = 0, P_c^f = 0)$$

Discrete-Fracture Model

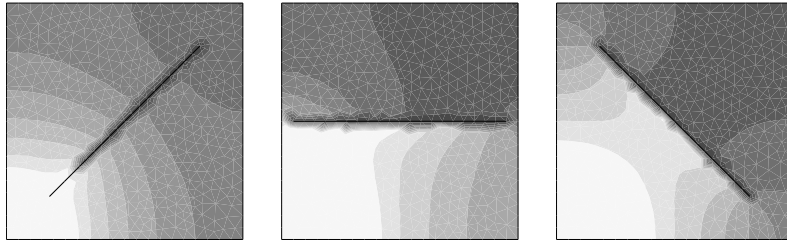


Single-Porosity Model

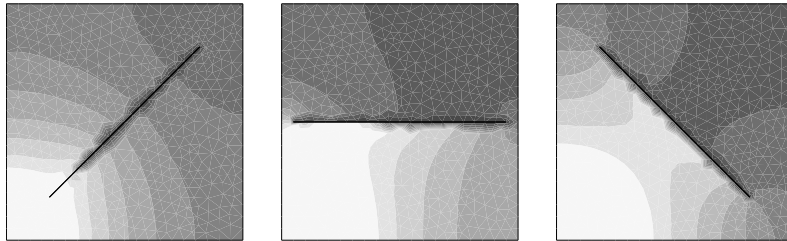


$$(P_c^m \neq 0, P_c^f = 0)$$

Discrete-Fracture Model



Single-Porosity Model



Water Saturation



Figure 7: Water saturation profiles at 0.5 PV water injection: fractured media with a single fracture. Domain size = 1m  $\times$  1m. 27



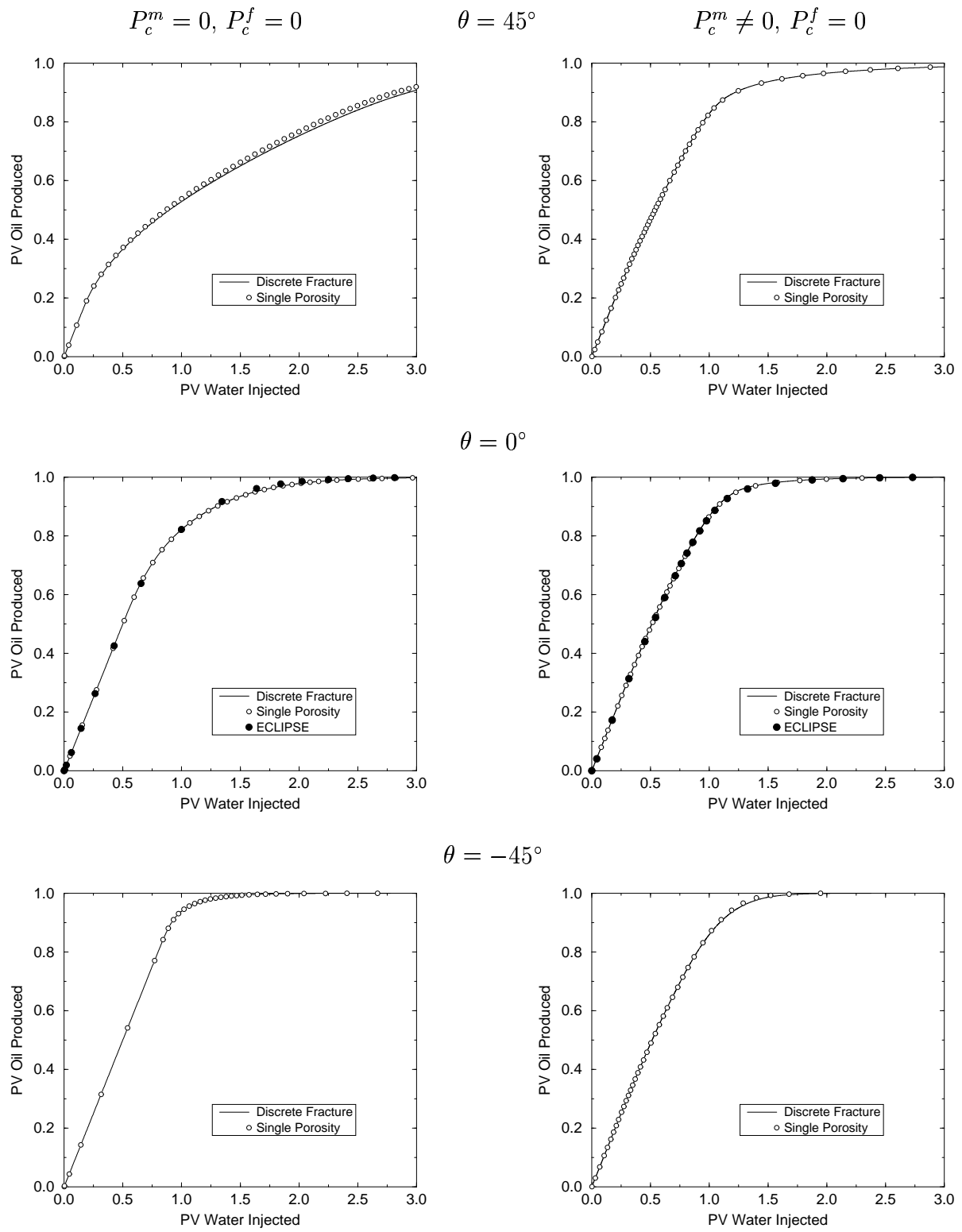
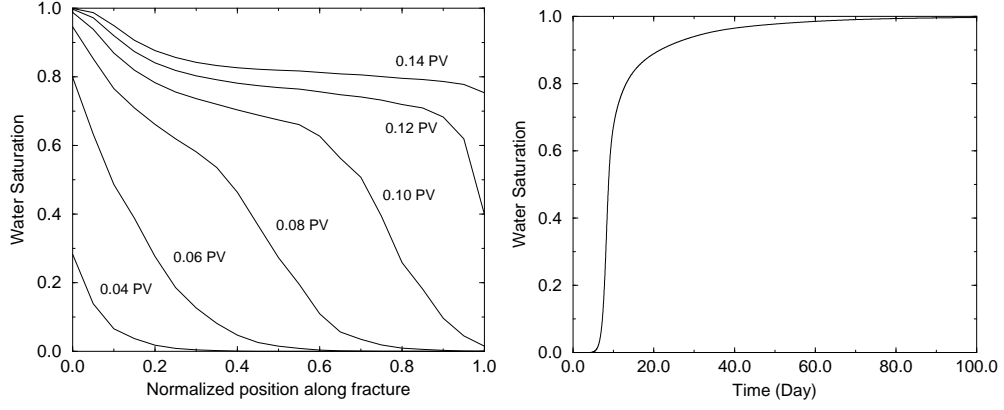


Figure 8: Oil production history: fractured media with a single fracture. Domain size =  $1\text{m} \times 1\text{m}$ .

$$(P_c^m = 0)$$



$$(P_c^m \neq 0)$$

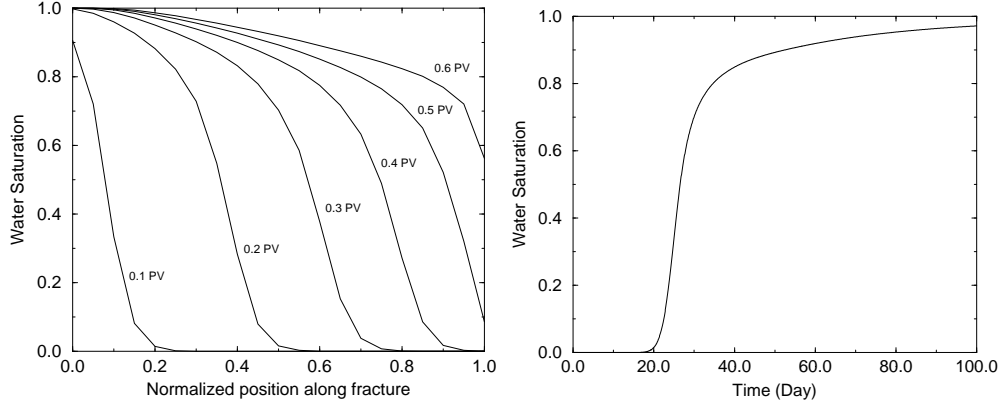


Figure 9: Water saturation profile along the fracture (left) and saturation evolution with time in the fracture at the center of the porous media (right). Single fracture configuration with  $\theta = +45^\circ$ . Domain size =  $1\text{m} \times 1\text{m}$ .

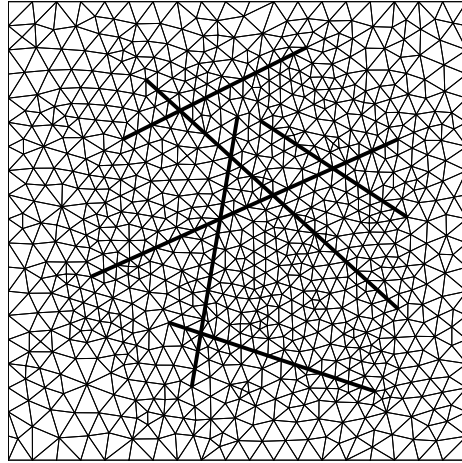


Figure 10: Gridding for the complex fractured media: number of mesh points = 898, domain size =  $1\text{m} \times 1\text{m}$ .

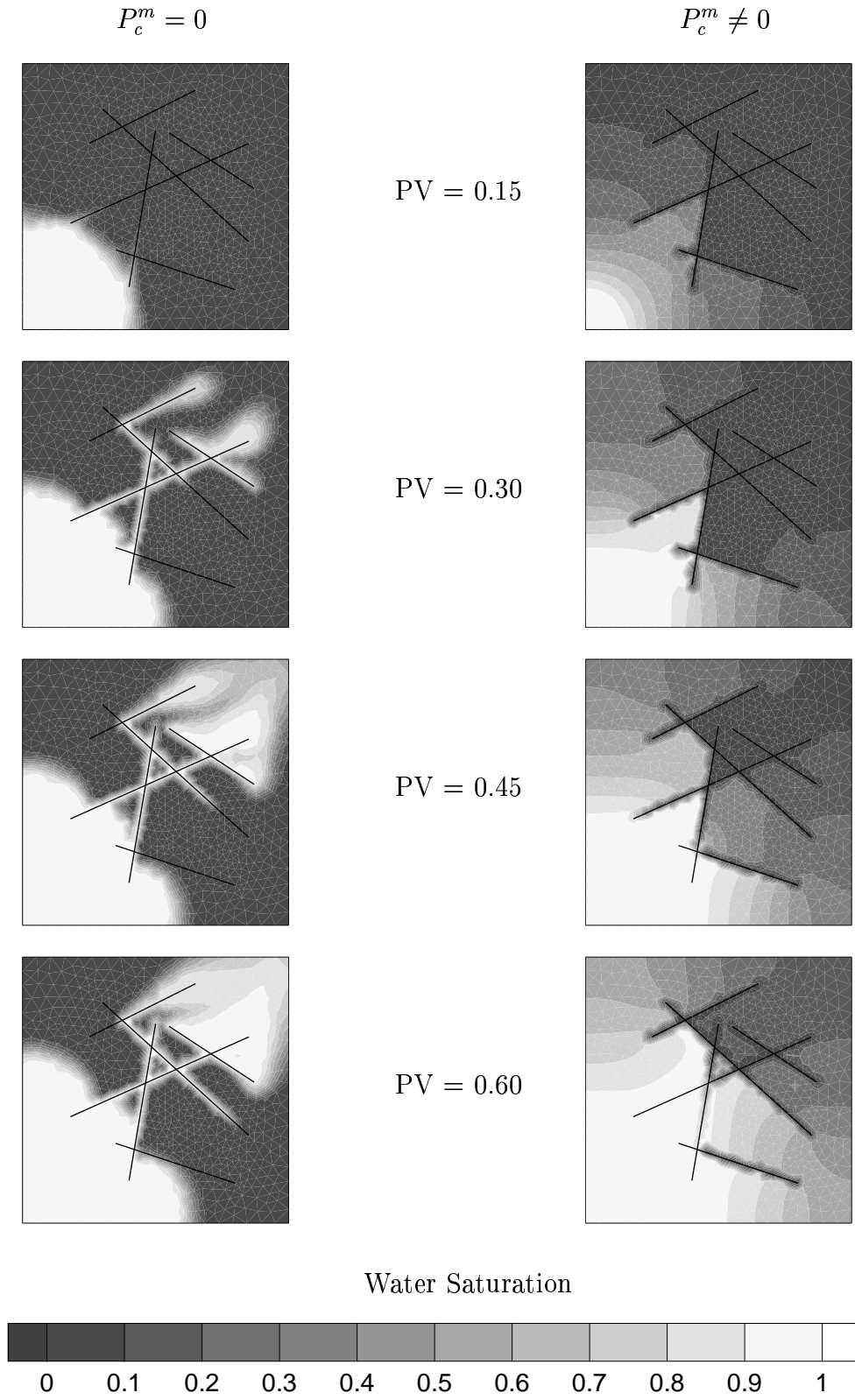


Figure 11: Water saturation profiles at 0.15, 0.30, 0.45 and 0.60 PV (from top to bottom) water injection: complex fractured media. Domain size =  $1\text{m} \times 1\text{m}$ .  $P_c^f = 0$ .

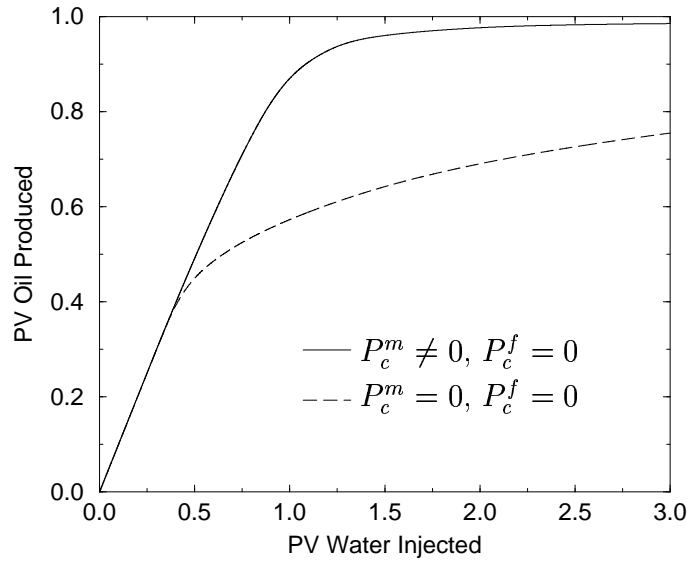


Figure 12: Effect of capillary pressure on oil recovery: fractured media with complex fractures, domain size =  $1\text{m} \times 1\text{m}$ .

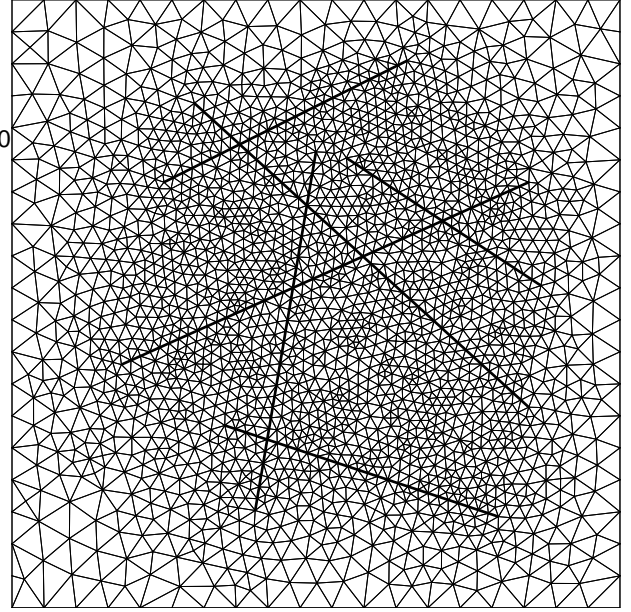


Figure 13: Gridding of the fractured porous media with complex fractures: Domain size =  $25\text{m} \times 25\text{m}$ , number of mesh points = 2277.

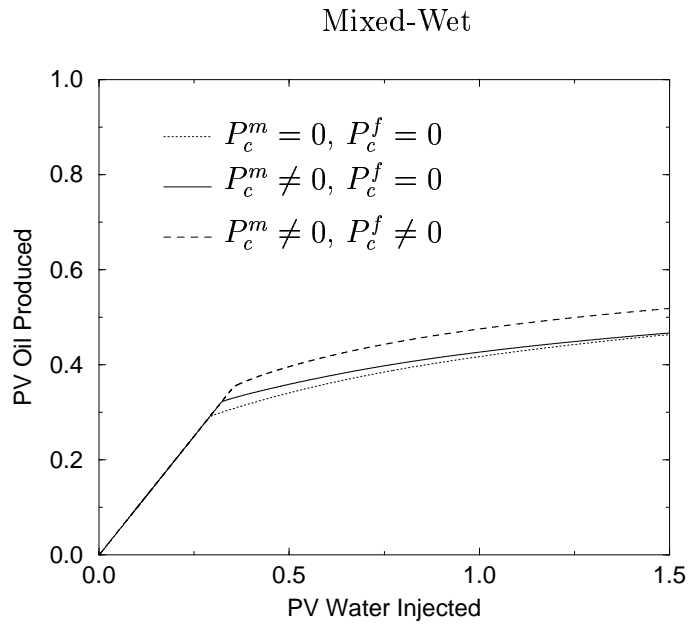
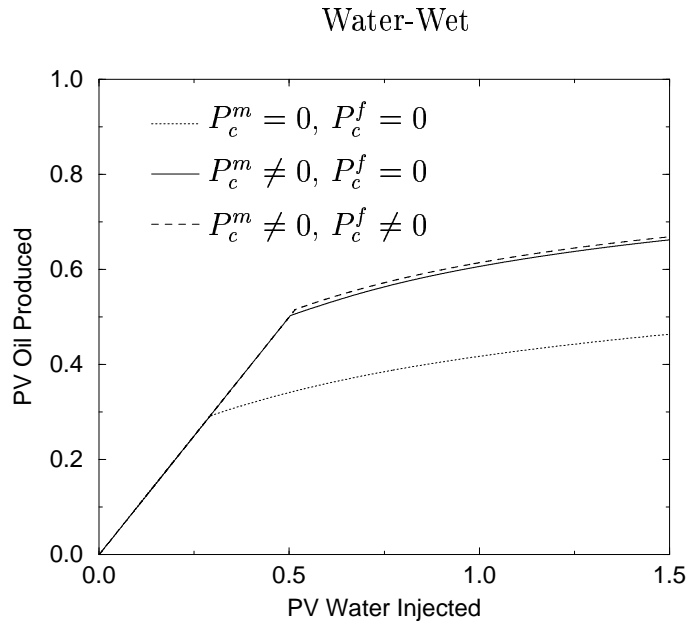


Figure 14: Influence of matrix and fracture capillary pressure on oil recovery.

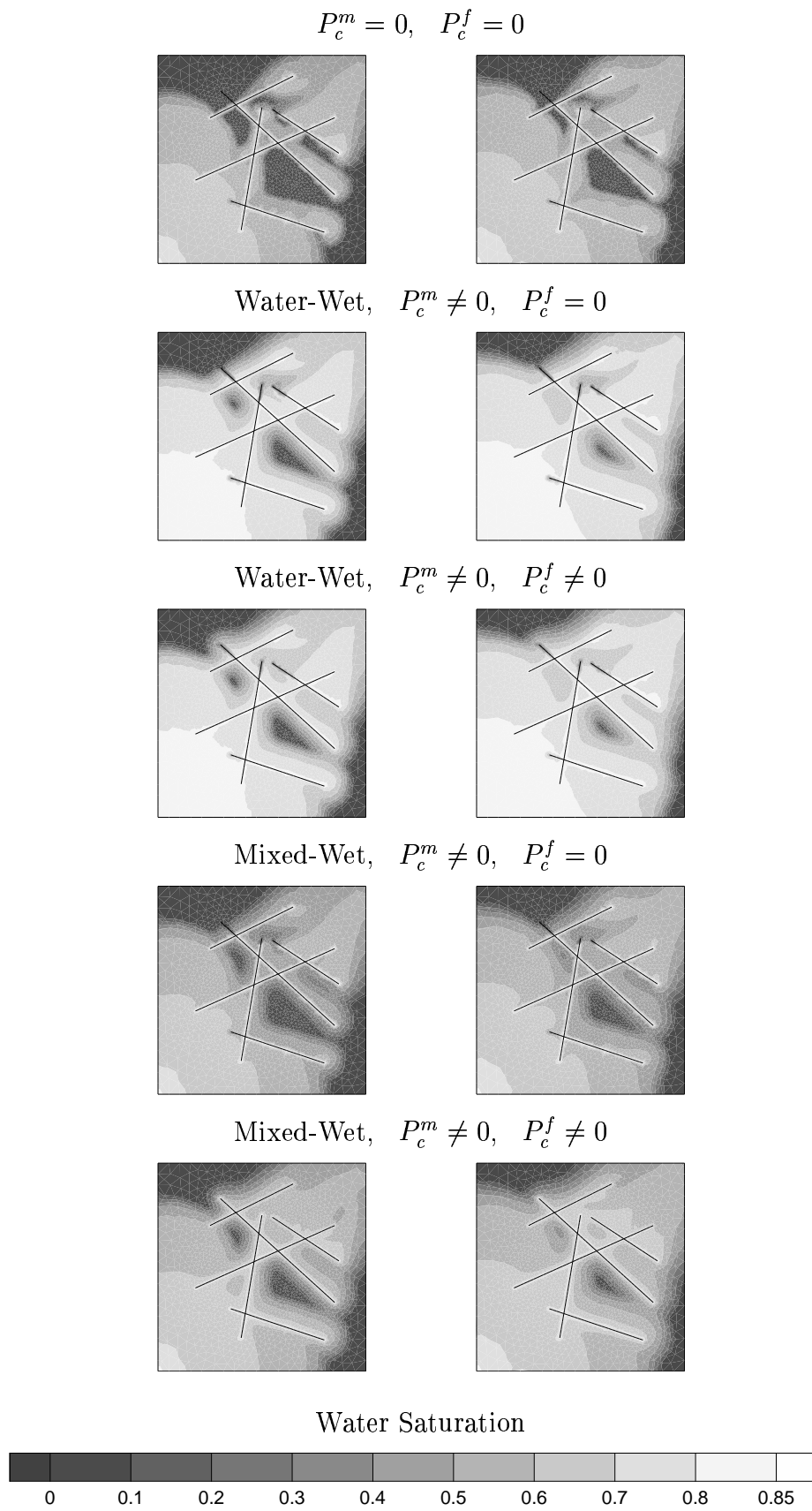


Figure 15: Water saturation profiles at 1 and 1.5 PV (from left to right) water injection:  
Domain size = 25m × 25m.

# Chapter I – Water Injection in Fractured Porous Media

## Part II – Analytical Solutions for 1-D Countercurrent Imbibition in Water-Wet Media

DIMO KASHCHIEV AND ABBAS FIROOZABADI

### Abstract

Analytical solutions for the initial stage of one-dimensional countercurrent flow of water and oil in porous media are presented. Expressions are obtained for the time dependence of the water saturation profile and the oil recovered during spontaneous countercurrent imbibition in rod-like, cylindrical and spherical cores for which water is the wetting liquid. Some of the analytical solutions are found to be in good agreement with existing numerical solutions and available experimental data for oil recovery from cores with strong water wettability.

### Introduction

Capillary-driven fluid flow is often important in two-phase flow in fractured porous media and in layered media where individual layers are thin. In such cases, the parameters in the flow equations are complicated functions of saturation due to high nonlinearity arising from a realistic shape of the capillary-pressure curve. The common approach to the problem solution is the use of numerical techniques.

Analytical solutions to fluid flow problems are desirable, because they allow a better understanding of the underlying physics and verification of numerical models. For capillary-driven flow, only a handful of authors have proposed analytical solutions of various degrees of complexity and with certain restrictive assumptions.

*Yortsos and Fokas* [1983] obtained an analytical solution for a one-dimensional flow with account of capillary pressure; the relative permeabilities and capillary pressure were, however, severely restricted in functional form. *Chen* [1988] proposed combined analytical-numerical techniques for analysis of radial one-dimensional flow. His work is based on the use of certain asymptotic conditions; it has a strong numerical component.

*McWhorter and Sunada* [1990] reported quasi-analytical solutions for one-dimensional linear and radial flow. Their work includes both countercurrent and cocurrent flow. These authors limited their solution to an infinite acting medium and assumed that the volume flux at the inlet is of the form  $At^{-1/2}$  where  $A$  is constant and  $t$  is time.

*Pavone et al.* [1989] also solved the one-dimensional and two-dimensional (gravity drainage) problem analytically; several assumptions were made by these authors to provide a closed-form solution. The assumptions included (i) infinite gas mobility, (ii) linear liquid-phase relative permeability, and (iii) capillary-pressure dependence on saturation in the form of logarithmic function. As a result of these assumptions, the flow equations became linear.

In this paper, we provide approximate analytical solutions for the initial stage of linear, cylindrical and spherical countercurrent flow of water and oil in a porous medium. We solve the flow equations without restricting the functional form of the relative permeabilities and the capillary pressure. We only assume that the imbibing and the displaced liquids are incompressible and that the porous medium is water-wet. These two assumptions have been made in the work of all authors referred to above.



## The “Diffusion” Coefficient

The flow of water and oil in a porous medium is described by a diffusion-type equation in which the quantity

$$D(S_w) = -\{k k_{rw}(S_w) k_{ro}(S_w) / [\mathbf{m} k_{rw}(S_w) + \mathbf{n} k_{ro}(S_w)] \mathbf{f}\} \frac{dP_c(S_w)}{dS_w} \quad (1)$$

plays the role of diffusion coefficient [McWhorter and Sunada, 1990; Pooladi-Darvish and Firoozabadi, 2000]. In this expression  $S_w$  is the water saturation,  $k$  ( $\text{m}^2$ ) is the absolute permeability of the medium,  $k_{rw}$  and  $k_{ro}$  are the relative permeabilities to water and oil, respectively,  $\mathbf{m}$  (Pa.s) and  $\mathbf{n}$  (Pa.s) are the viscosities of water and oil, respectively,  $\mathbf{f}$  is the fractional porosity of the medium,  $P_c = p_o - p_w$  is the capillary pressure (positive when water is the wetting liquid), and  $p_w$  (Pa) and  $p_o$  (Pa) are the water and the oil pressures, respectively.

The dependence of the relative permeabilities and the capillary pressure on  $S_w$  can be modeled in various ways [Parker *et al.*, 1987; Pooladi-Darvish and Firoozabadi, 2000] and that leads to different  $D(S_w)$  functions. In this study we adopt the expressions used by Pooladi-Darvish and Firoozabadi [2000] and present  $k_{rw}$ ,  $k_{ro}$  and  $P_c$  as

$$k_{rw} = k_{rw}^o S^{\mathbf{u}} \quad (2)$$

$$k_{ro} = k_{ro}^o (1 - S)^{\mathbf{v}} \quad (3)$$

$$P_c = -B \ln S. \quad (4)$$

Here  $\mathbf{m}$  and  $\mathbf{n}$  are positive numbers,  $k_{rw}^o$  and  $k_{ro}^o$  are the end-point relative permeabilities to water (the value of  $k_{rw}$  at  $S=1$ ) and oil (the value of  $k_{ro}$  at  $S=0$ ), respectively,  $B$  (Pa) is the capillary-pressure parameter (positive when water is the wetting liquid), and  $S$  is the normalized water saturation defined by

$$S = (S_w - S_{iw}) / (1 - S_{or} - S_{iw}). \quad (5)$$

As  $S_{iw}$  is the irreducible water saturation and  $S_{or}$  is the residual oil saturation,  $S$  is a number between zero and unity.

Combining (1) – (5) yields

$$D(S) = [aS^{\mathbf{u}} + (1-S)^{\mathbf{v}}] / D^* S^{\mathbf{u}-1} (1-S)^{\mathbf{v}} \quad (6)$$

where the parameter  $D^*$  ( $\text{m}^2/\text{s}$ ) and the mobility ratio  $a$  are given by

$$D^* = (1 - S_{or} - S_{iw}) / k k_{rw}^o B \mathbf{m} \mathbf{f} \quad (7)$$

$$a = \mathbf{n} k_{rw}^o / \mathbf{m} k_{ro}^o. \quad (8)$$

The solid curve in Figure 1 depicts the  $D(S)$  dependence (6) with  $\mathbf{m} \mathbf{n} = 4$ ,  $a = 0.267$  and  $D^* = 0.133 \text{ mm}^2/\text{s}$  [Pooladi-Darvish and Firoozabadi, 2000]. These and other parameter values

used in the graphical and numerical illustrations to follow are presented in Table 1. As seen in Figure 1,  $D$  is a bell-shaped function of  $S$  and at  $S=S_m=0.542$  has a maximum value  $D_m \equiv D(S_m)=0.014 \text{ mm}^2/\text{s}$ .

It turns out that it is mathematically advantageous to approximate  $D(S)$  from (6) by the expression

$$D(S) = D_0 S^m \exp(-cS^n) \quad (9)$$

in which  $m>0$  and  $n>0$  are fitting parameters, and  $D_0$  ( $\text{m}^2/\text{s}$ ) and  $c$  are related to the position  $S_m$  and the value  $D_m$  of the maximum of  $D$  according to

$$D_0 = S_m^m / D_m e^{m/n} \quad (10)$$

$$c = n S_m^n / m. \quad (11)$$

To ensure the same values of the maxima of  $D(S)$  from (6) and (9), in (10) and (11) we must use the values of  $S_m$  and  $D_m$  corresponding to  $D(S)$  from (6). This leads to

$$D_0 = D^* e^{m/n} S_m^{n-m-1} (1-S_m)^n / [a S_m^n + (1-S_m)^n]. \quad (12)$$

The dashed curve in Figure 1 exhibits  $D(S)$  from (9) with  $m=3.5$ ,  $n=4.5$ ,  $c=12.2$  and  $D_0=0.258 \text{ mm}^2/\text{s}$  (these values of  $c$  and  $D_0$  follow from (11) and (12) with  $m, n, a, S_m$  and  $D^*$  from Table 1). We observe a good correspondence between  $D(S)$  from (6) and (9). Thus,  $D(S)$  from (9) with the two free parameters  $m$  and  $n$  and the two additional parameters  $D_0$  and  $c$ , related to  $m, n, S_m$  and  $D_m$  via (10) and (11), is a useful model for the  $S$ -dependent “diffusion” coefficient in the flow of two immiscible liquids in a porous medium. The capillary-hydraulic properties of the liquids and the medium are reflected mainly in the parameter  $D_0$  (or  $D_m$ ): for instance, when  $k_{rw}^o$ ,  $k_{ro}^o$ , and  $P_c$  are modeled by (2) – (4),  $D_0$  is obtained from (12) in terms of the parameters  $D^*$  and  $a$  which characterize the liquid-porous medium system.

## Water Saturation Profile

### Linear Imbibition

We consider a rod-like porous core with length  $L$  (m), constant cross-sectional area and impermeable lateral surface (Figure 2a). The core is saturated with oil and immersed in water. As oil is the non-wetting liquid, and water is the wetting one, spontaneous countercurrent imbibition occurs by inflow of water and outflow of oil through the basal faces of the core. With negligible gravity and edge effects, the process is one-dimensional and the water saturation  $S_w$  depends only on the spatial coordinate  $x$  and time  $t$ . The  $S_w(x,t)$  function is then the solution of the diffusion-type equation [Marle, 1981]

$$\frac{\partial}{\partial x} \left[ D(S_w) \frac{\partial S_w}{\partial x} \right] = \frac{\partial S_w}{\partial t} \quad (13)$$

where  $D$  is the  $S_w$ -dependent “diffusion” coefficient defined by (1).

Assuming that, initially, the core contains the irreducible water saturation  $S_{iw}$ , for the initial condition to (13) we write

$$S_w(x,0) = S_{iw}. \quad (14)$$

Depending on the conditions of the water flow at the two faces of the core, (13) admits various boundary conditions. We shall consider here countercurrent imbibition occurring (i) at the maximum water saturation  $1-S_{or}$  at the left ( $x=0$ ) and the right ( $x=L$ ) ends of the core, and (ii) until the moment  $t^*$  at which the two advancing fronts of imbibing water meet at the middle of the core. Then the saturation profiles in the left and the right halves of the core are symmetrical and the boundary conditions read ( $t \leq t^*$ )

$$S_w(0,t) = 1-S_{or} \quad (15)$$

$$S_w(L/2,t) = S_{iw} \quad (16)$$

for the core-left half ( $0 \leq x \leq L/2$ ) and

$$S_w(L/2,t) = S_{iw} \quad (17)$$

$$S_w(L,t) = 1-S_{or} \quad (18)$$

for the core-right half ( $L/2 \leq x \leq L$ ).

As the evolution of the water saturation in the core is governed by a diffusion-type equation, the distance  $\mathbf{I}$  (m) traveled by each of the two water fronts into the core to time  $t \leq t^*$  obeys the Einstein-type relation ( $\mathbf{I} \leq L/2$ )

$$\mathbf{I}(t) = (\mathbf{e}D_m t)^{1/2} \quad (19)$$

where  $\mathbf{e} \approx 1$  to 2 is a numerical factor, and  $D_m$  is the maximum value of the “diffusion” coefficient  $D$  from (1). The circles in Figure 3 represent the numerical  $\mathbf{I}(t)$  data of *Pooladi-Darvish and Firoozabadi* [2000]; the curve is the best fit according to (19). From the value  $0.149 \text{ mm/s}^{1/2}$  of the parameter  $(\mathbf{e}D_m)^{1/2}$  of the best fit, with  $D_m = 0.014 \text{ mm}^2/\text{s}$  (see Table 1) we find that  $\mathbf{e} = 1.6$ .

Equation (19) allows determination of the moment  $t^*$  at which the two water fronts meet at the middle of the core: using  $\mathbf{I}(t^*) = L/2$ , we obtain

$$t^* = \frac{L^2}{4\mathbf{e}D_m}. \quad (20)$$

With the above  $D_m$  and  $\mathbf{e}$  and with, e.g.,  $L = 40 \text{ cm}$  (this  $L$  value corresponds to the core length used by *Pooladi-Darvish and Firoozabadi* [2000]), (20) leads to  $t^* = 500 \text{ h}$  ( $\approx 21$  days).

Employing the normalized water saturation  $S$  from (5) and accounting that for  $t \leq t^*$  there is no imbibed water between the two water fronts in the core, we can rewrite (13) as

$$\frac{\partial}{\partial x} \left[ D(S) \frac{\partial S}{\partial t} \right] = \frac{\partial S}{\partial t} \quad (21)$$

and present the initial and boundary conditions (14) – (18) as  $(0 \leq t \leq t^*)$

$$S(x,0) = 0, \quad (22)$$

$$S(0,t) = 1, \quad S[\mathbf{I}(t),t] = 0, \quad (0 \leq x \leq \mathbf{I}) \quad (23)$$

$$S[L-\mathbf{I}(t),t] = 0, \quad S(L,t) = 1, \quad (L-\mathbf{I} \leq x \leq L). \quad (24)$$

Finding the exact solution  $S(x,t)$  of (21), (22) and (23) for the left half of the core or, equivalently, of (21), (22) and (24) for the right half of the core is a formidable mathematical task, especially because (23) and (24) are moving boundary conditions. In what follows we shall find an approximate, quasi-stationary solution  $S[x, \mathbf{I}(t)]$  which depends implicitly on  $t$  via the function  $\mathbf{I}(t)$ . Physically, this solution corresponds to a sufficiently fast adjustment of the water saturation profile to the momentary value of  $\mathbf{I}$ . It is important to note also that this solution is exact when the position  $\mathbf{I}$  or  $L-\mathbf{I}$  of the respective water front is  $t$ -independent.

As for the quasi-stationary solution

$$\frac{\partial S}{\partial t} = 0 \quad (25)$$

(21) transforms into the ordinary differential equation

$$\frac{d}{dx} \left[ D(S) \frac{dS}{dx} \right] = 0 \quad (26)$$

which has to be solved under the boundary conditions

$$S(0) = 1, \quad S(\mathbf{I}) = 0, \quad (0 \leq x \leq \mathbf{I}) \quad (27)$$

$$S(L-\mathbf{I}) = 0, \quad S(L) = 1, \quad (L-\mathbf{I} \leq x \leq L) \quad (28)$$

for the left and the right halves of the core, respectively. Direct substitution in (26) – (28) shows that their solution  $S(x)$  is of the form  $(0 \leq t \leq t^*)$

$$\int_0^S D(S') dS' = [1 - x/\mathbf{I}(t)] \int_0^1 D(S) dS \quad (29)$$

for the left half  $(0 \leq x \leq \mathbf{I})$  and

$$\int_0^S D(S') dS' = [1 - (L-x)/\mathbf{I}(t)] \int_0^1 D(S) dS \quad (30)$$

for the right half  $(L-\mathbf{I} \leq x \leq L)$  of the core,  $\mathbf{I}(t)$  being specified by (19).

At a given moment, rather than the desired  $S(x)$  function, (29) and (30) give explicitly  $x$  as a function of  $S$ . The concrete form of these two functions can be obtained by introducing a

model  $D(S)$  dependence in the integrals in (29) and (30) and carrying out the integration either analytically or numerically. In this respect,  $D(S)$  from (9) is very convenient. Indeed, using it yields

$$\int_0^S D(S') dS' = [D_0/n c^{(m+1)/n}] \int_0^{cS^n} u^{(m+1)/n-1} e^{-u} du. \quad (31)$$

Combining (29) – (31) we thus obtain ( $0 \leq t \leq t^*$ )

$$\gamma[(m+1)/n, cS^n] = [1 - x/\mathbf{I}(t)] \gamma[(m+1)/n, c] \quad (32)$$

$$\gamma[(m+1)/n, cS^n] = [1 - (L-x)/\mathbf{I}(t)] \gamma[(m+1)/n, c] \quad (33)$$

for the left ( $0 \leq x \leq \mathbf{I}$ ) and the right ( $L - \mathbf{I} \leq x \leq L$ ) halves of the core, respectively. Here  $\gamma$  is the incomplete gamma function defined by [Abramowitz and Stegun, 1972, p. 260]

$$\gamma(\mathbf{b}, y) = \int_0^y u^{\mathbf{b}-1} e^{-u} du. \quad (34)$$

Like (29) and (30), with  $\mathbf{I}(t)$  from (19), (32) and (33) represent explicitly the  $x(S)$  dependence, but not the sought normalized water saturation  $S$  as a function of  $x$ . The explicit  $S(x)$  dependence can be obtained in the particular case of  $m+1=n$ . Then, and more generally when  $(m+1)/n=1, 2, 3, \dots$ , the integral on the left of (31) can be performed in terms of the exponential function. For  $m+1=n$ , the expression for  $S(x,t)$  for ( $0 \leq x \leq (\mathbf{eD}_m t)^{1/2}$  and  $0 \leq t \leq L^2/4\mathbf{eD}_m$ ) is given by,

$$S(x,t) = (-c^{-1} \ln\{1 - (1-e^{-c})[1-x/(\mathbf{eD}_m t)^{1/2}]\})^{1/n} \quad (35)$$

for the left half and in ( $L - (\mathbf{eD}_m t)^{1/2} \leq x \leq L$ ,  $0 \leq t \leq L^2/4\mathbf{eD}_m$ )

$$S(x,t) = (-c^{-1} \ln\{1 - (1-e^{-c})[1-(L-x)/(\mathbf{eD}_m t)^{1/2}]\})^{1/n} \quad (36)$$

for the right half of the core. These expressions follow from (32) and (33), because according to (34)  $\gamma(1,y)=1-e^{-y}$ . The original notation  $S(x,t)$  is employed as an abbreviation of  $S[x, \mathbf{I}(t)]$  in (35) and (36).

Figure 4 depicts the  $S(x,t)$  dependences (35) and (36) at  $t=2, 24, 120$  and 450 hours, respectively. The parameter values used for the plot are listed in Table 1; they were also used by Pooladi-Darvish and Firoozabadi [2000] for the numerical computation of  $S(x,t)$  for spontaneous countercurrent imbibition in the left half of a rod-like core at normalized inlet water saturation equal to unity. The  $S(x,t)$  data of these authors are, therefore, appropriate for verification of the accuracy of the approximate solution (35). The circles in Figure 4 represent these data at  $t=2, 24$  and 120 h – we observe a fair agreement between the numerical and the analytical  $S(x,t)$  dependences. Note that in Figure 4 there is a sharp change of the water saturation profile in the range of  $S$  values for which  $D(S)$  from (9) is virtually zero (see Figure 1). In contrast,  $S$  varies with  $x$  relatively slowly and almost linearly when it has values

corresponding to the width of the  $D(S)$  maximum in Figure 1.

### *Cylindrical Imbibition*

In this case the core is a sufficiently long cylinder with radius  $R$  (m) and impermeable basal faces (Figure 2b). The water inflow and the oil outflow is thus through the core lateral surface. With negligible gravity and edge effects,  $S(r,t)$  is the solution of the one-dimensional diffusion-type equation

$$\left(\frac{1}{r}\right)\frac{\partial}{\partial r}\left[rD(S)\frac{\partial S}{\partial r}\right] = \frac{\partial S}{\partial t} \quad (37)$$

in a cylindrical coordinate system with origin at the center of the core cross-section and  $z$ -axis parallel to the core axis. In this equation the radial coordinate  $r$  varies from 0 to  $R$ ,  $S$  is defined by (5), and  $D(S)$  corresponds to  $D(S_w)$  from (1) and can also be modeled by (9).

We shall again look for the quasi-stationary solution  $S[r, \mathbf{r}(t)]$  of (37). As this solution satisfies (25), (37) becomes

$$\frac{d}{dr}\left[rD(S)\frac{dS}{dr}\right] = 0 \quad (38)$$

and its boundary conditions are analogous to (28):

$$S(\mathbf{r}) = 0, \quad S(R) = 1. \quad (39)$$

Here  $\mathbf{r}$  (m), defined as  $\mathbf{r} \equiv R - \mathbf{l}$ , is the radial distance of the water front from the core axis at time  $t$ . In conformity with (19), the  $\mathbf{r}(t)$  dependence thus reads

$$\mathbf{r}(t) = R - (\mathbf{e}D_m t)^{1/2}. \quad (40)$$

When the water front is in the close vicinity of the core axis, its advancement cannot be described by the simple formula (19). That is, the quasi-stationary solution of (38) and (39) is valid to the moment  $t^{**}$  at which the water front is a few percent of  $R$  away from the core axis. Hence, defining  $t^{**}$  by  $\mathbf{r}(t^{**}) = 0.05R$  and using (40) yields (cf. (20))

$$t^{**} = 0.9R^2/\mathbf{e}D_m. \quad (41)$$

As can be verified by direct substitution, the solution of (38) and (39) is of the form ( $\mathbf{r} \leq r \leq R, 0 \leq t \leq t^{**}$ )

$$\int_0^S D(S') dS' = \{\ln[r/\mathbf{r}(t)]/\ln[R/\mathbf{r}(t)]\} \int_0^1 D(S) dS. \quad (42)$$

This general equation is the analogue of (30) and gives the quasi-stationary water saturation profile for an arbitrary  $D(S)$  dependence. When  $D(S)$  is modeled by (9), due to (31) and (34), (42) leads to the expression ( $\mathbf{r} \leq r \leq R, 0 \leq t \leq t^{**}$ )

$$\gamma [(m+1)/n, cS^n] = \{\ln[r/\mathbf{r}(t)]/\ln[R/\mathbf{r}(t)]\} \gamma [(m+1)/n, c]. \quad (43)$$

When  $m+1=n$ , as for linear imbibition, we can find the explicit dependence of  $S$  on the radial distance  $r$  in a cylindrical core. Recalling that  $\gamma(1,y)=1-e^{-y}$ , analogously to (36) we obtain  $(R-(\mathbf{e}D_m t)^{1/2} \leq r \leq R, 0 \leq t \leq 0.9R^2/\mathbf{e}D_m)$  for

$$S(r,t) = (-c^{-1} \ln[1 - (1-e^{-c}) \ln\{r/[R-(\mathbf{e}D_m t)^{1/2}]\} / \ln\{R/[R-(\mathbf{e}D_m t)^{1/2}]\}])^{1/n}. \quad (44)$$

The saturation profile (44) at  $t=2, 24, 120$  and  $450$  hours is illustrated in Figure 5a. The results correspond to  $R, n, c, \mathbf{e}$  and  $D_m$  from Table 1. Comparison of the results in Figures 4 and 5a shows that the saturation profiles in countercurrent linear and cylindrical imbibition are qualitatively the same.

### *Spherical Imbibition*

We consider a spherical core (Figure 2c) with small enough radius  $R$  (m) for the gravity effect to be negligible. In a spherical coordinate system with origin at the core center the saturation function  $S(r,t)$  is the solution of the diffusion-type equation

$$(1/r^2) \frac{\partial}{\partial r} \left[ r^2 D(S) \frac{\partial S}{\partial r} \right] = \frac{\partial S}{\partial t} \quad (45)$$

which parallels (21) and (37) for linear and cylindrical imbibition.

We are again interested in the quasi-stationary solution  $S[r, \mathbf{r}(t)]$  with  $\mathbf{r}(t)$  from (40). This solution satisfies (25) and is valid for  $t \leq t^{**}$  ( $t^{**}$  is specified by (41), because (19) cannot describe the advancement of the water front when this is too close to the sphere center). In analogously to (38) and (39),  $S$  is the solution of the equation

$$\frac{d}{dr} \left[ r^2 \frac{D(S)}{\partial r} \right] = 0 \quad (46)$$

with boundary conditions

$$S(\mathbf{r}) = 0, \quad S(R) = 1. \quad (47)$$

Direct substitution provides the solution of (46) and (47) ( $\mathbf{r} \leq r \leq R, 0 \leq t \leq t^{**}$ )

$$\int_0^S D(S') dS' = \{[1-\mathbf{r}(t)/r]/[1-\mathbf{r}(t)/R]\} \int_0^1 D(S) dS. \quad (48)$$

This general equation is the counterpart of (30) and (42) and can be used for determination of the quasi-stationary water saturation profile in a spherical core when the  $D(S)$  function is independently known. In the scope of the  $D(S)$  model (9), recalling (31) and (34), and from (48) we obtain ( $\mathbf{r} \leq r \leq R, 0 \leq t \leq t^{**}$ )

$$\gamma [(m+1)/n, cS^n] = \{[1-\mathbf{r}(t)/r]/[1-\mathbf{r}(t)/R]\} \gamma [(m+1)/n, c]. \quad (49)$$

This expression parallels (33) and (43) and gives explicitly only the dependence of  $r$  on  $S$ . As for linear and cylindrical imbibition, to determine  $S$  as an explicit function of  $r$  we shall use (49) when  $m+1=n$ . Then, recalling that  $\gamma(1,y)=1-e^{-y}$ , we find  $(R-(\mathbf{e}D_{\text{m}}t)^{1/2} \leq r \leq R, 0 \leq t \leq 0.9R^2/\mathbf{e}D_{\text{m}})$

$$S(r,t) = (-c^{-1} \ln[1 - (1-e^{-c})\{1-[R-(\mathbf{e}D_{\text{m}}t)^{1/2}]/r\}/\{1-[R-(\mathbf{e}D_{\text{m}}t)^{1/2}]/R\}])^{1/n}. \quad (50)$$

Figure 5b displays the saturation profile at  $t=2, 24, 120$  and  $450$  hours, respectively. This profile corresponds to the parameter values listed in Table 1. We observe that the water saturation profile for spherical imbibition does not differ qualitatively from the profiles for linear and cylindrical imbibition (cf. the saturations in Figures 4 and 5a).

## Oil Recovery

### Linear Imbibition

The fraction  $\mathbf{a}$  of oil recovered to time  $t$  is defined in general as

$$\mathbf{a}(t) = \frac{V(t)}{V_o} \quad (51)$$

where  $V$  ( $\text{m}^3$ ) is the volume of oil displaced by the imbibing water to the same time, and  $V_o$  ( $\text{m}^3$ ) is the volume of the total recoverable oil in the core. As  $V$  is equal to the volume of the water imbibed into the core to time  $t$ , for a rod-like core with a constant cross-sectional area  $A_c$  ( $\text{m}^2$ ) one can write

$$V(t) = \mathbf{f}A_c \int_0^L [S_w(x,t) - S_{iw}] dx \quad (52)$$

$$V_o = \mathbf{f}A_c L (1 - S_{or} - S_{iw}). \quad (53)$$

Combining (5) and (51) – (53) yields

$$\mathbf{a}(t) = (1/L) \int_0^L S(x,t) dx. \quad (54)$$

We shall now find the  $\mathbf{a}(t)$  dependence to the moment  $t^*$  at which the two water fronts meet at the middle of the core. Recalling that the two water saturation profiles are symmetric, taking into account that  $S(x,t)=0$  between the water fronts, replacing  $dx$  in (54) by  $(dx/dS)dS$  and calculating  $dx/dS$  using (29) for  $(0 \leq t \leq t^*)$

$$\mathbf{a}(t) = [2\mathbf{I}(t)/L] \int_0^1 S D(S) dS / \int_0^1 D(S) dS \quad (55)$$

where  $\mathbf{I}(t)$  and  $t^*$  are given by (19) and (20), respectively.

This general equation reveals that in linear countercurrent imbibition,  $\mathbf{a}$  initially does not



depend explicitly on the water saturation profile. The ratio of the integrals in this equation has a simple physical meaning – it represents the average value of  $S$  with respect to  $D(S)$  regarded as a distribution function. As this value is just a fixed number between 0 and 1 for whatever shape of the  $S(x,t)$  function, for  $t \leq t^*$  the temporal evolution of  $\mathbf{a}$  is governed solely by the  $\mathbf{I}(t)$  dependence (19) (i.e. by the advancement of the two water fronts):  $\mathbf{a}$  increases proportionally to  $t^{1/2}$ .

The general equation (55) allows to determine  $\mathbf{a}(t)$  analytically when  $D(S)$  is modeled by (9). Then, upon performing the integration using (31) and (34), we obtain ( $0 \leq t \leq t^*$ )

$$\mathbf{a}(t) = \{2\gamma[(m+2)/n, c]/c^{1/n} \gamma[(m+1)/n, c] L\} \mathbf{I}(t). \quad (56)$$

This expression is less complicated in the particular case of  $m+1=n$ . As  $\gamma(1,y)=1-e^{-y}$ , (56) then becomes ( $0 \leq t \leq t^*$ )

$$\mathbf{a}(t) = \{2\gamma[1+1/n, c]/c^{1/n}(1-e^{-c})L\} \mathbf{I}(t) \quad (57)$$

where  $\mathbf{I}(t)$  and  $t^*$  are given by (19) and (20). This formula simplifies to ( $0 \leq t \leq L^2/4\mathbf{eD}_m$ )

$$\mathbf{a}(t) = [2\Gamma(1+1/n)/c^{1/n}L](\mathbf{eD}_m t)^{1/2} \quad (58)$$

provided  $c > 5$ , a condition which is practically always satisfied. In (58) we have used the approximations  $1-e^{-c} \approx 1$  and  $\gamma(1+1/n, c) \approx \gamma(1+1/n, \infty) = \Gamma(1+1/n)$  where  $\Gamma$  is the complete gamma function defined by [Abramowitz and Stegun, 1972, p. 255]

$$\Gamma(\mathbf{b}) = \int_0^\infty u^{\mathbf{b}-1} e^{-u} du. \quad (59)$$

Inspection of (6)-(8) and (58) shows that in agreement with the finding of Rapoport [1955] and of Pooladi-Darvish and Firoozabadi [2000],  $t$  scales with  $k$ ,  $B$ ,  $\mathbf{f}$  and  $L^2$ . Note that according to (58),  $\mathbf{a}(t)$  cannot be correlated with viscosity ratio,  $\mathbf{m}/\mathbf{m}_0$ , as is often suggested by many authors. The recovery may not be also correlated with  $\mathbf{m}$ .

Setting  $t=t^*$  in (55) – (58), we can calculate the fraction  $\mathbf{a}^* \equiv \mathbf{a}(t^*)$  of oil recovered until the moment  $t^*$  at which the two water fronts meet at the middle of the core. From (11), (20) and (58) we find

$$\mathbf{a}^* = \Gamma(1+1/n)/c^{1/n} = [n/(n-1)]^{1/n} \Gamma(1+1/n) S_m. \quad (60)$$

This formula reveals that for  $m+1=n$ ,  $\mathbf{a}^*$  depends solely on the parameter  $n$  of the  $D(S)$  function (9) and on  $S_m$  at which this function passes through a maximum. As seen, higher  $S_m$  results in higher fractions  $\mathbf{a}^*$  of recovered oil. The use of  $n$  and  $c$  (or  $S_m$ ) from Table 1 in (60) yields  $\mathbf{a}^*=0.52$ .

Curve L in Figure 6 displays the oil recovery  $\mathbf{a}(t)$  from (58) for  $t \leq t^*$ , the parameter are those from Table 1. The circles represent the exact numerical  $\mathbf{a}(t)$  data of Pooladi-Darvish and Firoozabadi [2000] also for  $t \leq t^*$ . As seen, the simple approximate equation (58) provides a reliable description of the evolution of  $\mathbf{a}$  at the initial stage ( $t \leq t^*$ ) of spontaneous linear countercurrent imbibition – the error is less than about 7%.

### Cylindrical Imbibition

In this case, with  $L$  (m) being the length of the cylindrical core,

$$V(t) = 2\phi L \int_0^R [S_w(r,t) - S_{iw}] r dr \quad (61)$$

$$V_0 = \phi R^2 L (1 - S_{or} - S_{iw}). \quad (62)$$

Substitution of (5), (61), and (62) into (51) leads to

$$\mathbf{a}(t) = (2/R^2) \int_0^R S(r,t) r dr. \quad (63)$$

At the initial stage of imbibition  $S(r,t)=0$  for  $r \leq \mathbf{r}(t)$  and the lower limit of integration in (63) can be set at  $\mathbf{r}(t)$ . Using the derivative  $dr/dS$  calculated from (42), we can rewrite (63) in the form ( $0 \leq t \leq t^{**}$ )

$$\mathbf{a}(t) = (2/R^2) \ln[R/\mathbf{r}(t)] \int_0^1 S D(S) r^2(S) dS / \int_0^1 D(S) dS \quad (64)$$

where  $\mathbf{r}(t)$  and  $t^{**}$  are given by (40) and (41). Note that in (64)  $r$  is available from (42) as an explicit function of  $S$ .

From the general equation (64) we see that in cylindrical imbibition  $\mathbf{a}$  depends not only on the “diffusion” coefficient  $D(S)$  (cf. (55) for linear imbibition), but also on the water saturation profile expressed by the function  $r^2(S)$  in the first integral. For the  $D(S)$  model (9), and from (31), (34), and (64) we obtain ( $0 \leq t \leq t^{**}$ )

$$\mathbf{a}(t) = \{2nc^{(m+1)/n} \ln[R/\mathbf{r}(t)]/\gamma[(m+1)/n, c]R^2\} \int_0^1 S^{m+1} \exp(-cS^n) r^2(S) dS \quad (65)$$

where  $r(S)$  is given by (43). In the particular case of  $m+1=n$ ,  $\mathbf{a}(t)$  can be determined either from (65) or directly from (63) with  $S(r,t)$  from (44). From the latter we find ( $0 \leq t \leq 0.9R^2/\epsilon D_m$ )

$$(t) = (2/c^{1/n}R^2) \int_{\mathbf{r}(t)}^R (-\ln\{1-(1-e^{-c})\ln[r/\mathbf{r}(t)]/\ln[R/\mathbf{r}(t)]\})^{1/n} r dr. \quad (66)$$

Unlike linear imbibition (cf. (58)),  $\mathbf{a}$  for a cylindrical core is a complicated function of time through  $\mathbf{r}(t)$  which is given by (40). For that reason,  $\mathbf{a}$  can only be determined numerically from (66). The recovery  $\mathbf{a}(t)$  from (66) for  $t \leq t^{**}$  with the parameter values from Table 1 is illustrated in Figure 6 by curve C. We observe that the initial stage of cylindrical countercurrent imbibition and the applicability of (64) – (66) for typical values of  $m$ ,  $n$  and  $c$  extends up to about 70% of the total recoverable oil in the core. Comparing curves C and L, we observe also that in cylindrical imbibition, as expected, the increase of  $\mathbf{a}$  is faster than in linear imbibition.

### Spherical Imbibition

In this case,  $V$  and  $V_0$  are given by

$$V(t) = 4\mathbf{f}p \int_0^R [S_w(r,t) - S_{iw}] r^2 dr \quad (67)$$

$$V_0 = (4/3)\mathbf{f}pR^3 (1 - S_{or} - S_{iw}). \quad (68)$$

From (5) and (51) we obtain

$$\mathbf{a}(t) = (3/R^3) \int_0^R S(r,t) r^2 dr. \quad (69)$$

Similar to cylindrical imbibition, in (69) we set the lower integration limit at  $\mathbf{r}(t)$  and replace  $dr$  by  $(dr/dS)dS$  and calculate  $dr/dS$  from (48). As a result, (69) transforms into ( $0 \leq t \leq t^{**}$ )

$$\mathbf{a}(t) = (3/R^4) [R/\mathbf{r}(t) - 1] \int_0^1 S D(S) r^4(S) dS / \int_0^1 D(S) dS \quad (70)$$

where  $\mathbf{r}(t)$  and  $t^{**}$  are given by (40) and (41).

This expression allows the calculation of the initial temporal evolution of  $\mathbf{a}$  for any  $D(S)$  dependence; from (48), the  $r(S)$  function is known for any dependence of  $D$  on  $S$ . For the  $D(S)$  model (9), using (31) and (34) in (70) yields ( $0 \leq t \leq t^{**}$ )

$$\mathbf{a}(t) = \{3nc^{(m+1)/n} [R/\mathbf{r}(t) - 1] / \gamma[(m+1)/n, c] R^4\} \int_0^1 S^{m+1} \exp(-cS^n) r^4(S) dS \quad (71)$$

where  $r(S)$  is given by (49).

To provide  $\mathbf{a}(t)$  in the particular case of  $m+1=n$  we can use either (71) or directly (69) in conjunction with the  $S(r,t)$  dependence from (50). By the latter we obtain ( $0 \leq t \leq 0.9R^2/\mathbf{a}D_m$ )

$$\mathbf{a}(t) = (3/c^{1/n} R^3) \int_{\mathbf{r}(t)}^R (-\ln\{1 - (1-e^{-c})[1-\mathbf{r}(t)/r] / [1-\mathbf{r}(t)/R]\})^{1/n} r^2 dr. \quad (72)$$

It is seen from this expression that, similar to  $\mathbf{a}$  for cylindrical imbibition (cf. (66)) and in contrast to  $\mathbf{a}$  for linear imbibition (cf. (58)),  $\mathbf{a}$  depends in a complicated way on  $t$  through the  $\mathbf{r}(t)$  function (40). The numerical calculation of  $\mathbf{a}$  from (70) – (72) is, however, straightforward. Curve S in Figure 6 displays the calculated  $\mathbf{a}(t)$  dependence (72) for  $t \leq t^{**}$  and the parameter values from Table 1. Comparison of curves S, C and L in this figure shows that under otherwise equal conditions oil recovery is fastest in spherical imbibition, slower in cylindrical imbibition and slowest in linear imbibition. For typical values of  $m$ ,  $n$  and  $c$  the applicability of (70) – (72) extends up to about 80% of the total recoverable oil in the core; this percentage corresponds to the end of the initial stage of spherical countercurrent imbibition.

## Comparison With Experiment

In a recent experimental study, *Tang and Firoozabadi* [2001] determined the time dependence of the fraction  $\alpha$  of  $n$ -decane recovered from single cores of Kansas outcrop chalk. The circles in Figure 7 display their  $\alpha(t)$  data for a strongly water-wet cylindrical core with diameter and length of about 5 and 6 cm, respectively. The core was immersed in water at room temperature and the oil recovery was determined by weighing the core during the displacement of the oil by the spontaneously imbibing water. The water inflow and the countercurrent oil outflow occurred through the whole surface of the core.

Treating the core as a sphere of radius  $R=2.5$  cm (because of the liquid flow through the whole core surface) and modeling  $D(S)$  by (9) with  $m+1=n$ , we can examine the  $\alpha(t)$  function (72) for the description of the experimental  $\alpha(t)$  data in Figure 7. The free parameters in (72) are  $n$ ,  $c$ , and  $eD_m$  and a best-fit procedure is quite complicated. For that reason we use  $n=4.5$  and  $c=12.2$  from Table 1 and vary only the product  $eD_m$  until a reasonable fit is obtained. Although it is possible to find a better fit with somewhat different values of  $n$  and  $c$ , the corresponding  $eD_m$  value will differ relatively little from that given below.

The curve in Figure 7 represents the  $\alpha(t)$  from (72) with the above values of  $n$  and  $c$  and with  $eD_m=0.12$  cm<sup>2</sup>/min. We observe a good agreement between theory and experiment until  $t^{**}=47$  min (this estimate for  $t^{**}$ , the time limit of the validity of (72), follows from (41)). The conclusion is, therefore, that the  $D(S)$  function for the strongly water-wet Kansas outcrop chalk is of the form (9) with maximum value  $D_m=0.075$  cm<sup>2</sup>/min. This value of  $D_m$  corresponds to  $e=1.6$  from Table 1. For comparison, using the relative permeabilities and capillary pressure inferred from numerical solution for the experimental  $\alpha(t)$  data in Figure 7, we find  $D_m\approx 0.4$  cm<sup>2</sup>/min.

## Conclusions

The analysis presented in this work leads to the following conclusions.

1. The  $D(S)$  function (9) is a very convenient model for the “diffusion” coefficient in the displacement of two immiscible liquids in porous media.
2. The quasi-stationary solutions of the diffusion-type equations (21), (37) and (45) provide a simple and reliable description of the initial stage of linear, cylindrical or spherical countercurrent imbibition in water-wet porous media when gravity and edge effects are negligible. The advancement of the water front obeys the Einstein-type relation (19) and the normalized water saturation profile is given by the general expressions (29)-(30), (42) and (48) for linear, cylindrical and spherical cores, respectively.
3. Equations (55), (64) and (70) provide the general expressions for the temporal evolution of the fraction  $\alpha$  of oil recovered during the initial stage of linear, cylindrical or spherical countercurrent imbibition in water-wet porous media. For linear imbibition, initially (before waterfront reaches the other boundary),  $\alpha$  is proportional to  $t^{1/2}$  according to (58).
4. According to (1) and (58), there may not exist a simple scaling factor for viscosities and relative permeabilities.

## Acknowledgments

This work was supported by US DOE grant DE-FG26-99BC15177 and the member companies of the Reservoir Engineering Research Institute (RERI).

## References

1. Abramowitz, M., and I. Stegun, *Handbook of Mathematical Functions*, Dover, New York,

1972.

2. Chen, Z. X., Some invariant solutions to two-phase fluid displacement problems including capillary effect, *Soc. Pet. Eng. Reservoir Eng.*, 3, 691-700, 1988.
3. Marle, C. M., *Multiphase Flow in Porous Media*, Gulf Publishing Company, Edition Technique, Paris, 1981.
4. McWhorter, D., and D. K. Sunada, Exact integral solutions for two-phase flow, *Water Resour. Res.*, 26, 399-413, 1990.
5. Parker, J. C., R. J. Lenhard, and T. Kuppusamy, A parametric model for constitutive properties governing multiphase flow in porous media, *Water Resour. Res.*, 23, 618-624, 1987.
6. Pavone, D., P. Bruzzi, and R. Verre, Gravity drainage at low interfacial tension, paper presented at the Fifth European Symposium on Improved Oil Recovery, April 25 – 27, Budapest, 1989.
7. Pooladi-Darvish, M., and A. Firoozabadi, Cocurrent and countercurrent imbibition in a water-wet matrix block, *SPE J.*, 5, 3-11, 2000.
8. Rapoport, L. A., Scaling laws for use in design and operation of water/oil flow models, *Trans. AIME*, 204, 143-151, 1955.
9. Tang, G.-Q., and A. Firoozabadi, Effect of pressure gradient and initial water saturation on water injection in water-wet and mixed water-wet fractured porous media, *SPE Reservoir Evaluation and Engineering*, Dec. 2001.
10. Yortsos, Y. C., and A. S. Fokas, An analytical solution for linear waterflood including the effects of capillary pressure, *Soc. Pet. Eng. J.*, 23, 115-124, 1983.

**TABLE 1. Values of Various Parameters Used for Numerical and Graphical Illustrations**

Parameter	Value	Parameter	Value	Parameter	Value
$k$	$0.02 \text{ mm}^2$	$a$	0.267	$e$	1.6
$k_w$	0.2	$S_m$	0.542	$f$	0.3
$k_o$	0.75	$D^*$	$0.133 \text{ mm}^2/\text{s}$	$L$	40 cm
$m_w$	1 mPa.s	$D_m$	$0.014 \text{ mm}^2/\text{s}$	$R$	20 cm
$m_b$	1 mPa.s	$D_0$	$0.258 \text{ mm}^2/\text{s}$	$t^*$	500 h
$m$	4	$m$	3.5	$t^{**}$	450 h
$n$	4	$n$	4.5		
$B$	10 kPa	$c$	12.2		

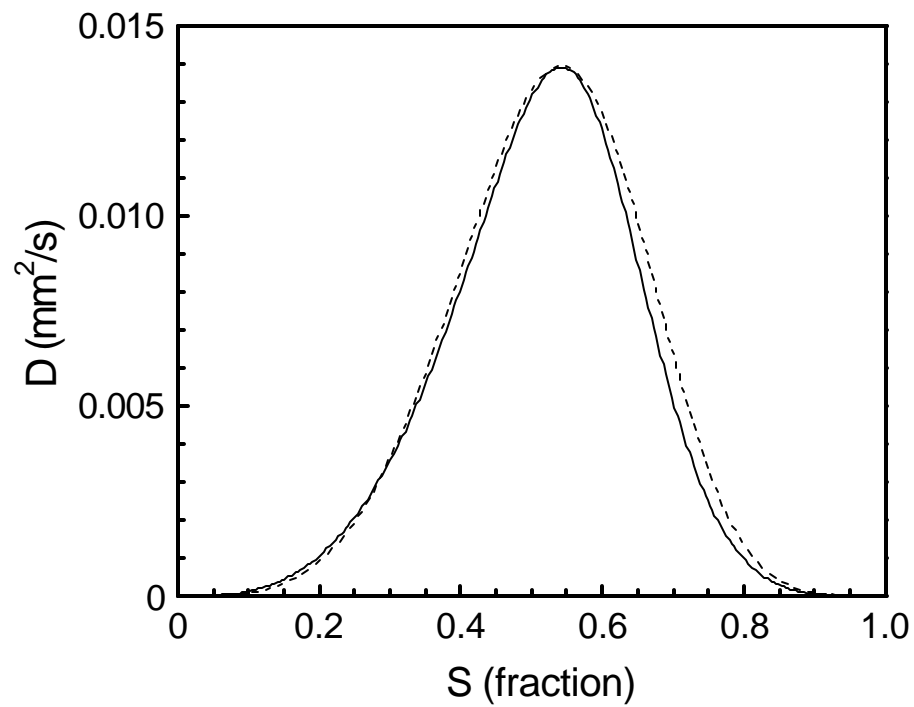


**Fig. 1 - Dependence of the “diffusion” coefficient on the reduced water saturation: solid curve – equation (6); dashed curve – equation (9).**

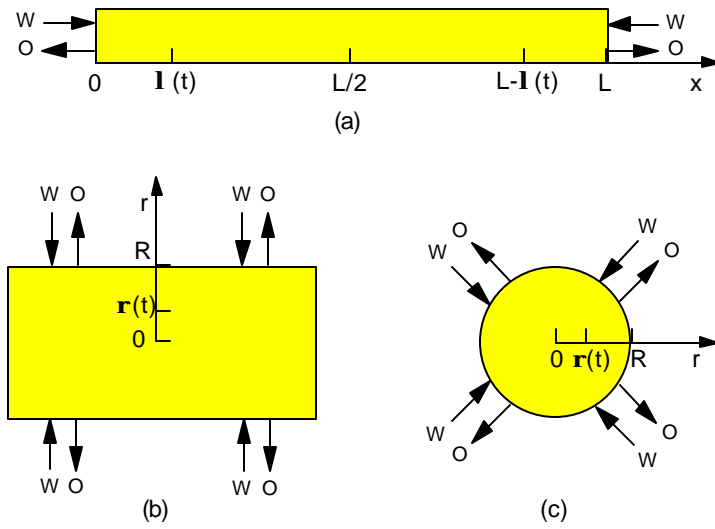


**Fig. 2 - Schematic of oil-saturated (a) rod-like, (b) cylindrical, and (c) spherical water-wet core immersed in water (the arrows indicate water (W) inflow and oil (O) outflow).**

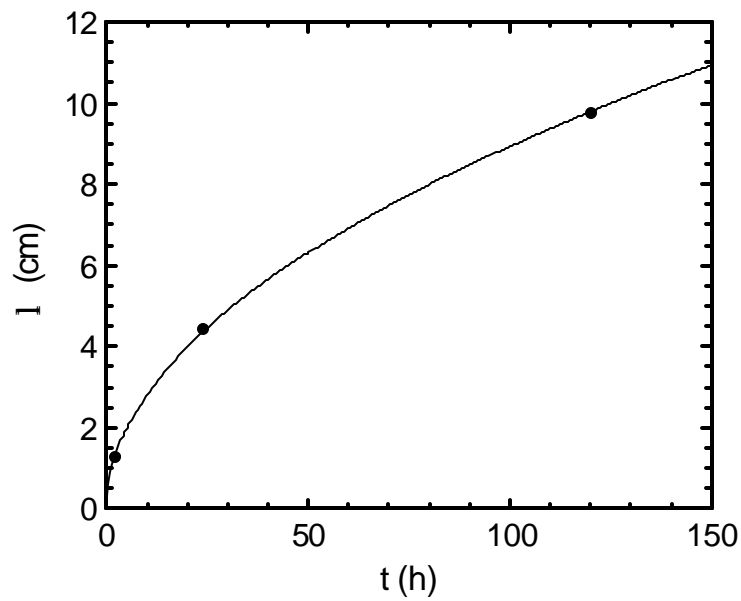


**Fig. 3 - Time dependence of the distance traveled by the water front in linear countercurrent imbibition: circles – numerical data of *Pooladi-Darvish and Firoozabadi* [2000]; line – best fit according to (19).**

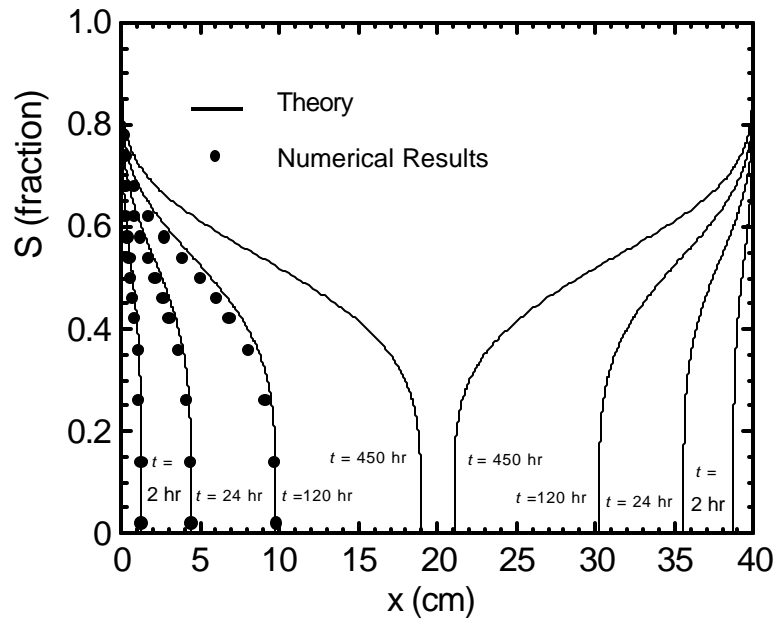


Fig. 4 - Water saturation profile in linear countercurrent imbibition.

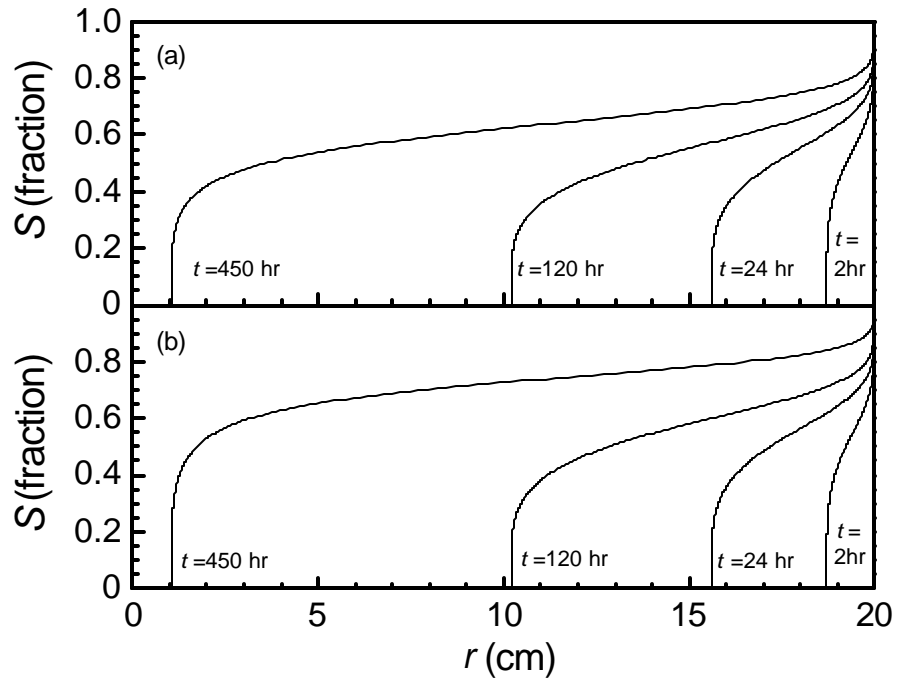


Fig. 5. Water saturation profile in (a) cylindrical, and (b) spherical countercurrent imbibition: equation (44) in (a) and equation (50) in (b).



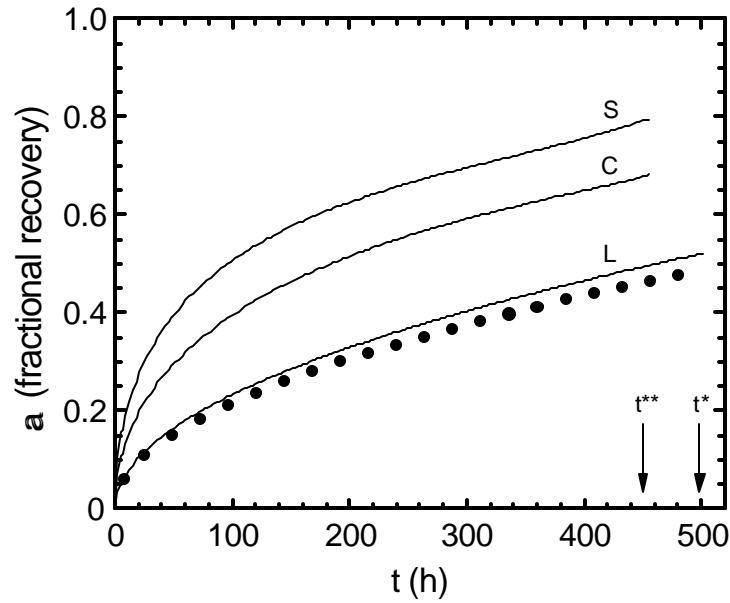


Fig. 6 - Time dependence of the fraction of oil recovered in countercurrent imbibition: curves L, C and S – equations (58), (66) and (72) for linear, cylindrical and spherical imbibition, respectively; circles – numerical data of *Pooladi-Darvish and Firoozabadi* [2000] for linear imbibition. The arrows indicate the end of the initial stage of the process.

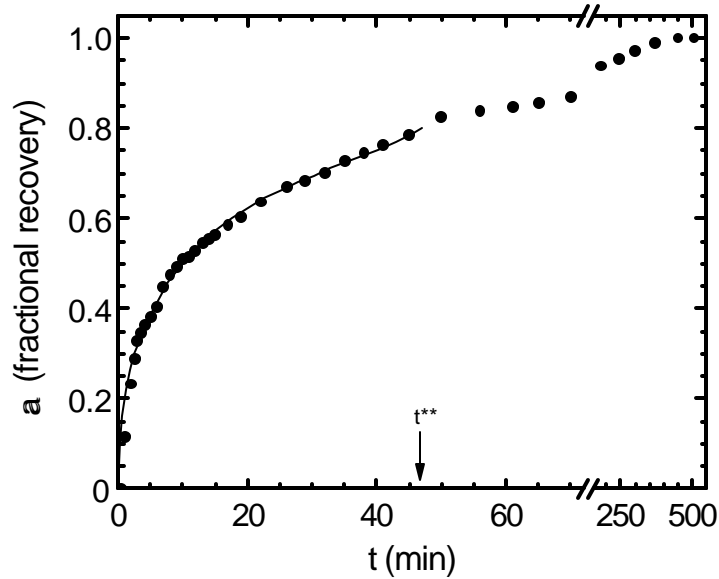


Fig. 7. Time dependence of the fraction of oil recovered in spherical countercurrent imbibition: circles – experimental data of *Tang and Firoozabadi* [2001]; line – equation (72). The arrow indicates the end of the initial stage of the process.

# Chapter I – Water Injection in Fractured Porous Media

## Part III – Effect of Viscous Forces and Initial Water Saturation on Water Injection in Water-Wet and Mixed-Wet Fractured Porous Media

GUO-QING TANG AND ABBAS FIROOZABADI

### Abstract

A systematic study of the effect of wettability and initial water saturation on water injection and imbibition was made in Kansas outcrop chalk samples. Water injection tests were conducted at different rates and at different pressure gradients to study the effect of viscous forces. Based on a large number of carefully conducted tests, the following conclusions are drawn.

1. Initial water saturation has a very pronounced effect on water injection in an intermediate-wet chalk. This effect is much less pronounced for a strongly water-wet chalk. The effects are also in opposite directions.
2. Viscous forces (which simulate the negative  $P_c$  effect) have a very strong effect on water injection performance on intermediate-wet chalks.

Our interpretation of the above experiments leads to the conclusion that the performance of the chalk reservoirs may be nearly independent of wettability state. The results from the experiments also reveal that there is no relation between laboratory measurements of spontaneous imbibition and field performance even when the wettability state is perfectly restored in the laboratory.

### Introduction

Wettability state and its effect on oil recovery has been the subject of numerous studies since 1928<sup>1-8</sup>. However, major issues of oil recovery related to wettability remain unresolved. A major parameter of wettability is contact angle. Some authors have even questioned the usefulness of contact angle in defining wettability<sup>5</sup>.

The state of wettability in some reservoirs can vary significantly with depth and rock properties. Jerauld and Rathmell<sup>4</sup> presented data showing that there is a clear dependence of residual oil saturation upon depth. In the Prodhoe Bay reservoirs, residual oil saturation to waterflood decreases with depth while the reservoir wettability changes from less water-wet to more water-wet conditions with increase in depth. In the Ekofisk field, despite wettability variation with depth, residual oil saturation to waterflooding remains unchanged.

Research concerning the effect of viscous and gravity forces on water injection in fractured reservoirs is rather limited. In 1968, Hamon<sup>9</sup> found that oil recovery by water drainage in oil-wet fractured porous media could be significant depending on matrix permeability. Similar results were recently reported by Putra et al.<sup>10</sup>. Zhou et al.<sup>11</sup> observed that decrease in water-wetness of Berea sandstone by adsorption of polar oil components could increase oil recovery by waterflooding. Graue et al.<sup>12</sup> obtained similar results for low permeability chalk.

The effect of initial water saturation on oil recovery remains controversial. Brown<sup>13</sup> studied the effect of initial water saturation on waterflood efficiency. He emphasized that connate water (retained as water film and in small pores) could become re-mobilized when water is invading.

His experimental results showed that flow of connate water improves waterflood recovery. Skauge et al.<sup>14</sup> studied the influence of connate water on oil recovery by gas gravity drainage using chalk samples. The maximum oil recovery was obtained at about 30% initial water saturation. Viksund et al.<sup>15</sup> carried out spontaneous imbibition tests with strongly water-wet chalk. A maximum oil recovery was obtained at about 34% of initial water saturation. However, results from Narahara et al.<sup>16</sup> are much different. They measured gas and oil relative permeability on water-wet and mixed-wet Berea at various initial water saturations and found that gas and oil relative permeabilities are independent of initial water saturation. Zhou et al.<sup>17</sup> observed that for a crude oil/brine/rock system, imbibition recovery increased with initial water saturation, but waterflood recovery decreased with initial water saturation. A long induction time (ranging from 10-1000 minutes) was observed in imbibition tests after the cores were aged with crude oil at  $T=88^{\circ}\text{C}$  for 10 days.

The main objective of this work is to understand the mechanisms that lead to a vast difference between laboratory spontaneous imbibition measurements and field performance. For this purpose, we have conducted an extensive set of laboratory measurements on Kansas outcrop chalk with a porosity of about 30% and a permeability of some 0.5 md. Waterflood and spontaneous imbibition performance of the Kansas outcrop chalk are studied before and after wettability alteration.

In this paper, we first present the experimental results that include wettability alteration by chemical adsorption, water injection and spontaneous imbibition in strongly water-wet and weakly water-wet chinks. We then draw some conclusions. Theoretical interpretation is the subject of a forthcoming publication.

## Materials and Experimental Setup

**Fluids and Chemicals.** Normal decane ( $n\text{-C}_{10}$ ) with a density of  $0.73\text{ g/cm}^3$  and a viscosity of 0.92 cp at  $24^{\circ}\text{C}$  was used as the oil phase. Stearic acid (octadecanoic acid), purchased from Sigma with purity of 99% and molecular weight of 284.5, was used as a surfactant to alter the chalk wettability. This chemical was dissolved in oil ( $n\text{-C}_{10}$ ) to make stearic acid solutions. Solubility tests at room temperature showed that stearic acid dissolves in oil when the concentration is less than 2000 ppm, but it hardly dissolves in water. NaCl and  $\text{CaCl}_2$  were used to prepare the 0.1% NaCl+0.1%  $\text{CaCl}_2$  brine which was used for both injection water and the establishment of initial water saturation. The viscosity and density of the brine are 1.0 cp and  $1.02\text{ g/cm}^3$  at  $24^{\circ}\text{C}$ , respectively.

**Rock.** We used Kansas outcrop chalk in all experiments. Two different configurations were used: A and B (**Fig.1**). Configuration A was a single cylindrical plug with a diameter of 5.1 cm and a length of 5.2 to 6.6 cm. The measured air permeability of the chalk was about 0.5 md and porosity of about 30%. Configuration B was a composite core that consisted of six-cylindrical plugs of 8.50 cm in diameter. The chinks were stacked and housed in an aluminum coreholder. The total length of the composite chalk was 104.7 cm. The measured annular aperture (between chalk and inside surface of coreholder) was about 250  $\mu\text{m}$  for one set of tests and 150  $\mu\text{m}$  for another set. The overall porosity (fracture/matrix) was about 30.7%; the matrix porosity was about 30%. The fracture volume was about 60-70  $\text{cm}^3$ . Total pore volume (matrix and fracture) was 1740  $\text{cm}^3$ . The effective permeability (fracture/matrix) was about 14.7 darcy when the fracture aperture was 250  $\mu\text{m}$  and about 4.5 darcy when the fracture aperture was 150  $\mu\text{m}$ .

**Apparatus.** Fig.2a shows the experimental apparatus for water injection. It consisted of water injection pumps, a high-pressure cylinder, a water reservoir, pressure transducers, a vertical aluminum coreholder, an oil and water collector, and a vacuum pump with a trap embedded in dry ice. The system can be used to perform water injection tests at either a constant injection rate or a constant inlet pressure. The outlet pressure was atmospheric pressure. Fig.2b shows the apparatus for spontaneous imbibition tests consisting mainly of an electronic balance.

## Experimental Procedure

**Establishment of Initial Water and Oil Saturations.** After the chalk sample was 100% saturated with brine, it was evacuated to 20-50 mbar to reduce water saturation. In order to reduce water saturation quickly, the coreholder was heated to 66°C, accompanied by evacuation. When the designated water saturation was established, the coreholder was cooled to room temperature gradually. The total water production was measured by weighing the chalk plug for Configuration A or measuring the produced water collected by the trap for Configuration B. This step provided the approximate initial water saturation. Then the core was vacuumed at 20-50 mbar for 4-6 hours before the oil saturation step, which lasted about two days. The initial water saturation,  $S_{wi}$ , was calculated using the difference between the total pore volume and total saturated oil volume. For Configuration B, the fracture volume was excluded from the total pore volume for the calculation of initial water saturation.

**Wettability Alteration.** We used stearic acid as a surfactant to alter the wettability of the chalk. The solution was prepared by dissolving stearic acid in oil. The chemical treatment procedures included following steps: the chalk sample was (1) saturated with the stearic acid solution (say 500 ppm solution), (2) aged with the same stearic acid solution at room temperature for 10-20 days, (3) dried and then aged at 105°C for 3-5 days, followed by cooling it to room temperature, and (4) re-saturated and re-aged with the same stearic acid solution at room temperature for 10-20 days. After chemical treatment, the wettability state was determined by running spontaneous imbibition and waterflooding tests. The chemical treatment procedures were repeated when the restored wettability was not stable. For this work, we repeated the above chemical treatment procedure twice to establish a stabilized wettability for most cores used in our study.

**Wettability Measurement.** The chalk plug saturated with oil was hung in a beaker that contained brine (0.1% NaCl+0.1% CaCl<sub>2</sub>). Change in the weight obtained by reading the electronic balance was recorded vs. time. At the end of the spontaneous imbibition test, the chalk plug was waterflooded at a rate of 2 cm<sup>3</sup>/min to residual oil saturation. The end-point oil recoveries by spontaneous imbibition and waterflood were used to calculate the Amott index to water<sup>18</sup>,  $I_{aw}$ .

**Water Injection.** Water injection tests were performed at either a constant injection rate or a constant inlet pressure with the outlet end open to atmospheric pressure. For Configuration A, all tests were performed at constant inlet pressure ( $D_p$  varied from 0 to 13.5 psi/cm). For Configuration B, a constant water injection rate (5 to 68 cm<sup>3</sup>/min) was used; the pressure gradients after water breakthrough,  $D_{p_{bt}}$ , were small due to the vertical fracture.

Note that all the experiments were performed at room temperature. The experimental data are listed in **Tables 1 and 2**.

## Results

**Wettability Alteration.** Change in wettability is assessed by both the rate of spontaneous imbibition and the Amott index to water ( $I_{aw}$ ).

**Initial Wettability.** Kansas outcrop chalk before wettability alteration is strongly water-wet<sup>19</sup>. The residual oil saturation to water from spontaneous imbibition is around 34%. In order to provide a reference for various wettability states, we carried out the spontaneous imbibition test using a chalk plug (Configuration A) before wettability alteration. The result is shown in **Fig.3**. Water imbibition occurred as soon as the chalk plug was placed in water; most oil was produced in less than 100 minutes. The final oil recovery by spontaneous imbibition was about 66% (*OOIP*). After the spontaneous imbibition test, the chalk plug was waterflooded; the total oil recovery by spontaneous imbibition and waterflooding was the same, about 67% (*OOIP*). Therefore, the Amott index to water,  $I_{aw}$ , for the chalk plug is close to 1.0 and it is strongly water-wet (SWW). A duplicate spontaneous imbibition test under the same test conditions was carried out and the results were duplicated. In this paper, the spontaneous imbibition curve presented in **Fig.3** was used as a reference to assess wettability alteration by adsorption of stearic acid.

**Wettability after Chemical Treatment.** In order to reduce the water-wetness by various degrees, the chalk plugs were treated with different concentrations of stearic acid. A series of experiments was conducted to optimize the treatment procedure. It was found that the wettability alteration was strongly influenced by aging time, aging temperature, and stearic acid concentration.

**Fig.4** shows the results for the chalk plug (Configuration A) treated with  $C_{SA}=100$  ppm at room temperature ( $C_{SA}$  is stearic acid concentration). The aging time was two days. Reduction of water-wetness for this chalk plug was small. The final oil recovery was close to that for the strongly water-wet state. The spontaneous imbibition rate increased as the chalk plug was used repeatedly (from run 2a to run 2c). This behavior indicated that the wettability state was not stable, which may be related to desorption of stearic acid from the rock surfaces. However, when the aging time and aging temperature increased, the wettability alteration was significant and stable. **Figs.5-7** show the results for the chalk plugs treated with  $C_{SA}=200$ , 500, and 1,000 ppm, respectively. These chalk plugs were aged at  $T=24^{\circ}\text{C}$  for 20 days, dried and aged at  $T=105^{\circ}\text{C}$  for 5 days, and then re-aged with the stearic acid solutions at room temperature for 10 days. In order to establish a stable wettability alteration, the chalk plugs were treated using the above procedure twice. Three spontaneous imbibition tests were repeatedly conducted with the same chalk plug to study the stability of the restored wettability. Test results presented in **Figs.5-7** are in the order in which they were carried out (for example, runs 3a to 3c in **Fig.5**).

**Fig.5** shows the recovery data for the chalk plug treated with  $C_{SA}=200$  ppm; the induction time was 600 minutes. Then, the water imbibition occurred and the imbibition rate increased quickly. The final oil recovery by spontaneous imbibition was about 53% (*OOIP*), which was about 13% less than before wettability alteration. The results were close for runs 3a to 3c, which confirmed that the restored wettability for this chalk plug was stable. **Fig.6** shows the recovery data for the chalk plug treated with  $C_{SA}=500$  ppm. The induction time was about 1,400 minutes and final oil recovery was about 48% (*OOIP*). However, increase in imbibition rate was slower than that for  $C_{SA}=200$  ppm, which reflected the effect of concentration of stearic acid. The reproducibility for all three runs was reasonable. **Fig.7** shows the results for the chalk plug treated with  $C_{SA}=1,000$  ppm. The induction time was about 2,200 minutes for runs 5a and 5b.

The imbibition rate was very slow and the final oil recovery was about 2-4% (*OOIP*). This chalk plug was intermediate-wet.

All three of the chalk plugs were waterflooded at a rate of 2 cm<sup>3</sup>/min to residual oil saturation after the spontaneous imbibition tests. The total oil recovery by spontaneous imbibition and waterflooding was 69.6% for  $C_{SA}=200$  ppm, 71.2% for  $C_{SA}=500$  ppm, and 67% for  $C_{SA}=1,000$  ppm. Therefore, the Amott index to water ( $I_{aw}$ ) for these chalk plugs were 0.74 for  $C_{SA}=200$  ppm, 0.66 for  $C_{SA}=500$  ppm, and 0.05 for  $C_{SA}=1,000$  ppm. Note that the water wetness of the chalk decreased systematically with increase in stearic acid concentration.

**Water Injection.** We divide the results for water injection into two parts, Part 1 and Part 2, based on the configurations of the chalk samples.

### **Part 1-Configuration A**

For Configuration A, no fractures were present and the coreholder was positioned horizontally. Water was injected from one end of the coreholder at a constant inlet pressure and the oil was produced from the other end at atmospheric pressure.

**Effect of Pressure Gradient.** The results presented in **Fig.8** are for a strongly water-wet plug with  $S_{wi}=0$ . The simple solid curve is for spontaneous imbibition of a strongly water-wet plug and is presented here as a reference (note that this curve is shown in all figures for Configuration A). The results suggested that increase in pressure gradient from 0.09 to 0.37 psi/cm did not affect the oil production rate. Further increase in pressure gradient from 0.37 to 12.9 psi/cm, however, increased oil production rate. For the pressure gradient of 12.9 psi/cm, it took less than 100 minutes to produce all the recoverable oil. The final oil recovery was not influenced by pressure gradients and it remained 66% (*OOIP*). After water breakthrough, very little oil was produced, even at a pressure gradient of 12.9 psi/cm. This result is consistent with the observations by Terez and Firoozabadi<sup>19</sup>. It seems that the viscous force does not affect residual oil saturation for strongly water-wet chalk in the range of our tests.

**Fig.9** shows the recovery data for a weakly water-wet plug treated with 500 ppm stearic acid solution; the Amott index to water is 0.55. The results show that increase in the pressure gradient affected oil production significantly. The induction time decreased from about 300 minutes to zero as pressure gradient increased from zero to 13.5 psi/cm. At pressure gradients of 3.55 and 13.5 psi/cm, the oil production rates were even higher than that for the strongly water-wet plug. The final oil recovery was about 72% (*OOIP*) at  $Dp=13.5$  psi/cm. **Fig.10** shows the results for the chalk plug treated with 1,000 ppm stearic acid solution; the Amott index to water was 0.09 and the induction time was about 20,000 minute for the spontaneous imbibition test. When the pressure gradient increased to 0.96 psi/cm, the oil recovery efficiency was not influenced much. Further increase in pressure gradient to 1.92 psi/cm resulted in a significant increase in oil production rate. When the pressure gradient was greater than 1.92 psi/cm, the oil recovery systematically increased with increase in pressure gradient. The final oil recovery for this plug at a pressure gradient of 13.5 psi/cm was about 78% (*OOIP*).

The results presented in **Figs.9** and **10** demonstrate that viscous forces affect oil recovery efficiency for weakly water-wet and intermediate-wet chinks appreciably.

In all the tests, the total liquid production rate (oil and water) after water breakthrough was less than those before breakthrough.

**Effect of Wettability.** Three chalk plugs with different wettabilities ( $I_{aw}=0.09, 0.55, \text{ and } 0.82$ ) were tested. Each chalk plug was used for water injection tests at two pressure gradients:

$\Delta p=0.96$  and 13.5 psi/cm, respectively. The initial water saturation was zero. **Fig.11** indicates that the effect of wettability on oil recovery by water injection depended on the applied viscous forces. For the tests at a small pressure gradient ( $\Delta p=0.96$  psi/cm), the oil recovery efficiency was strongly influenced by wettability; it increased systematically from 16 to 60% (OOIP) with increase in  $I_{aw}$  from 0.09 to 0.82. However, for the tests at a large pressure gradient ( $\Delta p=13.5$  psi/cm), the effect of wettability on oil recovery efficiency was small and opposite; the final oil recovery was 77% (OOIP) for  $I_{aw}=0.09$ , 72% (OOIP) for  $I_{aw}=0.55$ , and 68% (OOIP) for  $I_{aw}=0.82$ . Fig.11 reveals that the pressure gradient has the most influence on the least water-wet plug.

One may conclude that for a mixed-wet chalk, the effect of wettability on oil recovery is strongly dependent upon the viscous forces. Increase in viscous forces reduces the effect of wettability on oil recovery efficiency.

**Effect of Initial Water Saturation.** Strongly water-wet ( $I_{aw}=1.0$ ), weakly water-wet ( $I_{aw}=0.55$ ), and intermediate-wet ( $I_{aw}=0.09$ ) plugs were used to study the effect of initial water saturation. The pressure gradient for the tests was 0.96 psi/cm. For the strongly-water-wet plug, the tests were conducted at  $S_{wi}=0, 10, 21, 32, 33, 38$ , and 45%. For the weakly water-wet and intermediately water-wet plugs, tests were conducted at  $S_{wi}=0, 10$ , and at about 20%. In order to examine reproducibility, we repeated the test at  $S_{wi}=10\%$  after the test at  $S_{wi}=19\%$ .

The results presented in **Fig.12** are for the strongly water-wet plug. Increase in initial water saturation from 0 to 21% did not lead to obvious changes in oil recovery performance. The induction time was zero and all the recoverable oils were produced in less than 120 minutes. The final oil recovery was about 67% (OOIP). As the initial water saturation increased from 21 to 45%, the oil recovery decreased systematically. The final oil recovery was 64% (OOIP) for  $S_{wi}=33\%$ , 59.5% for  $S_{wi}=38\%$ , and 52% (OOIP) for  $S_{wi}=45\%$ . This result is consistent with those reported by Skauge et al.<sup>14</sup> and Viksund et al.<sup>15</sup>. **Fig.13** shows the recovery data for the chalk plug treated with 500 ppm stearic acid solution. For  $S_{wi}=0$ , there was a long induction time ( $t_{ind}=300$  minutes) before water began to imbibe into the chalk plug, even at a pressure gradient of 0.96 psi/cm. The final oil recovery was about 38% (OOIP); for  $S_{wi}=10\%$ , the induction time decreased to about 40 minutes and the final oil recovery increased to about 62% (OOIP); for  $S_{wi}=20\%$ , the induction time was about 15 minutes and the oil production rate was similar to that for strongly water-wet. **Fig.14** shows the recovery performance for an intermediate-wet plug. As the initial water saturation increased from zero to 19%, the induction time decreased from 20,000 to 200 minutes, and the final oil recovery increased from 7 to 57% (OOIP). The reproducibility of recovery performance for the tests at  $S_{wi}=10\%$  before and after the test at  $S_{wi}=19\%$  is another indication of stable wettability (see **Fig.14**).

## Part 2-Configuration B

For Configuration B, the coreholder was positioned vertically and water was injected from the bottom and oil was produced from the top. There were vertical fractures around the stacked cores. All the water injection tests were performed at a constant injection rate.

**Effect of Water Injection Rate.** Three tests were performed at 5, 11, and 27 cm<sup>3</sup>/min (4.1, 8.2, and 22.3 PV/day), respectively. Due to the fractures, the pressure gradients from viscous forces across the composite chalks was small; they were about 0.01 to 0.02 psi/cm (the gravity effect was excluded from the pressure gradients). **Fig.15** shows the oil recovery vs. water injection time for the strongly water-wet composite system. The results indicate that increase in water injection rate from 5.0 to 26.2 cm<sup>3</sup>/min did not lead to an appreciable change in oil production rate and final oil recovery. The final oil recovery was about 66 % (OOIP) for all three injection rates.

However, the breakthrough (*B.T.*) oil recovery systematically decreased with increase in injection rate. It was 42.1% for  $q_1=5$ , 25.1% for  $q_2=11$ , and 12.4% for  $q_3=27$  cm<sup>3</sup>/min ( $q_1$ ,  $q_2$ , and  $q_3$  are the injection rates). The results in **Fig.15** suggest that the final oil recovery efficiency for strongly water-wet rock of Configuration B (fractured chalk) is independent of rate. This is consistent with the results for the strongly water-wet rock of Configuration A.

**Fig.16** presents the results for the weakly water-wet composite system treated with 500 ppm stearic acid solution using the procedure described earlier. For these tests, the fracture aperture was reduced from 250 to 125  $\mu$ m in order to increase pressure gradient. The pressure gradients after breakthrough were 0.025, 0.046, and 0.101 psi/cm (corresponding to water injection rates of 10.0, 30.0, and 68.0 cm<sup>3</sup>/min, respectively). Because the oil production rate was very slow, the water was injected for 10 hours, and then was halted for 14 hours. Each water injection test lasted about 19 days. The discontinuity of the recovery curves in **Fig.16** (also in **Figs. 15, 17, and 18**) is due to the halts of water injection. The results show that the oil production rate after water breakthrough was slow for the weakly water-wet Configuration B. Prior to wettability alteration (that is *SWW* state), it took only 800 minutes to reach the final oil recovery (66% *OOIP*) at  $D_p=0.025$  psi/cm. However, it took about 15,000 minutes to reach the final oil recovery (48% *OOIP*) at the same pressure gradient for the weakly water-wet system of Configuration B.

Increase in pressure gradient from 0.025 to 0.101 psi/cm did not affect the oil production rate at the early stage. However, the oil production rate during the later stage and the final oil recovery increased with increase in pressure gradient. The final oil recovery was about 60% (*OOIP*) for  $D_p=0.101$  psi/cm, 53% (*OOIP*) for  $D_p=0.046$  psi/cm, and 48% (*OOIP*) for  $D_p=0.025$  psi/cm. These results demonstrate that increase in pressure gradient could lead to improvement of oil recovery by water injection in some fractured rocks. The pressure gradient establishes the effect of gravity (that is, the negative  $P_c$  effect) which can lead to appreciable recovery.

**Effect of Initial Water Saturation.** Water injection tests were conducted at different initial water saturations with the composite system before and after wettability alteration. **Fig.17** presents the results for the strongly water-wet composite chalk. The established initial water saturation varied from zero to 36.8%. The water injection rate was kept at 27 cm<sup>3</sup>/min (22.3 PV/day). The results show that when the initial water saturation increased from zero to 36.8%, the breakthrough oil recovery was nearly the same, with a variation from 12.4 to 13.9 % (*OOIP*). The oil production rate after water breakthrough and the final oil recovery decreased systematically with increase in initial water saturation. This result is consistent with that obtained for strongly water-wet system of Configuration A (see **Fig.12**).

Effect of initial water saturation on oil recovery for the weakly water-wet composite system (treated with 500 ppm stearic acid solution) is presented in **Fig.18**. The established  $S_{wi}$  was varied from zero to 20% and the water injection rate was 68 cm<sup>3</sup>/day (the corresponding pressure gradient was 0.1 psi/cm after breakthrough). Water injection was halted for 14 hours after each ten-hour water injection. Each test lasted about 20 days.

The results show that the oil production rate systematically increased with increase in initial water saturation, although the final oil recovery was not much influenced. The time to reach the residual oil saturation was about 8,000 minutes for  $S_{wi}=20\%$ , 15,000 minutes for  $S_{wi}=10\%$ , and 24,000 minutes for  $S_{wi}=0$ . This result was consistent with that observed for the weakly water-wet condition of Configuration A (see **Fig.13**).

The effect of initial water saturation on the oil recovery efficiency for the weakly water-wet composite system is opposite to that of the strongly water-wet condition. The result is, however, consistent to that in the Prodhoe Bay reported by Jerauld and Rathmell<sup>4</sup>. They found that residual



oil saturation decreased with increase in initial water saturation with depth as water-wetness increased.

**Capillary Pressure.** The coreflooding results under imposed pressure gradient can be used to estimate capillary pressure. The water-oil capillary pressure ( $P_{cwo}$ ) can be defined as:

$$P_{cwo} = p_o - p_w \quad (1)$$

where  $p_o$  and  $p_w$  are the oil phase and water phase pressures, respectively. In all the tests when the inlet pressure was kept constant, only  $p_w$  at the inlet remains constant. At equilibrium, when there is no further oil production, the oil pressure drop across the core is zero. At the core outlet, the gas-oil capillary pressure ( $P_{cgo}$ ) is given by:

$$P_{cgo} = p_g - p_o \quad (2)$$

where  $p_g$  is gas phase pressure. We assume no gas flow in the core and, therefore,  $p_g = p_o = 0$ . At equilibrium,  $p_o$  (at inlet) =  $p_o$  (at outlet) = 0 which provides the expression for  $P_{cwo}$  at the inlet:

$$P_{cwo} = -p_w \quad (3)$$

We make also the assumption that at equilibrium the saturation is uniform across the core. With this assumption, Eq.3 can be then used to estimate  $P_{cwo}$ .

**Fig.19** depicts the estimated capillary pressure curves obtained for the chalk plugs with different wettability states. Note that there is no change in saturation for the strongly water-wet condition up to  $P_{cwo} = -70$  psi. On the other hand, there is a substantial effect of capillary pressure on saturation for less water-wet conditions to  $P_{cwo} = -30$  psi. For  $P_{cwo} < -30$  psi, the saturation becomes nearly independent of the state of wettability. Note that **Fig.19** is based on the fact that due to viscous forces, one may create a condition for gravity force effect.

The negative side of the capillary pressure in water-oil systems in the laboratory is often created by gravity forces. Immersion of an oil-saturated core in water in a centrifuge test is an example. We are currently working on the comparison of the results in **Fig.19** and the results from centrifuge testing. We are also working on the theoretical and numerical aspects of the experiments presented in this paper. Those aspects are the subjects of a forthcoming publication.

## Discussion and Conclusions

Practical implications from all the experiments in Configurations A and B lead to the belief that for some fractured reservoirs, the water injection performance can be independent of the state of wettability. In such reservoirs, the negative side of the capillary pressure and the capillary continuity<sup>20</sup> establish conditions for efficient water injection process.

Other main conclusions drawn from this work are:

1. With increased viscous/gravity forces, the oil recovery efficiency can increase substantially in a mixed-wet chalk. The same behavior can also occur in a mixed-wet fractured porous medium.
2. The effect of initial water saturation on oil recovery depends on wettability. For a strongly water-wet condition, oil recovery by water injection can decrease mildly with an increase in initial water saturation. However, for weakly water-wetting, the oil recovery by water injection can increase significantly with an increase in initial water saturation.

## Nomenclature

- $B.T.$  = breakthrough  
 $C_{SA}$  = concentration of stearic acid, ppm  
 $d$  = diameter. cm

$L$  = length, cm  
 $I_{aw}$  = Amott index to water, fraction  
 $k$  = permeability, md or d  
 $OOIP$  = original oil in place, %  
 $p_{atm}$  = atmosphere pressure, psi  
 $p_{in}$  = injection pressure, psi  
 $P_{cgo}$  = capillary pressure between gas and oil, psi  
 $P_{cwo}$  = capillary pressure between oil and water, psi  
 $P_g$  = gas phase pressure, psi  
 $p_o$  = oil phase pressure, psi  
 $p_w$  = water phase pressure, psi  
 $p_{o(inlet)}$  = oil phase pressure at the inlet of the core, psi  
 $p_{o(outlet)}$  = oil phase pressure at the outlet of the core, psi  
 $p_{w(inlet)}$  = water phase pressure at the inlet of the core, psi  
 $p_{w(outlet)}$  = water phase pressure at the outlet of the core, psi  
 $\mathbf{Dp}$  = pressure gradient, psi/cm  
 $\mathbf{Dp}_{bt}$  = pressure gradient after water breakthrough, psi/cm  
 $PV$  = pore volume, cm<sup>3</sup>  
 $q$  = water injection rate, cm<sup>3</sup>/min (or PV/day)  
 $R_{im}$  = oil recovery by spontaneous imbibition, % (OOIP)  
 $R_{wf}$  = oil recovery by water injection, % (OOIP)  
 $S_{wi}$  = initial water saturation, %  
 $SWW$  = strongly water-wet  
 $T$  = temperature, °C  
 $t_{ind}$  = induction time, min  
**Greek Letter**  
 $\mathbf{f}$  = porosity, fraction

## Acknowledgements

This work was supported by the US DOE grant DE-FG22-96BC14850 and the members of the Reservoir Engineering Research Institute (RERI). Their support is appreciated. We thank Mr. R. Jahanian for his assistance in all the experimental work.

## References

1. Bartley, F.E. and Miller, F.I., "Degree of Wetting of Silica by Crude Petroleum Oils," *Ind. and Eng. Chem.* (1928) 20, No.7, 738.
2. Anderson, W.G., "Wettability Literature Survey-6: The Effects of Wettability on Waterflooding," *JPT*, Dec. 1987, pp.1605-1467.
3. Morrow, N.R., "Wettability and Its Effect on Oil Recovery," *JPT* (Dec. 1990) pp 1476.
4. Jerauld, G.R. and Rathmell, J.J.: "Wettability and Relative Permeability of Prudhoe Bay: A Case Study in Mixed-Wet Reservoirs" *SPE* 29576 presented at the *SPE Annual Technical Conference and Exhibition*, New Orleans, LA, Sept, 1994.
5. Fatt, I. and Klikoff, W.A., "Effect of Fractional Wettability on Multiphase Flow Through Porous Media," *SPE* 1275-G., 1959.
6. Salathiel, R.A. "Oil Recovery by Surface Film Drainage in Mixed-Wettability Rocks," *JPT*, Oct., 1973, pp 1216-1224.

7. Cuiec, L. "Rock /Crude-Oil Interactions and Wettability: An Attempt to Understand Their Interrelation," *SPE 13211 presented at the 59<sup>th</sup> Annual Technical Conference and Exhibition* held in Houston, TX, Sept 16-19, 1984.
8. Buckley, J., Liu, Y., and Monsterleet, S. "Mechanisms of Wetting Alteration by Crude Oils," *SPEJ*, Volume 13,
9. Hamon, G. "Oil/Water Gravity Drainage Mechanisms in Oil-Wet Fractured Reservoirs," *SPE 18366 presented at the SPE European Petroleum Conference*, London, UK, Oct. 16-19, 1988. March, 1998.
10. Putra, E. Fidra, Y, and Chechter, D.S., "Use of Experimental and Simulation Results for Estimating Critical and Optimum Water Injection Rates in Naturally Fractured Reservoirs," *SPE 56431 presented at 1999 SPE Annual Technical Conference and Exhibition* held in Houston, Oct 3-6, 1999.
11. Zhou, X., Toraseter, O., Xie, X. and Morrow, N.R., "The Effect of Crude Oil Aging Time and Temperature on the Rate of Water Imbibition and Long-Term Recovery by Imbibition," *SPE*, Dec., 1995, pp.259-265.
12. Graue, A., Viksund B.G., and Baldwin, A., "Reproducible Wettability Alteration of Low-Permeability Outcrop Chalk," *SPE 39622 presented at the 1998 SPE/DOE Improved Oil Recovery Symposium* held in Tulsa, OK, 19-22 April, 1998.
13. Brown, W.O., "The Mobility of Connate Water during A Water Flood," *SPE 694-G presented at the 31<sup>st</sup> Annual Fall Meeting of Petroleum Branch of the AIM*, Oct.14-17, 1953.
14. Skauge, A., Eleri,O.O, and Graue, A., "Influence of Connate Water on Oil Recovery by Gravity Drainage," *SPE/DEO 27817 presented at the Ninth Symposium on Improved Oil Recovery* held in Tulsa, OK., 17-20 April, 1994.
15. Viksund, B.G., Morrow, N.R., Ma, S., Wang, W., and Graue, A., "Initial Water Saturation and Oil Recovery from Chalk and Sandstone by Spontaneous Imbibition," *Proceedings of 1998 International Symposium of the Society of Core Analysts*," held in Hague, 14-16 Sept., 1998.
16. Narahara, G.M., Pozzl Jr., A.L., and Blackshear Jr., T.H., "Effect of Connate Water on Gas/Oil Relative Permeabilities for Water-Wet and Mixed-Wet Berea Rock," *SPE 20503 presented at the 65<sup>th</sup> SPE Annual Technical Conference and Exhibition* held in New Orleans, LA., Sept. 23-26, 1990.
17. Zhou, X, Morrow, N.R., and Ma, S., "Interpretation of Wettability, Initial Water Saturation, Aging Time, and Oil Recovery by Spontaneous Imbibition and Waterflooding, *SPE 35436 presented at the SPE/DOE 10<sup>th</sup> Improved Oil Recovery Symposium*, held in Tulsa, OK, April 21-24, 1996.
18. Amott, E., "Observations Relating to the Wettability of Porous Rock," *Trans., AIME*, 1959.
19. Terez, I. E. and Firoozabadi, A., "Water Injection in Water-Wet Fractured Porous Media: Experiments and a New Model with Modified Buckley-Leverett Theory," *SPEJ* 4 (2), June 1999.
20. Firoozabadi, A. and Hauge, J., "Capillary Pressure in Fractured Porous Media," *JPT*, June, 1990, 784-791, also *AIME Transactions*, Vol. 289, 1990.

<b>Table-1-Relevant Data for Configuration A</b>								
<b>Run</b>	<b><i>L</i></b> (cm)	<b><i>f</i></b> (%)	<b><i>S<sub>wi</sub></i></b> (%)	<b><i>C<sub>SA</sub></i></b> (ppm)	<b><i>I<sub>aw</sub></i></b>	<b><i>D<sub>p</sub></i></b> (psi/cm)	<b><i>R<sub>im</sub></i></b> (%)	<b><i>R<sub>wf</sub></i></b> (%)
<b>Initial Wettability</b>								
1a	6.35	30.6	0	0	1.0	0	66.2	-
1b	6.35	30.6	0	0	1.0	0	66.2	-
<b>Effect of <i>C<sub>SA</sub></i> on Wettability</b>								
2a	6.51	30.7	0	100	0.83	0	62.0	-
2b	6.51	30.7	0	100	0.83	0	62.4	-
2c	6.51	30.7	0	100	0.83	0	63.0	-
3a	6.62	30.1	0	200	0.74	0	53.0	-
3b	6.62	30.1	0	200	0.74	0	53.4	-
3c	6.62	30.1	0	200	0.74	0	53.4	-
4a	6.31	30.9	0	500	0.66	0	46.0	-
4b	6.31	30.9	0	500	0.66	0	46.5	-
4c	6.31	30.9	0	500	0.66	0	48.5	-
5a	6.50	30.2	0	1000	0.07	0	3.2	-
5b	6.50	30.2	0	1000	0.07	0	2.7	-
5c	6.50	30.2	0	1000	0.07	0	2.7	-
<b>Effect of <i>D<sub>p</sub></i> on Oil Recovery by Water Injection</b>								
6a	5.41	31.1	0	0	1.0	0	-	66.2
6b	5.41	31.1	0	0	1.0	0.09	-	66.2
6c	5.41	31.1	0	0	1.0	0.37	-	66.2
6d	5.41	31.1	0	0	1.0	0.93	-	66.2
6e	5.41	31.1	0	0	1.0	12.9	-	66.2
7a	5.21	30.7	0	500	0.55	0	-	39.0
7b	5.21	30.7	0	500	0.55	0.96	-	59.5
7c	5.21	30.7	0	500	0.55	3.85	-	66.2
7d	5.21	30.7	0	500	0.55	13.5	-	72.0
8a	5.20	30.6	0	1000	0.07	0	-	6.0
8b	5.20	30.6	0	1000	0.07	0.96	-	16.0
8c	5.20	30.6	0	1000	0.07	1.92	-	42.0
8d	5.20	30.6	0	1000	0.07	3.55	-	49.5
8e	5.20	30.6	0	1000	0.07	7.69	-	73.0
8f	5.20	30.6	0	1000	0.07	12.9	-	78.0
<b>Effect of <i>I<sub>aw</sub></i> on Oil Recovery by Water Injection</b>								
9a	5.22	30.0	0	200	0.82	0.96	-	60.5
7b	5.21	30.7	0	500	0.55	0.96	-	59.5
8b	5.20	30.6	0	1000	0.07	0.96	-	16.0
9b	5.22	30.0	0	200	0.82	13.5	-	66.2
7d	5.21	30.7	0	500	0.55	13.5	-	72.0
8f	5.20	30.6	0	1000	0.07	12.9	-	78.0
<b>Effect of <i>S<sub>wi</sub></i> on Oil Recovery by Water Injection</b>								
10a	6.01	29.6	0	0	1.0	0.93	-	66.7
10b	6.01	29.6	10	0	1.0	0.93	-	67.2
10c	6.01	29.6	21	0	1.0	0.93	-	66.2
10d	6.01	29.6	32	0	1.0	0.93	-	65.5
10e	6.01	29.6	33	0	1.0	0.93	-	65.0
10f	6.01	29.6	39	0	1.0	0.93	-	60.0
10g	6.01	29.6	45	0	1.0	0.93	-	53.2
11a	5.31	30.5	10	500	0.55	0.96	-	61.3
11b	5.31	30.5	20	500	0.55	0.96	-	61.0
12a	5.40	30.2	10	1000	0.09	0.96	-	38.0
12b	5.40	30.2	19	1000	0.09	0.96	-	58.5
12c	5.40	30.2	10	1000	0.09	0.96	-	39.1

Note:  $k=0.5$  md,  $d=5.08$  cm (runs 2 to 12) and  $=3.81$  cm (run 1)

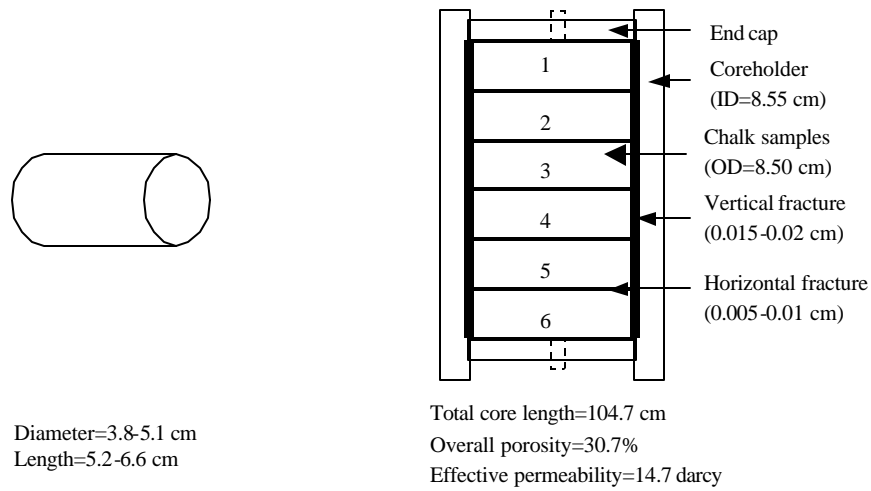
<b>Table-2-Relevant Data for Configuration B</b>								
Run	Core	$k$	$S_{wi}$	$C_{SA}$	$I_{aw}$	$q$	$Dp_{bt}$	$R_{wf}$
	(d)			(ppm)		(cm <sup>3</sup> /min)	(psi/cm)	(%)
<b>Effect of <math>q</math> on Oil Recovery by Water Injection</b>								
13	B-1	14.7	0	0	1.0	5.0	0.010	66.2
14	B-1	14.7	0	0	1.0	11.0	0.014	66.3
15a	B-1	14.7	0	0	1.0	26.2	0.020	66.4
15b	B-1	14.7	0	0	1.0	26.2	0.020	66.2
16a	B-2	4.5	0	500	-	10.0	0.025	47.0
16b	B-2	4.5	0	500	-	10.0	0.025	44.7
17	B-2	4.5	0	500	-	30.0	0.046	53.0
18	B-2	4.5	0	500	-	68.0	0.101	60.0
<b>Effect of <math>S_{wi}</math> on Oil Recovery by Water Injection</b>								
19	B-1	14.7	0	0	1.0	26.2	0.020	66.2
20	B-1	14.7	13.9	0	1.0	26.2	0.020	61.9
21	B-1	14.7	21.2	0	1.0	26.2	0.020	57.0
22	B-1	14.7	36.8	0	1.0	26.2	0.020	52.0
18	B-2	4.5	0	500	-	68.0	0.101	60.0
23	B-2	4.5	10.0	500	-	68.0	0.101	62.6
24	B-2	4.5	20.0	500	-	68.0	0.101	59.8

Note: (1) the fracture aperture was about 250  $\mu$ m for B-1 and 150  $\mu$ m for B-2

(2)  $Dp_{bt}$  is the differential pressure after water breakthrough

(3)  $d=8.5$  cm,  $L=104.7$  cm,  $f=30.7\%$

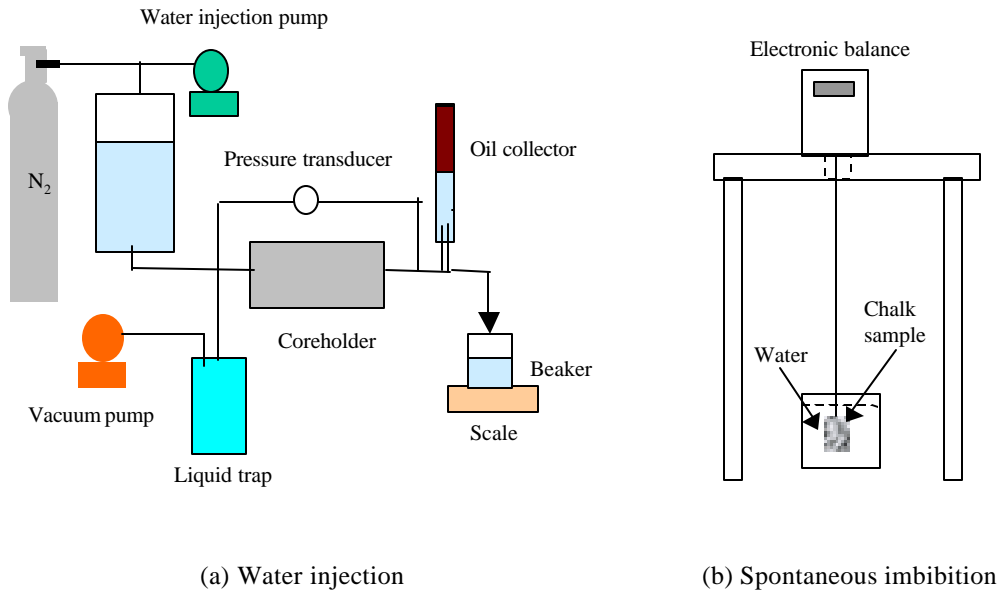
(4)  $I_{aw}$  is not valid for B-2 core



(a) Configuration A

(b) Configuration B

**Fig.1 - Configurations of Kansas Outcrop Chalks Used in the Experiments**



(a) Water injection

(b) Spontaneous imbibition

**Fig.2 - Schematic of Apparatuses for Water Injection and Spontaneous Imbibition Tests**

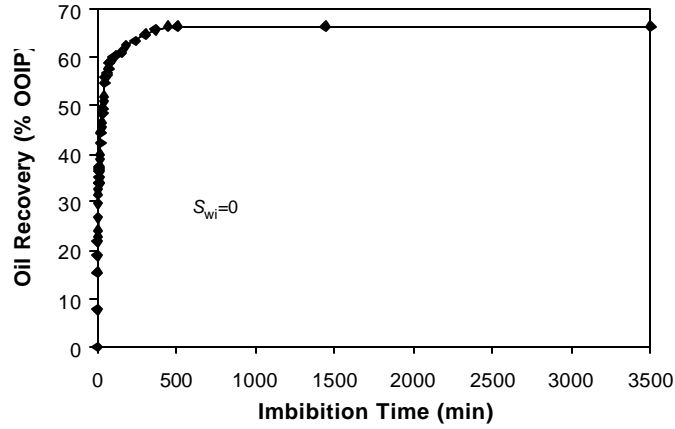


**Fig.3 - Spontaneous Imbibition of the Chalk Prior to Wettability Alteration: Configuration A**

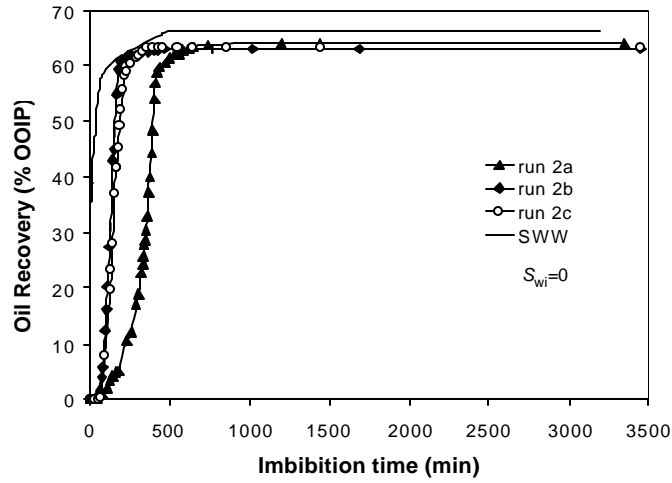


**Fig.4 - Wettability Transition Towards More Water-Wetness with Repeated Spontaneous Imbibition Tests: Configuration A**

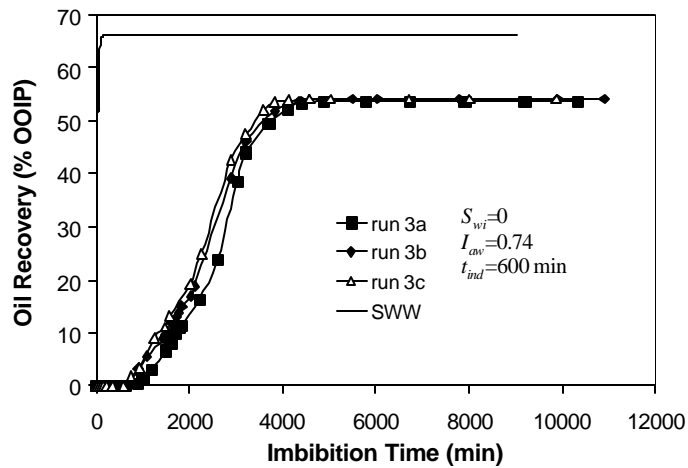


**Fig.5 - Spontaneous Imbibition of the Chalk after Wettability Alteration: Configuration A ( $C_{SA}=200$  ppm)**

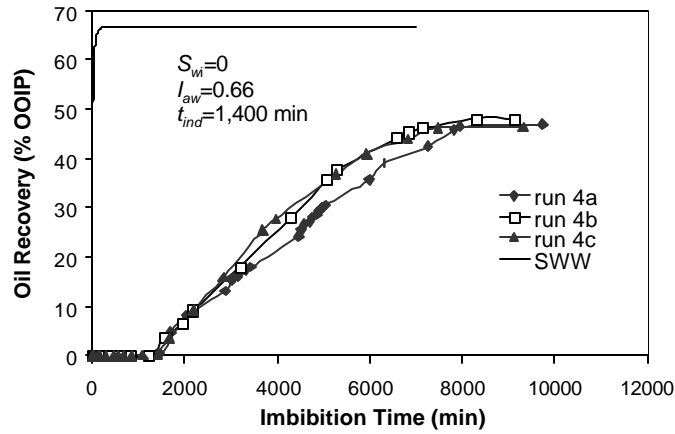


**Fig.6 - Spontaneous Imbibition of the Chalk after Wettability Alteration: Configuration A ( $C_{SA}=500$  ppm)**

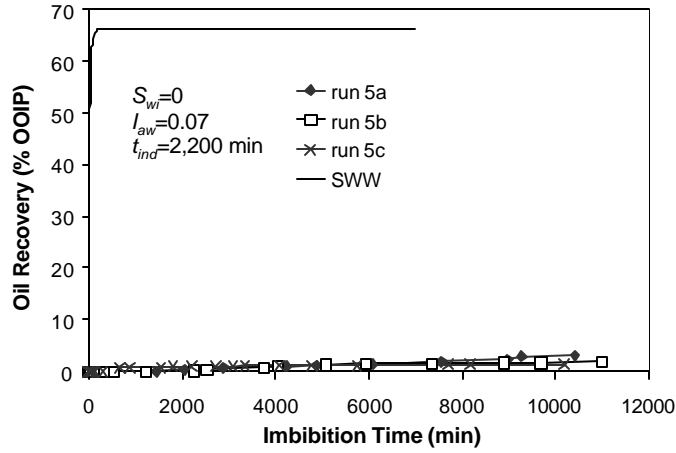


**Fig.7 - Spontaneous Imbibition of the Chalk after Wettability Alteration: Configuration A ( $C_{SA}=1,000$  ppm)**

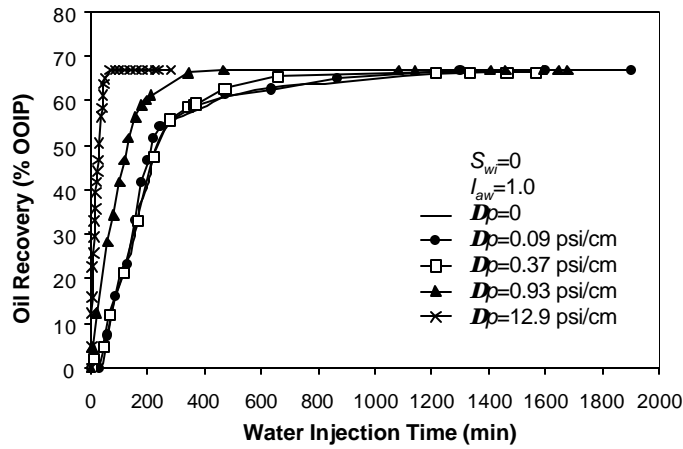


**Fig.8 - Effect of Pressure Gradient on Oil Recovery by Water Injection: Strongly Water-Wet, Configuration A**



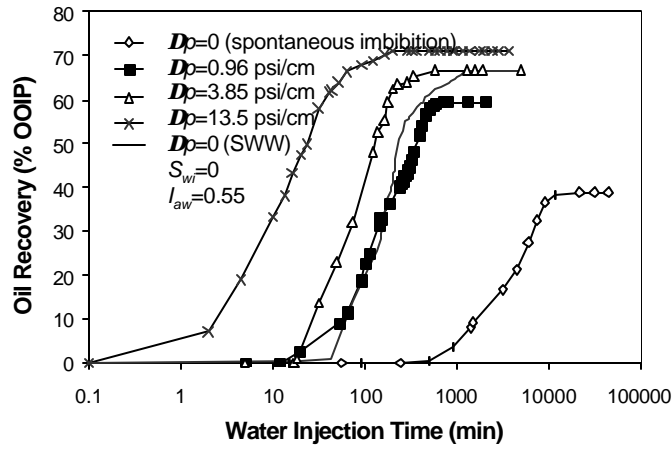


Fig.9 - Effect of Pressure Gradient on Oil Recovery by Water Injection: Weakly Water-Wet, Configuration A ( $C_{SA}=500$  ppm)

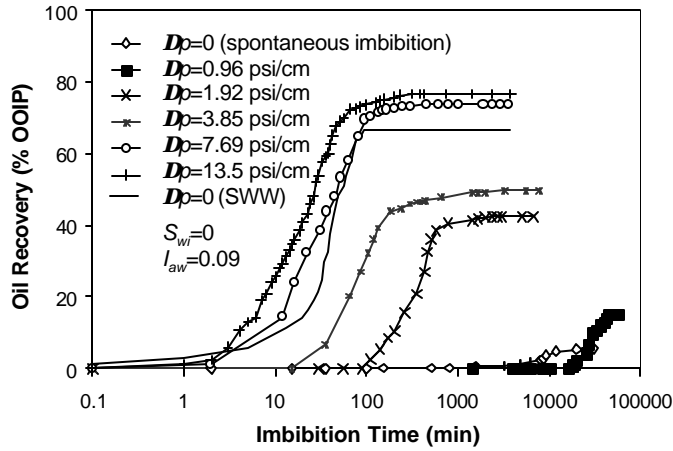


Fig.10 - Effect of Pressure Gradient on Oil Recovery by Water Injection: Intermediate-Wet, Configuration A ( $C_{SA}=1,000$  ppm)

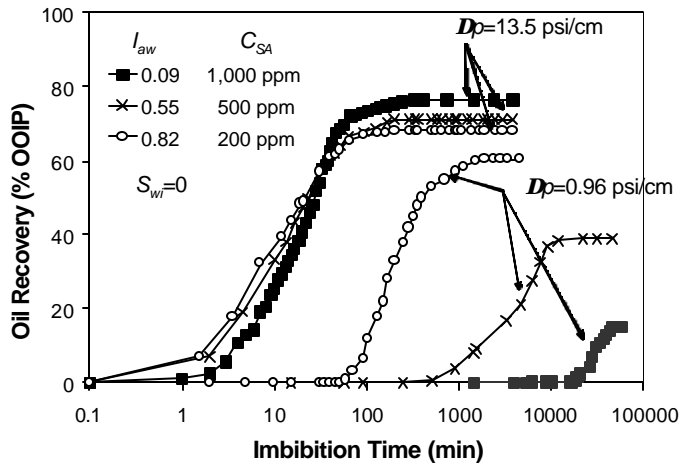


Fig.11 - Effect of Pressure Gradient on Oil Recovery by Water Injection for Three Wettability States: Configuration A

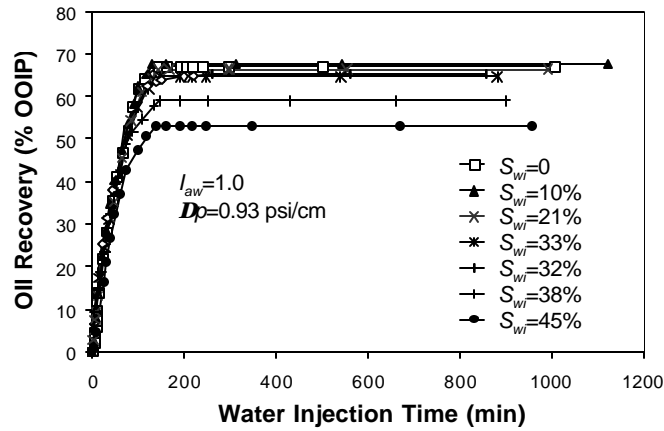


Fig.12 - Effect of Initial Water Saturation on Oil Recovery by Water Injection: Strongly Water-Wet, Configuration A

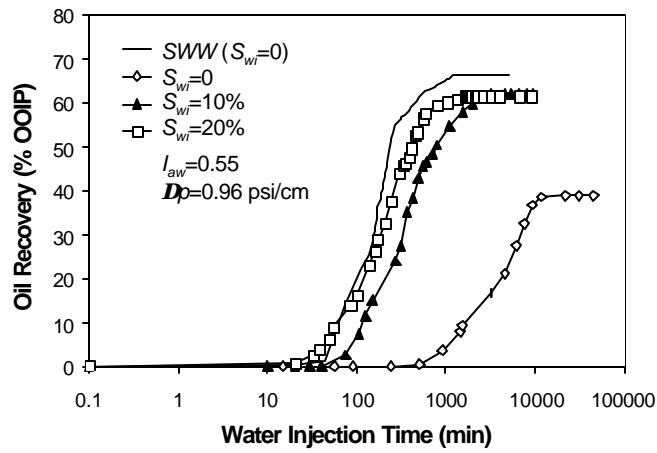


Fig.13 - Effect of Initial Water Saturation on Oil Recovery by Water Injection: Weakly Water-Wet, Configuration A ( $C_{SA}=500$  ppm)

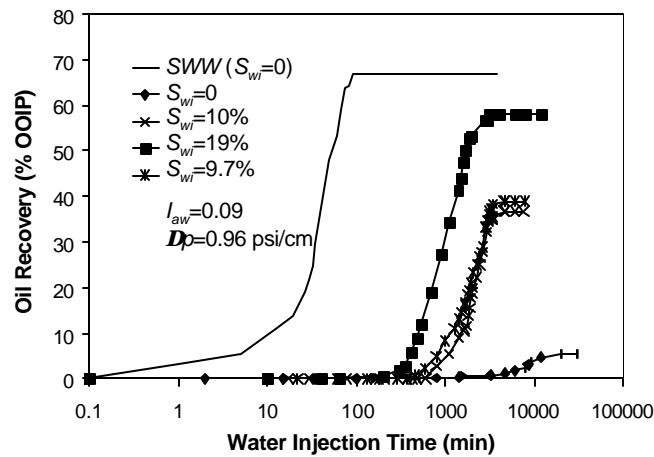
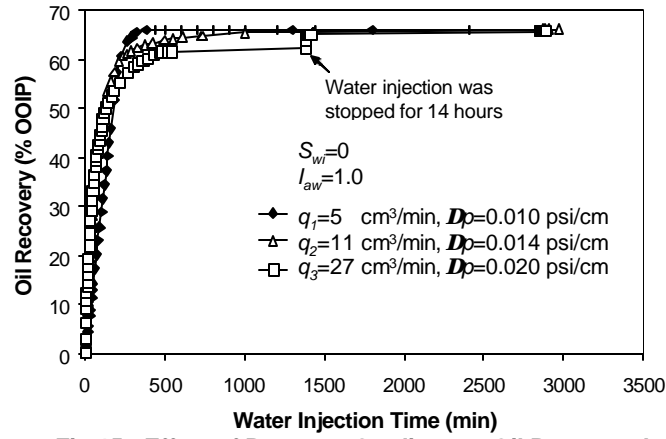
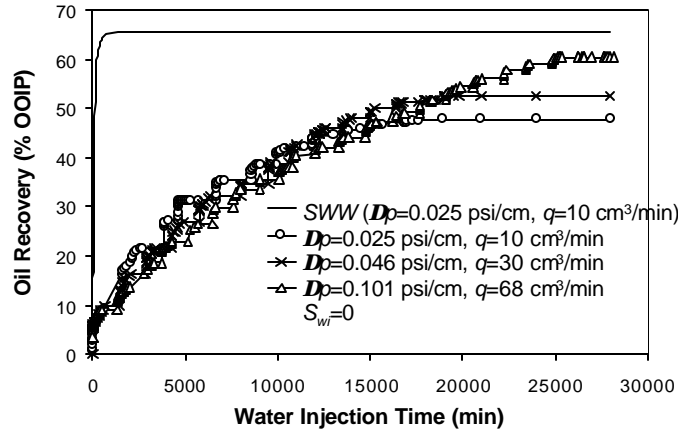


Fig.14 - Effect of Initial Water Saturation on Oil Recovery by Water Injection: Intermediate-Wet, Configuration A ( $C_{SA}=1,000$  ppm)



**Fig.15 - Effect of Pressure Gradient on Oil Recovery by Water Injection: Strongly Water-Wet, Configuration B**



**Fig.16 - Effect of Pressure Gradient on Oil Recovery by Water Injection: Weakly Water-Wet, Configuration B ( $C_{SA}=500$  ppm)**

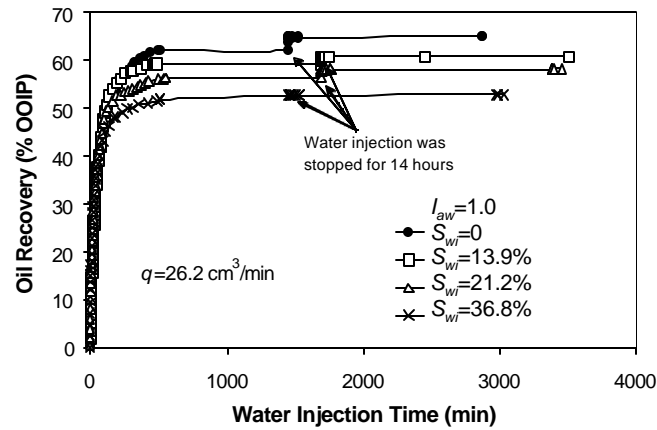


**Fig.17 - Effect of Initial Water Saturation on Oil Recovery by Water Injection: Strongly Water-Wet, Configuration B**

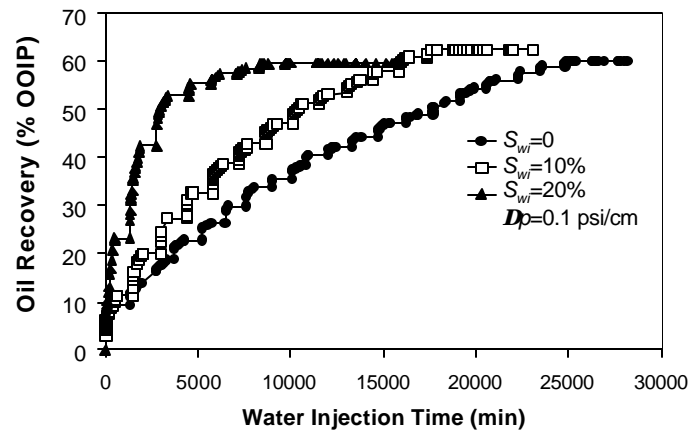


Fig.18 - Effect of Initial Water Saturation on Oil Recovery by Water Injection: Weakly Water-Wet, Configuration B ( $C_{SA}=500$  ppm)

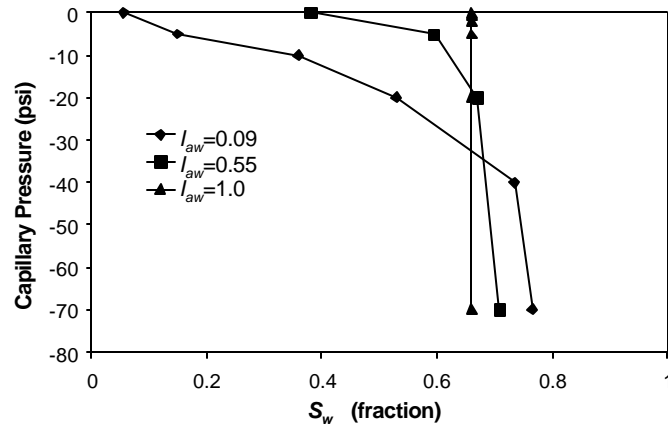


Fig.19 - Estimated Capillary Pressure Curves from Water Injection: Configuration A

# **Chapter I – Water Injection in Fractured Porous Media**

## **Part IV – Recovery Mechanisms in Fractured Reservoirs and Field Performance**

ABBAS FIROOZABADI

### **Summary**

Fractured petroleum reservoirs provide considerable challenge in studying natural depletion, immiscible gas injection, miscible gas injection, and water injection. In this overview, certain key aspects of two-phase flow in relation to gas injection and water injection in fractured reservoirs are reviewed. One main conclusion from the review is that the field performance can be very efficient by water injection in some weakly water-wet fractured reservoirs despite the poor recovery in the laboratory by the conventional imbibition testing.

### **Introduction**

Fractured hydrocarbon reservoirs provide over 20 percent of the world oil reserves and production. Examples of the prolific fractured petroleum reservoirs are: 1) the Asmari limestone reservoirs in Iran, 2) the vugular carbonate reservoirs in Mexico, and 3) the group of chalk reservoirs of the North Sea. These prolific reservoirs produce more than 5 million barrels of oil a day; their common feature is a long life span, which could last several decades. There are a large number of other fractured hydrocarbon reservoirs that may have features very different from the above reservoirs. Examples of such reservoirs are the Austin chalk field and the Keystone (Ellenberger) field in Texas, and the Tempa Rossa field in Italy. In the Keystone field, the average matrix porosity is around 2.5 percent; the Austin chalk and Tempa Rossa also have very low porosity. On the other hand, the average matrix porosity of the Ekofisk chalk field in the North Sea is around 35 percent.

Fractured reservoirs can be classified into three different groups. For group one, the bulk of the hydrocarbon resides in the matrix and fracture pore volume (PV) is very small in comparison to the matrix PV. The Ekofisk field in the North Sea is an example of this group<sup>(1)</sup>. In group two, most of the hydrocarbon is in the matrix, but fracture PV could be as high as 10 to 20 percent. The Asmari limestone reservoirs are example of the second group<sup>(2)</sup>. For group three, more than half of the hydrocarbon resides in the fracture; in some cases, the contribution of the matrix can be negligible. The Keystone (Ellenberger) field in Texas is an example of a fractured reservoir where most of the hydrocarbon is from the fractures<sup>(3)</sup>. There are very few reports of the production performance of group three in the literature. For all three groups, the matrix permeability is often low – of the order of several md to less than 0.01 md. The effective permeability due to fractures increases from one to several orders of magnitude. In some of the reservoirs of group three, the productive life varies from less than one year to several

years. The ultimate recovery from fractured reservoirs varies widely – from less than 10 percent to over 60 percent. The recovery factor in group three could vary from 10 percent to over 60 percent; the recovery factor of 10 percent is mostly from the fracture and rock compressibility, and the recovery of 60 percent is mainly from gravity drainage. Later we will study the key factors that affect recovery performance of fractured reservoirs.

There are fundamental differences between recovery performance of fractured and unfractured reservoirs. Capillarity is the main cause of this difference. More specifically, the difference in capillary pressure of matrix and fractures has a significant effect on recovery performance of fractured reservoirs.

In the following, gas displacement and water displacement processes in fractured porous media and a brief description of compressibility effect are presented.

### Gas-Oil Displacement in Fractured Media

Gas-oil immiscible displacement in the form of gas-oil gravity drainage could contribute to substantial recovery in fractured reservoirs. Two mechanisms affect the efficiency of gas-oil gravity drainage: 1) reinfiltration, and 2) capillary continuity. Reinfiltration may direct the path of oil flow to be primarily in the tight matrix, not through the high permeability fractures. Capillary continuity between the matrix blocks may improve the final recovery drastically. However, due to the contrast in matrix and fracture capillary pressure, the rate of drainage in fractured porous media can be substantially less than in a homogeneous tight matrix. Next we discuss reinfiltration in fractured porous media and then gravity drainage in layered and fractured media to elucidate these two mechanisms.

**Reinfiltration in Fractured Porous Media** - The rate of oil flow in a one-dimensional matrix block in the vertical direction is given by<sup>(4)</sup>

$$q = \frac{kk_{ro}}{\boldsymbol{m}_b} \left[ \Delta \boldsymbol{r} g - \frac{dP_c}{dS_o} \frac{dS_o}{dz} \right] \quad (1)$$

where  $\Delta \boldsymbol{r}$  is the density difference between the oil and gas phases,  $P_c$  is the gas-oil capillary pressure,  $S_o$  is the oil saturation,  $z$  is the vertical distance (positive upwards),  $k$  and  $k_{ro}$  are the absolute permeability and oil relative permeability, respectively,  $\boldsymbol{m}_b$  is the oil viscosity, and  $q$  is the rate of oil drainage or infiltration and is assumed to be positive in the downward direction. This equation gives the rate of drainage at the bottom face ( $z=0$ ) and the rate of reinfiltration of oil at the top face ( $z=L$ ) of a matrix block. The term  $dS_o/dz$  could be positive, zero, or negative. The term  $dP_c/dS_o$  is never positive. At  $z=0$ , when the matrix is fully saturated,  $dS_o/dz=0$ , and the initial rate is:

$$q|_{z=0} = \frac{kk_{ro}}{\boldsymbol{m}_b} \Delta \boldsymbol{r} g \quad (2)$$

As the matrix block desaturates  $dS_o / dz|_{z=0} < 0$  and the rate of drainage decreases. Therefore, the rate of drainage from the bottom face of the matrix block is always,

$$q|_{z=0} \leq \frac{kk_{ro}}{m_b} \Delta r g \quad (3)$$

From the top face of the matrix block at  $z = L$ , the rate of oil reinfiltration can be computed using Eq. 1. If enough liquid is provided,  $S_o|_{z=L} = 1$  and  $dS_o / dz|_{z=L} > 0$ , and therefore,

$$q|_{z=L} \geq \frac{kk_{ro}}{m_b} \Delta r g \quad (4)$$

The implication of the relationships given by Eqs. 3 and 4 is that as the matrix desaturates, the rate of reinfiltration is higher than the rate of drainage and, therefore, oil flows through the matrix. The above results are in the context of gas and oil flow far away from the wellbore where viscous effects are not pronounced.

Note that reinfiltration applies to gas-oil systems but not to water-oil systems (when water is the wetting-phase). When oil is the wetting-phase in a water-oil system, then the oil in fractures could reinfiltrate back into matrix rock. For the weakly water-wetting in oil-water flow, the rate of reinfiltration of the produced oil from a matrix block to the neighboring matrix blocks may not be significant.

**Gas-oil Gravity Drainage in Layered and Fractured Media** - Let us consider two sand columns each of 18-m height. One sand column is homogeneous and has a permeability of 750md. The other sand column is layered with alternate layers of 750md and 7500md. The height of each layer in the layered column is 1.8m. The geometric average permeability of the layered column is about 2200md – about three times the homogeneous column. The porosity and residual oil saturations of the less permeable sand and the more permeable sand are assumed the same (see theory and details in Firoozabadi<sup>(5)</sup> and Correa and Firoozabadi<sup>(6)</sup>).

Fig. 1 shows the drainage rate and the cumulative production of the two columns. Note that the less permeable sand column has a better recovery efficiency than the more permeable layered-sand column. The main reason for the difference in recoveries is due to the capillary pressure contrast between the two layers. From the drainage rate results (see Fig. 1), one may confidently conclude that there is no meaning to an average capillary pressure for a layered system when there is a contrast in capillary pressures. One may not also provide scale up for such a drainage problem.

Let us now consider the drainage performance of a 1.8-m long homogenous Berea sandstone with a cross sectional area of 220.5 cm<sup>2</sup>. After measuring the drainage performance of this tall block, it was cut into three equal pieces of 0.60m height each<sup>(7)</sup>. These blocks were stacked on top of each other. Four metallic spacers of 100-micron thickness and areal dimensions of 2×2 cm were inserted in the space between the matrix blocks. The insertion of spacers ensures uniform fracture aperture between the matrix blocks. The drainage performance of the three-block stack was also measured. Fig. 2

shows the drainage performance of the tall block and the three-stacked blocks. There is a significant difference between the two recovery curves. While the permeability of the stacked block system is more than the permeability of the tall block, the capillary pressure contrast between the fracture and the matrix media affects the recovery in favor of the less permeable tall block. Fig. 3 shows the fracture and matrix capillary pressures that were used to simulate the drainage results shown in Fig. 2 (see Ref. 8).

The two examples above reveal that the capillary pressure contrast between the two media next to each other has a pronounced adverse effect on recovery performance by gas-oil gravity drainage. When the two capillary pressures become identical, the gas-oil gravity drainage recovery performance improves significantly. One may reduce capillary pressure contrast by reducing the interfacial tension between the gas and oil phases through miscible displacement. Miscible displacement in fractured porous media can be a viable option for improved oil recovery. It will be discussed briefly next.

### **Miscible Displacement in Fractured Porous Media**

The common understanding of flow in fracture porous media is that fractures provide the oil flow path and the matrix provides the storage. This understanding is true in 1) single phase flow, 2) water-wet fractured media for water displacement of oil, and 3) flow around the wellbore with high viscous forces. As we have seen above, it may not be valid for gas-oil gravity drainage. When miscible injection in fractured porous media is considered, we need also to modify our thinking. In general, there are various crossflows between a less permeable and a more permeable porous medium due to capillary, gravity, and viscous forces or due to diffusion. Both experimental data and theoretical analysis (Refs. 9-11) show that in a miscible injection process, the injected fluids do not flow through the high permeability fractures. There is strong gravity and viscous crossflows between fractures and matrix. As a result, miscible gas injection in fractured porous media can be very efficient. State of the art in dual-permeability modeling does not currently allow to account for some of the basic crossflows in miscible gas injection in fractured reservoirs.

### **Water Displacement in Fractured Media**

Water injection has been very efficient in some fractured reservoirs. However, the general thinking in the literature centers around the idea that water injection in fractured reservoirs is mainly efficient for water-wet conditions. On the basis of this belief, laboratory experiments are conducted by immersing an oil-saturated core plug into water to study the imbibition recovery. The immersion forces the imbibition to be countercurrent. In the past, when the countercurrent imbibition tests in the laboratory gave poor recovery, water injection was assumed to be inefficient. As we will demonstrate soon, one can measure very poor recovery by countercurrent imbibition testing in the laboratory, but in the field, water injection may be very efficient. In other words, there may be no relation between laboratory measurements of spontaneous imbibition and field performance, even when the reservoir wettability state is perfectly restored in the laboratory. Hermansen et al.<sup>(1)</sup> have reviewed water injection performance of the Ekofisk fractured field in the North Sea. The field data show that the water-injection performance in Ekofisk is independent of its wettability state. Fig. 4 shows the oil production rate in Ekofisk from 1972 to 1997. Water injection in the field



commenced in 1987. Figure 4 shows the dramatic increase (from 70,000 BOPD in 1987 to 260,000 BOPD in 1997) in rate after water injection commencement. In the upper formation (where the reservoir is less water-wet) in-situ saturation measurements showed that recoveries were better than laboratory measured values. Field data show that in this fractured field there has been limited water breakthrough even after ten years of waterflood operation.

Now we discuss water injection in both water-wet and weakly water-wet (that is, intermediate-wet) fractured porous media.

The fracture network does not become flooded at once from water injection; the water-oil level in the fractures has an advancing behavior. Therefore, imbibition in a water-wet matrix block of a fractured medium may not be only due to countercurrent imbibition. When a water-wet matrix block is partially covered by water, oil recovery can be either mostly by cocurrent imbibition or by both countercurrent and cocurrent imbibition.

Pooladi-Darvish and Firoozabadi<sup>(12)</sup> have shown that the scaling of countercurrent imbibition, which is often used to evaluate water injection in water-wet fractured reservoirs may lead to pessimistic recovery performance. In countercurrent imbibition, the oil flow path is in two-phase; in cocurrent imbibition, the flow path for oil is mainly in single-phase, which can be very efficient. Fig. 5 shows the recovery performance of a single matrix block from water injection from the bottom, and immersion in water<sup>(13)</sup>. A single block of an outcrop chalk ( $k \approx 3\text{md}$ ,  $f \approx 30\%$ ) was placed in a visual coreholder and was surrounded by top, bottom, and side fractures. Fig. 5 shows that the initial rate of imbibition for the immersion tests is high. This is due to large contact area between the matrix block and the fracture water. Later on, however, production rate for injection tests is higher than the immersion tests. The immersion forces countercurrent imbibition, whereas injection gives the matrix a choice for cocurrent or countercurrent depending on rate of injection. Fig. 6 presents the fine grid simulation results of water injection from the bottom of the matrix surrounded by fractures. The height at zero is the bottom and top of the block is at 30cm. The water saturation in the fracture at 0.1 and 0.3 PV injection and the corresponding oil flux from the matrix to the fracture, and the water flux from the fracture to the matrix show that most of the oil is produced by cocurrent imbibition (the rates in the Fig. 6 are dimensionless). In other words, the oil is produced mainly above the water-oil contact in the fracture and water imbibes below the water-oil contact<sup>(14)</sup>.

Fig. 7 shows the effect of pressure gradient across a rock sample on oil recovery in a water-wet tight rock plug<sup>(15)</sup> ( $k = 1.3\text{md}$ ,  $f \approx 30\%$ ,  $L \approx 6\text{cm}$ ,  $d = 5.1\text{cm}$ ). This figure also shows the recovery performance from countercurrent imbibition for the same rock. Note that the final oil recovery is around 68 percent and is independent of the pressure gradient. The recovery from countercurrent imbibition is also 68 percent. In the countercurrent imbibition test, the oil-saturated rock is immersed in water. In the coreflooding tests, the core was sealed across the circumference and water was injected at a constant pressure. The outlet was at atmospheric pressure.

Fig. 8 plots the recovery performance of the weakly water-wet core (with the same permeability, porosity, and dimensions and similar to the core plug of Fig. 7). The Amott wettability index to water<sup>(16)</sup> is 0.09. Fig. 8 also shows the recovery performance of the water-wet rock as a reference when it is subjected to countercurrent imbibition.

For the countercurrent imbibition test in the weakly water-wet rock, there is no water imbibition to a time of about 6 days. The period in which the rate of imbibition is zero at the beginning is called the induction time, which is a common feature in a nucleation phenomena<sup>(17)</sup>. Even when the imbibition begins, the rate is low. The final recovery is only about 5 percent. In the flooding test, the recovery increases with the increase of pressure gradient. At a pressure gradient of 0.96 psi/cm, the induction time is about 14 days and the final recovery is about 11 percent. As the pressure gradient increases, the recovery performance improves. At pressure gradients of 3.85 and 13.5 psi/cm, the final recoveries are about 50% and 78%, respectively. Note that the final recovery for the countercurrent imbibition of the water-wet rock is about 68 percent.

Fig. 9 shows the estimated capillary pressures for the water-wet ( $I_{aw}=1.0$ ) and the weakly water-wet ( $I_{aw}=0.09$ ) rocks. Only the negative capillary pressures are estimated; the final recovery and pressure data from the corefloodings were used to estimate the capillary pressure, which is defined from  $P_c = p_0 - p_w$ . Note that at  $P_c = 0$ , the water saturations are 5 and 65 percent for the weakly water-wet and water-wet cores, respectively. These saturations are consistent with the countercurrent imbibition tests in Fig. 7. Note that there is no extra recovery for the water-wet rock at high negative capillary pressures. On the other hand, there is a major increase in oil recovery for the weakly water-wet rock as capillary pressure decreases. The contribution for the negative side of the capillary pressure curve to recovery is often called forced imbibition; the recovery from the positive side is called spontaneous imbibition.

### Fracture-Matrix-Fluid Compressibility

Knowledge of formation compressibility can be very important when a highly undersaturated oil in a fractured reservoir is considered. The total compressibility becomes critical when gas and water injection options are not available. Suppose we neglect the pore compressibility, and the fluid compressibility is  $6 \times 10^{-6}$  1/psia; then the recovery from 4000 psi pressure drop would be 2.4 percent. However if the combined fracture/matrix pore compressibility is  $c_f = 2 \times 10^{-5}$  1/psia, then the recovery would be 10.4 percent, which is substantial. High compressibility allows economical depletion of fractured reservoirs of group three (with no matrix porosity) where there is no active aquifer and there is a substantial oil undersaturation (say 4000 to 5000 psi).

### Discussion and Concluding Remarks

Fractured petroleum reservoirs are currently characterized by two main models. In the so-called sugar-cube model, all the fractures are connected and the size of the matrix blocks surrounded by fractures is an important parameter. Dual-porosity models are extensively used to simulate various production schemes from such characterization (Gilman and Kazemi<sup>(18)</sup>, and Thomas et al.<sup>(19)</sup>). In the discrete fracture model, the connectivity of fractures are realistically described. Efforts towards the use of discrete-fracture representation of fractured reservoirs in multiphase flow has begun<sup>(20)</sup>. In each of these two models it is a challenge to include various mechanisms of water and gas displacement. Nevertheless, as the understanding of physical processes improves, we use the improved physical understanding of flow processes either directly or indirectly in appropriate models for the characterization of fractured reservoirs. It seems that the

combination of laboratory research and interpretation of field performance is our best course of action for efficient production from fractured reservoirs.

### Acknowledgements

The work carried out on fractured petroleum reservoirs at the Reservoir Engineering Research Institute(RERI) has been supported by the US DOE grant DE-FG26-99BC15177 and the oil-company members of RERI in the past 10 years. We greatly appreciate their support.

### Nomenclature

$cf$	formation compressibility
$d$	core diameter
$g$	acceleration due to gravity
$I_{aw}$	Amott wettability index to water
$k$	permeability
$k_{ro}$	oil relative permeability
$L$	core length
$p$	pressure
$P_c$	capillary pressure
$p_o$	oil phase pressure
$p_w$	water phase pressure
$q$	oil flow rate
$S_o$	oil saturation
$z$	height
$\Delta\rho$	gas-oil density difference
$\mu$	oil viscosity

### References

1. Hermansen, H., Thomas, L.K., Style, J.E., and Aasboe, B.T.: "Twenty-five Years of Ekofisk Reservoir Management," SPE 38927, proceedings of the 1997 SPE Annual Fall Meeting, San Antonio, TX, Oct. 1997.
2. Saidi, A.M.: "Reservoir Engineering Reservoirs – Fundamentals and Practical Aspects, Total Edition Press, Paris (1987).
3. Holtz,M.H.,Kerans,C.," Characterization and Categorization of West Texas Ellenberger Reservoirs,"Bureau of Economics Geology,University of Texas-Austin.
4. Firoozabadi, A. and Ishimoto, K.: "Reinfiltration in Fractured Porous Media – Part 1 – One Dimensional Model," SPE Advanced Technology (April 1994) 35-44.
5. Firoozabadi, A.: "Recovery Issues of Immiscible and Miscible Gas-Oil Flow in Fractured Reservoirs: Laboratory Data and Theoretical Analysis." Invited keynote paper. Proceedings of the First JNOC-TRC International Symposium on Carbonate Rocks-Hydrocarbon Exploration and Reservoir Characterization, Chiba, Japan, March 1-5, 1993 (ed. K. Kimura).
6. Correa, A. and Firoozabadi, A.: "Concept of Gravity Drainage in Layered Porous Media," SPE J.(March 1996) 101-111.

7. Firoozabadi, A. and Markeset, T.: "Fracture-Liquid Transmissibility in Fractured Porous Media" SPE Reservoir Engineering (Aug 1994) 201-207.
8. Dindoruk, B. and Firoozabadi, A.: "Computation of Gas-Liquid Drainage in Fractured Porous Media Recognizing Fracture Liquid Flow," J. of Canadian Petroleum Technology (Dec. 1995) 39-49.
9. Firoozabadi, A. and Markeset, T.: "Miscible Displacement in Fractured Porous Media: Part I – Experiments," SPE/DOE 27743, paper presented at the Ninth Symposium on Improved Oil Recovery, April 17-20, Tulsa, OK 1996.
10. Dindoruk, B. and Firoozabadi, A.: "Crossflow in Fractured/Layered Media Incorporating Gravity, Viscous, and Phase Behavior Effects," SPE J. (June 1997) 120-135.
11. Tan, C.T. and Firoozabadi, A.: "Theoretical Analysis of Miscible Displacement in Fractured Porous Media – Part I - Theory," J. of Canadian Petroleum Technology (Feb. 1995) 17-27.
12. Pooladi-Darvish, M. and Firoozabadi, A.: "Cocurrent and Countercurrent Imbibition in a Water-Wet Matrix Block," SPE J.(March 2000)3-11.
13. Pooladi-Darvish, M. and Firoozabadi, A.: 'Laboratory Measurements of Water Injection in Water-Wet Fractured Porous Media," J. of Canadian Petroleum Technology (March 2000).
14. Terez, I. and Firoozabadi, A.: "Water Injection in Water-Wet Fractured Porous Media: Experiments and a New Model Using Modified Buckley-Leverett Theory," SPE J. (June 1999) 134-141.
15. Tang, G-Q. and Firoozabadi, A.: "Effect of Viscous and Initial Water Saturation on Water Injection in Water-Wet and Mixed-Wet Fractured Porous Media," SPE 59291, proceedings of the SPE/DOE Improved Oil Recovery Symposium, April 3-5, 2000, Tulsa.
16. Amott, E.: "Observations Relating to the Wettability of Porous Rock," Trans. AIME (1959).
17. Kashchiev, D.: "Nucleation: Basic Theory with Applications," Butterworth Heinemann, Oxford,UK, 2000.
18. Gilman, J. and Kazemi, H.: "Improvements in Simulation of Naturally Fractured Reservoirs," SPE J. (Aug. 1983) 695-707.
19. Thomas, L.K., Dixon, T.N., and Pierson, R.G.: "Fractured Reservoir Simulation," SPE J. (February 1983) 42-54.
20. Kim, J.G. and Deo, M.D.: "Finite Element, Discrete-Fracture Model for Multiphase Flow in Porous Media," AIChE J. (June 2000) 1120-1130.

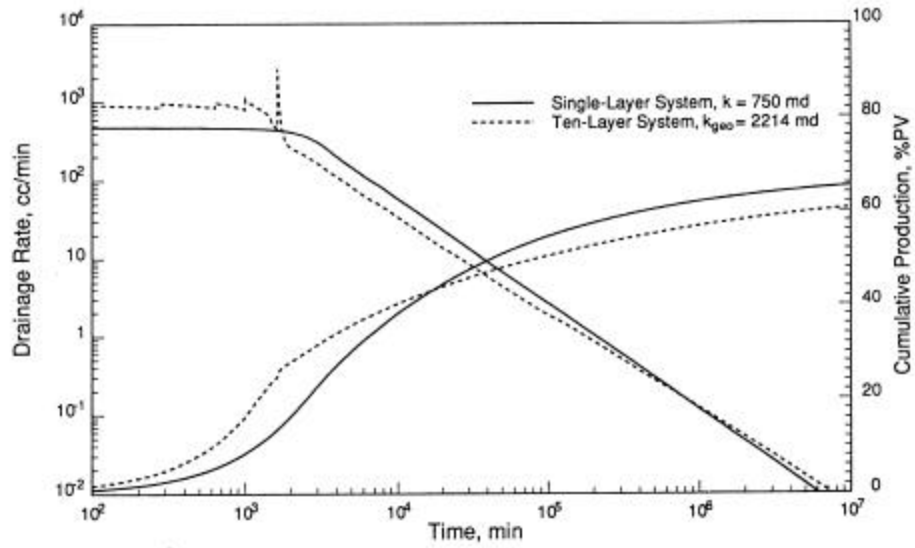


Fig. 1 – Gas-oil gravity drainage in a homogenous and in a layered column (adapted from Ref. 6).

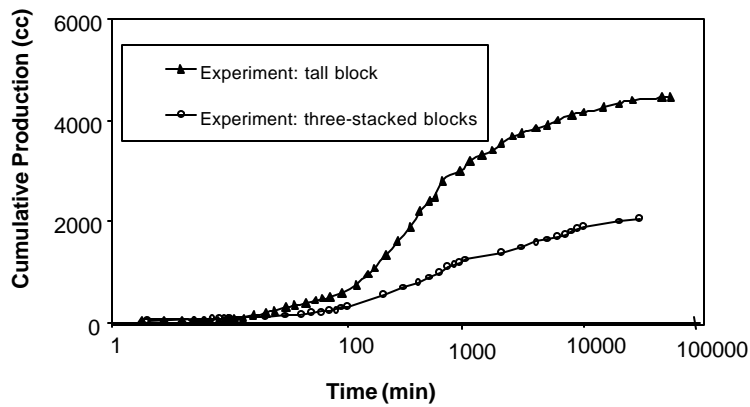


Fig. 2 - Gas-oil gravity from a tall block, and a stacked-block system (adapted from Ref. 7).

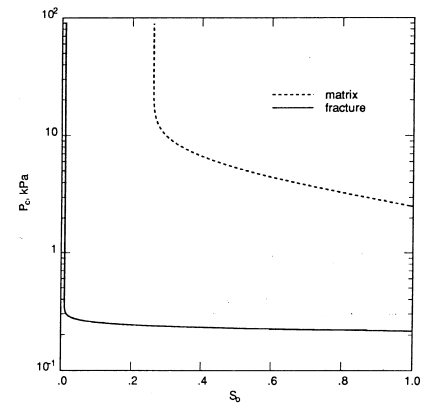


Fig. 3 – Matrix and fracture capillary pressures (Ref. 8).

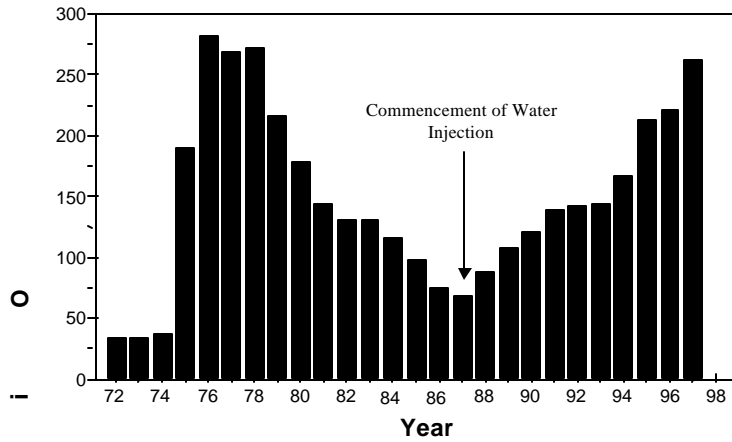


Fig. 4 - Ekofisk Field oil production rates and the response to water injection (adapted from Ref. 1).

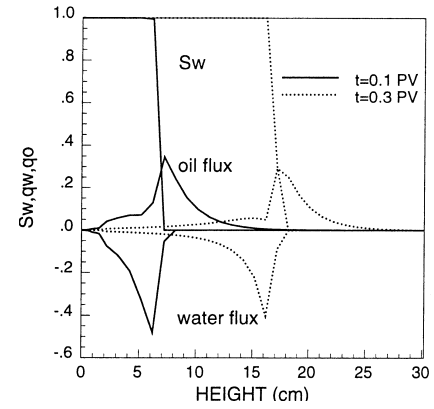


Fig. 5 - Fracture water saturation, and water and oil fluxes from fine-grid simulation (Ref. 14).

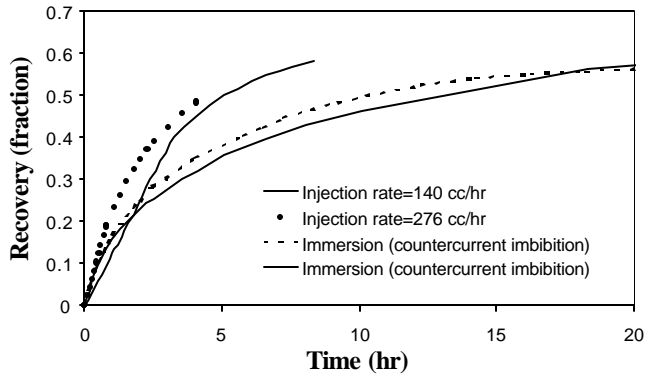


Fig. 6 - Recovery Performance of a Water-Wet Chalk Matrix Block ( $k=1.5\text{md}$ ,  $\phi \approx 30\%$ ) to water injection and to immersion (adapted from Ref. 12).

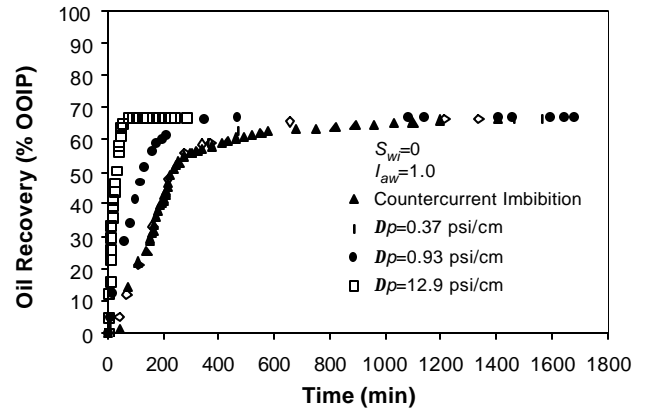
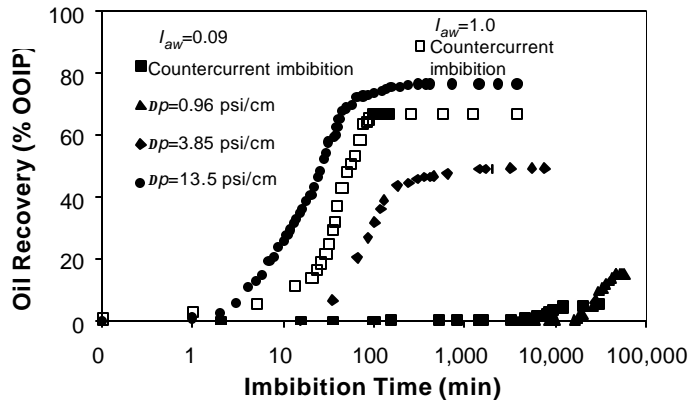
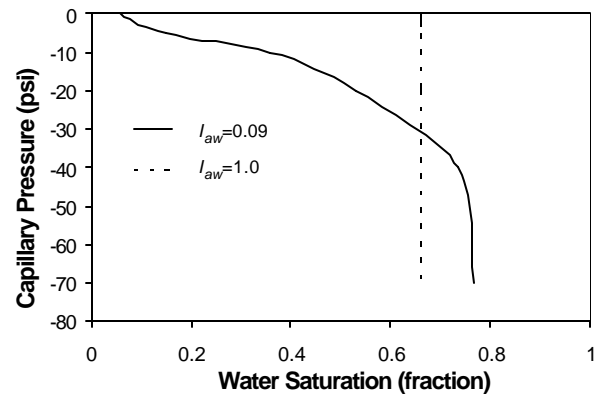


Fig. 7 - Effect of Pressure Gradient on Oil Recovery from the Chalk Sample ( $k=1.3\text{md}$ ,  $\phi \approx 30\%$ ): Water-Wet ( $I_{aw}=1.0$ ) (adapted from Ref. 15).



**Fig. 8 - Effect of Pressure Gradient on Oil Recovery from the Chalk Sample ( $k=1.3\text{md}$ ,  $\phi \approx 30\%$ ): Water-Wet ( $I_{aw}=1.0$ ) and Weakly Water-Wet ( $I_{aw}=0.09$ ) (adapted from Ref. 15).**



**Fig. 9 - Estimated Negative Capillary Pressure Curves for Water-Wet ( $I_{aw}=1.0$ ) and Weakly Water-Wet ( $k=1.3\text{md}$ ) Chalk Sample (adapted from Ref. 15).**

# **Chapter II – Gravitational Potential Variations of the Sun and Moon for the Estimation of Reservoir Properties**

## **Part I – Gravitational Potential Variations of the Sun and Moon for the Estimation of Reservoir Compressibility**

ERIC CHANG AND ABBAS FIROOZABADI

### **Abstract**

Total compressibility in a fractured reservoir is estimated using the pressure response due to gravitational potential variations. Both the lunar and the solar gravitational potentials are fully accounted for by inclusion of longer-period components. The semi-diurnal and diurnal pressure data show substantial long-term variations. The gravitational potential also contains the same variation trend; the ratio between the potential and pressure has a fairly uniform value over successive cycles. The computed total compressibility is also fairly constant and independent of the cycle.

### **Introduction**

Pressure test data taken with modern, high-resolution gauges often show small, but easily observable pressure variations, with a definite periodic behavior. These periodic fluctuations appear to occur on a semi-diurnal time scale (repeating every half-day). In addition, other variations with similar, but longer periods, such as diurnal (daily) may also be evident. The origin of the sinusoidal variation in reservoir pressure observed in well test data is the coincident periodic variation in the gravitational potential imposed on the earth by the moon and the sun. The potential variations are coupled to the reservoir pressure pulsations through the earth tide. The earth tide is similar to the more familiar and readily observable ocean tide. Both are similar manifestations of the same phenomena, in which the free surface of a body seeks a surface of constant potential of the imposed gravitational field in order to minimize potential energy. Observations of these pressure perturbations can provide estimates of reservoir fluid and petrophysical properties, because they couple the pressure response to the potential variation. Typically, there are two parameters that can be estimated in this way. These are the total compressibility-porosity product and the mobility of the fluid within the pores. The former is related to the amplitude of the pressure response, and the latter to the phase lag. If the pressure data are of good quality, and the tidally-induced variations are distinct, correspondence between the gravitational potential driving force and the associated response should be clear enough to make estimates with reasonable confidence.

This study uses a data set from a fractured oil-bearing formation with a clear semi-diurnal signal that is well above both the noise and trend threshold, providing an ideal opportunity to test the tidal analysis theory.

There are three tasks that are required in order to use the pressure variation data to estimate bulk reservoir properties. First, an expression for the gravitational potential due to the most important sources, the moon and the sun, must be obtained. Although this has been done previously in the literature, it is not in a form suitable for the current analysis, for reasons that will be examined in more detail later. Furthermore, it is desirable to show the derivation in a form that is sufficiently self-contained so that it may be used as a basis for independent investigation. Second, the dilatational response as a function of the magnitude of the gravitational potential is required. Unlike the ocean tide, the earth tide is restrained by the elastic properties of the solid earth. Thus, the pressure response to a varying gravitational field is influenced by the constitutive model (density, compressibility, and elasticity) selected for the interior of



the earth. Third, the dilatation, or compaction of the earth near the surface must be related to the observed pressure through the parameters that it is desirable to evaluate. Such relations can take the form of a simple volume balance proportionality, or a complicated time-dependent numerical solution of the flow around the wellbore that must be solved repeatedly and regressed against the observations.

## Previous Work

The estimation of reservoir parameters using the pressure due to gravitational potential variations has been undertaken in several contexts in previous investigations. Some of the earliest observations of pore volume changes induced by earth tides have been made on fluid height variations in an open wellbore. Since this type of measurement does not require sophisticated pressure monitoring equipment, it is straightforward and inexpensive to perform. Bredehoeft<sup>1</sup> has presented a comprehensive investigation of the fluid height oscillation in a water reservoir due to pore volume changes. The relation derived between the dilatation and the porosity is valid for the quasi-steady state estimation of the porosity from amplitude observations. He has also commented on observations from different locations. Moreland and Donaldson<sup>2</sup> extended the analysis to employ the phase lag to estimate flow parameters from observations of the fluid height as a function of time. They solved the flow equation with constant pressure boundary conditions at the wellbore. The flow into the wellbore caused by the differential compaction of the reservoir results in a phase lag that was studied for various values of the flow parameters.

In petroleum reservoirs, the measured data is usually in the form of the pressure, as the wellbore is closed. In this situation, the gravitationally-induced dilatation causes compaction or expansion which results in a uniform increase or decrease in pressure throughout the reservoir. Under quasi-steady state conditions, this pressure is the same as what is observed at the wellbore. Arditty et al.<sup>3</sup> studied the response of a closed system to periodic variations in the gravitational field generated by the moon, which is the body with the major influence. They only considered the principal semi-diurnal and diurnal components of the tidal signal. In addition, they extended Moreland and Donaldson's flow solution for the closed wellbore system in order to analyze critical frequency (equivalent to phase lag) as influenced by flow parameters. Many of their results were inconclusive, most probably due to poor data quality. In addition, the several smaller, but still important earth tide components that were ignored in their comparisons may still have had a substantial influence. This was a major impetus, along with observations from a fractured field, for including all the tidal components in the estimation procedure described in our investigation.

Other studies involving closed reservoir systems included the work of Hanson and Owen<sup>4</sup>, who studied principal fracture orientation via examination of the directional dependence of phase lag between the pressure response and the earth tide induced dilatation. A principal fracture orientation could be detected by examination of this quantity due to the fact that fluid flow parameters influence the phase lag. Hemala and Balnaves<sup>5</sup> studied the influence of ocean tide effects caused by the local changes in gravitational field brought about by the redistribution of ocean water mass on a periodic basis. They used the principal semi-diurnal lunar component of the gravitational potential in order to estimate compressibility and obtained reasonable agreement with triaxial tests.

The current study seeks to derive a full (multi-spectral) expression for the gravitational forcing potential for both the sun and the moon. This potential is then compared with the observed pressure fluctuations in an observation well from a fractured reservoir for the purpose of computing total compressibility of the formation. It was found that by employing the full expression, cycle-to-cycle trends could be explained by the inclusion of the longer period components, which would otherwise result in a misfit between observation and theory if only a single component forcing function were used.

## Data Analysis

**Fast Fourier Transform (FFT).** It is customary when studying a data stream whose key behavior is periodic to examine the data in the frequency domain. This has the advantage of highlighting the major frequency components. In fact, if the desired signal is deeply submerged in noise, filtering over a long period may still be able to extract the dominant spectral component. A 128K point FFT (Fast Fourier

transform) was performed on one pressure record from the observation well T. The frequency of sampling was  $120 \text{ hr}^{-1}$ , so the time interval was 1067 hr. A spectral plot of amplitude squared versus frequency is shown in Fig. 1. An excerpt of the pressure data, beginning 1750 hours after the start of the test, in the time domain is shown in Fig. 2. The periodic behavior of the signal is especially evident in the frequency domain plot, with two clear peaks at frequencies of  $0.04 \text{ hr}^{-1}$  and  $0.08 \text{ hr}^{-1}$  appearing, corresponding to periods of 24 and 12 hours (diurnal and semi-diurnal), respectively.

**Limitations of the FFT.** Also evident in Fig. 1 is the large tail of low frequency noise due to the slow decay of the spectral components excited by the windowing function implicit in the finite extent of the input data in the time domain. Since the window leakage occurs in the region of interest for tidal analysis (the diurnal terms, especially), it makes the task of estimating the total energy in that range of frequency difficult. Another problem with using the spectral plot to estimate energy in a frequency range is the presence of closely spaced components that are hard to resolve. In fact, resolving them amounts to individually estimating each one's amplitude, frequency and phase. Clearly, fitting this large quantity of parameters is undesirable for the comparatively more modest task of estimating the total spectral energy associated with the two peaks.

**Alternative Methods.** As was pointed out by Melchior<sup>6</sup>, there are better ways of regressing against this type of data, such as least-squares fitting in the time domain. Since the astronomical influences that generate the gravitational potential fluctuations are known with high accuracy, it should not be necessary to fit high-resolution amplitude and phase models through the use of Fourier analysis. The information would be redundant, and the procedure would be equivalent to the unnecessary amplification of noise. By imposing the already well-known forcing function on the linear elastic model of the earth, it should be possible to numerically fit the small number of desired unknowns by means of a regression against the computed and actual responses.

Note that this is quite different from simply extracting the dominant semi-diurnal spectral component and attempting to fit it to the observed pressure. As is clear from Fig. 2, there is more than one spectral component, so consequently the fit will be different depending on the time interval over which it is made. Thus, such a fit is only meaningful when many (or most) of the spectral components are retained in the gravitational potential forcing function. This procedure is similar to the one used for estimating the elasticity response parameters (explained in more detail in Appendix B) by comparison between theoretical and observed deformation of the earth's volume, as measured with tri-axial pendulums, resulting from the earth tides.

Comparison between the data processes and the gravitational potential will be deferred until later in the paper, when a full expression for the latter will be derived.

## Single-Component Based Estimates

**Limitations.** Despite the caveats mentioned in the preceding section, it is still instructive to attempt to estimate the total compressibility via a single component analysis following Arditty et al.<sup>3</sup> This rough calculation will also lay some groundwork for the more accurate analysis presented in the following section. The largest component in the Fourier representation of the combined lunar-solar induced potential is known as  $M_2$ . It arises from approximating the position of the lunar orbit as a mean band of distributed mass centered at the equator. Deviations from this base term are caused by longer term variations in the true orbit due to its obliquity as well as to the influence of the sun. The solar contribution is neglected in this preliminary simplified calculation.

**Contribution to Pressure Head.** There are actually two avenues by which temporal variations in the gravitational potential can cause corresponding pressure pulsations. The first is by compaction and expansion of the earth's volume, and the second is by varying the static pressure head.

The second contribution is so small that it is negligible compared to the first. This will be shown by performing a simple calculation. Note that this mechanism does not rely on coupling through the earth's

deformation in order for a pressure response to be generated. The variation in the field strength caused by the changes in distance between the attracting body and the earth gives rise to the pressure variations. The pressure head of a stationary fluid column is proportional to  $g$ , the gravitational acceleration, so changes in  $g$  result in proportional changes in the pressure,  $p$ . The total lunar influence comprises a peak-to-peak amplitude variation of approximately 0.17 milligal out of the approximately 980 gal ( $\text{cm/s}^2$ ) from the earth's field. Therefore, from  $Dp = rhDg$ , the pressure variations induced by this mechanism would be about  $10^{-7}$  times the pressure head, or 0.0001 psi per 1000 psi of original pressure head. Such small pressure perturbations are negligible in comparison to the dilatation-induced amplitude and, therefore, will be ignored for the remainder of this analysis.

**Estimates.** It is possible to make a rough estimate of the compressibility using only the single tidal component generated by the moon ( $M_2$ ). The dilatation induced by this component is tabulated by Arditty et al.<sup>3</sup>. The relation between the dilatation,  $q$ , and the gravitational potential changes which cause it are quite complex. It is the result of a linear elastic system in which the earth deforms quasi-statically under the influence of a non-uniform gravitational field. Details of this solution are given in Appendix B. This problem was formulated using an earth constitutive model with radially varying elasticity, density, and compressibility, and was first solved numerically by Takeuchi<sup>7</sup> in 1950. The dilatation induced by  $M_2$  is given as

$$Q = 4.5 \times 10^{-8} \quad (1)$$

In other words, the amplitude of the strain would be 0.0000045% in either direction (compaction or expansion).

The deformation of the reservoir volume is resisted by the rigidity of the pore network and the compressibility of the fluid within it. If the matrix grain compressibility is small compared to that of the pore space, most of the volume change upon deformation will occur in the latter. Therefore, one may write

$$Q = f c_f Dp \quad (2)$$

where  $f$  is the porosity,  $c_f$  is the total compressibility of the pore space, and  $Dp$  is the change in pressure. Since Arditty's value of  $Q$  was computed as a peak-to-peak value, an estimate of  $c_f$  would require the peak-to-peak amplitude of the pressure variations. In addition, a value for  $f$  is also required. As mentioned in the previous section, it is difficult to estimate the primary component's peak-to-peak variation, because the forcing function is not composed of solely one component. Examinations of a short run of data from the beginning of Fig. 2 shows sequential peak-to-peak values of 0.1479, 0.0576, 0.1026, 0.0064, 0.1275, 0.0635 psi. Clearly, there is no one value for the peak-to-peak variation. Integration of the spectral energy in the semi-diurnal bin, on the other hand, yields  $Dp$  of about 0.25 psi, but this value includes contributions from other closely spaced spectral components and is, therefore, not suitable for comparison with Eq. 1. Using the first estimates, then, in conjunction with a porosity of 0.02, results in values for  $c_f$  ranging from  $1.5$  to  $35 \times 10^{-5} \text{ psi}^{-1}$ . (Note that the pressure data in Fig. 2 should be detrended for proper compressibility calculations.) In the next section, the compressibility estimate will be refined by computing an expression of the potential (and, therefore, the dilatation) which uses the entire spectrum of lunar and solar components. This driving term will then be compared directly with the pressure signal in order to resolve some of the concerns raised above.

## Total Compressibility

**Conventional Methodology.** Traditionally, earth tide analysis has been carried out via a separation of the time varying potential into a series of pure sinusoidal components. Due to the complexity of the relative orbits of the sun, and especially the moon, such a separation results in an infinite number of

spectral terms. Then, only the first few terms with the largest amplitudes are selected for use. As shown in Appendix A, which gives a detailed derivation of the full gravitational potential, the terms in the expression involve products of sinusoidal functions of the astronomical longitudes and declinations (see Eq. A.8). Non-linear mixing between the components gives a long-term modulation that was evident in the peak values of the pressure data exhibited in Fig. 2.

The same methodology could be retained in the current exercise. Each of the tabulated harmonic components of the potential could be summed in declining order of importance, until an approximation of satisfactory accuracy could be obtained.

**Calculation of Full Expression for Potential.** For various reasons, it was decided that the full expression for the potential would be used. First, this method is actually somewhat simpler than the multiple component method, since the analytical expression for the potential does not have to be spectrally decomposed, only to be partially reconstructed later on. Furthermore, there are some questions about the validity of some of the expansions, and these inconsistencies can be bypassed by simply retaining the full expression.

In this era of high-speed digital computers, there is less of an advantage to a trade-off taking on algebraic complexity in exchange for simplifications in the data fitting later down the line. The fit between the derived potential and the pressure data should, with the full expression, also be independent of the time interval selected, because all components, even the ones with very long periods, are included. The expression for the potential is computed directly from Newton's law for the gravitational attraction between two masses, and requires the masses and separation distances (the latter being a function of time). These quantities are known with a great deal of accuracy, both from astronomical calculations and observations spanning more than a century. For reference, the expression for  $V_2$ , the first term in the spherical harmonic series of the potential due to a body in relative orbital motion with respect to the earth, is repeated here (see Appendix A).

$$V_2 = N_D \left( \frac{c}{R} \right)^3 \left[ 3 \left( \frac{1}{3} - \sin^2 \mathbf{d} \right) \left( \frac{1}{3} - \sin^2 \mathbf{f} \right) - \sin 2\mathbf{f} \sin 2\mathbf{d} \cos \mathbf{t}_l + \cos^2 \mathbf{f} \cos^2 \mathbf{d} \cos 2\mathbf{t}_l \right] \quad (3)$$

$N_D$  is Doodson's number, an astronomical parameter which depends on the mean separation distance between the moon (or the sun) and the earth, as well as their masses. It has units of  $\text{length}^2/\text{time}^2$ , the same as potential, the rest of the expression being dimensionless.  $c/R$  is the dimensionless deviation from the mean distance associated with the disturbing body's orbit,  $\mathbf{d}$  is the declination,  $\mathbf{f}$  the latitude, and  $\mathbf{t}_l$  the supplementary hour angle (or time, with 360 degrees being equivalent to a day).

It is clear how the complicated, multi-spectral dependence of the potential on time arises, since the second and third terms, besides containing sinusoidal functions of the basic time, also contain multiple harmonic terms dependent on the declination, which also varies periodically with time.  $\mathbf{t}_l$  contains an implicit dependence on the longitude. The declination may be computed from the true longitude and ecliptic obliquity associated with the moon or the sun. One value of  $V_2$  is calculated for the moon and one for the sun, and they are added together. Note that although the longitude and latitude of the observation point will be the same,  $\mathbf{d}$  and  $\mathbf{t}_l$  will be different between the lunar and solar terms. Addition of the two terms to obtain the full potential is permissible within the scope of this investigation, since the effect of the potential on the dilatation is coupled through a system of linear equations. Therefore, the principle of superposition applies.

**Comparison with Pressure Data.** The combined lunar-solar potential is computed and plotted along with the pressure data from the observation well T of a fractured reservoir. This fractured reservoir has a negligible matrix porosity, a fracture porosity of around 2%, and a highly undersaturated oil. Based on an extended production period of about a year, the total compressibility is calculated to be around  $2.5 \times 10^{-5}$

psia<sup>-1</sup>. Note that the total compressibility is very high compared to oil or water compressibility; the high compressibility can contribute to substantial recovery under certain conditions. The compressibility calculated from pressure drop of the reservoir is influenced by the estimated amount of fluid in place and is, therefore, subject to uncertainty. Fig. 3 shows the pressure in the observation well for two different tests. Note that during the interval of pressure data from the observation well, oil was produced from the field. The plot shown in Fig. 3a starts 1600 hours after the beginning of the test (1215, 10/17/1996), and that in Fig. 3b also starts after the beginning of the associated test (1231, 4/22/97). The pressure data in Figs. 3a and 3b reveal a cyclic variation; there are periods during which pressure variations are small. Such periods are not suitable for data collection to be used in the estimation of compressibility; the error maybe be too large. As we will see soon, the period of low pressure variation can be predicted from the potential calculations. Fig. 4 is a shorter time data for observation well T. Several features are immediately obvious from these graphs. The first is that the pressure is clearly being driven by the tidal potential. Each time there is a large peak in the potential there follows a large peak in the pressure curve, and vice versa with the small peaks. Closer examination of Fig. 4 shows a longer term trend in that the largest peak-to-peak difference is slowly decreasing first, then increasing and then decreasing. This pattern is also matched in the pressure signal. These features illustrate the benefit of using the full expression of the potential rather than an expression limited to a few spectral components, which would obviously show a different fit depending on the time window that the potential and pressure were compared in. A second notable feature is the phase lag evident in the pressure signal. Fig. 4 has had the  $x$ -axis (time) shifted by 12 hours to make the comparison between the pressure and potential peaks more clear. Such a lag is a result of a slight deviation from the quasi-static approximation implicit in the compressibility estimate. The wellbore, having a different (and lower) effective compressibility, must be charged from the surrounding reservoir volume. The mobility of the fluid is sufficiently low that a lag is generated between the pressure and the driving force associated with the potential. The phase lag points to the opportunity of computing fluid mobility ( $k/m$ ) which will be discussed in further detail in the following sections.

**Estimate of Compressibility.** The plots in Fig. 4 can be used to estimate total compressibility in much the same way that the peak-to-peak measurements in an earlier section were used. In this case, although the peak-to-peak distance in the pressure profile is seen to vary, the potential also contains the same trend in variation. Thus, the key quantity, which is the ratio between the potential and the pressure, maintains a fairly uniform value over successive cycles. For example, the maximal peak-to-peak difference (for the peaks in the middle of the graph in Fig. 4e) in the potential curve is approximately 71000 cm<sup>2</sup>/sec<sup>2</sup>, and the corresponding peak-to-peak difference in pressure is 0.167 psi. Using Eq. B.5 in conjunction with Eq. 2,

$$c_f = \frac{0.49}{f r g} \left( \frac{\Delta V_2}{\Delta p} \right) \quad (4)$$

where  $\Delta V_2$  is the peak-to-peak difference in the gravitational potential  $V_2$ ,  $\Delta p$  is the corresponding peak-to-peak difference in pressure,  $r$  is the radius of the earth ( $r = 6373.388$  km), and  $g$  is the acceleration of gravity. Substituting the values of the peak-to-peak variations  $\Delta V_2$  and  $\Delta p$  yields,  $c_f = 1.7 \times 10^{-5}$  psi<sup>-1</sup> which is in fair agreement with the total compressibility estimated from the extended production testing.

It may be demonstrated that this value of the compressibility computed in such a fashion is, to a large part, independent of the time or location of the measurement. Table 1 provides a list of estimates for the compressibility obtained from different times. Times and dates are given in local time, month/day/year format. For the purposes of making these estimates, the data were detrended with a simple linear calculation that equalized the starting and ending pressure of the track. Such a transformation removes

the linearly time-dependent portion of the trend. All the values of the compressibility fall in a fairly narrow range from approximately  $1.4 \times 10^{-5} \text{ psi}^{-1}$  to  $1.74 \times 10^{-5} \text{ psi}^{-1}$ . In fact, one estimate of the possible error is based on the decrease in pressure due to the long-term trend in the reservoir of about 0.1 psi/day.

**Table 1 – Estimated Compressibility**

Start Date	Time period (hours after start)	$c_f$ ( $10^{-5} \text{ psi}^{-1}$ )
1215 10/17/96	24-264	1.54
1215 10/17/96	3120-3360 (early)	1.43
1215 10/17/96	3120-3360 (late)	1.63
1231 4/22/97	24-264 (early)	1.68
1231 4/22/97	24-264 (late)	1.52
1231 4/22/97	1272-1512 (early)	1.74
1231 4/22/97	1272-1512 (late)	1.71

The computations may be extended to use a larger interval of the pressure data by regressing the constant of proportionality between the potential and the pressure. Unfortunately, such a fitting process is complicated by two factors. The first is the aforementioned phase lag between the pressure and the potential. A parametric fit for this quantity must also be included in the non-linear regression as an offset in the time variable. Since the dependence of the astronomical longitudes and declinations on time is fairly complicated, it is difficult to obtain the Hessian matrix of derivatives with respect to regression parameters that is required for a typical Levenberg-Marquardt non-linear regression. The second factor is the presence of an obvious trend in the pressure data. Superimposed on the tide-induced pressure variations is a long-term pressure decline that is part of the observation well pressure measurement. Using more than a few cycles of pressure data requires that this trend is more effectively removed. These concerns will be addressed in future work in which the estimation of flow parameters will also be included.

### Remarks

The current investigation shows that most of the higher frequency features in the pressure data can be explained by the earth tide. There is, however, a substantial phase lag. In addition, it is clear that longer-term trends in the pressure data, due to depletion of the reservoir, must be filtered out without overly affecting the desired signal. Note that the potential induced by the earth tide varies with a longer term trend than the diurnal or semi-diurnal variations associated with the earth's rotation. These variations should not be filtered out. They are caused by the slow changes in the declination of the moon due to both its orbit and the indirect influence of the sun on the orbit obliquity. Therefore, there are optimum periods, as well as more favorable locations, for carrying out pressure measurement. These points will be discussed in more detail below.

The pressure data show a phase lag (about 12 hours) with respect to the potential, as was discussed earlier. This lag arises from the fact that the characteristic time associated with fluid flow around the wellbore is comparable to the semi-diurnal time scale over which the most rapid oscillations in the potential take place. The phase lag has a secondary effect on the compressibility estimate. Close examination of comparisons between pressure and potential shows that the ratios between adjacent large and small peaks do not correspond. The reason for this “blurring” effect is that the phase lag makes the pressure response not only a function of the current, but also of the immediately preceding values of the potential.

Rather than being a hindrance to the compressibility computation, the phase lag is an avenue for estimating the fluid mobility ( $k/m$ ). This problem has been addressed by Moreland and Donaldson<sup>2</sup> for the

case in which the wellbore is at constant pressure. This boundary condition is sufficiently simple that it was possible to obtain an analytic (although not closed form) solution to the flow equations. The closed boundary, constant-volume problem is significantly more difficult, and although the governing equations are still linear, it may be difficult to obtain analytic solutions to them. A numerically-based regression procedure, however, does not require an analytic solution, although the computation of the required minimization derivatives becomes much more complicated.

In order to make an appropriate comparison between the potential and the pressure, it is necessary to remove as much of the trend in the latter that is not a result of the earth tide. The standard method for frequency-dependent filtering is to perform it in the frequency domain. A spectral model is constructed for the noise, and a filter is constructed to preferentially attenuate the components that occur in greater proportions in the noise. Of course, if there are noise components that have the same frequency as desirable ones in the data, a filter of this type will attenuate both of them without regard for their source. Future investigations will study the construction of this so-called optimal filter.

One way of approaching the signal-significance problem is suggested by the plots of potential over longer time periods. The higher frequency potential wave is modulated by a longer-term wave with a characteristic period of several days. This modulation is caused by the declination of the moon in its comparatively slow orbit causing its zenith point to drift closer to the observation site. Clearly, the strongest signal is obtained when the relative lunar trajectory passes most closely to directly overhead of this point. Such a time interval may be computed from astronomical tables or the formulas presented in Appendix A. Also, it is noted that this “optimal interval” will also depend on the latitude where the measurements are taken. Therefore, it is prudent to review the time interval over which the pressure measurements are carried out, with consideration of the test’s location.

## Conclusions

The analysis of the well pressure data shows that it is possible to make compressibility estimates if the measurements are of sufficiently high quality. In this case, the resolution was high enough so that the tidally-driven sinusoidal variations were clearly visible. Also, as shown by the temporal plots, the noise, or scatter in the data was well below the signal strength. These criteria can be attained with modern high-quality crystal strain devices. In addition, the location of the reservoir is sufficiently close to the equator ( $f \approx 40^\circ$ ) that the potential varies with a significant span. Finally, low fracture porosity, in conjunction with a high total compressibility, insured a strong pressure signal. It was shown that although a decent estimate of the compressibility could not be obtained by comparing the cyclical variation of the pressure with the dominant harmonic component of the earth tide, a good estimate could be made by admitting the full expression for the lunar-solar gravitational potential, since the former could be off by a large factor, depending on the time interval it was computed. The clear presence of a phase lag in the pressure data shows promise for use towards estimating flow parameters in the reservoir, such as fluid mobility ( $k/m$ ). This analysis will be carried out in the future.

## Acknowledgements

This work was supported by the US DOE grant DE-FG26-99BC15177 and the members of the Reservoir Engineering Research Institute (RERI). We thank Fina Italy for providing well pressure data.

## Nomenclature

- $c$  = mean distance from the center of the earth to the center of the disturbing body (without subscript the disturbing body is the moon, with subscript the disturbing body in the sun), cm
- $c_f$  = total compressibility of the pore space,  $\text{psi}^{-1}$
- $f$  = porosity, fraction
- $g$  = acceleration of gravity,  $\text{cm/sec}^2$
- $G$  = gravitational constant in Newton’s law of universal gravitation,  $\text{cm}^3/(\text{g}\cdot\text{cm}^2)$
- $h$  = mean solar longitude, degrees

$h_1$  = true solar longitude, degrees  
 $k$  = permeability, md  
 $l$  = distance from observation point on the surface of the earth to the center of the disturbing body, cm  
 $L$  = Longitude east from the reference meridian, degrees  
 $m$  = mass of the disturbing body (the moon or the sun), g  
 $N$  = side angle, see Fig. A.4, degrees  
 $N'$  = side angle, see Fig. A.4, degrees  
 $N_D$  = Doodson's number,  $\text{cm}^2/\text{sec}^2$   
 $p$  = pressure, psi; also mean perigee coordinate, degrees  
 $p_s$  = perihelion coordinate, degrees  
 $r$  = distance from the center of the earth to any point within the earth, cm; also earth radius, cm  
 $R$  = distance from the center of the earth to the center of the disturbing body, cm  
 $s$  = mean lunar longitude, degrees  
 $s_1$  = true lunar longitude, degrees  
 $u$  = displacement, cm  
 $V$  = gravitational potential,  $(\text{g}\cdot\text{cm}^2)/\text{sec}^2$

### Greek Letters

$\alpha$  = right ascension, degrees  
 $\delta$  = declination from ecliptic, degrees  
 $g$  = spring equinox, degrees  
 $d$  = declination (latitude of the zenith point), degrees  
 $e$  = obliquity of the ecliptic, degrees; also normal strain,  $\text{g}/(\text{cm}\cdot\text{sec}^2)$   
 $q$  = latitude in spherical coordinates, degrees  
 $q_o$  = Greenwich side real time, degrees  
 $Q$  = dilatation, dimensionless  
 $I_1$  = Lamé's modulus,  $\text{g}/(\text{cm}\cdot\text{sec}^2)$   
 $I_2$  = shear modulus,  $\text{g}/(\text{cm}\cdot\text{sec}^2)$   
 $\mu$  = viscosity,  $\text{g}/(\text{cm}\cdot\text{sec}^2)$   
 $\rho$  = density,  $\text{g}/\text{cm}^3$   
 $\sigma$  = normal stress,  $\text{g}/(\text{cm}\cdot\text{sec}^2)$   
 $\tau$  = hour angle, degrees  
 $t_1$  = supplementary hour angle, degrees  
 $\phi$  = latitude, degrees

### Subscripts

$r$  component along  $r$  axis  
 $q$  component along  $q$  axis  
 $f$  component along  $f$  axis

### References

- 1- Bredehoeft, J.D.: "Response of Well-Aquifer Systems to Earth Tides," Journal of Geophysical Research (June 15, 1967) 3075-3087.
- 2- Moreland, L.W. and Donaldson, E.C.: "Correlation of porosity and permeability of reservoirs with well oscillations induced by earth tides," Geophys. J. R. Astro Soc. (1984) 705-725.
- 3- Arditty, P.C., Ramey, H. Jr., and Nur, A.M.: "Response to a Closed Well-Reservoir System to Stress Induced by Earth Tides," SPE 7484, paper presented at the SPE 53rd Annual Fall Technical Conference and Exhibition, Houston, TX, Oct. 1-3, 1978.



- 4- Hanson, J.M., Owen, L.B.: “Fracture Orientation analysis by the Solid Earth Tidal Strain Method,” SPE 11070, paper presented at the 57th Annual Fall Technical Conference and Exhibition of the SPE, New Orleans, Sept. 26-29, 1982.
- 5- Hemala, M.L., and Balnaves, C.: “Tidal Effect in Petroleum Well Testing,” SPE 14607, paper presented at the 1986 SPE Offshore South East Asia Conference, Singapore, Jan. 28-31, 1986.
- 6- Melchior, P.: “*The Tides of the Planet Earth*,” 2nd Ed., Pergamon Press, Oxford (1983).
- 7- Takeuchi, H.: “On the earth tide of the compressible earth of variable density and elasticity,” Trans. Am. Geophys. Union (1950) Vol. 31, 651-689.
- 8- Bartles, J.: “Gezeitenkräfte,” Encyclopedia of Physics, S. Hügge ed., Springer-Verlag, Berlin (1957) 734-774.
- 9- Thurston, W.P.: “*Three-Dimensional Geometry and Topology, Vol. 1*,” Princeton University Press, Princeton, NJ, 1997.
- 10- Bullen, K.E.: “The density variation of the Earth’s central core,” Bull. Seis. Soc. Amer. (1942) Vol. 32, 19-30.
- 11- Espenak, F.: “NASA Reference Publication 1349 – Lunar Ephemeris,” <http://www-lep.gsfc.nasa.gov/code693/TYPE/moonkey.html>.

#### APPENDIX A - Derivation of the Expression for Gravitational Potential in Geocentric Coordinates

Astronomical motions are conveniently described using the celestial sphere. Specialized terminology such as ecliptic, ascension, equinox, etc. are used in such a description. One may refer to standard texts on astronomy and astrophysics for the terminology’s used in this Appendix.

From Newton’s law of universal gravitation, the gravitational potential  $V$  (defined from,  $g = \partial V / \partial l$ ) at a distance  $l$  from the center of mass of the disturbing body is given by

$$V = G \frac{m}{l} \quad (\text{A.1})$$

where  $G$  is the gravitational constant and  $m$  is the mass of the disturbing body. Now, consider a point P (see Fig. A.1) on the earth (of distance  $r$  from the earth’s center). The potential at point P due to the disturbing body whose center of mass is at M is given by

$$V = Gm \left( \frac{1}{l} - \frac{1}{R} - \frac{r \cos \vartheta}{R^2} \right) \quad (\text{A.2})$$

The disturbing body can be the moon (see Fig. A.1) or the sun. When both the sun and moon are considered, the total potential is given by  $V = V_m + V_s$ , where  $V_m$  is the lunar tide potential and  $V_s$  is the solar tide potential. Simple addition of these potentials suffices, since the equation determining the dilatational response is linear, and the principle of superposition applies.

In triangle OPM of Fig. A.1,  $l^2 = R^2 + r^2 - 2rR \cos \mathbf{q}$ .

Combining the expansion of this expression and noting that  $r/R \approx 1/60$  for the moon, and  $r/R \approx 1/23600$  for the sun, with Eq. A.2,

$$V = \frac{3}{4} \frac{Gm}{R} \left( \frac{r^2}{R^2} \right) \left[ \left( \cos 2\mathbf{q} + \frac{1}{3} \right) + \frac{1}{6} \left( \frac{r}{R} \right) (5 + \cos 3\mathbf{q} + 3\cos \mathbf{q}) + \dots \right] \quad (\text{A.3})$$

Using the definition of Doodson’s number,

$$N_D \equiv \frac{3}{4} Gm \frac{r^2}{c^3}, \quad (\text{A.4})$$

where  $c$  is the mean distance from the center of the earth to the center of the disturbing body,

$$V = N_D \left( \frac{c}{R} \right)^3 \left[ \left( \cos 2\mathbf{q} + \frac{1}{3} \right) + \frac{1}{6} \left( \frac{r}{R} \right) (5 + \cos 3\mathbf{q} + 3\cos \mathbf{q}) + \dots \right] \quad (\text{A.5})$$

From this point on, the presentation will specifically deal with the moon as the disturbing body. The corresponding procedure for the sun is much simpler, due to the fact that its orbit follows the ecliptic.

The contribution of the first term to  $V$  in Eq. A.5 is denoted by  $V_2$ ,

$$V_2 = N_D \left( \frac{c}{R} \right)^3 \left( \cos 2\mathbf{q} + \frac{1}{3} \right) \quad (\text{A.6})$$

The second term is denoted by  $V_3$ . Since  $V_3$  is smaller than  $V_2$  by a factor of approximately the radius of the earth to the separation distance, it is about 1/45 the size of  $V_2$  for the moon, and even smaller for the sun.

Eq. A.6 is still somewhat inconvenient to use because  $\mathbf{q}$  depends both on the observation point P and the position of the moon. It is desirable to separate this dependency by transformation into geocentric spherical coordinates. Such a transformation may be accomplished using the fundamental formula of the position triangle of spherical geometry<sup>9</sup>,

$$\cos \mathbf{q} = \sin \mathbf{f} \sin \mathbf{d} + \cos \mathbf{f} \cos \mathbf{d} \cos(\mathbf{t}_1 - 180^\circ). \quad (\text{A.7})$$

The coordinates are shown in Fig. A.2. In this new coordinate system, Eq. A.6 becomes

$$V_2 = D \left( \frac{c}{R} \right)^3 \left[ 3 \left( \frac{1}{3} - \sin^2 \mathbf{d} \right) \left( \frac{1}{3} - \sin^2 \mathbf{f} \right) - \sin 2\mathbf{f} \sin 2\mathbf{d} \cos \mathbf{t}_1 + \cos^2 \mathbf{f} \cos^2 \mathbf{d} \cos 2\mathbf{t}_1 \right] \quad (\text{A.8})$$

The first term gives the long-period excitation, and the second and third terms give the diurnal and semi-diurnal excitations, respectively. The declination (latitude of the zenith point) is denoted by  $\mathbf{d}$ ,  $\mathbf{f}$  is the latitude, and  $\mathbf{t}_1 - 180^\circ$  is the hour angle, in the celestial sphere of the moon. Evaluation of this expression requires the location of the observation point (latitude and longitude), as well as the time (date). The remainder of Appendix A shows how  $(c/R)^3$ ,  $\mathbf{d}$  and  $\mathbf{t}_1$  are calculated.

The earth-moon distance varies with a period approximately equal to that of the lunar orbit and is given by Brown's model<sup>8</sup>:

$$\begin{aligned} \frac{c}{R} = & 1 + 0.05450 \cos(s - p) + 0.00297 \cos 2(s - p) + 0.01002 \cos[(s - p) - (2h - p)] \\ & + 0.00825 \cos 2(s - h) + \dots \end{aligned} \quad (\text{A.9})$$

The quantities  $s$ ,  $p$ , and  $h$  are angles associated with various astronomical motions and are given at the end of this appendix in terms of time.

The declination,  $\mathbf{d}$ , has a fairly complex dependency on the above quantities, since the lunar orbit does not quite follow the ecliptic. In order to explain the computation of the lunar declination, it is helpful to study the simpler situation in which the orbit follows the ecliptic. This computation is directly applicable for analyzing the solar orbit, and with the addition of another spherical triangle, will be used for the lunar orbit. The simplified diagram is shown in Fig. A.3. The spherical triangle is made up of the equator, the meridian through the zenith point, and the lunar orbit. Application of Eq. A.7 yields,

$$\cos \mathbf{a} \cos \mathbf{d} = \cos s_1, \quad (\text{A.10})$$

Note that in this equation, with  $s_1$  replaced by  $h_1$ , the true solar longitude is directly applicable to the computation of the gravitational potential due to the sun. For the effect of the moon, however, the deviation of the lunar orbit from the ecliptic must be accounted for, and consequently the simple spherical triangle shown in Fig. A.3 must be modified accordingly. The true lunar longitude is not measured directly from the spring equinox. Instead,  $s_l$  is measured first to the intersection of the upper transit of the moon with the ecliptic, then along the lunar orbit. This is shown in Fig. A.4. In this figure,  $N'$  is defined as the angle from the lunar upper transit intersection to the ecliptic intersection with the intersection of the zenith point meridian and the ecliptic.

There are two triangles formed by the lunar and solar trajectories:

$$\cos \mathbf{d}' \cos \mathbf{a} = \cos (N + N') \quad (\text{A.11})$$

for the lower one, and

$$\cos (\mathbf{d} - \mathbf{d}') \cos \alpha = \cos (s_1 - N) \quad (\text{A.12})$$

There is one additional equation from the ecliptic triangle:

$$\sin \mathbf{d}' = \sin \mathbf{e} \sin (N + N') \quad (\text{A.13})$$

The above three equations give the three unknowns  $\mathbf{a}$ ,  $N'$ , and  $\mathbf{d}'$ .

To solve these equations, first the computation must be performed along the lunar orbit, followed by the simple analog (as alluded to previously) along the ecliptic. Specifically, the numerical computation of  $N'$ , from Eq. A.11, must be made differently in each of the four quadrants of  $s_1 - N$ .

$$\begin{aligned} \cos N' &= \cos(s_1 - N) / \cos \mathbf{b} & 0 \leq s_1 - N < 90^\circ \\ \cos N' &= \cos(180^\circ - (s_1 - N)) / \cos \mathbf{b} & 90^\circ \leq s_1 - N < 180^\circ \\ \cos N' &= \cos(s_1 - N - 180^\circ) / \cos \mathbf{b} & 180^\circ \leq s_1 - N < 270^\circ \\ \cos N' &= \cos(360^\circ - (s_1 - N)) / \cos \mathbf{b} & 270^\circ \leq s_1 - N < 360^\circ \end{aligned} \quad (\text{A.14})$$

Once  $N'$  has been obtained,  $\mathbf{a}$  may be calculated based on the standard ecliptic relations, Eqs. A.10 and A.11. Since  $\mathbf{e}$  is known,  $\mathbf{d}'$  may be eliminated. It is known that  $\mathbf{d}' < 90^\circ$ , so Eq. A.11 may be inverted immediately without regard for quadrant. Then, Eq. A.10 is solved in exactly the same way as above, with the different forms for each quadrant. By means of conditional statements, this procedure may readily be coded as a computer program.

Note that the upper triangle in Fig. A.4 does not lie alongside the zenith point meridian precisely. Therefore,  $\mathbf{d}$  is not quite equal to  $\mathbf{d}' + \mathbf{b}$ . Nonetheless, the resulting computation will give a value of  $\mathbf{a}$  accurate to within a few degrees as compared to NASA lunar observations<sup>11</sup>. The maximum error occurs at angles furthest from the compass points (0, 90°, 180°, and 270°), and it is not cumulative. It is possible to do an exact trigonometric computation, but the equations are non-linear and therefore require a

numerical iterative solution. The approximate computation above was considered to be accurate enough for the current purposes.

The hour angle  $t$  (or supplementary hour angle,  $\tau_1$ ) may be computed from the following expression

$$t = t_1 - 180^\circ = q_0 + L - a, \quad (\text{A.15})$$

where  $q_0$  is the Greenwich sidereal time,  $L$  is the longitude east from the reference meridian, and  $a$  is the right ascension as computed from the spherical triangles. The sidereal time is simply the stellar longitude, which differs from the solar time by one day in a year due to the earth's orbit around the sun. This quantity is obtained from a program, which starts at a fixed reference and uses the relation, sidereal day = 0.997270 solar days.

The analogous computation for the sun is identical, with the exception of the spherical triangle computation of  $d$  and  $a$ . In this case, the single triangle expression given by equation A.13 may be applied to the spherical triangle generated by the equator, the ecliptic, and their connecting meridian. The resulting expression is

$$\sin d = \sin e \sin h_1 \quad (\text{A.16})$$

which provides  $d$  directly from the quantities, due to the fact that the sun's orbit follows the ecliptic. With  $d$ ,  $a$  may be obtained from Eq. A.10, with  $s_1$  replaced by  $h_1$  (the true solar longitude suffices, since the sun's orbit follows the ecliptic). Doodson's number is modified by the ratio between the potential associated with the sun and the moon, respectively, due to their differing masses and distances from the earth. This ratio is 0.46051, with the influence of the sun being weaker by this factor than the moon.

The astronomical parameters required in the above calculations are<sup>8</sup>:

$$\begin{aligned} e &= 23^\circ 27' && \text{obliquity of the ecliptic} \\ h &= 279.69668 + 36000.76892T + 0.00030T^2 && \text{mean solar longitude} \\ s &= 270.43659 + 481267.89057T + 0.00198T^2 \\ &\quad + 0.000002T^3 && \text{mean lunar longitude} \\ p_s &= 281.22083 + 1.71902T \\ &\quad + 0.0045T^2 && \text{perihelion coordinate} \\ p &= 334.32956 + 4069.03403T - 0.01032T^2 \\ &\quad - 0.00001T^3 && \text{mean perigee coordinate} \\ N &= 259.18328 - 1934.14201T + 0.00208T^2 \\ &\quad + 0.000002T^3 && \text{ascending lunar node} \end{aligned}$$

Here,  $T$  is the number of Julian centuries (36525 mean solar days) since noon, 1899 December, Greenwich mean time. The following parameters are corrections to the solar quantities as influenced by the eccentricity of the earth's orbit.

$$\begin{aligned} h_1 &= h + 115' \sin(h - p_s) + 1.2' \sin 2(h - p_s) + \dots && \text{true solar longitude} \\ \frac{c_s}{R_s} &= 1 + 0.01675 \cos(h - p_s) + 0.00028 \cos 2(h - p_s) + \dots && \text{dimensionless earth-sun distance} \end{aligned}$$

As mentioned previously, the true lunar parameters are more complicated due to the fact that the lunar orbit does not quite follow the ecliptic. The formulas below use Brown's model for lunar motion<sup>8</sup>.

$$\begin{aligned} s_1 = & s + 377' \sin(s - p) + 13' \sin 2(s - p) \\ & + 76' \sin[(s - p) - 2(h - p)] + 40' \sin 2(s - h) \\ & - 11' \sin(h - p_s) + \dots \quad \text{true lunar longitude} \end{aligned}$$

$$\begin{aligned} \mathbf{b} = & 308' \sin(s - N) + 17' \sin(2s - p - N) - 17' \sin(p - N) \\ & + 10' \sin[(2(s - h) - (s - N))] + \dots \quad \text{declination from ecliptic} \end{aligned}$$

## APPENDIX B-The Dilatational Response of the Earth to a Non-uniform Gravitational Field

In the presence of a gravitational potential given by  $V_2$  in Eq. A.6, the earth becomes distorted into a prolate spheroid whose long axis points toward the moon (or the sun). An exaggerated diagram showing this effect is given in Fig. B.1. In order to relate the gravitational potential to a pressure change observed in the reservoir, it is necessary to obtain the resulting strain of the earth's volume<sup>8</sup>. The key component of the strain is the isotropic volume change (volumetric strain), or dilatation, denoted by  $Q$ . The dilatation is simply the trace of the strain matrix:

$$Q = \mathbf{e}_{rr} + \mathbf{e}_{\mathbf{q}\mathbf{q}} + \mathbf{e}_{\mathbf{f}\mathbf{f}} \quad (\text{B.1})$$

where  $\mathbf{e}$  is the normal strain along the appropriate spherical axes. The normal stresses are related to normal strains. In an isotropic medium, the radial stress  $\mathbf{s}_{rr}$  is given by  $\mathbf{s}_{rr} = \mathbf{I}_1 \mathbf{q} + 2\mathbf{I}_2 \mathbf{e}_{rr}$ . The parameters  $\mathbf{I}_1$  and  $\mathbf{I}_2$  are the Lamé modulus and the shear modulus, respectively. They are a measure of elasticity and rigidity. Similar relations for  $\mathbf{e}_{\mathbf{q}\mathbf{q}}$  and  $\mathbf{e}_{\mathbf{f}\mathbf{f}}$  hold. The radial stress at the surface of the earth is zero,

$$\mathbf{s}_{rr} = \mathbf{I}_1 \mathbf{q} + 2\mathbf{I}_2 \mathbf{e}_{rr} = 0 \quad (\text{B.2})$$

Therefore, at (or near) the surface of the earth,

$$Q = \left( \frac{2\mathbf{I}_2}{\mathbf{I}_1 + 2\mathbf{I}_2} \right) (\mathbf{e}_{\mathbf{q}\mathbf{q}} + \mathbf{e}_{\mathbf{f}\mathbf{f}}) \quad (\text{B.3})$$

The strains are related to the displacement  $u$ . In spherical coordinates

$$\mathbf{e}_{\mathbf{q}\mathbf{q}} = \frac{1}{r} \left( \frac{\partial u_{\mathbf{q}}}{\partial \mathbf{q}} + u_r \right), \mathbf{e}_{\mathbf{f}\mathbf{f}} = \frac{1}{r} \left( \frac{1}{\sin \mathbf{q}} \frac{\partial u_{\mathbf{f}}}{\partial \mathbf{f}} + u_{\mathbf{q}} \frac{\cos \mathbf{q}}{\sin \mathbf{q}} + u_r \right) \quad (\text{B.4})$$

One can write the equations of motion relating displacement to gravity potential  $V_2$ , and normal stresses. Three parameters,  $\mathbf{I}_1$ ,  $\mathbf{I}_2$ , and  $\mathbf{r}$  (earth's density) appear in the equations of motion. The first solution computed using a realistic earth model was carried out numerically by Takeuchi<sup>7</sup>. The earth model hypothesized a compressible but non-rigid core (from the observation that seismic S, or shear waves do not propagate through the earth's core) with density given by Bullen<sup>10</sup> of  $12.284 (1 - 0.64014 \mathbf{x}^2)$ , in

units of  $\text{g/cm}^3$ , with  $\mathbf{x}$ =dimensionless distance from the center of the earth, varying from 0 to 1. Between the core boundary and the surface of the earth, the constitutive properties of the earth were considered to vary as a function of radius, with several distinct regions with linear variations of the properties within each. The following table gives the density,  $\mathbf{r}$ , the Lamé constant,  $\mathbf{I}_1$ , and the shear modulus,  $\mathbf{I}_2$ , as a function of  $\mathbf{x}$ . The constants  $\mathbf{I}_1$  and  $\mathbf{I}_2$  are estimated from velocities of  $P$  and  $S$  seismic waves.

The tabular data shows a discontinuity at 500 km. Note that  $\mathbf{I}_1$  and  $\mathbf{I}_2$  are given in cgs units times  $10^{12}$ .

The solution with these parameters results in

$$\mathbf{Q} = 0.49 \frac{V_2}{ag}, \quad (\text{B.5})$$

The factor 0.49 is a constant of integration which results from this particular choice of earth model, and consequent spherically symmetric numerical elasticity solution, that Takeuchi performed. The 3axis pendulum measurements of the actual dilatation results in a constant factor of 0.50, which is in good agreement with the theoretical value, 0.49, obtained by Takeuchi<sup>6</sup>.

**Table B-1 – Variants of  $\mathbf{r}$ ,  $\mathbf{I}_1$ , and  $\mathbf{I}_2$  in the outer core of the earth**

Depth (km)	$\rho$ ( $\text{g/cm}^3$ )	$\mathbf{I}_1$	$\mathbf{I}_2$	$\frac{d\mathbf{r}}{d\mathbf{x}}$	$\frac{d\mathbf{I}_1}{d\mathbf{x}}$	$\frac{d\mathbf{I}_2}{d\mathbf{x}}$
0	3.30	0.680	0.600			
250	3.51	0.936	0.772	-4.9686	-6.5815	-4.1558
500	3.69	1.197	0.926			
500	4.22	1.644	1.217	-4.6730	-8.4296	-9.9371
800	4.44	2.041	1.685	-4.4590	-6.4443	-8.2172
1100	4.64	2.251	1.991	-3.7158	-8.5570	-4.5970
1400	4.79	2.847	2.118	-3.1850	-8.3977	-3.6203
1700	4.94	3.042	2.332	-3.0788	-4.6713	-4.2466
2000	5.08	3.287	2.518	-3.0788	-8.3340	-3.0788
2300	5.23	3.827	2.622	-3.1850	-10.9350	-2.7072
2600	5.38	4.317	2.773	-3.1850	-8.2916	-3.2805
2900	5.53	4.608	2.931	-3.1850	-6.1789	-3.3549

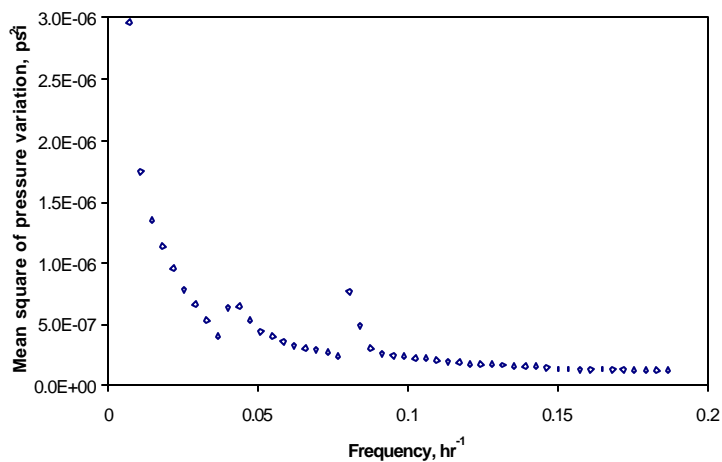


**Figure 1 - Amplitude squared of pressure variation as a function of frequency from a 128K FFT - Well T.**

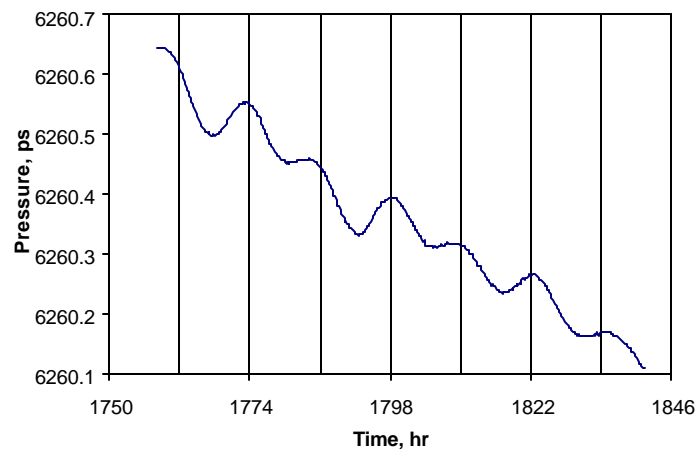


**Figure 2 - Short interval of pressure data plotted in the time domain, which was used for the spectral plot of Fig. 1 - Well T: Starting at 1215 10/17//96.**

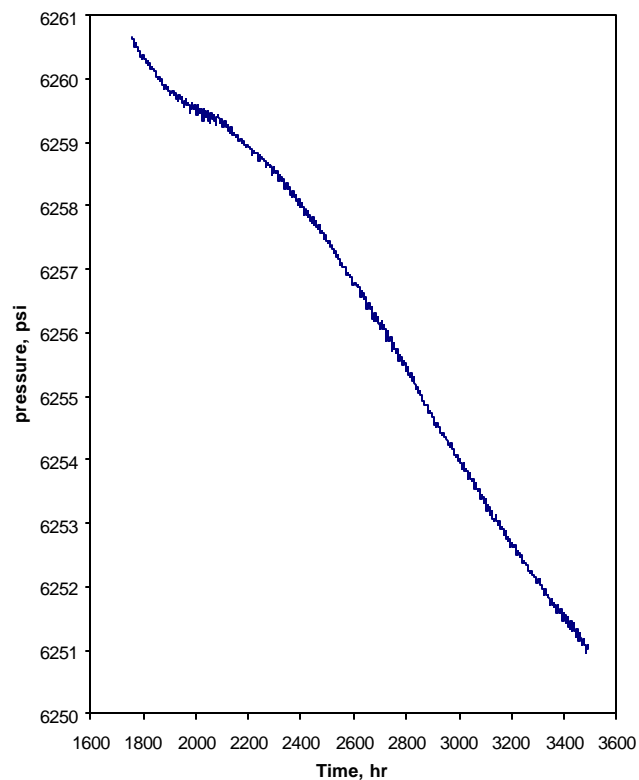


**Figure 3a. Pressure Data from Well T: Starting at 1215, 10/17/96.**

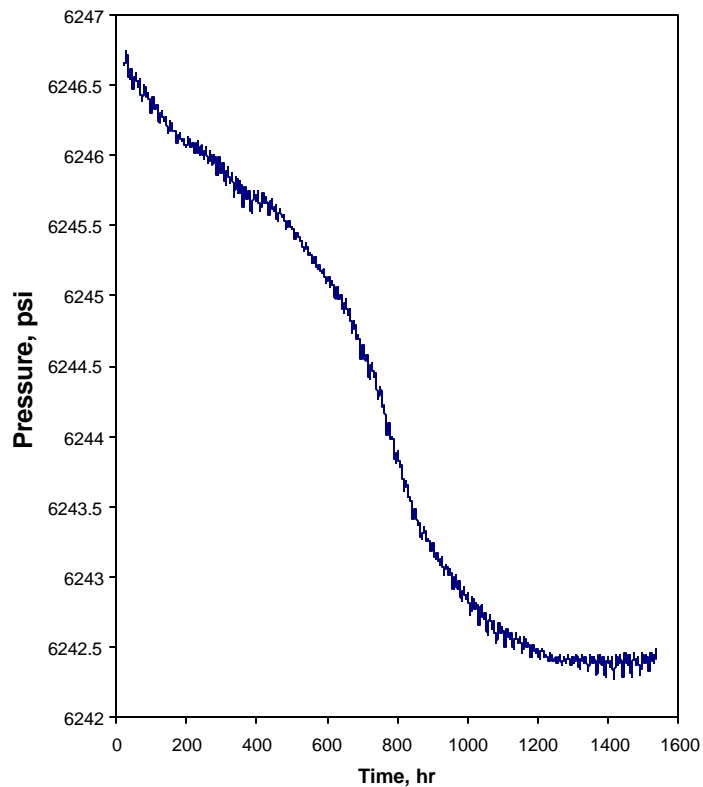


**Figure 3b. Pressure Data from Well T: Starting at 1231 4/22/97.**

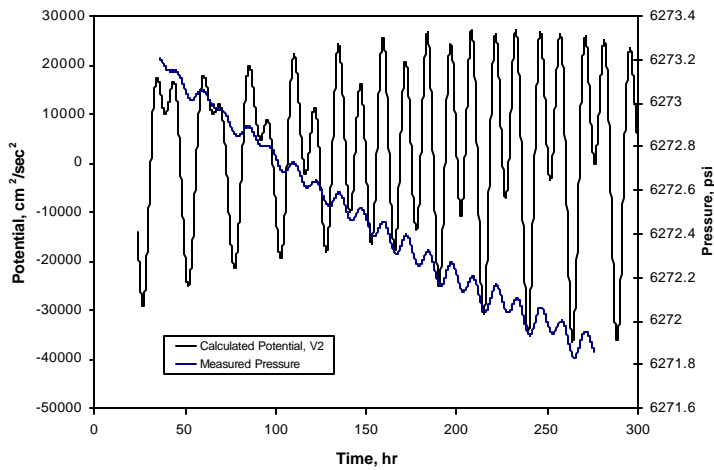


**Figure 4a. Potential and Pressure from Well T: Starting at 1215 10/17/96 (time lag adjusted).**

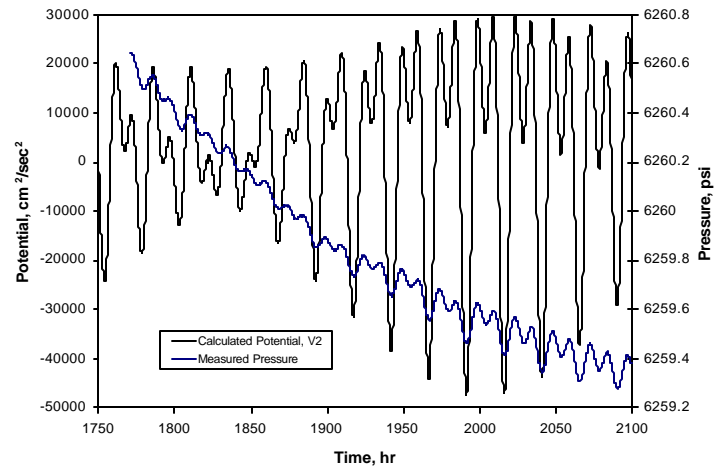


**Figure 4b. Potential and Pressure from Well T: Starting at 1215 10/17/96 (time lag adjusted).**

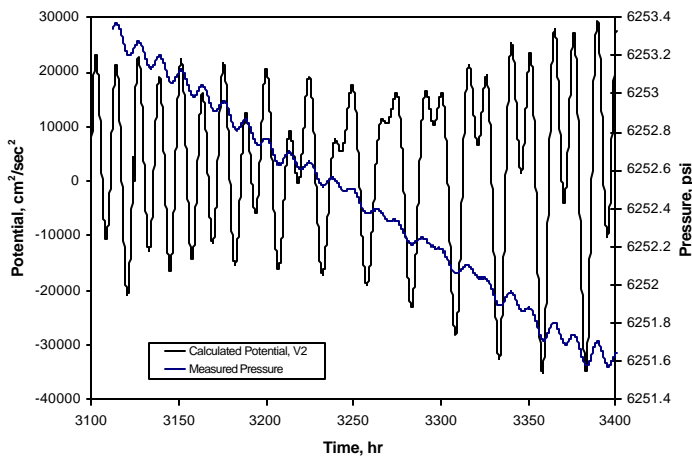


**Figure 4c. Potential and Pressure from Well T: Starting at 1215 10/17/96 (time lag adjusted).**

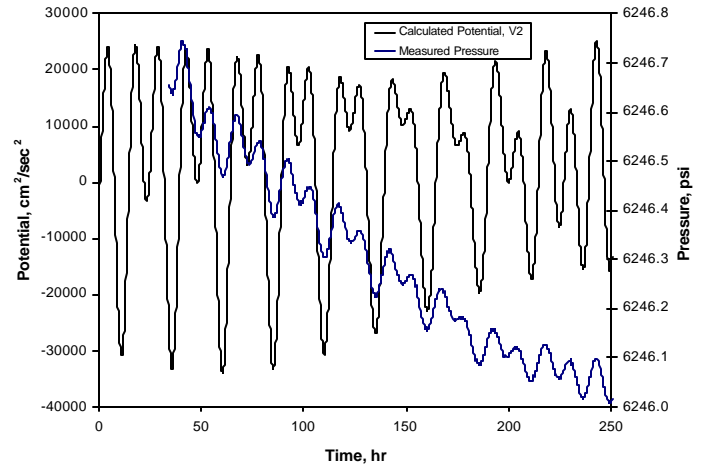


**Figure 4d. Potential and Pressure from Well T: Starting at 1231 4/22/97 (time lag adjusted).**



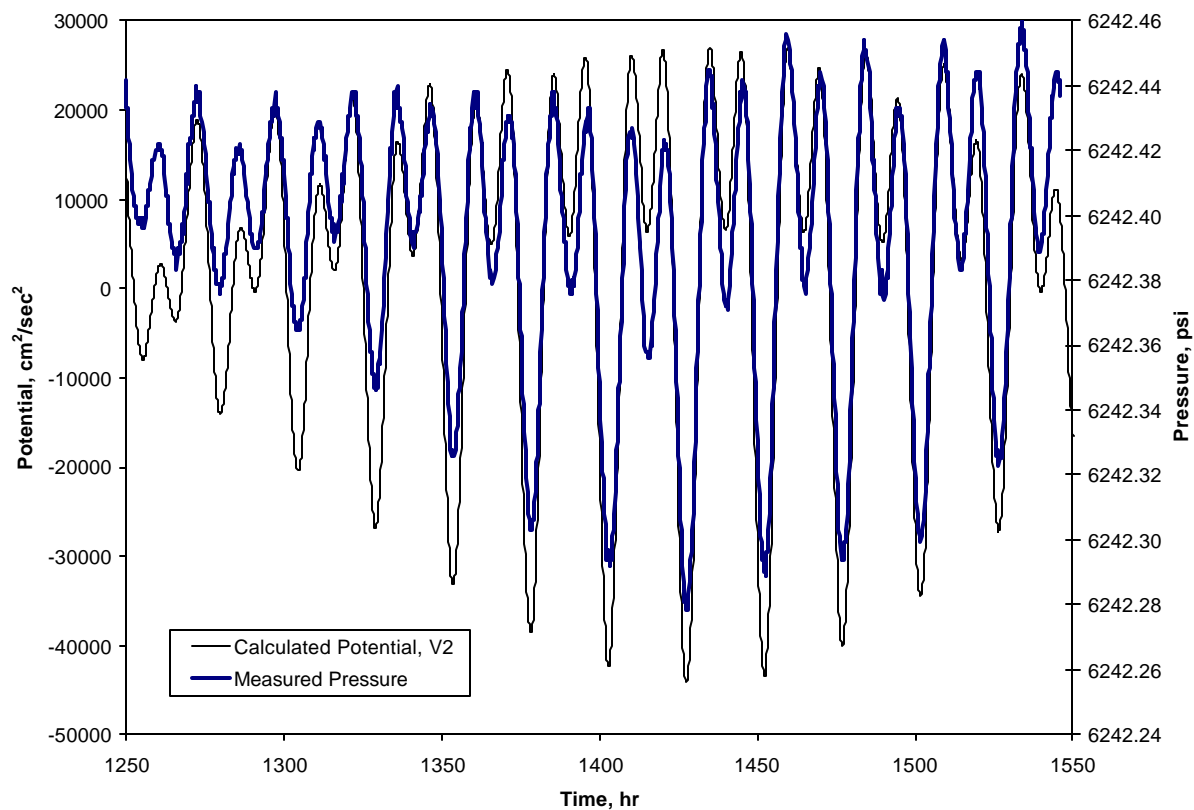


**Figure 4e. Potential and Pressure from Well T: Starting at 1231 22/04/97 (time lag adjusted).**

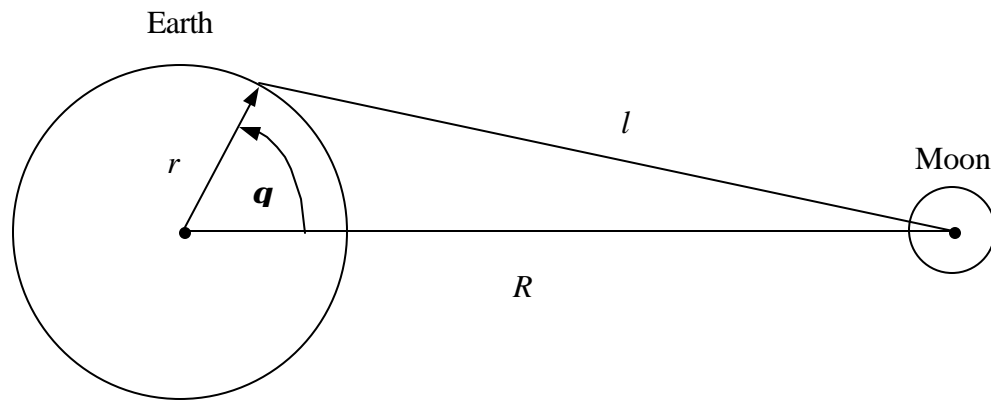


**Figure A.1 – Bispherical axisymmetric coordinate system about the earth and the moon.**

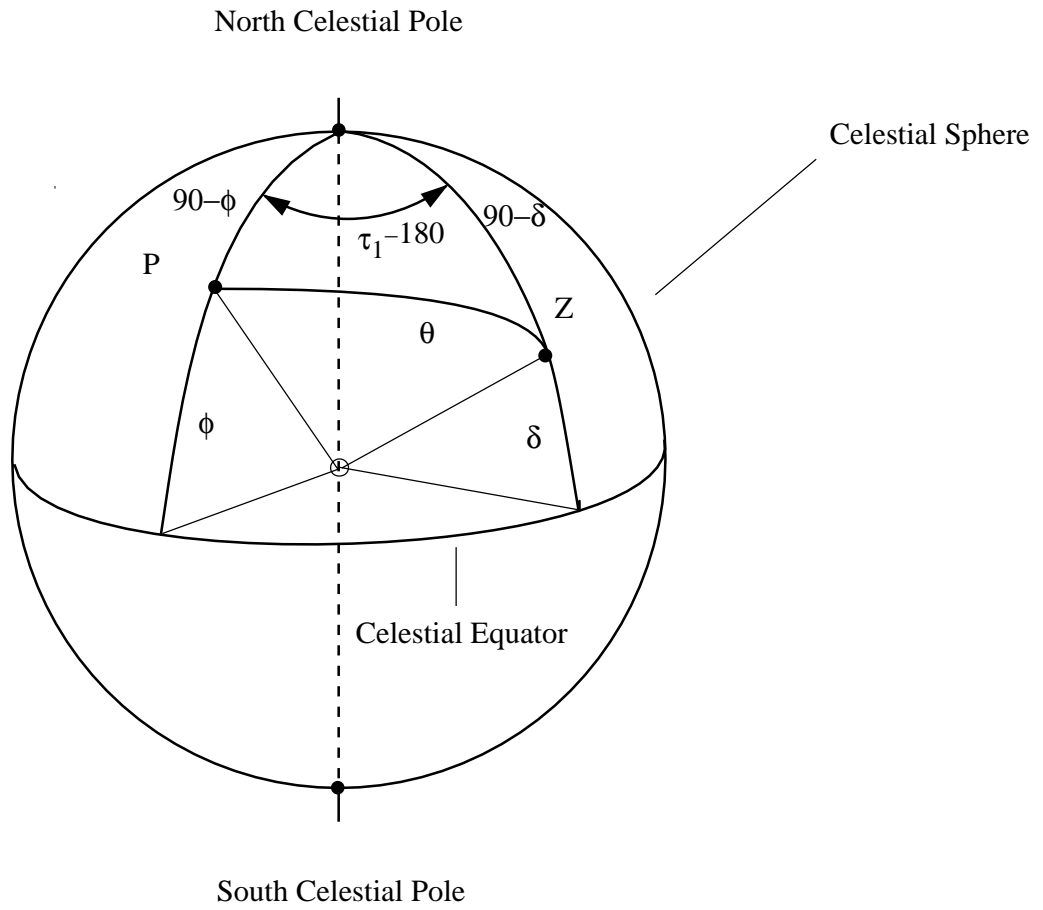


**Figure A.2 – Geocentric coordinates for the potential expression. P is the observation point, Z is the lunar zenith point, and  $\tau_1$  is the moon sidereal time.**

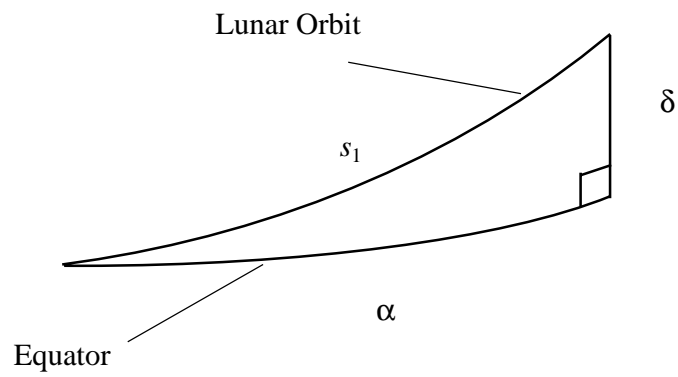


**Figure A.3 – The right spherical triangle with the lunar orbit as its hypotenuse.  $s_1$  is the lunar longitude,  $\alpha$  is the right ascension, and  $\delta$  is the declination.**

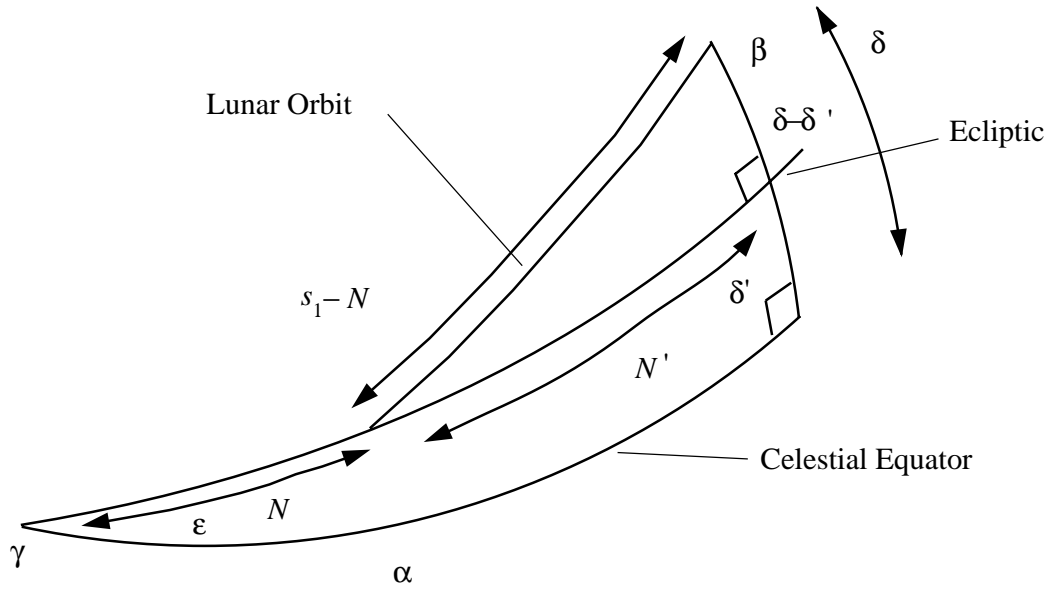


**Figure A.4 – The two spherical triangles formed by the equator, the ecliptic, and the lunar orbit.  $\beta$  is the declination of the lunar orbit with respect to the ecliptic,  $N$  is the angle between the spring equinox and the ascending intersection between the lunar orbit and the ecliptic, and  $\gamma$  is the spring equinox.**

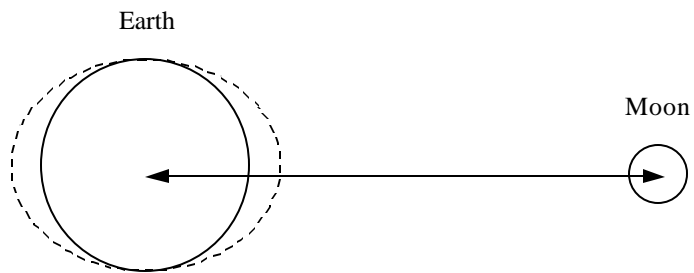


**Figure B.1 – First order deformation, shown by the dotted contour, in response to the gravitational field generated by a mass in proximity to the earth. The scale of the deformation is exaggerated for clarity. Points at the top and bottom of the earth undergo differential expansion, and points along the axis of the line joining the earth and the mass undergo differential compaction.**

# **Chapter II – Gravitational Potential Variations of the Sun and Moon for the Estimation of Reservoir Properties**

## **Part II – Gravitational Potential Variations of the Sun and Moon for the Estimation of Reservoir Permeability**

ABBAS FIROOZABADI AND ERIC CHANG

### **Abstract**

The flow in a reservoir due to gravitational potential variation from the sun and the moon is formulated. Based on this formulation, three parameters affect the flow: 1) a Fourier number which is the ratio between the increase in the amount of a mass around the wellbore and the amount transferred by flow from the wellbore for one period, 2) storativity ratio of the wellbore which is the ratio of wellbore storativity to the reservoir, and 3) the peak to peak variation of the gravitational potential. Results show that the time lag between the wellbore pressure and the pressure far away from the wellbore is sensitive to permeability for a certain range of the parameters.

### **Introduction**

Sensitive pressure measurements taken in closed wellbores often exhibit small periodic pulsations with periods that are approximately diurnal (24 hour) or semidiurnal (12 hour). These are especially evident under quiescent conditions, such as periods of slow pressure decline. The origin of these pulsations is the periodic dilation of the reservoir's porous rock by a varying gravitational field generated by the (relative) orbital motions of the moon and the sun.

It has been shown previously that the peak-to-peak magnitude of these pressure oscillations is inversely proportional to the reservoir's total compressibility<sup>1</sup>. Depending on the fluid mobility  $k / \mu$  ( $k$  is the permeability and  $\mu$  is the viscosity) the observed pressure signal may not always be in phase with the imposed varying gravitational potential field from the sun and the earth. As we will see in this paper, the phase lag can be due to the pressure oscillations in the reservoirs far from the well and pressure oscillations in the well from fluid flow. This phase lag may be used to give some indication of the fluid mobility without the need for producing fluids during well testing.

The main goal of this paper is to formulate the transient flow equations around the wellbore and provide the pressure response as a function of the time-varying gravitational field. The solution is expected to provide an explanation for the time lag. The solution is also expected to be useful to estimate fluid mobility in a closed well.

**Previous Work** – The problem of estimating the wellbore flow response to a periodically varying gravitational field has been examined previously by several investigators. The principles and reservoir coupling mechanisms (and, therefore, the conclusions) proposed in the various studies have shown some differences, but they are all based on the general principle that periodic

variations in the gravitational field generate dilatations in the porous media volume via coupling mechanisms. These dilatations force some fluid into the wellbore, which must subsequently drain back into the reservoir rock during the subsequent period of lower pressure. Delays due to the time required for fluid to move towards (or away from) the wellbore give rise to the phase lag between the gravitational potential and the observed pressure.

Moreland and Donaldson<sup>2</sup> modeled the system with an oscillating rigid overburden. Variations in the gravitational field modulated the weight of the overburden, which was directly transmitted to the reservoir media via rock constitutive coefficients, which described the relations between rock stress, strain, and pore pressure. The resulting system of linear elasticity and flow equations was solved semi-analytically, and the phase lag obtained as the angle associated with the complex-valued response magnitude.

Rehbinder<sup>3</sup> considered a porous material composed of horizontally oriented fractures which exhibited a compressibility (independent from the fluid compressibility) with respect to the  $z$ -component of the variation in the gravitational field. Although the mechanism is simpler, the physical coupling is equivalent to that used by Moreland and Donaldson. Rather than the pressure or fluid height within a wellbore, the position of the free surface was sought. In this case, flow is entirely in the vertical direction, as manifested in the oscillation of the water table height. The water table motion also exhibits a phase lag, since it requires a non-zero amount of time for fluid to enter the well and increase the height of the water table once the formation has been compacted.

Furnes et al.<sup>4</sup>, in addition to Hemala and Balnaves<sup>5</sup>, considered a different coupling mechanism between the gravitational field variations and the observed pressure response. Overburden force variations due to the sea tide causes corresponding porosity variations in the reservoir, by means of a Hooke's law based mechanism. This physical mechanism is particularly interesting, since it predicts a different phase relationship between the gravitational forcing and the anticipated pressure variations at zero phase lag (high mobility) than the ones discussed earlier.

Finally, Arditty et al.<sup>6</sup>, following Bodvardsson<sup>7</sup>, employed a global deformation mechanism based on the numerical solution derived by Takeuchi<sup>8</sup> for the deformation of the earth's volume in response to a gravitational potential variation in the form of the second growing spherical harmonic expanded about the earth's center. For reasons discussed in Ref. 1 (and repeated briefly in this paper), this mechanism seems to be the most plausible for coupling gravitational potential variations to the observable pressure signal.

## Field Observations

In Ref. 1, the total compressibility of an Italian onshore reservoir was estimated using an earth tide deformation model. A phase lag of about 12 hours was observed between the calculated gravitational potential and measured pressure (see Fig. 1). Fig. 2 shows measured pressure data and the calculated gravitational potential from a well in a Colombian reservoir. There is no phase lag between the measured data and the calculated potential. In the Colombian onshore reservoir, the mobility is about two orders of magnitude higher than the Italian reservoir; both reservoirs are fractured with very low matrix porosity. The contrast between the mobility in the two reservoirs may be related to the phase lag between wellbore pressure and imposed gravitational potential variation.

We point out that observations from offshore reservoirs can show another complication in the phase lag between pressure response and imposed gravitational potential variation. In Ref. 3, Rehbinder showed that the well response almost exactly follows the sea floor pressure. This



pressure, in turn, is driven by the ocean tide, and gives rise to a pressure driving force that is a half cycle (approximately 6 hours) out of phase with the perturbations caused by the earth tide. Therefore, this additional driving term must be accounted for when considering measurements taken in offshore reservoirs.

### Fluid Flow Model

Since the relationship between phase lag and fluid mobility may be dependent on the nature of fluid flow towards and away from the wellbore, it is necessary to discriminate between the various possible candidates. The overburden-driven flow proposed by Moreland and Donaldson<sup>2</sup> and Moreland<sup>9</sup> is one of these candidates. These authors considered both rectangular (flow driven into a channel and depleted uniformly at one end) and axisymmetric (flow into a cylindrical wellbore with static pressure drive at infinity) domains. The driving force for flow in these systems is the modulation of the weight, or force exerted by the overburden, on the producing formation. The force is simply the vector sum of the gravitational force of the earth and that due to the disturbing body. A net flow is generated by the squeezing action of this varying overburden, volumetrically dilating the fluid-bearing porous medium. The overburden force, in turn, is resisted by the elastic nature of the rock matrix as well as by the varying pore pressure.

The phase of the static pressure under these conditions is such that it is lowest when the astronomical body (the moon, for example) is directly overhead. The normal component of the gravitational force to the earth's surface will decline to zero at a 90° offset to the direction of the force, and tend to increase the overburden when the body is directly below (with respect to the earth's center) the observation location. Therefore, the pressure signal will have a 24-hour fundamental component. Since observations show that the fundamental component is closer to 12 hours, this flow model may not be able to explain the dominant component.

As mentioned in Ref. 1, the amplitude of the static pressure variations predicted by the overburden model also does not agree with the observations. The simple linear model mentioned Ref. 1 will be expanded somewhat for clarity. The concept of a force balance between the overburden and the reservoir stresses may be written in the following way,

$$F_0 / A = \mathbf{s} + p , \quad (1)$$

where  $F_0$  is the overburden force,  $A$  is the area element in consideration,  $\mathbf{s}$  is the rock stress, and  $p$  is the pressure. The overburden term may be written in terms of the depth and the average fluid and rock density as  $\rho g l$ , where  $l$  is the overburden height. Let us consider the response of the system to a small change in the local gravitational potential, or equivalently  $g$  where  $g$  would change to  $g + \Delta g$ . Because linearity applies in the elastic response of the reservoir, the reservoir stress is a result of a linear operation on  $g$ .

$$\mathbf{s} = L(g) \quad (2)$$

The response to  $g + \Delta g$  may be computed by using the property of linearity as

$$L(g + \Delta g) = L(g) + L(\Delta g) = \left(1 + \frac{\Delta g}{g}\right) L(g) = \left(1 + \frac{\Delta g}{g}\right) \mathbf{s} \quad (3)$$

Evaluating Eq. 1, the gravitational potential then yields

$$\mathbf{r}g h \left( 1 + \frac{\Delta g}{g} \right) = \left( 1 + \frac{\Delta g}{g} \right) \mathbf{S} + (p + \Delta p) \quad (4)$$

By comparing Eq. 4 with Eq. 1, the pressure increase  $\Delta p = (\Delta g / g) p$ . As noted in Ref. 1,  $\Delta g / g \approx 10^{-4} \text{ gal} / 10^3 \text{ gal} = 10^{-7}$ ; for  $p = 10^4 \text{ psi}$ ,  $\Delta p = 10^{-3} \text{ psi}$ , which is much smaller than the observed pressure variations in the reservoirs (see Figs. 1 and 2). The unit gal is shorthand used in the earth tide literature<sup>10</sup> for  $\text{cm-sec}^{-2}$ .

The overburden mechanism proposed by Furnes et al.<sup>4</sup>, although similar, cannot be dismissed in the same fashion. One factor is the extremely strong correlation with field data. In this case, the driving force also has a semi-diurnal fundamental period, which is in agreement with the observed field pressure. The key difference is that the model considers ocean tide overburden, which has the correct period. In addition, ocean tide surface loading is not a proportional effect, as the model discussed above exhibited, but rather an additive one.

Both the two reservoirs considered in this study are onshore, so the mechanism of ocean tide loading is not present. In order to generate a response of sufficient size to produce the observed pressure variations, it is clear from the above considerations that the model must account for influence over global scales so that the angular variation of the gravitational field becomes significant.

The earth tide dilation model used in Refs. 1, 5, and 6 does fulfill the criterion in which the earth deforms to match the shape of the isopotential surface of the gravitational perturbation. In Ref. 1, we have shown that such a model is successful for predicting the static properties of the reservoir (total compressibility). In this paper, the dynamic behavior of this model will be examined in order to shed some light on the computation of mobility from phase lag.

Consider an axisymmetric system with a well in the center (see Fig. 3). During the period that the static pressure in the formation from the wellbore is increasing, the pressure in the well if there was no communication with formation, will vary much less in the same period. As the gravitational cycle reverses, the pressure far away from the wellbore decreases. If there is communication between the formation and the well during high pressure period in the far-field, the fluid moves toward the wellbore, and during the low pressure cycle, the fluid moves from the wellbore to the formation. The process also follows a phase lag between the maximum pressure in the wellbore and the maximum pressure in the far-field. In the far-field, the pressure increase is accompanied by a decrease in the gravitation potential and vice versa, as we will see later. The dynamic flow of the process depends on the geometry of the axisymmetric system and the importance of the regions of fluid nearer the wellbore for providing pressure support. This, in turn, is related to the Stokes or Whitehead paradox, in which the disturbance of a cylinder to Stokes flow becomes unbounded at infinity (see, for example, chapter 7 in Ref. 11). Or, for the system being investigated, there is no steady state solution to the flow problem with a non-zero wellbore flow rate and bounded pressure at infinity, implying limited deliverability of far-field regions, and therefore, a restriction of most of the flow to a bounded region surrounding the wellbore.

The simplified problem domain still retains the physical features of the system necessary for studying the phase lag-mobility relationship. It consists of an infinite fluid filled cylindrical

wellbore of radius  $R_1$  surrounded by a fluid saturated (viscosity  $\mathbf{m}$ ) porous medium (permeability  $k$ ) extending out to infinity (see Figure 3). The equation for pressure within the porous medium portion is<sup>12</sup>:

$$\frac{1}{r} \frac{\partial}{\partial r} \left( \frac{k \mathbf{r}}{\mathbf{m}} r \frac{\partial p}{\partial r} \right) = \frac{\partial(\mathbf{f} \mathbf{r})}{\partial t} \quad (5a)$$

This equation follows from applying Darcy's law in conjunction with conservation of mass in a compressible system with varying porosity ( $\mathbf{f}$ ). Here,  $\mathbf{r}$  is the fluid density,  $t$  is time, and  $r$  is the radial coordinate and is positive away from the wellbore.

The boundary conditions are:

$$p(r, t) = p_{well}(t), \text{ at } r = R_1, \quad (6)$$

$$p(r, t) = p_s(t), \text{ at } r = \infty. \quad (7)$$

The initial condition is

$$p(r, 0) = p_0 \quad (8)$$

where  $p_0$  is an average or baseline reservoir pressure and  $p_s(t)$  is the static pressure far from the wellbore.

In light of the physical system (and its parameters) that is being modeled, some further approximations are also made.

1) The wellbore does not move. Although the wellbore does actually move, if it dilated in accordance with the reservoir volume, this movement would be negligible for the purpose of accounting for fluid flow, since the dilatation must be substantially larger than those associated with the porous medium in the reservoir to generate equivalent pressure changes. The reason for this difference is that the pressure change in the reservoir is magnified by a factor of  $1/\mathbf{f}$ , and those in the wellbore attenuated by increase in effective volume due to the ratio between the formation thickness and the completion interval.

2) Ignore non-uniform compaction due to the cavity effect. The local solution to the deformation equations will be affected by the presence of the wellbore. Typically, the deformation will be greater in its vicinity because the material is less rigid there. Immediately inside the wellbore, the effect of this difference is minimized due to the factor in 1) and in its neighborhood, the effect is diminished due to the penetration distance of the cylindrical flow.

3) Eq. 5a is slightly non-linear. On the other hand, it deals with tiny perturbations to the pressure, density, and porosity. It may be linearized by retaining the effect of varying density in the source term driving the flow, but neglecting its contribution to the mass balance with respect to influx due to flow. This approximation amounts to neglecting terms of order of the perturbation squared (that is,  $(\partial p / \partial r)^2$  is neglected in comparison to  $\partial^2 p / \partial r^2$  and  $\partial p / \partial r$ ). Formally, this assumption corresponds to considering  $\mathbf{r}$  to be independent of  $r$ , but not of  $t$ , and  $k$  to be independent of  $r$ . With this assumption, Eq. 5a can be written as

$$\left(\frac{k\mathbf{r}}{\mathbf{m}}\right)\frac{1}{r}\frac{\partial}{\partial r}\left(r\frac{\partial p}{\partial r}\right)=\frac{\partial(\mathbf{r}\mathbf{f})}{\partial t} \quad (5b)$$

4) The porous medium is homogeneous and of infinite extent. All reservoirs are bounded, but often the extent is sufficient for the further regions to contribute little to the flow towards the wellbore. This approximation will be checked by an a posteriori estimate of the penetration depth.

5) The linearity of the equations allows superposition. After linearization is performed, the now linear system of equations may be solved by superposition. This brings a powerful array of Fourier techniques<sup>13</sup> to bear, which will prove to be both useful and insightful.

6) The motion of the solid phase is negligible. This approximation is valid when the porosity is low. At higher values of the porosity, the velocity of the fluid is modified by a constant factor which is approximately  $1 - \mathbf{f}$ . The density and porosity become coupled with the pressure solution and the solution to the full equations of motion is required. The static pressure will also be a solution to the full-coupled elasticity and flow equations that apply when the porous medium is not stationary<sup>14</sup>.

$$\frac{\partial(\mathbf{r}\mathbf{f})}{\partial t} + \nabla \bullet (\mathbf{r}\mathbf{f}\vec{v}) = 0 \quad (9a)$$

$$\frac{\partial[\mathbf{r}_{solid}(1-\mathbf{f})]}{\partial t} + \nabla \bullet [\mathbf{r}_{solid}(1-\mathbf{f})\vec{V}] = 0 \quad (9b)$$

$$\mathbf{f}(\vec{v} - \vec{V}) = -\frac{k}{\mathbf{m}}\nabla p \quad (9c)$$

$$\begin{aligned} \frac{\partial p}{\partial x_i} = & \frac{\partial}{\partial x_j} \left( \mathbf{h} \left( \frac{\partial V_i}{\partial x_j} + \frac{\partial V_j}{\partial x_i} \right) \right) \\ & + \frac{\partial}{\partial x_i} \left( \mathbf{z} - \frac{2}{3}\mathbf{h} \right) \nabla \bullet \vec{V} - (1-\mathbf{f})(\mathbf{r}_{solid} - \mathbf{r})g\mathbf{d}_{i3} \end{aligned} \quad (9d)$$

The above expressions are the equations of continuity for the fluid and solid and momentum for the fluid and solid, respectively. The velocities of the fluid and solid are  $\vec{v}$  and  $\vec{V}$ , and the bulk and shear elasticity are  $\mathbf{z}$  and  $\mathbf{h}$ . The momentum equation for the solid is written in index notation, where  $\mathbf{d}_3$  represents the unit vector in the  $z$  (gravitation) direction.

The solution to Eq. 5b for the region far from the well is called the static pressure,  $p_s$ ; it varies in time in phase with the oscillating astronomical gravity perturbations. Although it appears necessary to solve the full system of equations for both fluid and solid phases to obtain this result, Bredehoeft<sup>15</sup> noted that a substantial simplification may be made if the equations are linearized in terms of the order of the pressure variation,  $O(\Delta p)$ . In systems of interest, this approximation is valid, since the pressure variation due to earth tidal forces is several orders of magnitude smaller than the average pressure. This allows the fractional change in volume due to

the earth tide dilatation and the change due to the resulting pressure variation to be considered separately, and then simply added. Any error will be of the order  $O(\Delta p^2)$ . The total dilatation is written as the sum of the tidal dilatation and the pore volume change due to the pressure variation.

$$\Delta_{total} = \Delta_{earth} + \Delta_{pressure} \quad (10)$$

One way of looking at this simplification is to note that the first term on the right side corresponds to the fractional change in volume due to the deformation of the earth. This deformation causes the fluid pressure in the pores to change. Since porosity is an increasing function of pore pressure in a deformable media, a deformation will occur in response to the earth tidal dilatation, but in the opposite direction. This dilatation, denoted by  $\Delta_{pressure}$ , is also proportional to  $\Delta p$ . Of course, the increase in pore pressure also changes the strain field within the reservoir, resulting in a correction to  $\Delta_{earth}$ , but this correction is  $O(\Delta p^2)$ , and is, therefore, neglected in the current analysis of the problem. Each of the terms in Eq. 10 may be evaluated in turn to arrive at an expression for the static pressure far from the well. Takeuchi obtained a numerical solution<sup>8</sup> of the linear elastic equations in conjunction with a constitutive model of the earth. The result is an expression for the earth's volumetric dilatation as a function of the astronomical gravity potential,

$$\Delta_{earth} = \frac{\Delta V_2}{0.49ag} \quad (11)$$

where  $\Delta V_2$  is the contribution of the second spherical harmonic of the gravitational potential expanded about the earth's center and  $a$  is the radius of the earth. The factor of 0.49 arises from the particular elastic parameters (shear and bulk moduli) assigned to the earth's interior, as well as their radial variation.

The term in the left side of Eq. 10 is the total dilatation; it may be expressed as

$$\Delta_{total} = \frac{\Delta V}{V} \quad (12)$$

where  $V$  is the total reservoir volume and  $\Delta V$  is its change under the influence of the gravitational potential. If the dilatation of the solid matrix is negligible in comparison to the fluid filling the pores,  $\Delta V = \Delta V_f$ , the change in fluid volume. Here  $V$  and  $V_f$  are the total and fluid volume in the reservoir, respectively. Moreover, the porosity  $\mathbf{f} = V_f / V$  may be introduced, giving

$$\Delta_{total} = \frac{\Delta V_f}{V_f} \mathbf{f} \quad (13)$$

The change in fluid volume is directly related to the change in density by

$$\frac{\Delta V_f}{V_f} = -\frac{\Delta \mathbf{r}}{\mathbf{r}} \quad (14)$$

where  $\Delta \mathbf{r}$  is the variation in density due to  $\Delta V_2$ . Using  $\Delta \mathbf{r} = (\partial \mathbf{r} / \partial p) \Delta p$  and Eq. 13 and 14,

$$\Delta_{total} = -\mathbf{f} \frac{1}{\mathbf{r}} \frac{\partial \mathbf{r}}{\partial p} \Delta p \quad (15)$$

From the definition of the fluid compressibility,  $c \equiv (1 / \mathbf{r})(\partial \mathbf{r} / \partial p)$ , Eq. 15 becomes

$$\Delta_{total} = -\mathbf{f} c \Delta p \quad (16)$$

The last term,  $\Delta_{pressure}$ , in Eq. 10 is the response of the pore volume to changes in pressure. Even when the matrix is considered to be incompressible in comparison to the pore fluid, the pore space itself is deformable, so the pore volume changes in response to the pressure. This quantity is related to the pore compressibility  $c_p \equiv (1 / \mathbf{f})(\partial \mathbf{f} / \partial p)$  by

$$\Delta_{pressure} = \Delta \mathbf{f} = \frac{\partial \mathbf{f}}{\partial p} \Delta p = \mathbf{f} c_p \Delta p \quad (17)$$

Substituting Eqs. 11, 16, and 17 into Eq. 10 yields

$$\Delta p = -\frac{\Delta V_2}{0.49 \mathbf{f} a g c_f} \quad (18)$$

where  $c_f \equiv c + c_p$  is the formation compressibility. The static pressure far from the well  $p_s$ ,  $p_s = p_0 + \Delta p$  is not exactly a solution to Eq. 5b, not even to  $O(\Delta p)$ . The reason is that Eq. 5b is only approximate when the porous media is undergoing compaction by means of a deformation of the pore space. This can be seen by substituting  $p_s$  into Eq. 5b. The left side is identically zero, since  $p_s$  is only a function of time. The right side is the derivative of the fluid mass per unit volume. The fluid mass per unit volume, however, is not constant, even though there is no net flow. The reason is that there is a bulk motion of the fluid saturated porous medium into a given volume upon compaction. It is clear that  $\mathbf{r} \mathbf{f}$  will increase when the reservoir is compacted and vice versa. The deviation is only  $O(\mathbf{f})$ , and since  $\mathbf{f}$  is small in many cases, this can be ignored as a first approximation.

Although the static pressure is an approximate solution of Eq. 5b, it does not satisfy the boundary condition in Eq. 6. To satisfy this condition, a new candidate solution, the total pressure, denoted by  $p_t$  is defined.

$$p_t(r, t) = p_s(t) + p(r, t) \quad (19a)$$

Here,  $p(r,t)$  is a spatially varying perturbation pressure due to flow in the wellbore. Note that  $p$  satisfies Eqs. 5b and 7. Eq.6 should be modified according to the above definition.

$$p_{well} = p_s(t) + p(R_I, t) \quad (19b)$$

It is useful to first write the system of equations in dimensionless form so that the key parameters of influence may be identified. This is done by replacing each of the dimensional variables with its dimensionless counterpart. Characteristic values used for this normalization are:

$\bar{f}_0 \equiv$  average porosity

$p_0 \equiv$  average or baseline reservoir pressure

$R_1 \equiv$  wellbore radius

$T \equiv$  fundamental excitation period ( $= 2\pi/\omega$ ) where  $\omega$  is the angular frequency. In this work,  $T=12$  hours/ cycle

$\bar{r}_0 \equiv$  average or baseline density

The baseline pressure, which may be slightly different than the reservoir pressure is the pressure when the astronomical potential is at its baseline (or starting) value. The variables  $p$ ,  $r$ ,  $t$ ,  $\mathbf{r}$ , and  $\mathbf{f}$  may be replaced by their dimensionless forms, which will be denoted by the same variables with an overbar. For the purposes of solving Eq. 5b, its right side must be expressed in terms of the total pressure. Under general conditions, this task is complicated by the fact that, when  $\bar{r}$  depends on  $\bar{p}_t$  (which is the case of interest), the full equations of motion, Eqs. 9, are nonlinear. For the special situation of earth-tide induced reservoir pressure, however, the variations in pressure are so small compared to the average that several approximations may be made. This is realized by means of a perturbation expression. The density may be expanded as follows (in dimensionless form),

$$\bar{\mathbf{r}} = 1 + \frac{\partial \bar{\mathbf{r}}}{\partial \bar{p}_t} (\bar{p}_t - 1) + O(\Delta \bar{p}_t^2) \quad (20)$$

From Eqs. 19a and 20,

$$\bar{\mathbf{r}} = 1 + \frac{\partial \bar{\mathbf{r}}}{\partial \bar{p}_t} (\bar{p}_s - 1) + \frac{\partial \bar{\mathbf{r}}}{\partial \bar{p}_t} \bar{p} \quad (21)$$

where the squared terms have been omitted for brevity. Similarly, the porosity is given by,

$$\bar{\mathbf{f}} = 1 + \frac{\partial \bar{\mathbf{f}}}{\partial \bar{p}_t} (\bar{p}_s - 1) + \frac{\partial \bar{\mathbf{f}}}{\partial \bar{p}_t} \bar{p} \quad (22)$$

The right of Eq. 5b can be written as

$$\frac{\partial(\bar{\mathbf{r}}\bar{\mathbf{f}})}{\partial \bar{t}} = \bar{\mathbf{r}} \frac{\partial \bar{\mathbf{f}}}{\partial \bar{t}} + \bar{\mathbf{f}} \frac{\partial \bar{\mathbf{r}}}{\partial \bar{t}} \quad (23)$$

Combining Eqs. 21-23, one obtains

$$\frac{\partial(\bar{\mathbf{r}}\bar{\mathbf{f}})}{\partial\bar{t}} = \bar{\mathbf{f}}\frac{\partial\bar{\mathbf{r}}}{\partial\bar{p}_i}\frac{\partial\bar{p}_s}{\partial\bar{t}} + \bar{\mathbf{f}}\frac{\partial\bar{\mathbf{f}}}{\partial\bar{p}_i}\frac{\partial\bar{p}}{\partial\bar{t}} + \bar{\mathbf{r}}\frac{\partial\bar{\mathbf{f}}}{\partial\bar{p}_i}\frac{\partial\bar{p}_s}{\partial\bar{t}} + \bar{\mathbf{r}}\frac{\partial\bar{\mathbf{f}}}{\partial\bar{p}_i}\frac{\partial\bar{p}_s}{\partial\bar{t}} \quad (24)$$

From pore compressibility  $c_p = p_o(1/\bar{\mathbf{f}})(\partial\bar{\mathbf{f}}/\partial\bar{p}_i)$  and fluid compressibility  $c = (1/\bar{\mathbf{r}})(\partial\bar{\mathbf{r}}/\partial\bar{p}_i)$ , Eq. 24 is transformed into

$$\frac{\partial(\bar{\mathbf{r}}\bar{\mathbf{f}})}{\partial\bar{t}} = \bar{\mathbf{r}}\bar{\mathbf{f}}p_o(c + c_p)\frac{\partial\bar{p}}{\partial\bar{t}} + \bar{\mathbf{r}}\bar{\mathbf{f}}p_o(c + c_p)\frac{\partial\bar{p}_s}{\partial\bar{t}} \quad (25)$$

For the reason to be state next,

$$\frac{\partial(\bar{\mathbf{r}}\bar{\mathbf{f}})}{\partial\bar{t}} = \bar{\mathbf{r}}\bar{\mathbf{f}}p_o(c + c_p)\frac{\partial\bar{p}}{\partial\bar{t}} \quad (26)$$

The above expression applies only to the perturbation pressure, and not the static pressure, since the latter does not vary according to the derivatives that define the fluid and pore compressibilities. For example,  $c_p$  is positive when increasing pressure causes increasing porosity, but the compaction process that causes static pressure variation is in the opposite direction, i.e. increasing pressure follows decreasing porosity.

Eq. 5b in dimensionless form for the perturbation pressure  $\bar{p}(\bar{r}, \bar{t})$  when combined with Eq. 2b, may be written as,

$$2p\mathbf{x}^{-2}\frac{1}{r}\frac{\partial}{\partial\bar{r}}\left(\bar{r}\frac{\partial\bar{p}}{\partial\bar{r}}\right) = \frac{\partial\bar{p}}{\partial\bar{t}} \quad (27)$$

where

$$\mathbf{x}^2 = (2p\mathbf{f}_0R_1^2\mathbf{m}_f/(Tk)) \quad (28a)$$

$\mathbf{x}^2$  is the Fourier number, which is a ratio between capacity and amount of fluid transferred in a period. This number is traditionally associated with transient heat transfer systems for which it is the ratio between the heat capacity of a material and the heat transferred by conduction within one characteristic time period. For the fluid flow problem, the Fourier number plays the same role, but this time for mass, rather than heat transfer. This can be seen by rewriting the expression for the dimensionless parameter as follows.

$$\mathbf{x}^2 = 4p\frac{pR_1^2c_f\mathbf{r}\Delta p}{2pR_1\frac{k}{\mathbf{m}\mathbf{f}_0}T\mathbf{r}\frac{\Delta p}{R_1}} \quad (28b)$$



The numerator is recognized to be the increase in the amount of mass in a circular region due to an increase in pressure, and the denominator is the amount transferred by flow for one period,  $T$ .

It is natural, since the system of equations is linear, and the driving force (imposed by  $p_s$ ) is near-periodic, to seek a solution based on a single pure spectral component. Harmonics of this single frequency component will not be generated since the equation is linear. Only  $\bar{p}$  or its derivatives appear (differentiation does not change the frequency of the signal), and there are no product terms. Although this principle is true in general, it will become evident in this special case. Once the solution is obtained at a single frequency, it can be generalized to any forcing function by means of a Fourier decomposition of the forcing function and an application of the principle of superposition. The trial form for the perturbation pressure is

$$\bar{p}(\bar{r}, \bar{t}) = P(\bar{r})e^{2\pi i \bar{t}}. \quad (29)$$

with the understanding that the real or imaginary part will be extracted to obtain the physical solution. The approach has been used in the well test analysis in terms of  $\bar{p}(\bar{r}, \bar{t})$  with cyclic boundary conditions<sup>16</sup>. The boundary conditions in Eqs. 6 and 7 become

$$\bar{p}(1, \bar{t}) = \bar{p}_{well}(\bar{t}) - \bar{p}_s(\bar{t}) \quad (30)$$

$$\bar{p}(\infty, \bar{t}) = 0 \quad (31)$$

Substituting Eq. 29 into Eq. 27 yields,

$$\bar{r}^2 \frac{d^2 P}{d\bar{r}^2} + \bar{r} \frac{dP}{d\bar{r}} - i\mathbf{x}^2 \bar{r}^2 P = 0 \quad (32)$$

The solutions of Eq. 33 are Kelvin functions<sup>17</sup>, which are analytic continuations of Bessel functions into the complex plane.

$$P(r) = A[\ker(\mathbf{x}\bar{r}) + i\text{kei}(\mathbf{x}\bar{r})] + B[\text{ber}(\mathbf{x}\bar{r}) + i\text{bei}(\mathbf{x}\bar{r})] \quad (33)$$

Here,  $A$  and  $B$  are constants of integration that are determined by applying the boundary conditions, Eqs. 30 and 31. Applying the boundary condition given by Eq. 31 provides  $B = 0$ . The full expression for the perturbation pressure is, therefore,

$$\bar{p}(\bar{r}, \bar{t}) = A[\ker(\mathbf{x}\bar{r}) + i\text{kei}(\mathbf{x}\bar{r})]e^{2\pi i \bar{t}} \quad (34)$$

The real or imaginary part of Eq. 34 would be extracted to form the final physical solution.

The remaining boundary condition, Eq. 30, is used to determine  $A$  and, therefore, specify the full solution. This condition is applied by considering mass balance within the wellbore. The mass flux into the wellbore from the reservoir must equal the accumulation within the wellbore. In dimensional form,

$$-2\mathbf{p}h\mathbf{r}q_r\big|_{r=R_1} = \frac{\partial}{\partial t}(\mathbf{p}R_1^2\mathbf{r}H)\big|_{r=R_1} \quad (35)$$

where  $h$  is the perforation thickness, and  $H$  is the height of the fluid column in the wellbore. The  $-$  sign arises from the convention that the flow rate is positive when it is in the direction of the unit radial vector. The radial flux,  $q_r$ , may be obtained from the pressure via Darcy's Law:

$$q_r = -\frac{k}{\mathbf{m}} \frac{\partial p_t}{\partial r} \bigg|_{r=R_1} \quad (36)$$

Using  $\partial \mathbf{r} / \partial r = (\partial \mathbf{r} / \partial p_t)(\partial p_t / \partial t) = \mathbf{r}(\partial p_t / \partial t)$ , Eq. 35 becomes

$$2h \frac{k}{\mathbf{m}} \frac{\partial p_t}{\partial r} \bigg|_{r=R_1} = R_1 H c \frac{\partial p_{well}}{\partial t} \quad (37)$$

Rendering the above equation dimensionless gives,

$$2\mathbf{p} \frac{\partial \bar{p}_t}{\partial \bar{r}} \bigg|_{\bar{r}=1} = \mathbf{x}^2 \mathbf{a} \frac{\partial \bar{p}_{well}}{\partial \bar{t}} \quad (38)$$

Since  $(\partial \bar{p}_t / \partial \bar{r}) = (\partial \bar{p} / \partial \bar{r})$ , Eq. 38 can be written as

$$2\mathbf{p} \frac{\partial \bar{p}}{\partial \bar{r}} \bigg|_{\bar{r}=1} = \mathbf{x}^2 \mathbf{a} \frac{\partial \bar{p}_{well}}{\partial \bar{t}} \quad (39)$$

Note that another dimensionless parameter

$$\mathbf{a} \equiv \frac{cH}{2\mathbf{f}_0 c_f h} \quad (40)$$

has appeared. This parameter represents the storativity of the wellbore as compared to the rest of the reservoir. In other words, a given volume of the wellbore will increase its mass if the pressure increases. Likewise, a volume of the porous media will increase in fluid content with an increase in pressure. The parameter  $\mathbf{a}$  is the ratio of these two amounts for a fixed pressure increment.

Let us write the following expression for the static pressure,

$$p_s(t) = p_0 + p_{so} \sin 2\mathbf{p} \quad (41)$$

The above equation in dimensionless form is

$$\bar{p}_s(t) = 1 + \bar{p}_{so} \sin 2\mathbf{p} \quad (42)$$

Alternatively, Eq. 42 can be written as

$$\bar{p}_s(t) = 1 + \text{Im}[\bar{p}_{so} e^{2pi\bar{t}}] \quad (43)$$

where the symbol Im denotes the imaginary part of  $\exp(2pi\bar{t})$ . In this work, the imaginary part of the exponential term will be extracted to obtain the physical solution. Note that once the solution is obtained at a single frequency  $\omega$ , it can be generalized to any forcing function by means of a Fourier decomposition of the forcing function and the application of the principle of superposition, as was stated earlier. From Eqs. 30, 34, and 43

$$\bar{p}_{well}(t) = 1 + \text{Im}[\bar{p}_{so} + A(\ker \mathbf{x} + i\ker' \mathbf{x})]e^{2pi\bar{t}} \quad (44)$$

Combining Eqs. 34, 39, and 44, one obtains

$$A[\ker' \mathbf{x} + i\ker' \mathbf{x}]e^{2pi\bar{t}} = \mathbf{x}\bar{\mathbf{a}}[\bar{p}_{so} + A(\ker \mathbf{x} + i\ker' \mathbf{x})]e^{2pi\bar{t}} \quad (45)$$

The pressure at the wellbore can be written as

$$\bar{p}_{well}(t) = 1 + b\bar{p}_{so} \sin(2pi\bar{t} + \mathbf{d}), \quad (46)$$

where  $b$  is the amplitude factor and  $\mathbf{d}$  is the dimensionless time lag. Note that Eq. 46 has the same form as Eq. 42 with the exception of amplitude factor and phase lag. The main goal of this work is to derive expressions for  $b$  and  $\mathbf{d}$ . In the following, these two expressions are provided (details are given in Appendix A).

$$\mathbf{d} = \arctan \frac{A_r \ker \mathbf{x} + A_i \ker' \mathbf{x}}{\bar{p}_{so} + A_r \ker \mathbf{x} - A_i \ker' \mathbf{x}} \quad (47)$$

and

$$b = \frac{1}{\bar{p}_{so}} \left\{ [\bar{p}_{so} + A_r \ker \mathbf{x} - A_i \ker' \mathbf{x}]^2 + [A_r \ker \mathbf{x} + A_i \ker' \mathbf{x}]^2 \right\}^{1/2} \quad (48)$$

where  $A_r$  and  $A_i$  are the real and imaginary part of  $A$  given by

$$A_r = \frac{\mathbf{x}\bar{\mathbf{a}}\bar{p}_{so}[\mathbf{a}\mathbf{x}\ker \mathbf{x} - \ker' \mathbf{x}]}{[\mathbf{a}\mathbf{x}\ker \mathbf{x} - \ker' \mathbf{x}]^2 + [\mathbf{a}\mathbf{x}\ker' \mathbf{x} + \ker \mathbf{x}]^2} \quad (49)$$

and

$$A_i = \frac{\mathbf{x}\bar{\mathbf{a}}\bar{p}_{so}[\mathbf{a}\mathbf{x}\ker' \mathbf{x} + \ker \mathbf{x}]}{[\mathbf{a}\mathbf{x}\ker \mathbf{x} - \ker' \mathbf{x}]^2 + [\mathbf{a}\mathbf{x}\ker' \mathbf{x} + \ker \mathbf{x}]^2} \quad (50)$$

In addition to Eqs. 47 and 48, we also use the expression for the static pressure in the following form,

$$\bar{p}_{so} = -\frac{|\Delta V_2| h}{0.49 a g p_0 c H} \mathbf{a} \quad (51)$$

The above equation is obtained from Eqs. 18 and 40,  $\Delta p = p_s - p_0$ , and the value of  $|dV_2|$  at peak of  $V_2$  which corresponds to  $\sin 2\bar{\mathbf{p}} = 1$ . Note that in Eq. 51  $\bar{p}_{so}$  is only related to  $\mathbf{a}$  because the coefficient terms including fluid compressibility are known. The unknowns are  $c_f$ , mobility  $\mathbf{I} (\mathbf{I} = k / \mathbf{m})$ , and  $\bar{p}_{so}$ . There are also three equations to solve for these three unknowns.

One may provide  $\mathbf{x}$ ,  $\mathbf{a}$ , and  $|\Delta V_2|$ . Then  $\bar{p}_{so}$  is estimated from Eq. 51 followed by the solution of Eqs. 47 and 48 for  $\mathbf{d}$  and  $b$ . As a result, the well pressure  $\bar{p}_{well}$  is determined. For the evaluation of pressure test data, the inverse problem is of interest. In other words, given  $|dV_2|$ , the phase lag  $\mathbf{d}$  and the observed amplitude  $b\bar{p}_{so}$ , it is desired to estimate the mobility ( $k / \mathbf{m}$ ), the total compressibility, and the amplitude of  $\bar{p}_s$ . The solution of nonlinear Eqs. 47, 48, and B-6 (Appendix B) provides these parameters. The parameters  $A_r$  and  $A_i$  for the inverse problem should be obtained from Eqs. B-2 and B-5 in Appendix B.

### Radius of Investigation

It is of interest to estimate the influence of the permeability on fluid flux as a function of distance from the wellbore. Regions further from the wellbore are expected to exert less influence in determining the perturbation observed to the static pressure

One may estimate the radius of influence by computing the maximum flow rate over time at different distances from the wellbore. The maximum flow rate is obtained by taking the derivative with respect to time and setting it to zero. Note that this also provides the minimum, but since only the absolute magnitude of this quantity is important, this is the same as the maximum if sinusoidal excitations are considered. The expression for the magnitude of the flux is

$$|q_r| = \left( \frac{k}{\mathbf{m}} \right) \left| \frac{\partial \bar{p}_i}{\partial \bar{r}} \right| = \left( \frac{k}{\mathbf{m}} \right) \left| \frac{\partial \bar{p}}{\partial \bar{r}} \right| \quad (52)$$

From Eqs. 34 and 52,

$$|q_r| = \left( \frac{k}{\mathbf{m}} \right) \left[ \left( (-A_i \ker'(\mathbf{x}\bar{r}) + A_r \text{kei}'(\mathbf{x}\bar{r})) \sin 2\bar{\mathbf{p}} + (A_r \ker'(\mathbf{x}\bar{r}) + A_i \text{kei}'(\mathbf{x}\bar{r})) \cos 2\bar{\mathbf{p}} \right) \mathbf{x} \right] \quad (53)$$

Note that only the radially dependent perturbation pressure appears, since the static pressure is only a function of time. Computing the derivative of Eq. 53 with respect to time  $\bar{t}$  and setting it equal to zero gives

$$\bar{t} = \frac{1}{2p} \arctan \frac{-A_i \ker'(\mathbf{x}\bar{r}) + A_r \operatorname{kei}'(\mathbf{x}\bar{r})}{+A_r \ker'(\mathbf{x}\bar{r}) + A_i \operatorname{kei}'(\mathbf{x}\bar{r})} \quad (54)$$

Eq. 54 may be evaluated by using the value of  $A$  obtained as a function of  $\mathbf{a}$  and  $\mathbf{x}$ . The value of  $\bar{t}$  at which the maximum flow occurs may then be substituted into Eq. 53, giving the maximum flow rate over time as a function of  $\bar{r}$ .

## Results

Fig. 4 shows the phase lag and amplitude factor as a function of  $\mathbf{x}$  for  $\mathbf{a} = 200$ ; the phase lag is not appreciable below  $\mathbf{x} = 0.01$ . The amplitude factor is also close to one for  $\mathbf{x} < 0.01$ . At  $\mathbf{x} = 0.1$ , there is a appreciable increase of phase lag from the value at  $\mathbf{x} = 0.01$ . The amplitude factor decreases drastically for  $\mathbf{x} = 0.1$  and for  $\mathbf{x} > 0.1$ . Approximate values for  $\mathbf{x}$  and  $\mathbf{a}$  for the two field examples (Figures 1 and 2) are of the order of  $10^{-3}$  and 100, respectively. With these parameters, a large phase cannot be expected (exact basic data for the calculation of  $\mathbf{x}$  and  $\mathbf{a}$  are not available for the two reservoirs). Because the data in Fig. 1 show a phase lag of 12 hours, one should investigate other factors including surface temperature fluctuations.

Figure 5 shows the phase lag and amplitude factor for  $\mathbf{a} = 5000$ . A trend similar to that in Fig. 4 is observed.

Fig. 6 shows the maximum flow rate vs. dimensionless distance  $\bar{r}$  from the wellbore. The maximum flow rate is made dimensionless by dividing it by the maximum flow rate at  $\bar{r} = 1$ . Note that the radius of investigation is small – of the order of several wellbore radius.

## Concluding Remarks

We have formulated and solved for the flow in a reservoir around the wellbore due to the gravitational potential variation. The formulation may allow the estimation of permeability by varying the production interval in a well.

In order to examine the proposed model, there is need to have data with perforation interval known. These data are not currently available to us. We are planning to seek such data from the industry.

There is the possibility that surface temperature variation affects the pressure variation due to extreme sensitivity of thermal expansion on temperature. Because of the phase lag between the gravitational potential variation and the surface temperature variations, it is likely that the phase lag in the wellbore pressure is affected by surfaced temperature variation. We are currently studying this effect.

## Acknowledgements

This work was supported by the National Petroleum Technology Office (NPTO) of US DOE grant DE-FG26-99BC15177 and the oil company members of the Reservoir Engineering Research Institute (RERI).

## References

1. Chang, Eric, and Firoozabadi, A.: "Gravitational Potential Variations of the Sun and Moon for Estimation of Reservoir Compressibility," SPE Journal (December 2000) 5, 456.
2. Moreland, L. W. and Donaldson, E. C.: "Correlation of Porosity and Permeability of Reservoirs with Well Oscillations Induced by Earth Tides," Geophys. J. R. Astron. Soc. (1984) 79, 705.
3. Rehbindler, G.: "Theory of Groundwater Tide. A Basis for Measurement of Large-scale Hydraulic Properties of Bedrock," to appear in Water Resources Research.
4. Furnes, G. K., Kvamme, O. B., and Nygaard, O.: "Tidal Response on the Reservoir Pressure at the Gullfaks Oil Field," PAGEOPH (1991) 135, 421.
5. Hemala, M. L., and Balnaves, C.: "Tidal Effect in Petroleum Well Testing," paper SPE 14607 presented at the Offshore East Asia Conference and Exhibition, Singapore, 28-31 January, 1986.
6. Arditty, P. C., Ramey, H. Jr., and Nur, A. M.: "Response of a Closed Well-Reservoir System of Stress Induced by Earth Tides," paper SPE 7484 presented at the 1978 SPE ATCE, Houston, 1-3 October, 1978.
7. Bodvarsson, G.: "Confined Fluids as Strain Meters," J. Geophys. Res., 10 May 1970, 75, 2711.
8. Takeuchi, H.: "On the Earth Tide of the compressible Earth of Variable Density and Elasticity," Trans. Am. Geophys. Union (1950) 31, 651.
9. Moreland, L. W.: "Earth Tide Effects on Flows in Horizontal Permeable Elastic Layers Connected to Wells," Geophys. J. R. Astr. Soc. (1977) 51, 371.
10. Melchior, P.: The Earth Tides, Pergamon (1966).
11. Deen, W. M.: Analysis of Transport Phenomena, Oxford University Press (1998).
12. Dake, L. P.: Fundamentals of Reservoir Engineering, Elsevier Scientific Publishing Co. 1978.
13. Jacob, Max: "Heat Transfer," John Wiley & Sons, Inc., New York, NY (1949).
14. Spiegelman, M., "Flow in Deformable Porous Media. Part 1 Simple Analysis," J. Fluid Mech, (1993) 247, 13.
15. Bredehoeft, J. D., "Response of well-aquifer systems to Earth Tides," J. Geophys. Res., (1967) 72, 3075.
16. Rosa, A. J. and Horne, R., "Reservoir Description by Well Test Analysis Using Cyclic Flow Rate Variation," paper 22698 presented at the 1991 SPE ATCE, Dallas, 6-9 October, 1978.
17. McLachlan, N. W., Bessel Functions for Engineers, Oxford (1961).
18. Abramowitz, M. and Stegun, I.: "Handbook of Mathematical Functions, Dover Publications, New York (1972).
19. Press, W. H., et. al.: Numerical Recipes, Cambridge University Press (1992).

## Appendix A – Derivation of Paramters $A_r$ and $A_i$ in Direct Solution

Eqs. 47 and 48 are used to calculate the phase lag  $\mathbf{d}$ , and the amplitude factor  $b$ . For that purpose,  $A$  can be separated into its real and imaginary parts,  $A_r$  and  $A_i$ , respectively; that is,  $A = A_r + iA_i$ . We take the imaginary part from Eq. 45 after substituting the expression for  $e^{2pi i} = \cos 2\mathbf{p} + i \sin \mathbf{p}$ . Then equate the coefficients of the cosine and sine terms to obtain

$$\mathbf{x}a[\bar{p}_{so} + A_r \ker \mathbf{x} - A_i \text{kei} \mathbf{x}] = A_r \text{kei}' \mathbf{x} + A_i \ker' \mathbf{x} \quad (\text{A-1})$$

$$\mathbf{x}\mathbf{a}[A_r \text{kei}\mathbf{x} + A_i \text{ker}\mathbf{x}] = -A_r \text{ker}'\mathbf{x} + A_i \text{kei}'\mathbf{x} \quad (\text{A-2})$$

, respectively.

The solution to the above two equations provides  $A_r$  and  $A_i$  given by Eqs. 49 and 50 in the text.

From Eqs. 44 and 46 of the text, Eqs. 47 and 48 are derived.

## Appendix B – Derivation of Parameters $A_r$ and $A_i$ in the Reverse Solution

We will first derive the expression for  $\mathbf{a}$ . From Eq. A-2 ,

$$\mathbf{a} = \frac{A_i \text{kei}'\mathbf{x} - A_r \text{ker}'\mathbf{x}}{\mathbf{x}[A_r \text{kei}\mathbf{x} + A_i \text{ker}\mathbf{x}]} \quad (\text{B-1})$$

From Eqs. 44 and 46,

$$A_r = \frac{\bar{p}_{so}[\text{ker}\mathbf{x}(b \cos \mathbf{d} - 1) + \text{kei}\mathbf{x} \sin \mathbf{d}]}{\text{ker}^2 \mathbf{x} + \text{kei}^2 \mathbf{x}} \quad (\text{B-2})$$

$$A_i = \frac{\bar{p}_{so}[b \text{ker}\mathbf{x} \sin \mathbf{d} + \text{kei}\mathbf{x}(\cos \mathbf{d} + 1)]}{\text{ker}^2 \mathbf{x} + \text{kei}^2 \mathbf{x}} \quad (\text{B-3})$$

Substituting Eqs. B-2 and B-3 into Eq. B-1, one obtains

$$\mathbf{a} = \frac{\sin \mathbf{d}(\text{ker}\mathbf{x} \text{kei}'\mathbf{x} - \text{kei}\mathbf{x} \text{ker}'\mathbf{x}) + ((1/b) - \cos \mathbf{d})(\text{kei}\mathbf{x} \text{kei}'\mathbf{x} + \text{ker}\mathbf{x} \text{ker}'\mathbf{x})}{\mathbf{x} \sin \mathbf{d}(\text{ker}^2 \mathbf{x} + \text{kei}^2 \mathbf{x})} \quad (\text{B-4})$$

From Eqs. 51 and B-4,

$$\begin{aligned} & \frac{\bar{p}_{so}(0.29agcHp_o)}{-h|\Delta V_2|} \\ &= \frac{\sin \mathbf{d}(\text{ker}\mathbf{x} \text{kei}'\mathbf{x} - \text{kei}\mathbf{x} \text{ker}'\mathbf{x}) + ((1/b) - \cos \mathbf{d})(\text{kei}\mathbf{x} \text{kei}'\mathbf{x} + \text{ker}\mathbf{x} \text{ker}'\mathbf{x})}{\mathbf{x} \sin \mathbf{d}(\text{ker}^2 \mathbf{x} + \text{kei}^2 \mathbf{x})} \end{aligned} \quad (\text{B-5})$$

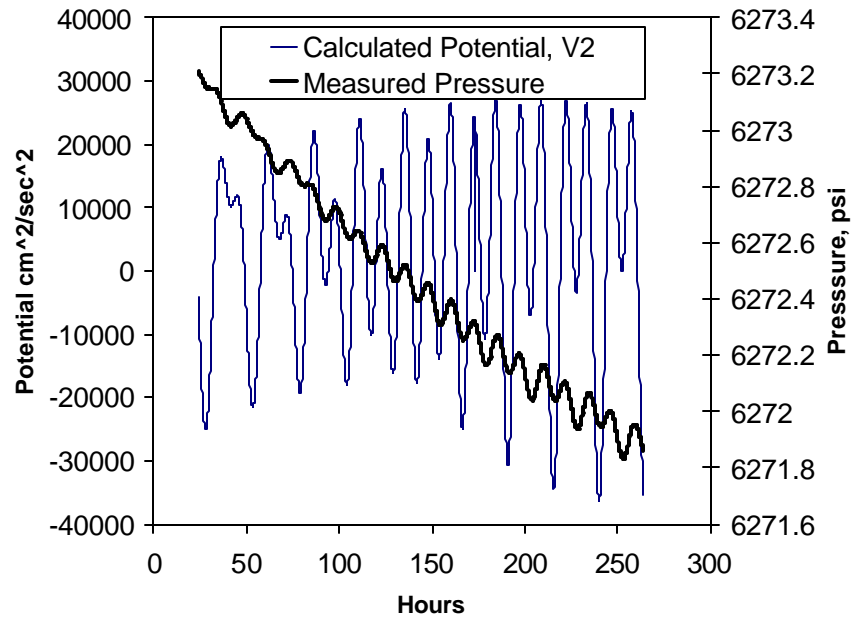


**Figure 1. Observations of the wellbore pressure in the Italian field. The phase lag appears to be nearly 12 hours.**

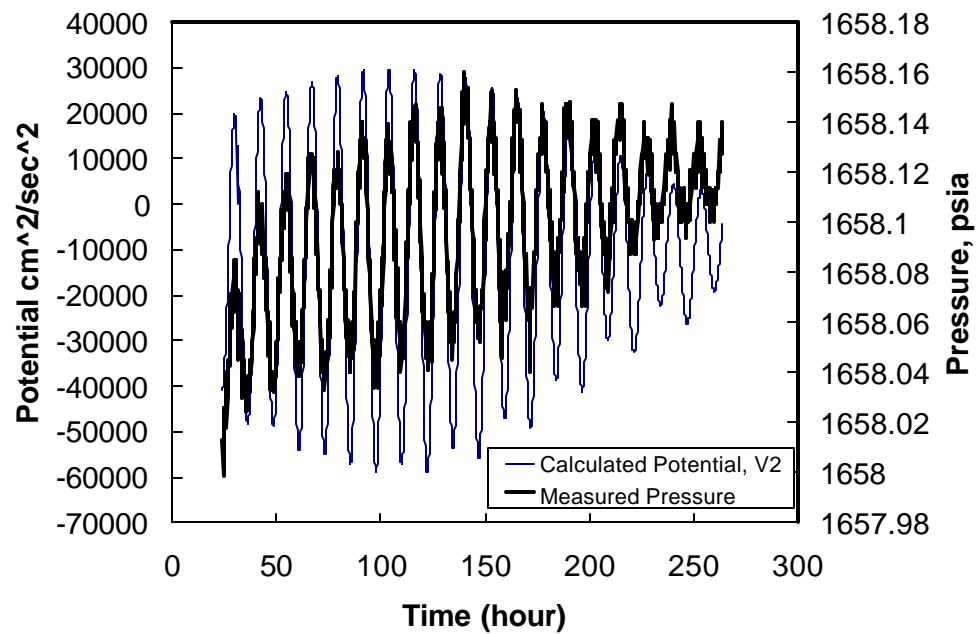


**Figure 2. Observations of the wellbore pressure in the Colombian field. Note the evidence of high mobility in the near absence of phase lag between the potential excitation and the wellbore pressure response.**



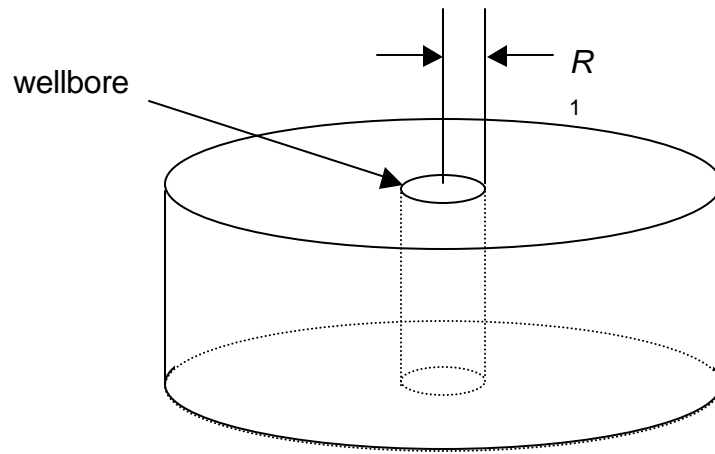


**Figure 3. Problem domain: radial axisymmetric system centered about the wellbore with radius  $R_1$ . The region outside the wellbore is filled with a dilatating porous medium with porosity  $f$  and permeability  $k$ .**

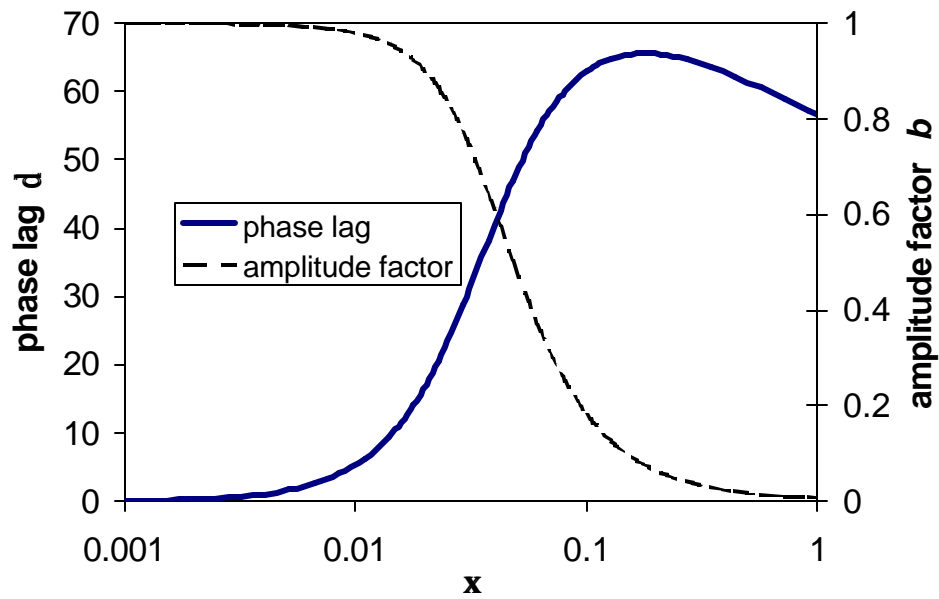


**Figure 4. Phase lag and amplitude factor  $b$  vs. the Fourier number  $x$  for  $a = 200$ .**

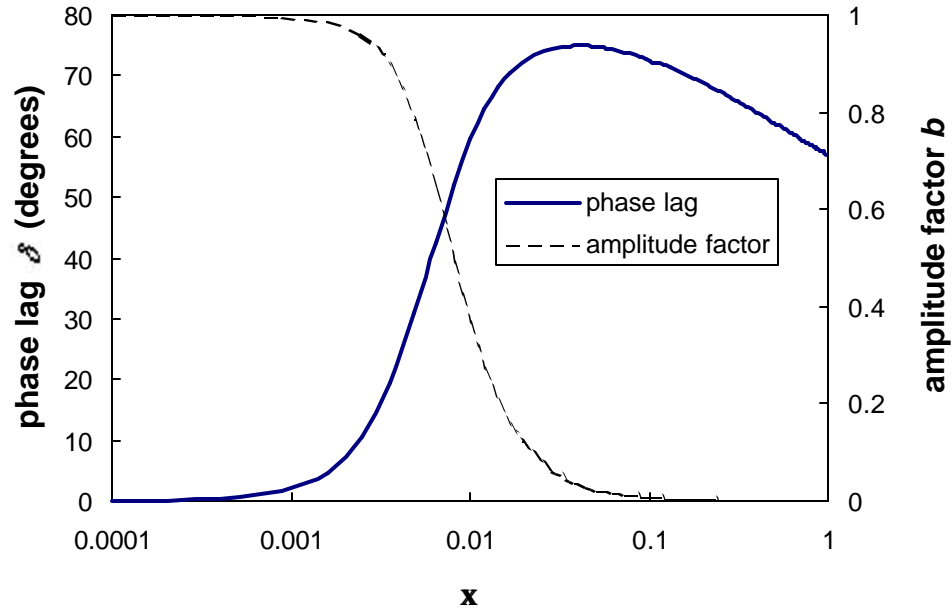


Figure 5. Phase lag  $d$  and amplitude factor  $b$  vs. the Fourier number  $x$  for  $a = 5000$

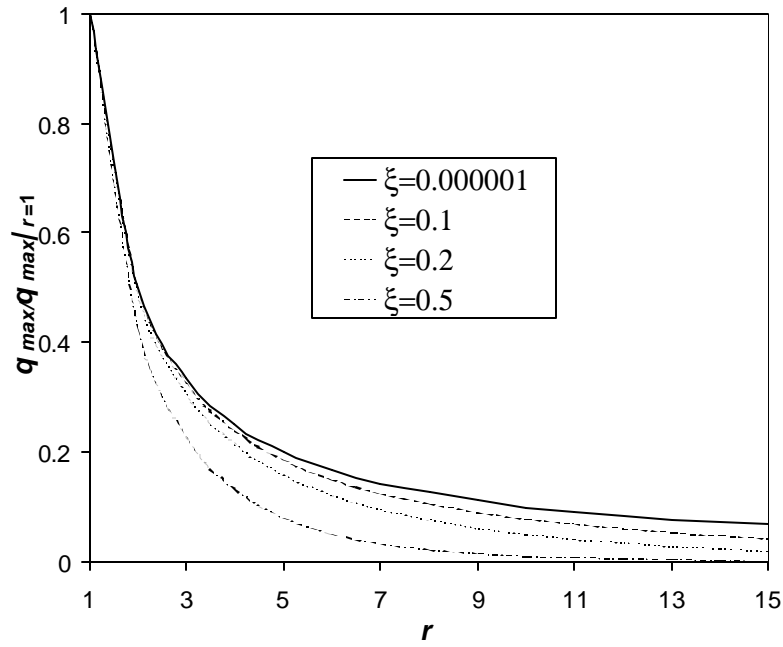


Figure 6. The ratio of the maximum flow rate to the maximum of the flow rate at  $r = 1$  vs.  $r$  for different values of  $x$ :  $a = 200$ .

# **Chapter III - Diffusion in Porous Media from Irreversible**

## **Thermodynamics**

### **Part I- TWO-PHASE MULTICOMPONENT DIFFUSION AND CONVECTION FOR RESERVOIR INITIALIZATION**

KASSEM GHORAYEB AND ABBAS FIROOZABADI

#### **Abstract**

Initialization of composition, pressure, and fluid distribution is an important element in the numerical simulation of hydrocarbon reservoirs. Currently, initialization is not based on a sound theory.

Hydrocarbon reservoirs in general are not in an equilibrium state mainly because of the geothermal temperature gradient. Temperature gradient produces entropy and, therefore, the criterion of equilibrium cannot be invoked to initialize composition, fluid phase distribution, and pressure. If there exists a gas-oil contact (GOC), one may assume equilibrium only at the interface between gas and oil phases. The gas cap and the oil leg are not in equilibrium.

In this paper, we first present the formulation of the two-phase multicomponent diffusion and convection in porous media. Thermal, pressure, and molecular diffusion are included in the diffusion expression from thermodynamics of irreversible processes. In the recent past, we have worked on a single-phase model of the same problem. The two-phase problem is considerably more complicated, and has not been formulated in the literature to the best of our knowledge.

A model based on the above formulation is used to perform calculations for initialization in two-dimensional cross sections. Numerical examples for a binary mixture of  $C_1/C_3$  with natural convection and diffusion in the two-phases are presented. Results show a pronounced effect of natural convection on species distribution and the location of the GOC. Results also show that two main counter-rotating cells develop at steady state— one cell in the gas region and another one in the oil region.

## Introduction

Proper initialization is an important aspect of reliable reservoir simulations. The use of the Gibbs segregation condition generally cannot provide reliable initialization in hydrocarbon reservoirs. This is due, in part, to the effect of thermal diffusion (caused by the geothermal temperature gradient) which cannot be neglected in most cases; thermal diffusion might be the main phenomenon affecting compositional variation in hydrocarbon reservoirs especially for near-critical gas-condensate reservoirs.<sup>1</sup> On the other hand, the horizontal temperature gradient (which can be significant in some hydrocarbon reservoirs) causes natural convection which might have a significant effect on species distribution.<sup>2</sup> The combined effects of diffusion (pressure, thermal and molecular) and natural convection on compositional variation in multicomponent mixtures in porous media have been recently investigated for single-phase systems.<sup>3,4</sup> The results from Refs. 3 and 4 show the importance of natural convection which, in some cases, overrides diffusion and results in a uniform composition.

Ref. 1 provides a robust model for convection-free compositional variation accounting for pressure, thermal and molecular diffusion in two-phase hydrocarbon reservoirs. The combined effects of convection and diffusion in two-phase hydrocarbon reservoirs has not yet, however,

been studied to the best of our knowledge. In this work, we present the mathematical model for convection and diffusion in two-phase multicomponent mixtures. We then discuss results for a binary mixture of  $C_1/C_3$ . The work on multicomponent mixtures is currently in progress and will be reported later.

## Mathematical Formulation

The mass conservation for component  $i$  in a two-phase,  $n$ -components mixture in an arbitrary volume  $V$  reads:

$$\frac{d}{dt} \iiint_V \phi \sum_{j=1}^2 S_j c_{ji} dV = \iiint_V q_i dV, \quad i = 1, \dots, n, \quad (1)$$

where  $S_j$ ,  $c_{ji}$ ,  $q_i$  and  $\phi$  are the saturation of phase  $j$ , the molar density of component  $i$  in phase  $j$ , the molar production rate per unit volume of component  $i$ , and the porosity, respectively. The left and right terms of the above expression represent the rate of change of component  $i$  in the system and the total production rate of component  $i$ , respectively;  $j = 1$  and  $2$  denote the vapor (gas) and liquid (oil) phases, respectively. Assuming a time-independent porosity, Eq. 1 can be written as

$$\begin{aligned} \iiint_V \left[ \phi \frac{\partial}{\partial t} \sum_{j=1}^2 (S_j c_{ji}) + \phi \nabla \cdot \sum_{j=1}^2 (S_j c_{ji} \mathbf{v}_{ji}) - q_i \right] dV \\ = 0, \quad i = 1, \dots, n, \end{aligned} \quad (2)$$

where  $\mathbf{v}_{ji}$  is the velocity of component  $i$  in phase  $j$ . Let  $\mathbf{n}_i = \sum_{j=1}^2 (S_j c_{ji} \mathbf{v}_{ji})$ ;  $\mathbf{n}_i$  is the total molar flux of component  $i$ . The bulk velocity,  $\mathbf{v}_j$ , of phase  $j$  is defined as

$$S_j c_{ji} \mathbf{v}_{ji} = c_{ji} \mathbf{v}_j + S_j \mathbf{J}_{ji}, \quad i = 1, \dots, n, \quad (3)$$

where  $\mathbf{J}_{ji}$  is the molar diffusive flux (molecular, pressure, and thermal) based on the molar average velocity of component  $i$  in phase  $j$ ;  $\mathbf{n}_i$  can be, thus, written as:

$$\mathbf{n}_i = \sum_{j=1}^n (c_{ji}\mathbf{v}_j + S_j\mathbf{J}_{ji}), \quad i = 1, \dots, n, \quad (4)$$

From Eqs. 2 and 4, the local form of the mass conservation of component  $i$  reads

$$\begin{aligned} \phi \frac{\partial}{\partial t} \sum_{j=1}^2 (S_j c_{ji}) + \phi \nabla \cdot \sum_{j=1}^2 (c_{ji}\mathbf{v}_{ji} + S_j\mathbf{J}_{ji}) - q_i \\ = 0. \quad i = 1, \dots, n. \end{aligned} \quad (5)$$

In terms of the mole fraction,  $x_{ji}$ , of component  $i$  in phase  $j$ , Eq. 5 can be written as:

$$\begin{aligned} \phi \frac{\partial}{\partial t} \sum_{j=1}^2 (S_j c_j x_{ji}) + \phi \nabla \cdot \sum_{j=1}^2 (c_j x_{ji}\mathbf{v}_j + S_j\mathbf{J}_{ji}) - q_i \\ = 0, \quad i = 1, \dots, n, \end{aligned} \quad (6)$$

where  $c_j$  is the molar density of phase  $j$ . By summing Eqs. 6 for  $i = 1, \dots, n$ , and using

$$\sum_{i=1}^n x_{ji} = 1, \quad j = 1, 2, \quad (7)$$

the total mass conservation expression is given by:

$$\phi \frac{\partial}{\partial t} \sum_{j=1}^2 (S_j c_j) + \phi \nabla \cdot \sum_{j=1}^2 (c_j \mathbf{v}_j) - q = 0, \quad (8)$$

where  $q$  is the total molar production rate ( $q = \sum_{i=1}^n q_i$ ).

The bulk velocity of phase  $j$ ,  $\mathbf{v}_j$ , is given by Darcy's law:

$$\mathbf{v}_j = -\frac{k k_j^r}{\phi \mu_j} (\nabla p + \rho_j g \mathbf{z}), \quad j = 1, 2, \quad (9)$$

where  $p$ ,  $g$ ,  $k$ ,  $k_j^r$ ,  $\mu_j$ , and  $\rho_j$  are the pressure, the acceleration due to gravity, the permeability, the relative permeability of phase  $j$ , the viscosity of phase  $j$ , and the mass density of phase  $j$ ,

respectively. Note that Eq. 9 is valid when capillary pressure is neglected. The total molar density  $c$  can be expressed by:

$$c = \sum_{j=1}^2 (S_j c_j), \quad (10)$$

Using Eqs. 9 and 10, Eqs. 6 and 8 can be written as

$$\begin{aligned} \phi \frac{\partial (cz_i)}{\partial t} - \nabla \cdot \sum_{j=1}^2 \frac{c_j k k_j^r x_{ji}}{\mu_j} (\nabla p + \rho_j g \mathbf{z}) + \\ \nabla \cdot \sum_{j=1}^2 S_j \mathbf{J}_{ji} = q_i, \quad i = 1, \dots, n, \end{aligned} \quad (11)$$

and

$$\phi \frac{\partial c}{\partial t} - \nabla \cdot \sum_{j=1}^2 \frac{c_j k k_j^r}{\mu_j} (\nabla p + \rho_j g \mathbf{z}) = q, \quad (12)$$

respectively. In Eq. 11,  $z_i$  is the overall composition of component  $i$ ;  $cz_i = \sum_{j=1}^2 S_j c_j x_{ji}$ . The term  $\nabla \cdot \sum_{j=1}^2 S_j \mathbf{J}_{ji}$  represents the contribution of diffusion to the mass transfer in a multi-component mixture. It is often neglected in the numerical simulation of production processes (forced convection). However, the diffusion flux can be the key transport process in reservoir initialization.

The local equilibrium condition implies the equality of the fugacities of each component in the two phases:

$$\begin{aligned} f_{1i} (T, p, x_{11}, \dots, x_{1(n-1)}) = \\ f_{2i} (T, p, x_{22}, \dots, x_{2(n-1)}) \cdot i = 1, \dots, n, \end{aligned} \quad (13)$$

The following saturation constraint completes the problem formulation given by Eqs. 11, 12, and 13:

$$\sum_{j=1}^2 S_j = 1. \quad (14)$$

This equation can be written as:

$$1 - c \left[ \frac{\alpha}{c_1} + \frac{1 - \alpha}{c_2} \right] = 0, \quad (15)$$

where  $\alpha$  is the mole fraction of phase 1.

The above formulation applies for the general case of a three-dimensional domain. In this paper, we focus on a 2D vertical rectangular porous medium of width  $b$  and height  $h$  (Fig. 1). We assume that the temperature varies linearly in both horizontal and vertical directions, that is,  $T = T_x x + T_z z + a$ , where  $T_x$  and  $T_z$  are the temperature gradients in the horizontal and vertical directions, respectively. If we set the temperature at  $x = x_0$  and  $z = z_0$  equal to  $T_0$ , then,  $T = T_x (x - x_0) + T_z (z - z_0) + T_0$ .

**Boundary/Initial Conditions.** Appropriate boundary and initial conditions are required to complete the two-phase multicomponent formulation. The cross section is assumed to be bounded by an impervious rock so that the total mass flux for all the components vanish at the boundaries:

$$\sum_{j=1}^n (c_j x_{ji} \mathbf{v}_j + S_j \mathbf{J}_{ji}) \cdot \mathbf{n} = 0, \quad i = 1, \dots, n, \quad (16)$$

$$x = 0, \quad b, \quad \text{and} \quad z = 0, \quad h.$$

where  $\mathbf{n}$  is the normal vector. Eq. 16 provides the boundary conditions necessary to integrate the total mass conservation equation (Eq. 11). Because  $\sum_{i=1}^n \mathbf{J}_{ji} = 0, j = 1, 2$ , one obtains the following boundary condition necessary to integrate Eq. 12:

$$\sum_{j=1}^n c_j \mathbf{v}_j \cdot \mathbf{n} = 0, \quad x = 0, \quad b, \quad \text{and} \quad z = 0, \quad h, \quad (17)$$

Various initial conditions can be used in the above formulation. One can start, for instance, with a constant overall composition (either in single-phase or in two-phase) and constant pres-



sure in the entire 2D cross-section. One can also use a specified composition and pressure at a single point to obtain the convection-free (that is zero permeability) composition and pressure distribution using the model presented in Ref. 1 (a summary of the model is provided in Appendix). Once the convection-free field is obtained, one can investigate the effect of convection on the phase composition and the GOC location and, therefore, obtain an initial state for reservoir simulation taking into account both diffusion and natural convection. The example presented in this paper uses the latter approach for setting the initial conditions .

**Diffusion Flux.** The expression for diffusion flux of component  $i$ ,  $i = 1, \dots, n - 1$ , in phase  $j$ ,  $j = 1, 2$  is given by:

$$\mathbf{J}_j = -c_j (\mathbf{D}_j^M \cdot \nabla \mathbf{x} + \mathbf{D}_j^T \nabla T + \mathbf{D}_j^P \nabla P) . \quad (18)$$

where  $\mathbf{D}_j^M \equiv [D_{jik}]$ ,  $\mathbf{D}_j^T \equiv [D_{ji}^T]$ ,  $\mathbf{D}_j^P \equiv [D_{ji}^P]$ , and  $\nabla \mathbf{x} \equiv [\nabla x_{ji}]$ .  $D_{jik}^M$ ,  $D_{ji}^T$ , and  $D_{ji}^P$  are the molecular diffusion coefficients, the thermal diffusion coefficients, and the pressure diffusion coefficients, respectively. Details of the diffusion coefficients are provided in Refs. 5 and 6. The above diffusion coefficients are, in general, different for gas and liquid phases. In this work, we assume that the diffusion coefficients of a given phase depend only of the thermophysical properties of that phase; it is as if the phase was alone. Note that at steady state, there is a complete phase segregation (with no capillary pressure).

## Method of Solution

The above  $2n + 1$  equations: Eqs. 11 through 14 (15), with  $2n + 1$  unknowns:  $p$ ,  $c$ ,  $\alpha$ ,  $z_i$ ,  $i = 1, \dots, n - 1$ , and  $x_{1i}$ ,  $i = 1, \dots, n - 1$ , and the corresponding initial and boundary

conditions, govern the multicomponent two-phase flow in porous media. The molar production rate,  $q$ , is accounted for by considering it as a source (sink) in the appropriate meshes (corresponding to the perforation interval). These equations are solved following Young and Stephenson<sup>7</sup> with some differences. In our work, the updated values of  $\alpha$  and  $x_{1i}, i = 1, \dots, n-1$  are calculated directly from the flash instead of calculating them using the appropriate linearized equations after calculating the pressure increment in a Newton iteration as described by Young and Stephenson. Phase recognition which is an important part of the simulation is performed by a systematic decrease (or increase) of pressure to establish the saturation pressure. Phase equilibrium calculations are performed using a combination of the successive substitution method and the Newton method. The diffusion term  $\nabla \cdot \sum_{j=1}^2 S_j \mathbf{J}_{ji}$  in Eq. 11 is accounted for explicitly in order to conserve the pentadiagonal structure of the matrix for inversion in each Newton iteration for pressure calculations.

The pressure and concentration gradients are discontinuous at a two-phase interface. For this reason, matching boundary conditions are required at the interface (based on the continuity of the diffusive and convective mass fluxes and pressure, and the thermodynamic equilibrium condition at the interface). In this study we do not fulfill this condition; we attenuate it with appropriate upstream weighting which may affect the accuracy of results in a narrow region near the interface.

A sound numerical technique for the solution of a moving interface problems with pure components is a moving grid and matching grid boundaries at the interface.<sup>8</sup> This technique requires a new grid to be defined at each computational step which is very expensive and even not practical for large scale two-phase natural convection in multicomponent mixtures.

## Example: Binary Mixture

Let us consider a 2D vertical rectangular porous medium of width 1000m and height 200m saturated with a binary mixture of  $C_1/C_3$ . The vertical and horizontal temperature gradients are  $-3\text{K}/100\text{m}$  and  $1.5\text{K}/\text{km}$ , respectively. We have performed calculations for three permeabilities:  $k = 0.01, 0.1$ , and  $1 \text{ md}$ . The Peng-Robinson equation of state<sup>9</sup> is used to calculate the density. The porosity is set to 20% and the viscosity is calculated using the correlation of Lohrenz *et al.*<sup>10</sup> The purpose of the calculations is to investigate the combined effect of diffusion and convection on compositional variation and GOC location for the binary mixture. We neglect thermal diffusion in this example to focus on the study of the unsteady two-phase convective flow with molecular and pressure diffusion.

The gridding considered in this example is  $101 \times 41$ ; the time step varies with permeability; it is of the order of  $10^7$  days for  $k = 0.01 \text{ md}$ . At time step  $m$  we perform flash calculations for the mesh points that are in the two phase region at time step  $m - 1$  as well as the neighboring mesh points. This drastically reduces the computational cost. Furthermore, the phase recognition is performed only at the first time step. If the mixture at a mesh point is in single-phase at time step  $m - 1$  and remains single-phase at time step  $m$ , we assume that no phase change has occurred during this step for that mesh point. If the mixture is in single-phase at time step  $m$  while it was two-phase at time step  $m - 1$  with higher gas (liquid) saturation; the mixture is, thus, gas (liquid) at time step  $m$ . This procedure was extensively tested (in our example) by comparing the results with those obtained with flash calculation and phase recognition for all the mesh points at each time step in the entire domain.

The initial condition for this example is selected to be the convection-free state which is obtained using the model described in Ref. 1. The convection-free solution is obtained based on

a reference point (located at the center of the cavity:  $x = 500\text{m}$ ,  $z = 100\text{m}$ ). At the reference point, the composition, temperature and pressure are set at:  $20\%C_1/80\%C_3$ ,  $T = 346\text{K}$ , and  $p = 57.5$  bar (slightly above the bubblepoint pressure, see Fig. 2). The reason for the choice of the pressure close to the bubblepoint pressure is to allow for the GOC to be near  $z = 100\text{m}$  for  $x = 500\text{m}$  (the middle of the cavity).

The calculations are first performed for  $k = 0.01$  md. The results for  $k = 0.01$  md at steady state are used to perform the calculation for  $k = 0.1$  md. A similar procedure is used for  $k = 1$  md. The steady state is considered to be reached when the difference of compositions in any point of the cavity does not change from one time step to another within a given tolerance. Fig. 3 presents the methane composition vs. time at  $x = 100\text{m}$ ,  $z = 50\text{m}$  for  $k = 0.01$ ,  $k = 0.1$  and  $k = 1$  md showing the evolution of the steady state.

Fig. 4 shows liquid saturation plots for different permeabilities at steady state. Note that, due to the horizontal temperature gradient, the GOC is not horizontal for the convection-free case; the gas leg is thicker near the hot vertical wall (left side) of the cavity. Results from this example show that natural convection has an important effect on the GOC. A small amount of convection (for  $k = 0.01$  md) affects significantly the GOC location. Due to convection, the GOC is almost horizontal at  $k = 0.01$  md. This is clearly shown in Fig. 5 where one observes that the 15m-difference between the GOC location in the left and right sides has disappeared due to natural convection. However, there is no further effect when the permeability increases from 0.01 to 1 md.

Figs. 6 and 7 show the methane mole fraction vs. depth for different permeabilities at two different sections:  $x = 100$  m (near the cold side) and  $x = 500$  m (the middle of the cavity). As shown in Fig. 6, the liquid leg is thicker for the convection-free case; it becomes almost

constant in the entire 2D section with a small amount of convection. However, composition is not significantly affected by natural convection as shown in Figs. 6 and 7.

Fig. 8 shows the velocity contours at steady state. There two main counter-rotating cells in the liquid and gas regions as shown in Fig. 8. Note that for  $k=0.01$  md, there are two cells in the main cell in the gas region. Fig. 9 depicts in more detail the horizontal velocity of both phases vs. depth at  $x = 500$ m for different permeabilities. There is an increase of velocity as the permeability increases. For all three permeabilities, the horizontal velocity increases in the gas phase is greater than the horizontal velocity in the liquid phase as expected.

## Discussion and Conclusions

A model for two-phase multicomponent diffusion and convection in porous media is presented. Results for the binary mixture of  $C_1/C_3$  show the importance of natural convection on the GOC in a non-isothermal medium with no thermal diffusion. Due to natural convection, the GOC is almost horizontal in the entire 2D cross-section. A weak natural convection (that is the case with  $k = 0.01$  md) has an important effect on the phase distribution. Results also show that two main rotating cells develop— one in the gas region and the other in the oil region.

In the example presented in the paper, the thermal diffusion effect is excluded. Thermal diffusion is likely to have a significant effect on GOC, especially when the critical region is approached. The effect of thermal diffusion, and field examples are being studied. The results will be presented in the future.

We believe the model presented in this paper will set the stage for the proper initialization of hydrocarbon reservoirs where the non-equilibrium effects are often important.

## Nomenclature

$b$	= reservoir width, m
$c_{ji}$	= molar density of component $i$ in phase $j$ , mole/m <sup>3</sup>
$c_j$	= molar density of phase $j$ , mole/m <sup>3</sup>
$c$	= total molar density, mole/m <sup>3</sup>
$D_{ij}^M$	= molecular diffusion coefficient, m <sup>2</sup> /s
$D_i^p$	= pressure diffusion coefficient, m <sup>2</sup> /s.Pa
$D_i^T$	= thermal diffusion coefficient, m <sup>2</sup> /s.K
$\mathbf{J}_i$	= molar diffusive flux of component $i$
$f_{ji}$	= fugacity of component $i$ in phase $j$ , Pa
$h$	= reservoir hight, m
$g$	= acceleration of gravity, m/s <sup>2</sup>
$k$	= permeability, m <sup>2</sup>
$k_j^r$	= relative permeability of phase $j$
$n$	= number of components
$\mathbf{n}$	= normal vector
$p$	= pressure, Pa
$q_i$	= molar production rate of component $i$ , mole/s
$q_i$	= total molar production rate, mole/s
$S_j$	= saturation of phase $j$
$T$	= temperature, K
$x, z$	= coordinates,

$x_{ji}$  = mole fraction of component  $i$  in phase  $j$ , dimensionless

$\mathbf{v}_{ji}$  = velocity of component  $i$  in phase  $j$ , m/s

$\mathbf{v}_j$  = bulk velocity of phase  $j$ , m/s

$\phi$  = porosity

$\mu_j$  = viscosity of phase  $j$ , kg/m.s

$\rho_j$  = mass density of phase  $j$ , kg/m<sup>3</sup>

## Acknowledgments

The funding for this work was provided by the members of the Reservoir Engineering Research Institute (RERI) and the US DOE National Petroleum Technology Office (NPTO) grant DE-FG22-96BC14850. Their support is appreciated.

## References

1. Ghorayeb, K., Anraku, T., and Firoozabadi, A.: "Interpretation of the fluid distribution and GOR behavior in the Yufutsu fractured gas-condensate field," paper SPE 59437 presented at the 2000 SPE Asia Pacific Conference on Integrated Modelling for Asset Management, Yokohama, 25-26 April 2000.
2. Firoozabadi A.: "Thermodynamics of Hydrocarbon Reservoirs," Chapter II, Mc Graw-Hill, New York, 1999.
3. Riley M.F. and Firoozabadi A.: "Compositional variation in hydrocarbon reservoirs with natural convection and diffusion," *AIChE J.* (1998) **44**, 452.

4. Ghorayeb, K., and Firoozabadi, A.: “Modeling multicomponent convection and diffusion in porous media,” *SPEJ* (June 2000) 158.
5. Ghorayeb, K., and Firoozabadi, A.: “Molecular, pressure, and thermal diffusion in non-ideal multicomponent mixtures,” *AIChE J.* (May 2000) 883.
6. Firoozabadi, A., Ghorayeb, K., and Shukla, K.: “Theoretical model of thermal diffusion factors in multicomponent mixtures,” *AIChE J.* (May 2000) 892.
7. Young, L. C., and Stephenson, R. E.: “A generalized compositional approach for reservoir simulation,” *SPE J.* (October 1983) 727.
8. Ramesh, P. S., and Torrance, K. E.: “Numerical algorithm for problems involving boiling and natural convection in porous media,” *Num. Heat Transer, Part B* (1990), Vol. 17, 1.
9. Peng, D. Y., and Robinson, D. B.: “A new two-constant equation of state,” *Ind. Eng. Chem. Fund.* (1976), Vol. 15, 59.
10. Lohrentz, J., Bray, B., and Clark, R.: “Calculating viscosities of reservoir fluids from their compositions,” *JPT* (October 1964) 1171.
11. Shukla, K., and Firoozabadi A.: “A new model of thermal diffusion coefficients in binary hydrocarbon mixtures,” *Ind. Eng. Chem. Res.* (1998), Vol. 37, 3331.

## Appendix – Convection-Free Model

We restrict the following presentation to phase  $j$  and omit the subscript  $j$  for the sake of clarity.

The molar diffusion flux based on the molar average velocity,  $\mathbf{J} = \left( \vec{J}_1, \dots, \vec{J}_{n-1} \right)$  in a non-ideal fluid mixture of  $n$  components reads:<sup>5</sup>

$$\mathbf{J} = -c \left( \mathbf{D}^M \cdot \nabla \mathbf{x} + \mathbf{D}^T \cdot \nabla T + \mathbf{D}^P \cdot \nabla P \right). \quad (\text{A-1})$$



Detailed expressions for the above coefficients are provided in Ref. 5. Eq. A-1 can also be written as<sup>5</sup>

$$\begin{aligned} \mathbf{J} = & -c \left( \mathbf{D} \cdot \mathbf{M} \cdot \mathbf{L} \cdot \mathbf{W} \cdot \mathbf{F} \cdot \nabla \mathbf{x} + \frac{M_n x_n}{RT^2} \mathbf{D} \cdot \mathbf{M} \cdot \mathbf{L} \cdot \mathbf{Q} \cdot \nabla T \right. \\ & \left. + \mathbf{D} \cdot \mathbf{M} \cdot \mathbf{L} \cdot \mathbf{V} \cdot \nabla p \right), \end{aligned} \quad (\text{A-2})$$

where  $\mathbf{L} \equiv [L_{ij}]$  is the matrix of the phenomenological coefficients. The symbols in Eq. A-2 are defined by:

$$\begin{aligned} \mathbf{D} & \equiv [D_{ij}] = \left[ \frac{RL_{ii}}{cM_i M_n x_i x_n} \delta_{ij} \right] \quad i, j = 1, \dots, n-1, \\ \mathbf{F} & \equiv [F_{ij}] = \left[ \frac{\partial \ln f_i}{\partial x_j} \bigg|_{\mathbf{x}_j, T, P} \right] \quad i, j = 1, \dots, n-1, \\ \mathbf{M} & \equiv [M_{ij}] = \left[ \frac{M_i x_i}{L_{ii}} \delta_{ij} \right] \quad i, j = 1, \dots, n-1, \\ \mathbf{W} & \equiv [W_{ij}] = \left[ \frac{M_j x_j + M_n x_n \delta_{ij}}{M_j} \right] \quad i, j = 1, \dots, n-1. \end{aligned}$$

In the above expressions,  $R$ ,  $f_i$  and  $\delta_{ij}$  denote the universal gas constant, the fugacity of component  $i$ , and the Kronecker delta, respectively; the subscript  $\mathbf{x}_j$  is defined by  $(x_1, \dots, x_{j-1}, x_{j+1}, \dots, x_{n-1})$ .

The column vector  $\mathbf{Q}$  is given by

$$\mathbf{Q} \equiv \left[ \frac{Q_i^*}{M_i} - \frac{Q_n^*}{M_n} \right] \quad i = 1, \dots, n-1;$$

$Q_i^*$  is the net heat of transport of component  $i$  given by<sup>5</sup>

$$\begin{aligned} Q_i^* = & -\frac{\Delta \bar{U}_i}{\tau_i} + \left[ \sum_{j=1}^n \frac{x_j \Delta \bar{U}_j}{\tau_j} \right] \frac{\bar{V}_i}{\sum_{j=1}^n x_j \bar{V}_j} \\ & i = 1, \dots, n, \end{aligned} \quad (\text{A-3})$$

where  $\Delta \bar{U}_i$  is the partial molar internal energy departure of component  $i$  and  $\tau_i = \Delta U_i^{vap} / \Delta U_i^{vis}$ ;  $\Delta U_i^{vap}$  and  $\Delta U_i^{vis}$  are the energy of vaporization and the energy of viscous flow of pure component

$i$ , respectively.  $\Delta\bar{U}_i$  is calculated using the PR-EOS<sup>9</sup>; the value of  $\tau_i$  used in this work is fixed equal to 4 based on a previous study by Shukla and Firoozabadi.<sup>11</sup> At steady state, the diffusion flux vanishes; Eq. A-2 then reduces to

$$\mathbf{W} \cdot \mathbf{F} \cdot \nabla \mathbf{x} + \frac{M_n x_n}{RT^2} \mathbf{Q} \cdot \nabla T + \mathbf{V} \cdot \nabla P = 0. \quad (\text{A-4})$$

At isothermal conditions, Eq. A-4 reads

$$\mathbf{W} \cdot \mathbf{F} \cdot \nabla \mathbf{x} + \mathbf{V} \cdot \nabla P = 0 \quad (\text{A-5})$$

which provides the condition for thermodynamic equilibrium in an isothermal  $n$  components mixture. Eq. A-4 is integrated using a forward first-order finite difference scheme to calculate composition and pressure in the entire column.<sup>1</sup>

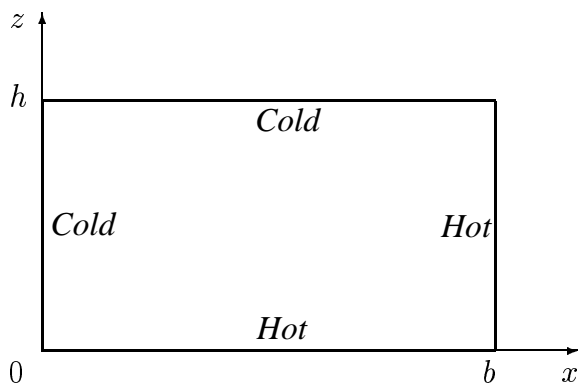


Figure 1: Geometry.

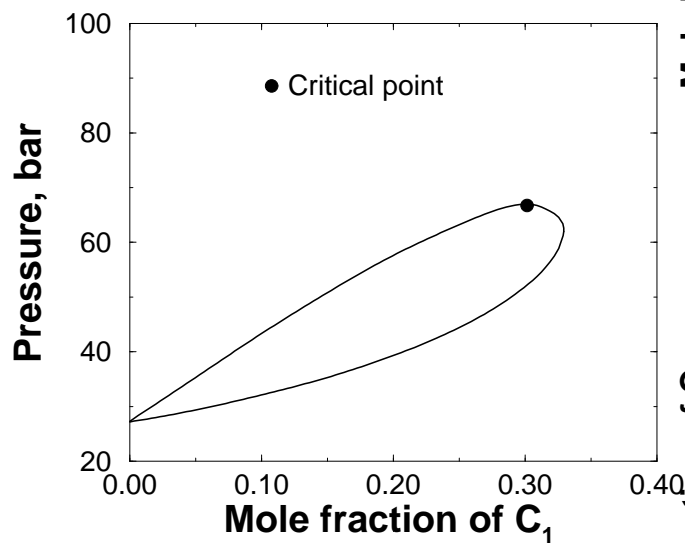


Figure 2: Pressure-composition diagram for  $C_1/C_3$  mixture at  $T = 346\text{K}$ .

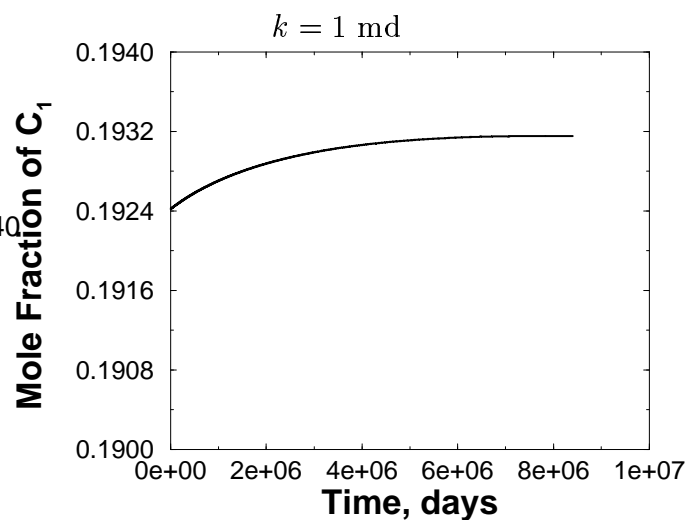
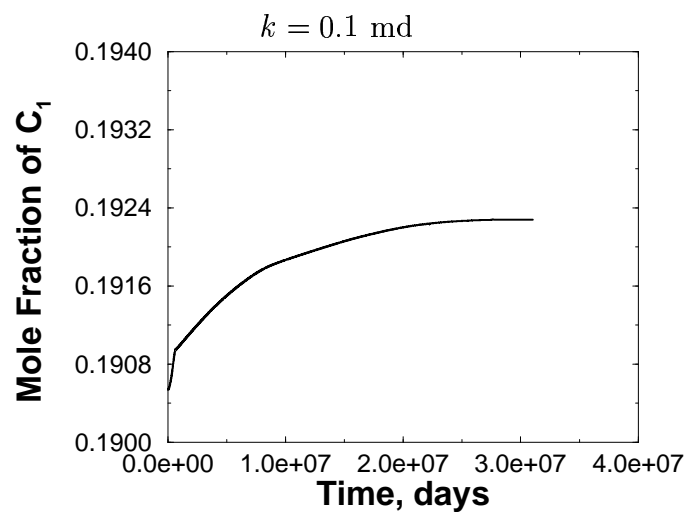
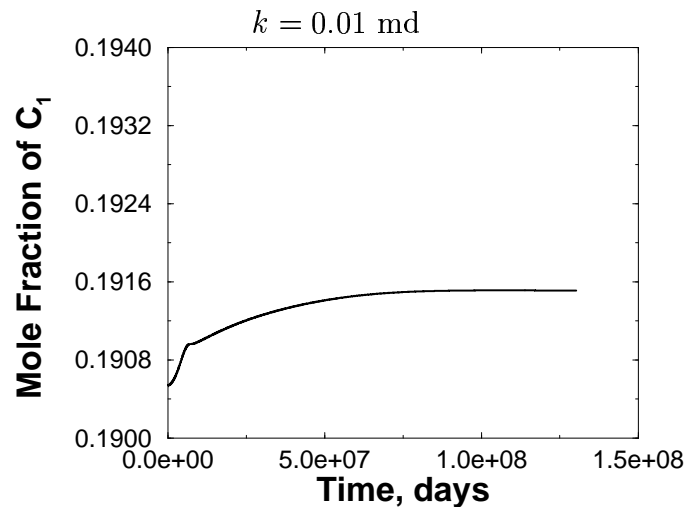


Figure 3: Methane Composition vs. time at  $x = 100$  m,  $z = 50$  m for different permeabilities.

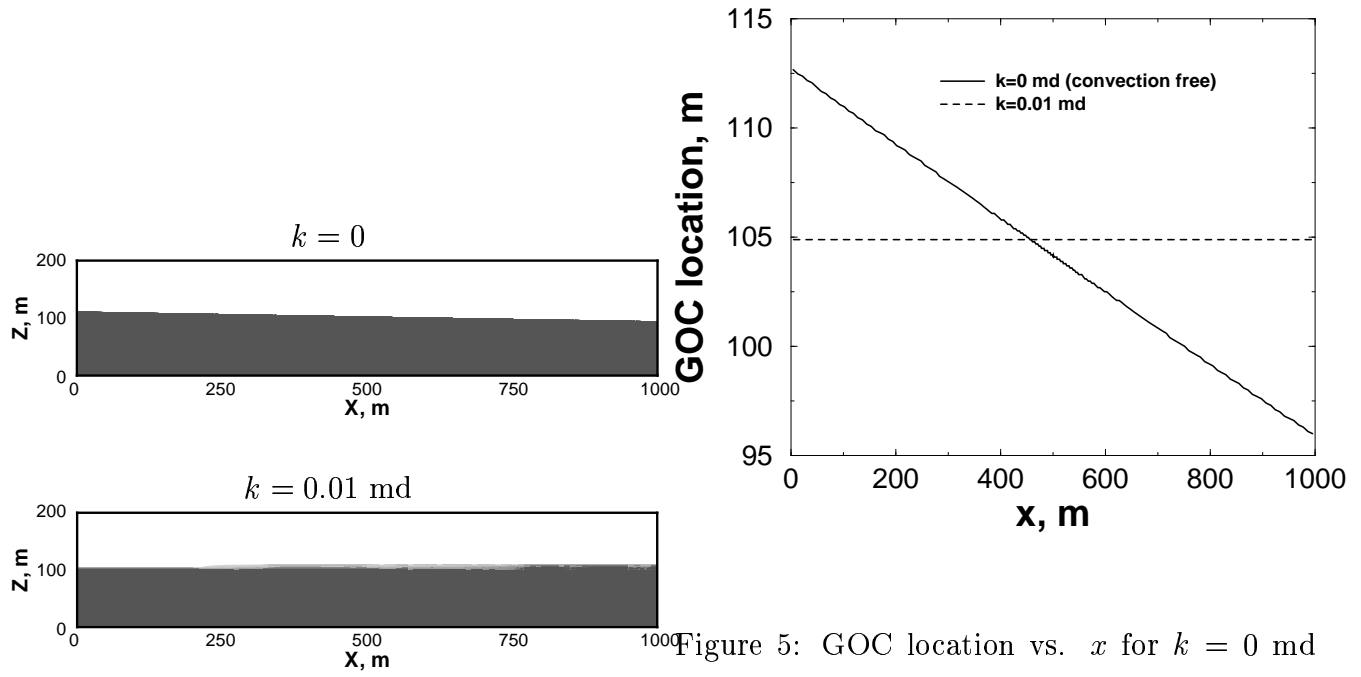


Figure 5: GOC location vs.  $x$  for  $k = 0$  md (convection-free) and  $k = 0.01$  md: steady state

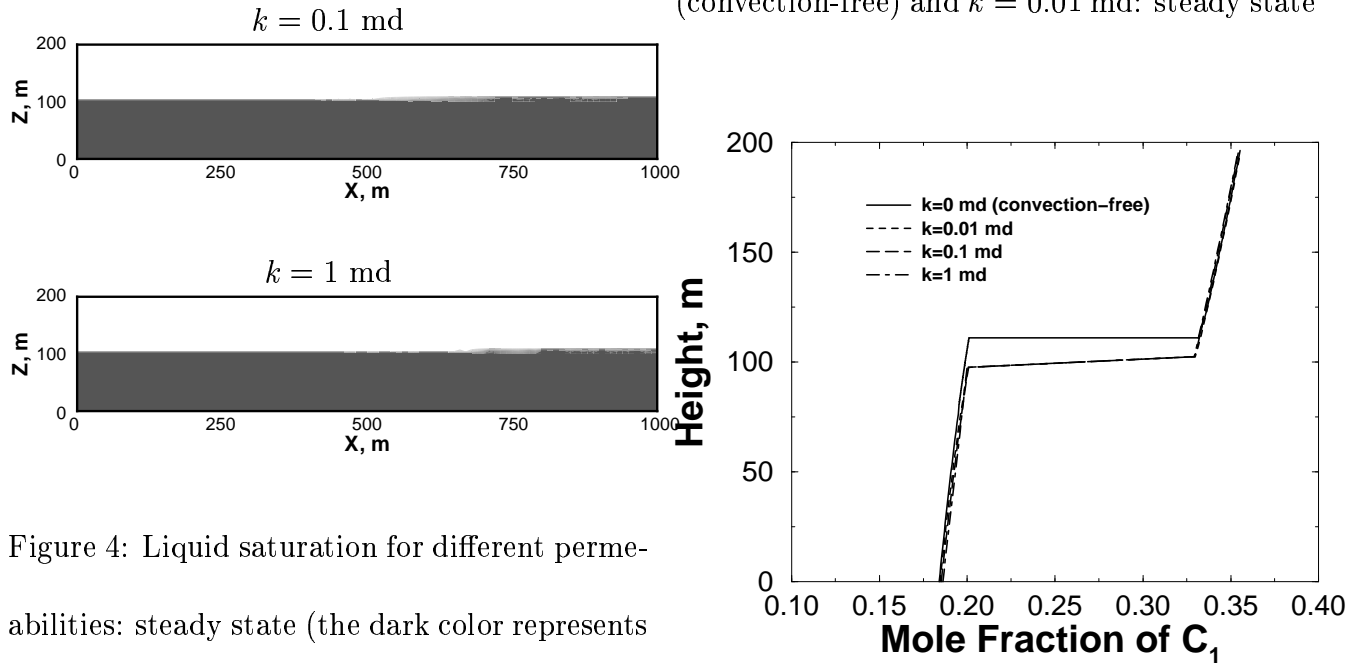


Figure 4: Liquid saturation for different permeabilities: steady state (the dark color represents the liquid phase).

Figure 6: Methane composition vs. depth at  $x = 100$  m in both the gas and liquid columns for various permeabilities: steady state.

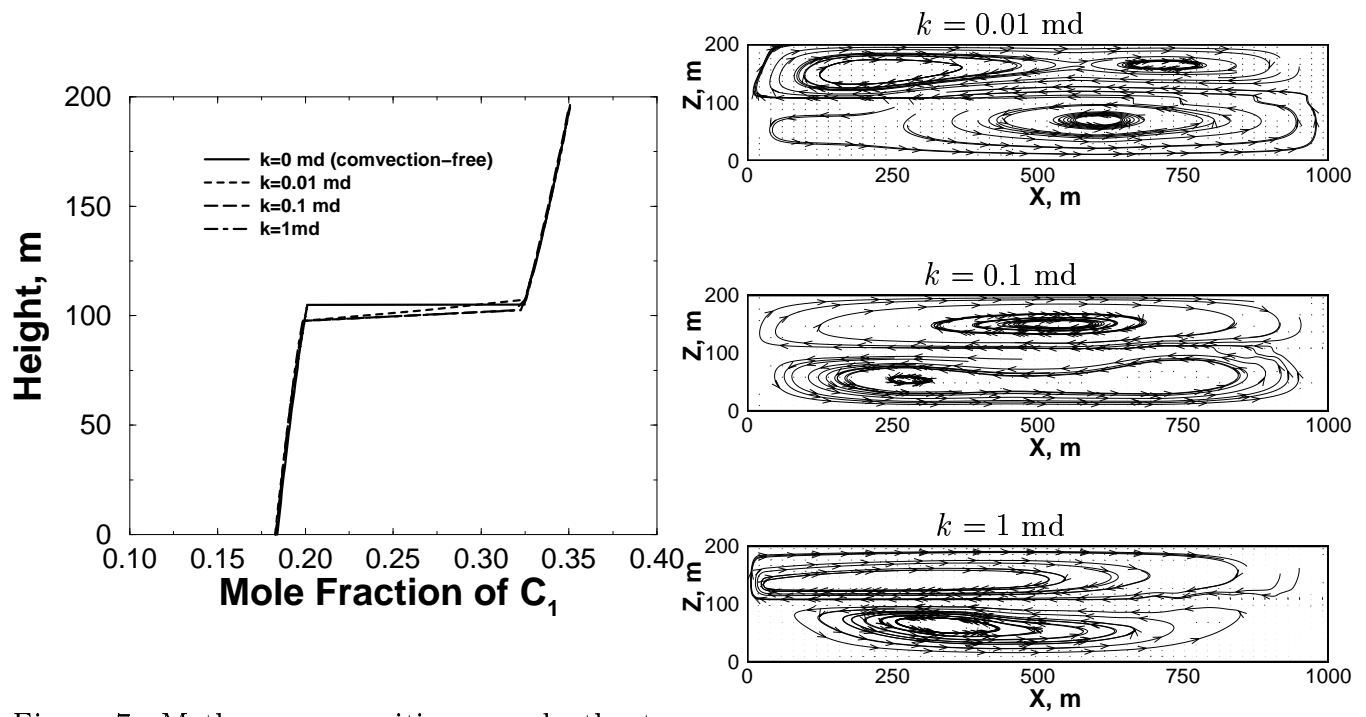


Figure 7: Methane composition vs. depth at

$x = 500$  m in both the gas and liquid columns

for various permeabilities: steady state.

Figure 8: Velocity Contours of the gas and liq-

uid regions for different permeabilities: steady

state.

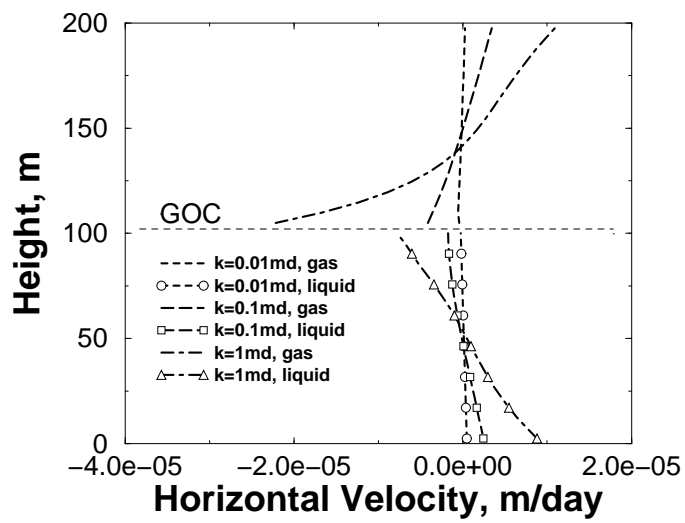


Figure 9: Horizontal velocity vs. depth at  $x =$   
500 m in both the gas and liquid regions for  
three different permeabilities: steady state.

# **Chapter III - Diffusion in Porous Media from Irreversible**

## **Thermodynamics**

### **Part II- Interpretation of the Unusual Fluid Distribution in the Yufutsu**

#### **Gas-Condensate Field**

KASSEM GHORAYEB, ABBAS FIROOZABADI AND TOSHIYUKI ANRAKU

#### **Summary**

It is generally believed that at steady state, a heavy fluid mixture cannot float, without motion, at the top of a light fluid mixture in a cavity. The expectation is that due to pressure diffusion, segregation occurs with the light fluid at the top and the heavy fluid at the bottom. We present, for the first time, an extensive set of measurements in 5-km vertical tubes in the earth's subsurface and in a large hydrocarbon formation of 1-km thickness with horizontal dimensions of the order of several kilometers, which show a high-density fluid mixture at the top of a light-density fluid mixture at steady state. The data in the 5-km tubes show liquid in the middle, and gas at the top and bottom. In the hydrocarbon formation, there is a gradual decrease of density with depth.

A theoretical model based on the thermodynamics of irreversible processes is used to provide an interpretation of the unusual density variation vs. depth both in the hydrocarbon formation and in the long tubes, as well as the unusual species distribution in the hydrocarbon formation. The results reveal that thermal diffusion (due to geothermal temperature gradient) causes the segregation of heavy components in the subsurface fluid mixture to the cold side in the earth (that

is, the top), overriding pressure and molecular diffusion (Fickian diffusion). As a consequence of the competition of these three diffusion effects, a heavy fluid-mixture can float at the top with a light fluid-mixture underneath. In the past, thermal diffusion has been thought of as a second-order effect. For the fluid mixture in our work, thermal diffusion is the main phenomenon affecting the spatial density and species distribution.

## Introduction

Hydrocarbon formations are large porous media saturated with hydrocarbon fluid mixtures in the earth's subsurface with a thickness of as much as 1 km or more, and horizontal dimensions in the order of kilometers or more. In these formations, denser fluid mixture is at the bottom and lighter fluid mixture is at the top. The species distribution follows density distribution; methane, which is usually the main component and often the smallest molecule of the fluid mixture, is more concentrated at the top while large molecules are more concentrated at the bottom. These variations are commonplace despite the geothermal temperature gradient in the earth.

The variation of species and density in an isothermal medium can be described by invoking the Gibbs criterion of thermodynamic equilibrium<sup>1</sup> in the gravity field for an  $n$  components fluid mixture, which leads to the following differential equation:<sup>2</sup>

$$\left( \frac{d\mu_i}{dz} = M_i g \right)_T, \quad i = 1, \dots, n. \quad (1)$$

In the above equation, the chemical potential of component  $i$ ,  $\mu_i$ , is a function of composition and pressure; it varies with vertical position,  $z$  ( $z$  is chosen to be positive downwards in Eq. 1). Other symbols in Eq. 1 are:  $M_i$ , the molecular weight of component  $i$ , and  $g$ , the gravitational



acceleration. Given composition and pressure at a reference point in the  $z$ -direction, Eq. 1 can be used to calculate the variation of composition and pressure as a function of depth ( $z$ ) or height ( $-z$ ).

Various authors have used the above equation to investigate the distribution of species in underground hydrocarbon formations.<sup>3,4</sup> In such calculations, the fluid density increases with depth. The concentration of the smallest molecular weight component, that is, methane, decreases with depth and that of heavy species increases with depth. Abundant data from hydrocarbon formations from different parts of the world (both onshore and offshore) are in qualitative agreement with predictions from Eq. 1.<sup>3,5-7</sup> The general consensus among geoscientists and especially petroleum engineers is that there is always gas at the top and oil at the bottom whenever there is more than one phase. Results from Eq. 1 are also in support of phase segregation.

We have recently conducted an extensive set of pressure, composition, and temperature measurements in a large gas field in Japan in order to investigate its unusual fluid distribution. Data in several 5-km deep vertical tubes (that is, wells) which extend from the earth surface to a depth of 5 km, and in the 1-km thick formation are measured. The data from the tubes show that there exists a motionless liquid in the middle with lighter gas at the top and the bottom of the tube. This is the first report of such an observation in geoscience and petroleum engineering literature to the best of our knowledge. Careful measurements in the hydrocarbon formation show that: 1) methane concentration increases with depth, 2) the concentration of heavy species which are grouped as heptane-plus (heptane and heavier species) decreases with depth, and 3) the fluid density decreases with depth. These are also first reports of their kind in the literature to the best of our knowledge. Previously, Temeng *et al.*<sup>8</sup> reported a heptane-plus decrease with depth in a hydrocarbon formation in Saudi Arabia without conclusive evidence.

Our measurements both in the formation and in the tubes (which are connected), confirm the existence of a dense fluid mixture floating on the top of a light fluid mixture.

In this article, we first present the measured data in detail, and then use a model based on the irreversible thermodynamics to interpret the fascinating trends in the data.

## Measured Data

We conducted extensive measurements in the naturally-fractured Yufutsu field, which is located in Hokkaido, Japan. The hydrocarbon formation is comprised of granite (age = 100-120 Ma) and conglomerate (age = 37-50 Ma) with negligible permeability and porosity; it has approximate horizontal dimensions of 4 km  $\times$  8 km with a maximum thickness of 1 km. The top of the formation is at 3800-m sbu-sea level (SSL) from the earth surface. The pressure at 4500-mSSL prior to producing hydrocarbons from the formation was 550 bar. Production of hydrocarbons began in February 1996. The temperature at 4500-mSSL is around 423 K. There is a horizontal temperature gradient of about 0.5 K/km in the formation. The vertical temperature gradient in the formation is about 2 K/100m and in the tubes is approximately equal to 2.5 K/100m. Measured data from fluid samples in various locations in the formation establish that the fluid is a near-critical gas in single phase state. Gas is defined as the fluid with temperature greater than the critical temperature.

A total of twelve wells have been drilled into the Yufutsu field. Various measurements from the wells establish good communication in the formation. Pressure interference testing between the wells establishes that all the wells have good communication with each other; the interference testing thus reveals horizontal communication in the formation. Tracer testing within each

well by injection of tracer from the top and tracer detection from the bottom reveals good vertical communication. In addition to pressure interference testing, and tracer testing, the initial formation pressure from all the wells provides the evidence of good communication in the entire formation.

In the Yufutsu field, only one well has been used for fluid production. Several wells are used as observation wells; there is no continuous fluid production from the observation wells except for short duration for testing purposes. These wells provide the opportunity for pressure measurement. Figure 1 shows a schematic of a well and the formation. Figure 2 shows the measured data in four different wells located in different parts of the field (see Fig. 3 for well locations). Figure 2-**a** shows measured pressure in the wells. Pressure is measured within the continuous hydrocarbon column inside the well tubing. The data show a high pressure gradient in the middle at a depth of around 2500 m. Using the pressure data, one can use the simple hydrostatic pressure expression  $dp = \rho g dz$  to calculate density when there is no convection, where  $p$  and  $\rho$  are pressure and density, respectively. We will later discuss the fact that natural convection is negligible in the formation and in the shut-in wells at steady state. Figure 2-**b** depicts the density data. At the bottom of the tube, the density is around 400 kg/m<sup>3</sup>; it gradually increases to over 500 kg/m<sup>3</sup> in the middle of the tube. Then there is a sharp density decrease to about 350 kg/m<sup>3</sup>. A density of 500 kg/m<sup>3</sup> corresponds to a liquid mixture while a density of 400 kg/m<sup>3</sup> and less corresponds to a gas mixture. The correspondence between density and phase-state will be discussed later. Pressure data and densities at different time intervals demonstrate that a steady state has been established for the data presented in Figure 2. Figure 4-**a** shows measured pressure data for well MY2 at different time intervals after the well is closed at the surface. Note that the wells are always connected to the formation. The pressure data

show that a steady state is reached after a few days of shut-in from the surface. Calculated densities from pressure data in well MY2 also show the establishment of steady state (see Fig. 4-b). Results for other wells show the same trend as in well MY2.

The composition, density, and pressure data in the formation from well AK1 (which is about 5 km from MY2, see Fig. 3) are shown in Fig. 5. Figure 5-a shows that methane concentration decreases from about 81% (mole) at the bottom to about 79% at the top of the formation in well AK1. Data also reveal that the high molecular weight species are more concentrated at the top; heptane-plus concentration increases from about 5% at the bottom, to about 6% at the top (see Fig. 5-b). Both methane and heptane-plus concentrations have an unusual vertical distribution. The data in the literature have an opposite trend;<sup>3,5-7</sup> methane concentration decreases with depth, while heptane-plus concentration increases with depth. Figure 5-c shows measured density with a decreasing trend vs. depth in the formation; the fluid density at the top is 25% higher than that at the bottom. The measured dew-point pressure is shown in Fig. 5-d; the dew-point pressure increases significantly with depth. For the published data in the literature, the dew-point pressure has the opposite trend.

## Theoretical Background

Pressure gradient in an isothermal cavity containing a multicomponent mixture results in a diffusion mass flux (the so-called pressure diffusion) and leads to the segregation of the large molecules to the high pressure side. In a gravity field, the high pressure side is the bottom in the direction of depth increase. The segregation expression in the form of the simple differential equation, that is, Eq. 1, can predict the effect of pressure diffusion (in the gravity field) on

species spatial distribution at isothermal conditions. The use of Eq. 1 may not produce valid results in a non-isothermal field. In subsurface hydrocarbon formations, temperature increases around 2 to 4 K/100m with depth. When there is no gravity effect, a temperature gradient in a hydrocarbon formation may result in the segregation of the light components (methane, for instance) towards the hot side (bottom of the formation) and the large molecular species (heptane-plus, for instance) toward the cold side (top of the formation) due to thermal diffusion—the so-called “Soret effect”.

In a non-isothermal multicomponent system, three diffusion processes compete: pressure diffusion, thermal diffusion, and molecular diffusion (Fickian diffusion, which has the tendency to homogenize the multicomponent mixture). The species distribution is mainly the result of these three competing diffusion processes in a convection-free system. When there exists a horizontal temperature gradient, convection always occurs in the formation; it is, consequently, the combined effect of convection and diffusion that determines the phase and species distribution in a formation.

In a recent theoretical study, Riley and Firoozabadi<sup>9</sup> included the effect of convection and all three diffusion processes on species distribution in a cavity. They demonstrated that for a binary mixture of methane and normal butane with typical horizontal and vertical temperature gradients of hydrocarbon formations, methane (light component) segregates to the bottom region when the permeability is low. This tendency from the thermal diffusion overrides pressure diffusion (that is gravity), so that butane (heavy component) “floats” above methane. Riley and Firoozabadi selected methane-butane mixture because thermal diffusion coefficient, molecular diffusion coefficient and volumetric behaviour have been measured for this binary. In two recent papers, Bou-Ali *et al.*<sup>10,11</sup> present experimental data in annular slot of height equal to 44 cm and

annular gap width equal to 0.193 cm (aspect ratio  $\approx 220$ ) —in the so-called thermogravitational column, and demonstrate that in fact the coupling of convection and thermal diffusion can give rise to a steady state adverse density gradient; a heavy liquid mixture floats on the top of a lighter liquid mixture in a thermogravitational column with a horizontal temperature gradient of  $10^4$  K/m. These authors considered binary mixtures of benzene and toluene with methanol and ethanol.

In the Yufutsu field, due to the combined effect of low horizontal temperature gradient, the low effective permeability (below 0.1 md in most parts), and the near-critical fluid,<sup>2</sup> the effect of convection on the fluid distribution in the formation can be neglected. We modeled convection in some calculations and the results show that in fact convection is negligible at low permeability as we will discuss soon.

Until very recently, there were no sound models for thermal diffusion flux and thermal diffusion ratios for a mixture of more than two components. Firoozabadi *et al.*<sup>12</sup> derived a theoretical model for thermal diffusion ratios using the thermodynamics of irreversible processes and the molecular kinetic approach incorporating explicitly the effect of non-equilibrium properties and equilibrium properties. With their formulation, we can proceed to model the data presented in Figs. 2, 4, and 5.

It is established in the literature that the effect of thermal diffusion on the species spatial distribution increases as the critical point is approached.<sup>13,14</sup> From the model derived by Firoozabadi *et al.*,<sup>12</sup> it has been shown that the thermal diffusion effect is closely related to the distance to the critical point; the closer the multicomponent mixture is to the critical point, the more significant is thermal diffusion. Because of the near-criticality of the hydrocarbon mixture in the Yufutsu field, thermal diffusion is the main phenomenon affecting compositional variation; it

causes the unusual observations discussed in the previous section.

In the theoretical modelling presented in the following, we do not include the process of filling, leakage, and biodegradation in the formation. We have carried out, however, calculations for the transient time with and without convection. An element of the formation of width equal to 1 km and thickness equal to 100 md was filled with a homogeneous fluid mixture from the reference interval (data to be presented in next section). It takes 1 to 3 million years to establish steady state from the combined effect of the three diffusion processes. With convection, it takes somewhat longer –about 2 to 6 million years for permeabilities of 0.01 to 1 md. With a permeability of 0.1 md, which is a typical permeability for the formation, there is very little effect of convection on species distribution when results are compared with the free-convection case.

In the wells, the aspect ratio is tubing diameter/tubing length  $\approx 0.15\text{m}/5000\text{m}=3\times 10^{-5}$  and there is a very low horizontal temperature gradient in the formation  $=5\times 10^{-4}\text{K/m}$ . One may, therefore, neglect natural convection. In view of these facts, and that the analysis of the stability with pressure diffusion has not yet been established in the convection literature, we will include only diffusion processes in our modelling. The comparison of the predicted results with measured data can then verify the validity of the assumption.

## Model

A theoretical model based on the powerful concepts of the thermodynamics of irreversible processes is employed to predict the unusual data described above. The model uses the expression of the diffusion flux from Ghorayeb and Firoozabadi;<sup>15</sup> it incorporates the thermal diffusion factors

from the model derived by Firoozabadi *et al.*<sup>12</sup>

Ghorayeb and Firoozabadi<sup>15</sup> used: 1) the entropy production expression;<sup>16</sup> 2) phenomenological laws of the thermodynamics of the irreversible processes;<sup>17,18</sup> 3) Onsager's reciprocal relations;<sup>17,18</sup> and 4) equilibrium thermodynamics at a local level<sup>16</sup> to derive the molar diffusion flux based on the molar average velocity  $\mathbf{J} = (\vec{J}_1, \dots, \vec{J}_{n-1})$  in a non-ideal fluid mixture of  $n$  components. The flux expression reads

$$\mathbf{J} = -c (\mathbf{D}^M \cdot \nabla \mathbf{x} + \mathbf{D}^T \cdot \nabla T + \mathbf{D}^P \cdot \nabla p), \quad (2)$$

where

$$\mathbf{D}^M \equiv [D_{ij}],$$

$$\mathbf{D}^T = (D_1^T, \dots, D_{n-1}^T),$$

$$\mathbf{D}^P = (D_1^P, \dots, D_{n-1}^P),$$

and

$$\nabla \mathbf{x} = (\nabla x_1, \dots, \nabla x_{n-1});$$

$c$  and  $x_i$ ,  $i = 1, \dots, n - 1$  are the total molar density and the mole fraction of component  $i$ , respectively. Other symbols are: the molecular diffusion coefficients  $D_{ij}$  ( $\text{m}^2 \text{s}^{-1}$ ), the thermal diffusion coefficients  $D_i^T$  ( $\text{m}^2 \text{s}^{-1} \text{K}^{-1}$ ), and the pressure diffusion coefficients  $D_i^P$  ( $\text{m}^2 \text{s}^{-1} \text{Pa}^{-1}$ ). Detailed expressions of the above coefficients are provided by Ghorayeb and Firoozabadi.<sup>15</sup> Eq. 2 can also be written as Ghorayeb and Firoozabadi<sup>15</sup>

$$\mathbf{J} = -c (\mathbf{D} \cdot \mathbf{M} \cdot \mathbf{L} \cdot \mathbf{W} \cdot \mathbf{F} \cdot \nabla \mathbf{x} + \mathbf{D} \cdot \mathbf{K}_T \cdot \nabla T + \mathbf{D} \cdot \mathbf{M} \cdot \mathbf{L} \cdot \mathbf{V} \cdot \nabla p), \quad (3)$$

where  $\mathbf{L} \equiv [L_{ij}]$  is the matrix of the phenomenological coefficients Ghorayeb and Firoozabadi.<sup>15</sup>



The symbols in Eq. 3 are defined by:

$$\begin{aligned}
\mathbf{D} &\equiv [D_{ij}] = \left[ \frac{RL_{ii}}{cM_iM_nx_ix_n} \delta_{ij} \right] & i, j = 1, \dots, n-1, \\
\mathbf{F} &\equiv [F_{ij}] = \left[ \frac{\partial \ln f_i}{\partial x_j} \Big|_{\mathbf{x}_j, T, P} \right] & i, j = 1, \dots, n-1, \\
\mathbf{M} &\equiv [M_{ij}] = \left[ \frac{M_ix_i}{L_{ii}} \delta_{ij} \right] & i, j = 1, \dots, n-1, \\
\mathbf{W} &\equiv [W_{ij}] = \left[ \frac{M_jx_j + M_nx_n\delta_{ij}}{M_j} \right] & i, j = 1, \dots, n-1.
\end{aligned}$$

In the above expressions,  $R$ ,  $f_i$  and  $\delta_{ij}$  denote the universal gas constant, the fugacity of component  $i$ , and the Kronecker delta, respectively; the subscript  $\mathbf{x}_j$  is defined by  $(x_1, \dots, x_{j-1}, x_{j+1}, \dots, x_{n-1})$ .

$\mathbf{K}_T$  represents the column vector of the thermal diffusion ratios in a multicomponent mixtures.

From Firoozabadi *et al.*<sup>12</sup>  $\mathbf{K}_T$  can be written as:

$$\mathbf{K}_T = \frac{M_nx_n}{RT^2} \mathbf{M.L.Q.} \quad (4)$$

The column vector  $\mathbf{Q}$  is given by

$$\mathbf{Q} \equiv \left[ \frac{Q_i^*}{M_i} - \frac{Q_n^*}{M_n} \right] \quad i = 1, \dots, n-1;$$

$Q_i^*$  is the net heat of transport of component  $i$  given by Firoozabadi *et al.*<sup>12</sup>

$$Q_i^* = -\frac{\Delta \bar{U}_i}{\tau_i} + \left[ \sum_{j=1}^n \frac{x_j \Delta \bar{U}_j}{\tau_j} \right] \frac{\bar{V}_i}{\sum_{j=1}^n x_j \bar{V}_j}, \quad i = 1, \dots, n, \quad (5)$$

where  $\Delta \bar{U}_i$  is the partial molar internal energy departure of component  $i$  and  $\tau_i = \Delta U_i^{vap} / \Delta U_i^{vis}$ ;  $\Delta U_i^{vap}$  and  $\Delta U_i^{vis}$  are the energy of vaporization and the energy of viscous flow of pure component  $i$ , respectively.  $\Delta \bar{U}_i$  is calculated using the PR-EOS;<sup>19</sup> the values of  $\tau_i$  used in this work are described later in this article. Using Eq. 4, Eq. 2 reads

$$\mathbf{J} = -c \left( \mathbf{D.M.L.W.F.} \nabla \mathbf{x} + \frac{M_nx_n}{RT^2} \mathbf{D.M.L.Q} \nabla T + \mathbf{D.M.L.V} \nabla p \right). \quad (6)$$

At steady state, the diffusion flux vanishes; Eq. 6 then reduces to

$$\mathbf{W} \cdot \mathbf{F} \cdot \nabla \mathbf{x} + \frac{M_n x_n}{RT^2} \mathbf{Q} \cdot \nabla T + \mathbf{V} \cdot \nabla p = 0. \quad (7)$$

At isothermal conditions, Eq. 7 reads

$$\mathbf{W} \cdot \mathbf{F} \cdot \nabla \mathbf{x} + \mathbf{V} \cdot \nabla p = 0 \quad (8)$$

which provides the condition for thermodynamic equilibrium in an isothermal  $n$  components mixture. One can readily derive Eq. 1 from Eq. 8.

When pressure and composition are known at a reference-point (the sample point), one can calculate composition and pressure in the entire column starting from the reference-point. The superscript  $m$  and  $m - 1$  appearing in the following denote grids  $m$  and  $m - 1$  in the vertical direction (assuming that composition and pressure are known at grid  $m - 1$ ). Given pressure and composition at depth  $z^{m-1}$ , Eq. 7 can be written at depth  $z^m$  to obtain the unknowns using a forward first-order finite difference scheme:

$$\sum_{j=1}^{n-1} \sum_{k=1}^{n-1} \mathbf{W}_{ik} \mathbf{F}_{kj} (x_j^m - x_j^{m-1}) + \rho g \mathbf{V}_i (z^m - z^{m-1}) + \frac{M_n x_n}{RT^2} \mathbf{Q}_i (T^m - T^{m-1}) = 0, \quad i = 1, \dots, n - 1. \quad (9)$$

Eq. 9 is solved using the Newton method. Given  $p^{m-1}$ , and  $x_i^{m-1}$ ,  $i = 1, \dots, n - 1$  at depth  $z^{m-1}$ , the initial guess for solution at depth  $z^m$  for  $p^m$  and  $x_i^m$  is taken as  $p^{m-1}$  and  $x_i^{m-1}$ , respectively. This procedure converges quadratically everywhere in the vertical column except when crossing a gas-liquid interface. Because of the discontinuity of composition and pressure gradient across a gas-liquid interface, a special numerical treatment is used for convergence. Assume that the mixture at  $z^{m-1}$  is liquid. After each Newton iteration, the state of the intermediate solution

is tested (whether it is single- or two-phase). Once we find that the intermediate solution is in a two-phase state, it is forced to come back to the single-phase state by selecting the liquid-phase composition as an intermediate solution. We repeat the process a fixed number of times (say 30 times); if the mixture is still in a two-phase state, the implication is that there is a phase change through an interface.

If the transition from liquid to gas occurs between depths  $z^{m_0}$  and  $z^{m_0+1}$ , we assume isothermal conditions between the two depths, which is a good approximation, provided that  $z^{m_0+1} - z^{m_0}$  is very small. The isothermal assumption implies that the temperatures at point  $z^{m_0}$  and  $z^{m_0+1}$  are equal and allows the use of Eq. 8 for calculating the solution at  $z^{m_0+1}$ . The numerical solution of Eq. 8 at  $z^{m_0+1}$  (starting from the solution at  $z^{m_0}$  as the initial guess) converges, provided that the state of the intermediate solution is tested at each Newton iteration; when the two-phase region is encountered, the gas-phase is selected as the appropriate state.

## Results and Discussion

Table 1 presents composition and other relevant information for the reference-interval in well AK1 selected as the reference-point (the depth of the reference-point is the mid-depth of the reference-interval). The sample contains small amounts of nitrogen and carbon dioxide which are added to methane. The critical parameters and the acentric factor of  $C_{30+}$  (triacontane and heavier species) are slightly adjusted to match the measured constant volume depletion (CVD) data.<sup>20</sup> The agreement between data and calculations is very good, except for the dew-point pressure, where calculations using the Peng Robinson equation of state (PR-EOS)<sup>19</sup> provide a value which is about 20 bar lower than the measured dew-point pressure. The critical parameters

are from the Cavett correlation;<sup>21</sup> the critical temperature, the critical pressure and the acentric factor for  $C_{30+}$  are:  $T_c = 910.55$  K,  $p_c = 8.620$  bar and  $\omega = 1.955$ . To match the measured CVD data with the calculations from the PR-EOS,  $T_c$ ,  $p_c$  and  $\omega$  of  $C_{30+}$  are decreased 9%, 18%, and 25%, respectively.<sup>22</sup> The temperature varies almost linearly vs. depth as previously discussed.

Figure 6 shows the model results together with data. The agreement between model predictions and data is good for methane (Fig. 6-a), heptane-plus (Fig. 6-b), and density (Fig. 6-c). However, the agreement between dew-point data and the predictions is not good (Fig. 6-d). This is to be expected because even at the reference-point the predicted dew-point is some 20 bar lower than the measured value. For  $z < 3941$  mSSL, the predicted hydrocarbon mixture exhibits a dew-point pressure behaviour (Fig. 6-d). At  $z = 3941$  mSSL a transition dew-point pressure / bubble-point pressure behaviour is predicted. The transition gas-liquid causes a significant increase in density (Fig. 6-c) without a distinct gas-liquid interface; composition and pressure gradient are continuous in the formation. Note that without thermal diffusion, methane and heptane-plus segregate towards the top and the bottom of the formation, respectively (results are not shown). It is only due to the strong effect of thermal diffusion that this opposite effect is observed.

One main purpose of this work is to predict data in Fig. 2 using our diffusion model and relate the observed well-tube data to those in the formation. In the following, we present results from wells MY1 and NM1 since recent samples from these two wells at shut-in conditions are available. Table 2 presents composition and other relevant data at the reference-point for these two wells.

In view of the large variation of the molecular weight of  $C_{30+}$  across a vertical column of 5 km, we assume that  $C_{30+}$  molecular weight varies linearly with its mole fraction. The slope and the

constant of this linear variation are determined from data at the reference-point, and assuming that, when the mole fraction of  $C_{30+}$  becomes very small, the molecular weight of  $C_{30+}$  is equal to that of  $C_{30}$ . The  $C_{30+}$  critical properties and acentric factor are not adjusted, however, for the change in the molecular weight. The  $\tau$  values (see Eq. 5) in Table 1 are for the critical region (in the formation). Above the formation in the tubes, the fluid moves away from the critical region as depth decreases. We assume that  $\tau$  used for calculating the thermal diffusion coefficients varies linearly vs. depth with values at the bottom of the well equal to those in Table 1; at the top of the well (far from the critical conditions),  $\tau_i = 4.0$ ,  $i = 1, n$ .<sup>23</sup> A constant value  $\tau_i = 4.0$ ,  $i = 1, n$  from Ghorayeb and Firoozabadi<sup>24</sup> provides results which are in good agreement with data. Note that due to the assumptions in deriving the expression for the thermal diffusion factors in the critical region,<sup>23</sup> the adjustment of the  $\tau$  values is justified in the manner performed in this work.

Figure 7 depicts density and pressure vs. depth from the data and the model for wells MY1 (Fig. 7, left) and NM1 (Fig. 7, right). An excellent agreement between density and pressure data and theory is observed. In order to analyze the results, we calculate the saturation pressure along the 5-km long tubes; the results are presented in Figs. 7-a and c. Results from the saturation pressure calculation show that there exists liquid in the middle of the tube and gas at the bottom and at the top. A transition gas-liquid (without a distinct gas-liquid interface) occurs in the lower part of the tube (Fig. 7-a and Fig. 7-c), as already shown in the previous section. Composition and pressure gradient are continuous when crossing this transition; the mixture changes from a dew-point pressure to a bubble-point pressure behaviour. This transition occurs at  $z = 3801$  and  $z = 3550$  mSSL for MY1 and NM1, respectively. A liquid leg exists for  $2465 < z < 3801$  and  $2775 < z < 3550$  mSSL for MY1 and NM1, respectively. Density reaches a maximum at  $z = 2465$  and  $z = 2775$  mSSL for wells MY1 and NM1, respectively, as shown in Fig. 7-b and Fig. 7-d.

At the top, a liquid-gas transition occurs via a distinct gas-liquid interface where composition and pressure gradient are discontinuous. Density is, consequently, discontinuous at this depth; it drops from 583.5 to 319.5 kg/m<sup>3</sup> for well MY1. Note that the dew-point pressure increases with depth for  $z < 2775$  mSSL while it decreases with depth for  $z > 3801$  mSSL. This is the first report of such a behaviour for dew-point pressure vs. depth in the literature for a hydrocarbon formation.

For further investigation of the correspondence between density and phase-state, we calculated the phase envelopes (pressure-temperature diagrams) for five representative samples in the shut-in well MY1: one sample from each of the three regions described above and depicted in Fig. 7, as well as two other samples corresponding to the limit of the gas and liquid regions (which meet at the gas-liquid interface around the middle of the tube). The results are shown in Fig. 8. The temperature for samples (II) and (III) is less than the critical temperature (liquid region), while it is greater than the critical temperature for sample (I) (gas region). Note that the critical point for the top two samples (IV and V), if it exists, should be to the left of the solid circles in the pressure-temperature diagrams.

In summary, model results, which are in excellent agreement with data, show a unique behaviour: the shut-in tubes consist of three regions 1) gas in the lower part where the dew-point pressure decreases with depth, 2) liquid in the middle where the bubble-point pressure increases with depth, 3) gas in the upper part where the dew-point pressure increases with depth. The expressions used in our calculations are mainly based on the relations derived from the thermodynamics of irreversible processes. This work shows clearly the usefulness of the thermodynamics of irreversible processes in the understanding of unusual fluid distributions in the earth's subsurface.

## Nomenclature

- $c$  = total molar density, mole/m<sup>3</sup>
- $D_{ij}^M$  = molecular diffusion coefficient, L<sup>2</sup>/t, m<sup>2</sup>/s
- $D_i^p$  = pressure diffusion coefficient, L<sup>3</sup>t/m, m<sup>2</sup>/s.Pa
- $D_i^T$  = thermal diffusion coefficient, L<sup>2</sup>/tK, m<sup>2</sup>/s.K
- $f_i$  = fugacity of component  $i$ , m/Lt<sup>2</sup>, Pa
- $g$  = acceleration of gravity, L/t<sup>2</sup>, m/s<sup>2</sup>
- $\mathbf{J}_i$  = molar diffusive flux of component  $i$ , mole/m<sup>2</sup>.s
- $k_{Ti}$  = thermal diffusion ratio of component  $i$
- $L_{ij}$  = phenomenological coefficients
- $M$  = total molecular weight, kg/mole
- $M_i$  = molecular weight of component  $i$ , kg/mole
- $N_h$  = number of grids in the horizontal direction
- $n$  = number of components
- $p$  = pressure, m/Lt<sup>2</sup>, bar
- $Q_i^*$  = net heat of transport of component  $i$
- $R$  = gas constant, Pa.m<sup>3</sup>/K.mole
- $T$  = temperature, T, K
- $U_i^{vap}$  = energy of vaporization of component  $i$
- $U_i^{vis}$  = energy of viscous flow of component  $i$
- $\bar{U}_i$  = partial molar internal energy of departure of component  $i$
- $\bar{V}_i$  = partial molar volume of component  $i$

$x_i$  = mole fraction of component  $i$ , dimensionless

$z$  = vertical position (positive downwards)

$\mu_i$  = chemical potential of component  $i$

$\delta$  = Kronecker delta, dimensionless

$\rho$  = density, kg/m<sup>3</sup>

$\omega$  = acentric factor, dimensionless

## Superscript

0 = reference-point

$b$  = reservoir bottom

$c$  = critical point

$bub$  = bubblepoint

$dew$  = dewpoint

$n$  = Newton iteration

$m$  = grid in the vertical direction

$t$  = reservoir top

$sat$  = saturation

## Acknowledgments

A grant from Japan National Oil Corporation (JNOC) to Japex provided the major funding for this work. Support was also provided by Japex and other members of the Reservoir Engineer-



ing Research Institute (RERI) and the US DOE grant DE-FG22-96BC14850. Their support is appreciated. We also thank Japex for permission to publish this work.

## References

1. Gibbs, J.W.: *Collected Works—Vol. I—Thermodynamics*, Yale University Press. (1957).
2. Firoozabadi, A.: *Thermodynamics of Hydrocarbon Reservoirs*, McGraw-Hill, New York (1999).
3. Schulte A.M.: “Compositional variation within a hydrocarbon column due to gravity,” paper SPE 9235 presented at the 1980 SPE Annual Technical Conference and Exhibition, Dallas, Texas, September 27-30.
4. Hirschberg A.: “Role of asphaltenes in compositional grading of a reservoir’s fluid column,” *JPT* (January 1988) 89.
5. Wheaton R.J.: “Treatment of variations of composition in gas-condensate reservoirs,” *SPERE* (May 1991) 239.
6. Creek, J.L. and Schrader, M.L.: “East Painter reservoir: an example of a compositional gradient from a gravitational field,” paper SPE 14411 presented at the 1985 SPE Annual Technical Conference and Exhibition, Las Vegas, NV, 22-25 September.
7. Metcalfe R.S., Vogel J.L. and Morris R.W.: Compositional gradients in the Anschutz Ranch East field, *SPERE* (August 1988) 1025.
8. Temeng K.O., Al-Sadeg M.J. and Al-Mulhim A.: “Compositional grading in the Ghawar

- Khuff Reservoirs,” paper SPE 49270 presented at the 1998 SPE Annual Technical Conference and Exhibition, New Orleans, Louisiana, 27-30 September.
9. Riley M.F. and Firoozabadi A.: “Compositional variation in hydrocarbon reservoirs with natural convection and diffusion,” *AIChE J.* (1998) **44**, 452.
  10. Bou-Ali M.M., Ecenarro O., Madariaga J.A., and Santamaria, C.M.: “Stability of convection in a vertical binary fluid layer with an adverse density gradient,” *Phys. Rev. E* (1999), Vol. 59, 1250.
  11. Bou-Ali M.M., Ecenarro O., Madariaga J.A., and Santamaria, C.M.: “Measurement of negative Soret coefficients in a vertical fluid layer with an adverse density gradient,” *Phys. Rev. E* (2000), Vol. 62, 1420.
  12. Firoozabadi, A., Ghorayeb, K., and Shukla K.: “Theoretical Model of thermal diffusion factors in multicomponent mixtures,” *AIChE J.* (May 2000) 892.
  13. Luettmer-Strathmann, J., and Sengers, J.V.: The transport properties of fluid mixtures near the vapor-liquid critical line,” *J. Chem. Phys.* (1996), Vol. 104, 3026.
  14. Haase, R., Dücker, K.H., Buchner, H., and Schwinum, J.: “Thermal diffusion in the critical region of binary liquid systems,” *Zeitschrift für Physikalische Chemie* (1994), Vol. 18, 113.
  15. Ghorayeb, K., and Firoozabadi, A.: “Molecular, pressure, and thermal diffusion in nonideal multicomponent mixtures,” *AIChE J.* (May 2000) 883.
  16. de Groot, S. R., and Mazur, P.: *Non-Equilibrium Thermodynamics*, Dover Edition, New York, (1984).

17. Onsager, L.: "Reciprocal relations in irreversible processes. I," *Phys. Rev.* (1931), Vol. 37, 405.
18. Onsager, L.: "Reciprocal relations in irreversible processes. II.," *Phys. Rev.* (1931), Vol. 38, 2265.
19. Peng, D. Y., and Robinson, D. B.: "A new two-constant equation of state," *Ind. Eng. Chem. Fund.* (1976), Vol. 15, 59.
20. Dake, L.P.: *Fundamentals of Reservoir Engineering*, Elsevier, 1978.
21. Cavett, R. H.: "Physical data for distillation calculations-vapor-liquid equilibria," Proc. API 27th Mid-Year Meeting (1962), Vol. 52, 351.
22. Arbabi S. and Firoozabadi, A.: "Near critical phase behavior of reservoir fluids using equations of state," *SPE Advanced Technology Series* (1995), Vol. 3, No.1, 139.
23. Shukla, K. and Firoozabadi, A.: "A new model of thermal diffusion coefficients in binary hydrocarbon mixtures." *Ind. Eng. Chem. Res* (1998), Vol. 37, 3331.
24. Ghorayeb, K., and Firoozabadi, A.: "Modeling multicomponent diffusion and convection in porous media," *SPEJ* (June 2000) 158.

Composition	$x_i$	$M_i$	$k_{C_1j}$	$\tau_i$
C <sub>1</sub>	0.7923	16.043	0.000	4.0
C <sub>2</sub>	0.0758	30.070	0.000	4.0
C <sub>3</sub>	0.0312	44.097	0.000	4.0
iC <sub>4</sub> -nC <sub>4</sub>	0.0177	58.124	0.000	3.5
iC <sub>5</sub> -nC <sub>5</sub>	0.0076	72.151	0.000	2.5
C <sub>6</sub>	0.0157	84.0	0.000	2.2
C <sub>7</sub> -C <sub>9</sub>	0.0196	107.0	0.016	2.0
C <sub>10</sub> -C <sub>12</sub>	0.0108	147.0	0.019	1.8
C <sub>13</sub> -C <sub>15</sub>	0.0086	190.0	0.029	1.6
C <sub>16</sub> -C <sub>19</sub>	0.0076	237.0	0.035	1.4
C <sub>20</sub> -C <sub>24</sub>	0.0062	305.0	0.037	1.2
C <sub>25</sub> -C <sub>29</sub>	0.0039	374.0	0.037	1.1
C <sub>30+</sub>	0.0029	585.0	0.045	0.9
Mid-depth=4032 mSSL $T = 409.81$ K $P = 530.39$ bar $P_{dew} = 524.53$ bar Perforation intervals (mSSL): 4002.0 – 4026.0 and 4038.0 – 4062.0				

Table 1: Data at the reference-interval in well AK1: composition ( $x_i$ ), molecular weight ( $M_i$ ), interaction coefficients between methane and all the components /pseudo-components ( $k_{C_1j}$ ), and  $\tau_i$

Composition	MY1	NM1
C <sub>1</sub>	0.7646	0.8003
C <sub>2</sub>	0.0815	0.0778
C <sub>3</sub>	0.0379	0.0326
iC <sub>4</sub> -nC <sub>4</sub>	0.0230	0.0179
iC <sub>5</sub> -nC <sub>5</sub>	0.0094	0.0072
C <sub>6</sub>	0.0066	0.0049
C <sub>7</sub> -C <sub>9</sub>	0.0305	0.0252
C <sub>10</sub> -C <sub>12</sub>	0.0131	0.0091
C <sub>13</sub> -C <sub>15</sub>	0.0093	0.0068
C <sub>16</sub> -C <sub>19</sub>	0.0080	0.0061
C <sub>20</sub> -C <sub>24</sub>	0.0066	0.0051
C <sub>25</sub> -C <sub>29</sub>	0.0040	0.0030
C <sub>30+</sub>	0.0055	0.0040
Mid-depth, mSSL	4614.0	4233.8
<i>T</i> , K	422.03	414.82
<i>P</i> , bar	531.84	535.70
<i>P<sub>dew</sub></i> , bar	483.23	529.63
<i>M<sub>C30+</sub></i> , g/mole	762	630
Perforation intervals (mSSL)	4394.3 – 4423.0	4181.7 – 4289.1
	and	
	4474.8 – 4752.8	

Table 2: Relevant data at the reference-interval in wells MY1 and NM1

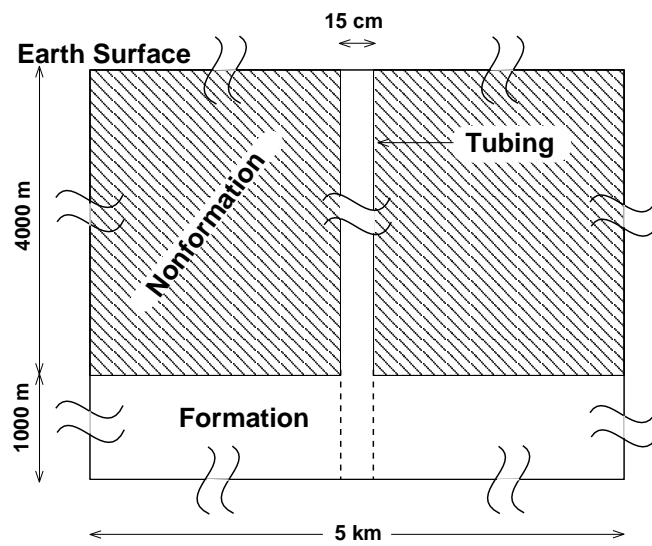


Figure 1: Schematic of a well tube and the hydrocarbon formation. The geometry is a 5-km vertical tube with 15 cm as diameter. The tube bottom part (around 1 km) is perforated allowing its communication with the hydrocarbon formation. The well is an open space and the hydrocarbon formation is a permeable medium. The shaded area is not part of the hydrocarbon formation.

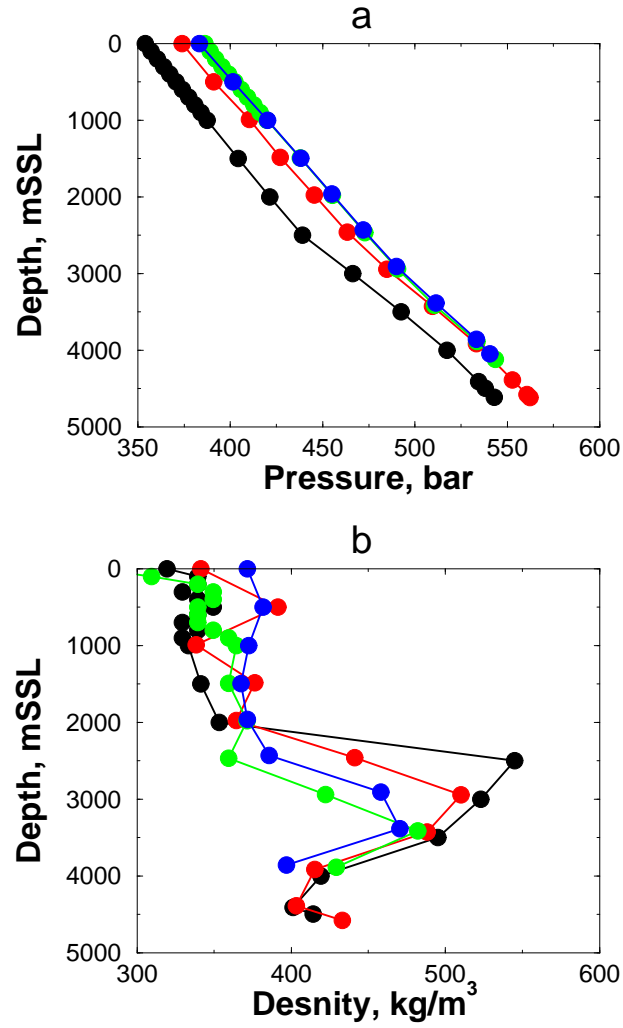


Figure 2: Measured pressure (a), and density (b) data of four different wells. (●): MY1, sampling date: 03/1999, shut-in period = 9 days; (●): MY2, sampling date: 10/1999, shut-in period = 560 days; (●): NM1, sampling date: 03/1999, shut-in period = 148 days; (●): NM2, sampling date: 10/1999, shut-in period = 1112 days. Measured pressure data for MY1 is about 20 bar less than the other wells (MY1 is the only producing well in the Yufutsu field).

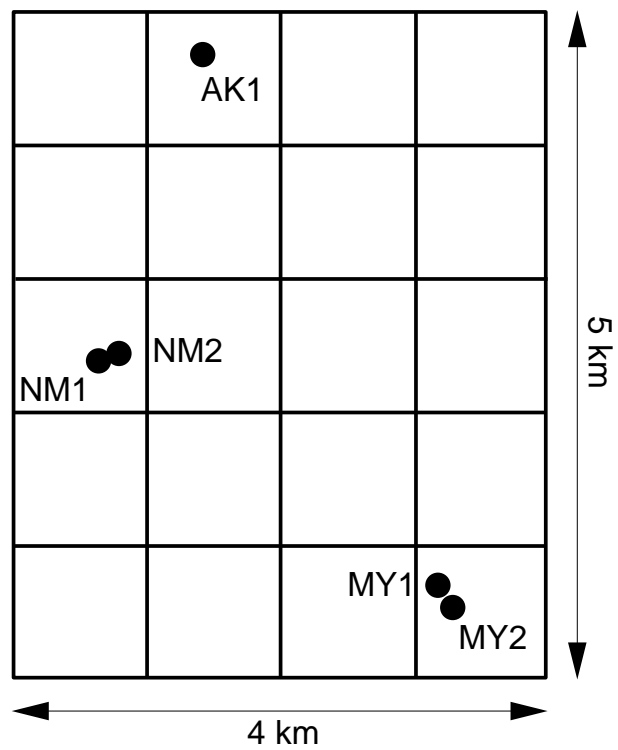


Figure 3: Location of wells in the horizontal plane



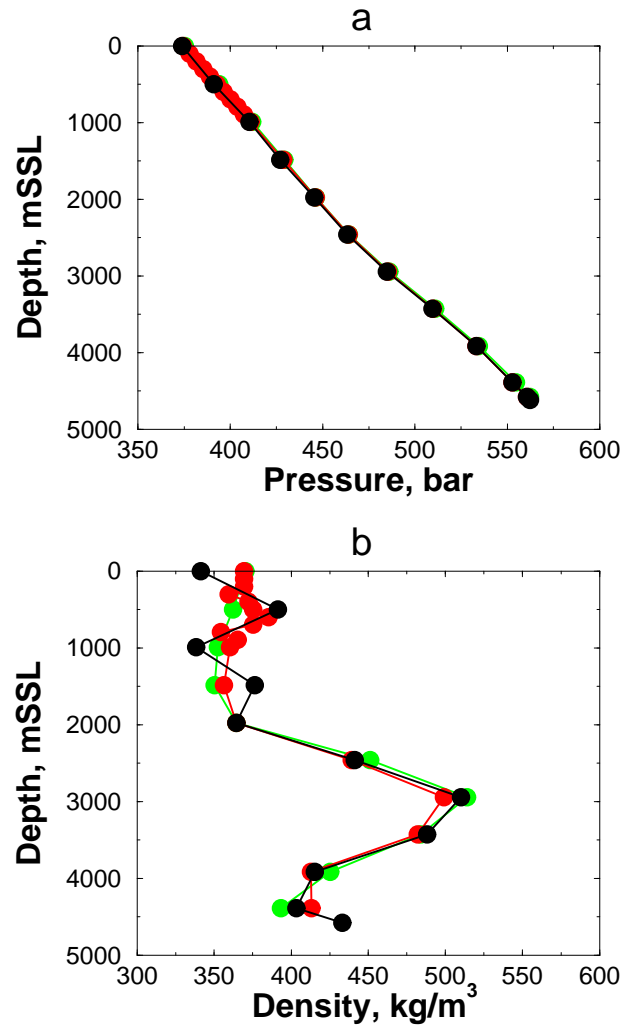


Figure 4: Measured pressure (a) and density (b) data for Well MY2. (●) sampling date: 03/1996, shut-in period = 61 days; (●) sampling date: 03/1999, shut-in period = 357 days; (●) sampling date: 10/1999, shut-in period = 560 days.

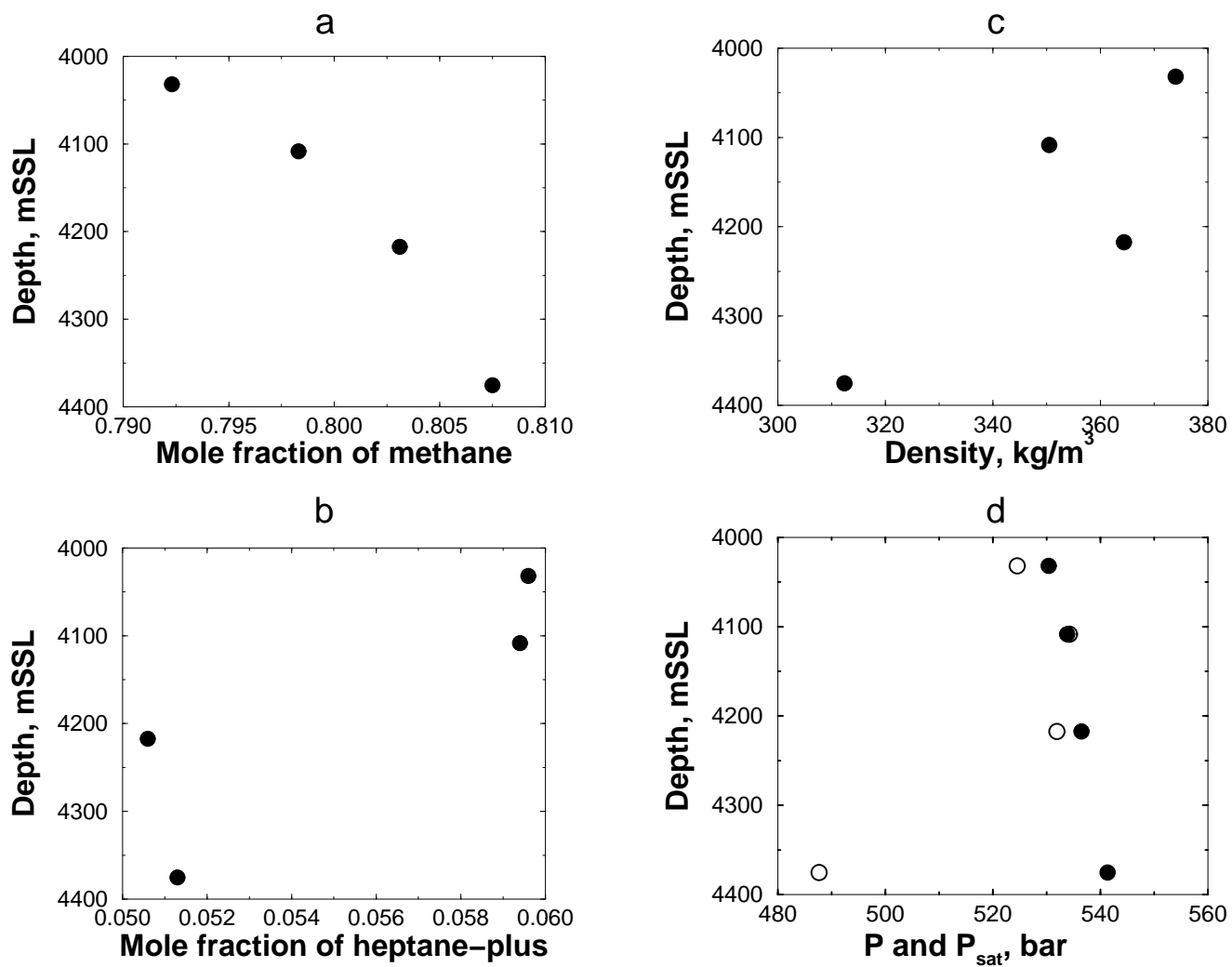


Figure 5: Measured data at four different depths from well AK1. (•) represents: the mole fraction of methane (a), mole fraction of heptane-plus (b), density (c), and pressure (d). (○) represents the measured dew-point pressure (d).

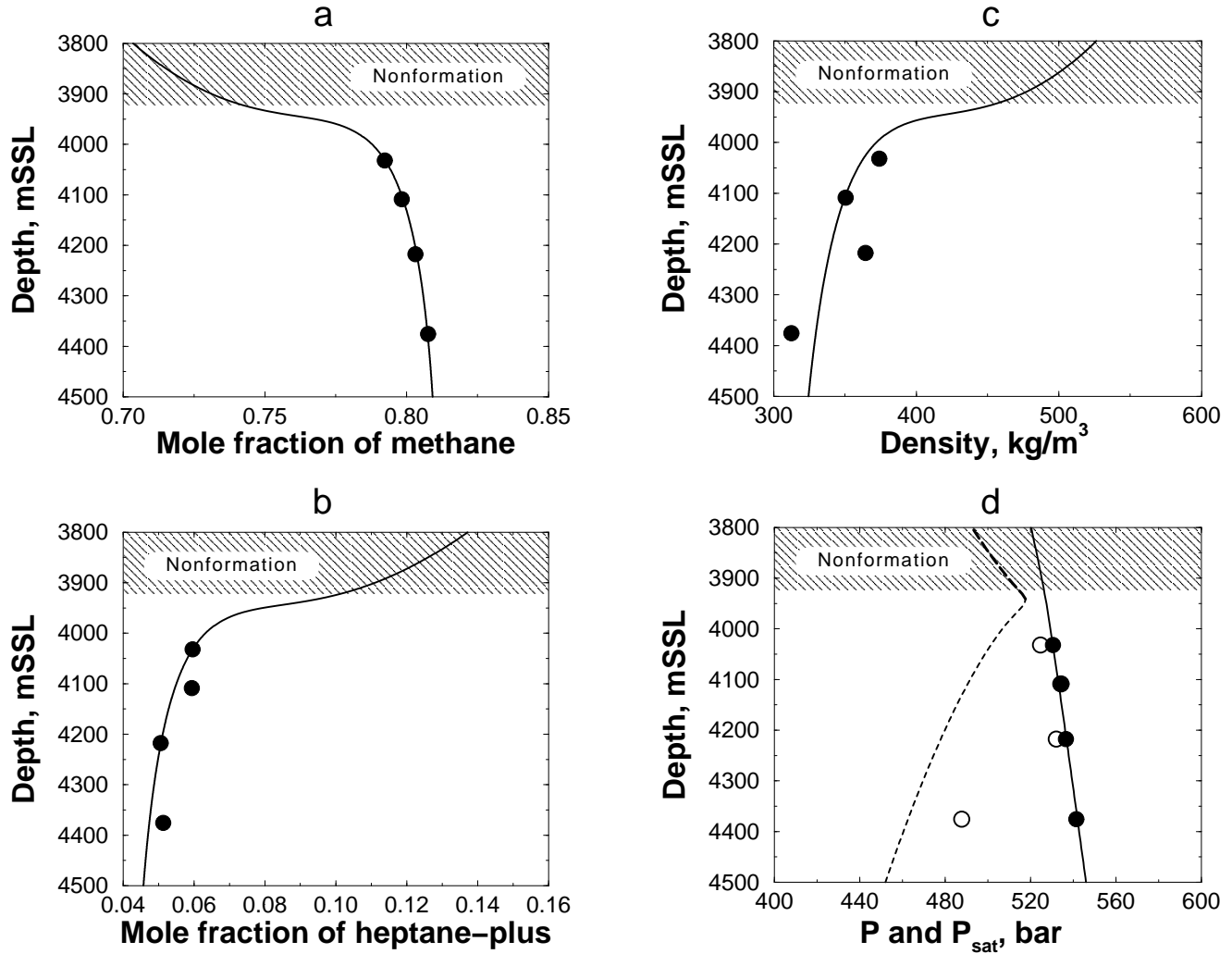


Figure 6: Measured data and model predictions for well AK1: predicted results from our model for the mole fraction of methane (a), mole fraction of heptane-plus (b), density (c), and pressure (d) are shown by solid lines. (●) represents: the mole fraction of methane (a), mole fraction of heptane-plus (b), density (c), and pressure (d). (○) represents the measured dew-point pressure (d). The dashed line in d represents a dewpoint pressure region (gas region); the long dashed line represents a bubblepoint pressure region (liquid region). The shaded part in a, b, c, and d is not part of the hydrocarbon formation.

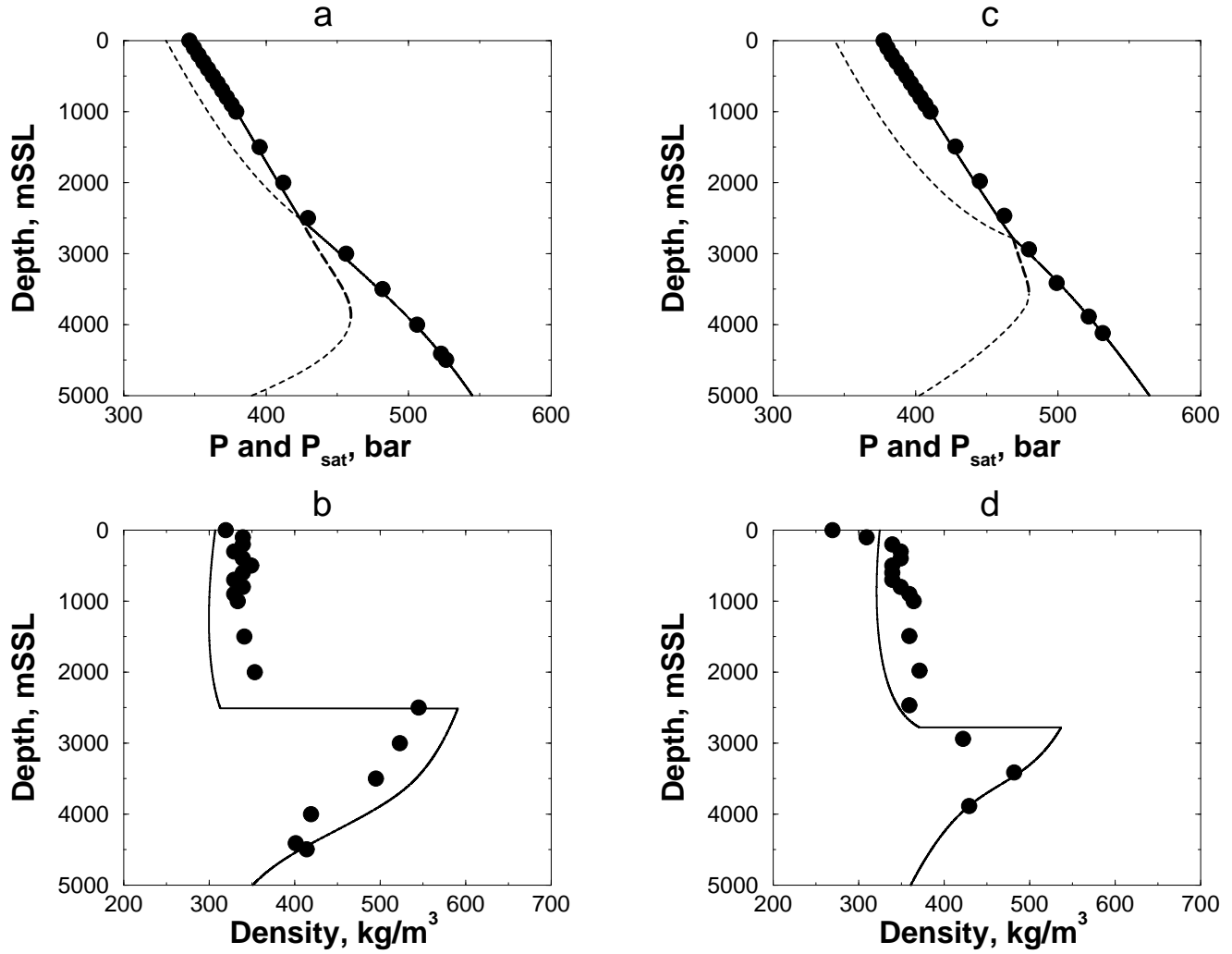


Figure 7: Measured data and model predictions from two different shut-in wells: MY1 (left) and NM1 (right) which are about 4 km apart. (•) represents measured data for both pressure and density; predicted results from our model for pressure (a and c) and density (b and d) are shown by solid lines. The dashed lines in a and c represent a dewpoint pressure region (gas region); the long dashed lines represent a bubblepoint pressure region (liquid region). Detailed information about these regions is provided in Fig. 8.

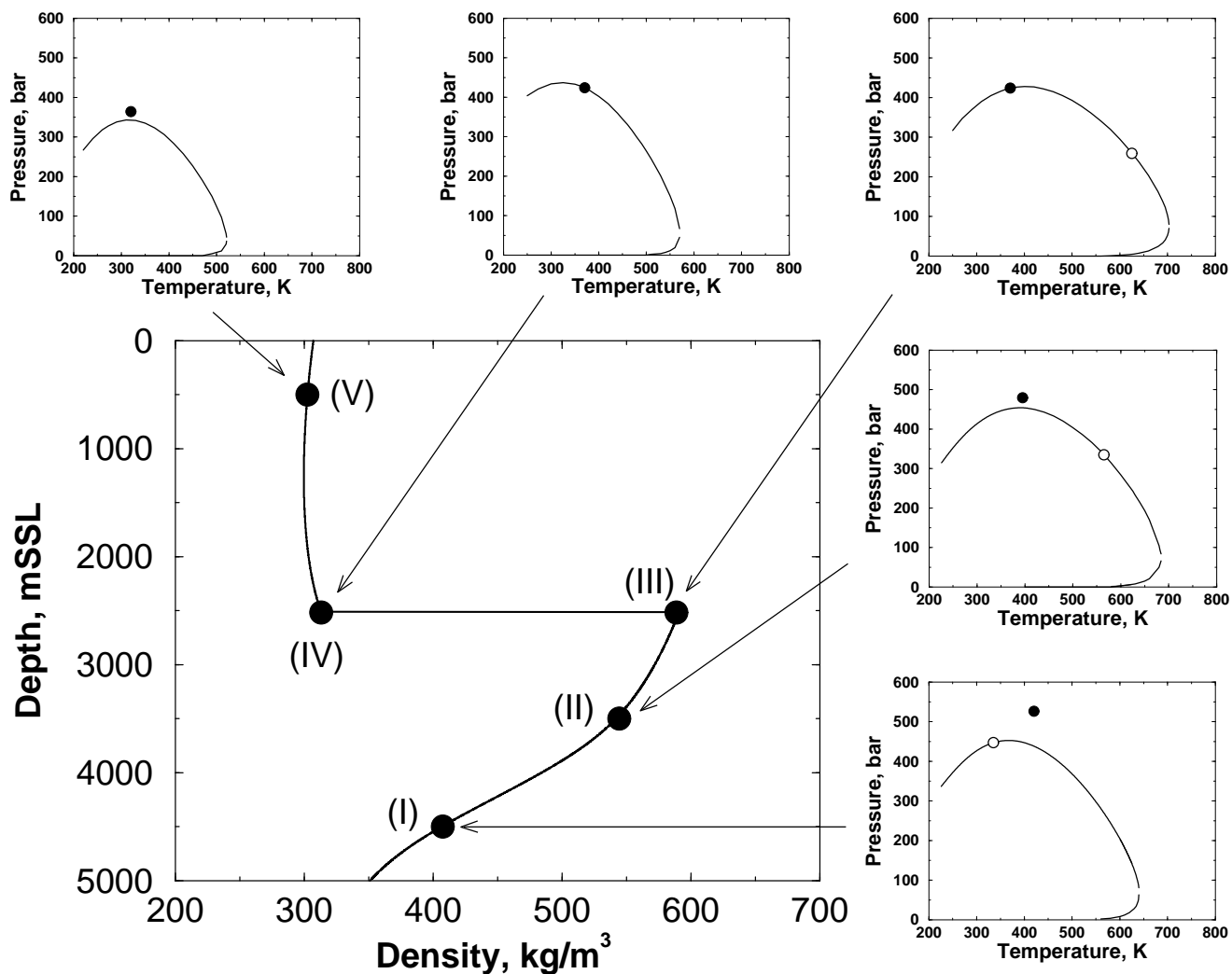


Figure 8: Predicted phase envelopes (pressure-temperature diagrams) at five depths for well MY1: (I) gas; (II) liquid; (III) liquid at bubble-point pressure (limit of the liquid region); (IV) gas at dew-point pressure (limit of the gas region); (V) gas. The exact depths of these samples are shown by  $\bullet$  in the density/depth plot; ( $\bullet$ ) also represents the location in the pressure-temperature diagrams of samples (I) through (V). ( $\circ$ ) represents the critical point at the corresponding composition. The critical temperature for (IV) and (V), if it exists, is less than 200 K.